INFORMATION TO USERS

This manuscript has been reproduced from the microfilm master. UMI films the text directly from the original or copy submitted. Thus, some thesis and dissertation copies are in typewriter face, while others may be from any type of computer printer.

The quality of this reproduction is dependent upon the quality of the copy submitted. Broken or indistinct print, colored or poor quality illustrations and photographs, print bleedthrough, substandard margins, and improper alignment can adversely affect reproduction.

In the unlikely event that the author did not send UMI a complete manuscript and there are missing pages, these will be noted. Also, if unauthorized copyright material had to be removed, a note will indicate the deletion.

Oversize materials (e.g., maps, drawings, charts) are reproduced by sectioning the original, beginning at the upper left-hand corner and continuing from left to right in equal sections with small overlaps.

ProQuest Information and Learning
300 North Zeeb Road, Ann Arbor, MI 48106-1346 USA
800-521-0600

CO-DEFORMATION
OF
A TWO-PHASE
FCC/BCC MATERIAL

By

CHAD SINCLAIR, B. Eng.

A Thesis

Submitted to the School of Graduate Studies

in Partial Fulfillment of the Requirements

for the Degree of

Doctor of Philosophy

McMaster University

CO-DEFORMATION OF A TWO-PHASE FCC/BCC MATERIAL

DOCTOR OF PHILOSOPHY
(Materials Science and Engineering)

McMASTER UNIERSITY
Hamilton, Ontario

TITLE:	Co-deformation of a Two-phase FCC/BCC Material
AUTHOR:	Chad W. Sinclair, B. Eng. (McMaster University)
SUPERVISORS:	Professors J.D. Embury and G. C. Weatherly
NUMBER OF PAGES:	xxii,, 236

ABSTRACT

The drive to produce materials with novel or beneficial combinations of properties has prompted research into a range of new materials and processing routes. In many applications one of the important design variables is the mechanical strength. Exceptional strengths can be achieved in certain materials consisting of two deformable phases when they are drawn into fine wires or rolled into thin sheets, the common example being pearlitic steel wire which can achieve strengths in excess of 5 GPa. The mechanisms that permit co-deformation and result in the observed strengthening are, however, not well understood.

In this thesis an approach was adopted whereby co-deformation of a well characterized model material has been studied primarily using uniaxial tensile tests. Directional solidification of a Cu-1.56at%Cr eutectic alloy has been used to produce material consisting of submicron diameter single crystals of Cr embedded within a polycrystalline Cu matrix. It has been shown that these two phases exhibit preferred crystallographic orientation relationships, habit planes and growth directions the same as those found for solid state precipitates of Cr in Cu. On deforming this material it is found that the Cr fibres yield at stresses close to the theoretical limit. However, their are able to continue to co-deform with the Cu matrix to large plastic strains. This process of co-deformation is observed to cause a rate of nearly constant work hardening that results in both high strength and high ductility. This behaviour has been attributed to the fact that the Cr fibres continue to carry increasing elastic strain beyond their yield thereby contributing to an increasing level of internal stress in the material. It is suggested that this mechanism may play an important role in other co-deformed two phase materials. In particular, it is suggested that this may provide one mechanism for the continued high rate of work hardening in heavily co-deformed two phase materials.

ACKNOWLEDGEMENTS

It has been a sincere privilege to have worked under the guidance of Prof. Embury and Prof. Weatherly for the duration of this project. Their encouragement, patience and knowledge have benefitted me in countless ways over the past four years. The knowledge gained at their hands will carry with me for the rest of my life.

This project could not have been started had it not been for the expertise of Mr. Jim Garrett of the Brockhouse Institute for Materials Research at McMaster. It was this expertise and "knowhow" that allowed for the production of directional solidified Cu-Cr. It was a pleasure to have worked with and to have learned from him.

Dr. Kelly Conlon of the NPMR, Chalk River Laboratories deserves a great deal of thanks for his time and patience in setting up the difficult experiments at Chalk River and for the many discussions concerning their interpretation. The late evenings and weekends were always greatly appreciated. The aid of Mr. John Fox in the form of technical expertise and Dr. John Root in the many incredibly useful conversations are also deeply appreciated.

Thanks are due to Dr. Olaf Engler, formerly of Los Alamos National Laboratory, who acted as host during two stays at the Center for Materials Science and who helped perform a number of experimental measurements. The knowledge gained on these trips has been of great value. Also at LANL, Dr. Ke Han and Dr. Marc Verdier are thanked for their advice and experimental help.

It was a pleasure to have had Dr. Aleksandra Perovic's help and suggestions regarding TEM work. Also, thanks must be extended to Dr. Muriel Veron who was assigned the (unenviable) task of teaching me electron microscopy when I first arrived. Dr. C. P. Luo is thanked for his experimental help in sorting out the crystallography of the as cast material and for his expertise in preparing the foils. The gracious and efficient help of the technical staff of the Brockhouse Institute and the Department of Materials Science and Engineering are also acknowledged.

It has been my privilege and pleasure to have been a part of the physical metallurgy group at McMaster. I have learned enormously from the faculty and students of this group. In particular, I am grateful to the past and present members of the A206 office. Although there is insufficient room here to thank them all individually, I owe a great dept of gratitude to each and everyone for the countless discussions, suggestions, and explanations and for the constant friendship that has seen me through these years.

Finally, I would like to thank my wife Jill for her understanding, patience and caring over this period. Her contributions to this thesis extend far beyond her help in editing this document. Without her unwavering support this would not have been possible.

TABLE OF CONTENTS

	Page
Abstract	iii
Acknowledgements	iv
Table of Contents	vi
List of Figures	viii
List of Tables	xxii
CHAPTER 1 - INTRODUCTION	1
CHAPTER 2 - LITERATURE REVIEW	4
2.1 Introduction	4
2.2 Macroscopic Characterization of the Co-deformation of Two-phase Materials	6
2.3 Mesoscopic Characterization of the Co-deformation of Two-phase Materials	23
2.4 Microscopic Characterization of the Co-deformation of Two-phase Materials	41
2.5 Previous Work on the Deformation of Cu-Cr Alloys	50
2.6 Summary of Literature Review	55
CHAPTER 3 - EXPERIMENTAL METHODS	56
3.1 Directional Solidification	56
3.2 Metallography	59
3.3 Electron Microscopy	60
3.4 Neutron Diffraction	62
3.5 Mechanical Testing	74
CHAPTER 4 - EXPERIMENTAL RESULTS	77
4.1 Introduction	77
4.2 The As-cast State of a Directionally Solidified Cu-1.56at% Cr Eutectic Alloy	77
4.3 The Deformation Behaviour of a Directionally Solidified Cu-1.56at% Cr Eutectic Alloy	101
4.4 Summary of Salient Experimental Results	139

CHAPTER 5 - DISCUSSION 142

5.1 Introduction 142
5.2 The As-cast State 142
5.3 Deformation Response of the Cu-Cr Eutectic Alloy in Uniaxial Tension 152
5.4 Large Strain Behaviour and the Process of Continued Co-deformation 183

CHAPTER 6 - EXTENSIONS FOR FUTURE WORK 222

CHAPTER 7 - CONCLUSIONS 227

BIBLIOGRAPHY 229

LIST OF FIGURES

		Page
Figure 2.1	Examples of fine-scale two-phase materials processed by a) solidification (directionally solidified Al-Al_3Ni, Davies, 1971), b) deformation processing (Cu-Nb, Han, 1999), and c) deposition (Kung et al., 1995).	5
Figure 2.2	Schematic illustration of macroscopic, mesoscopic and microscopic scales along with some of the important variables at each length scale.	6
Figure 2.3	a) Schematic stress-strain response for a material reinforced with continuous ductile fibres. b) The first three stages of deformation showing the response of matrix, fibres and overall composite.	8
Figure 2.4	Uniaxial stress-strain response of directionally solidified eutectic alloys. a) Ductile Ni-W (Garmong and Williams, 1975). b) Brittle Ni-NbC (McLean, 1983).	9
Figure 2.5	Cellular growth in a directionally solidified $Mg_{17}Al_{12}$-Mg eutectic alloy. Near colony boundaries eutectic growth becomes perturbed due to a non-planar interface (Kraft, 1966).	10
Figure 2.6	Effect of eutectic orientation on the uniaxial stress-strain behaviour of Al-Al_3Ni directionally solidified alloy (George et al., 1968).	10
Figure 2.7	Progressive refinement of Nb dendrites with drawing strain (Raabe, 1995). The Nb filaments have been chemically extracted from the Cu after strains of a) 0 b) 88.9% c) 94.8% and d) 99995%.	12
Figure 2.8	a) Stress-strain response of Cu-Nb alloys pre-strained by wire drawing to the indicated reductions in area (η) (Spitzig and Krotz, 1987). b) Similar to (a) but for Cu-Ta alloys (Frommeyer and Wasserman, 1975).	13
Figure 2.9	Ultimate tensile strength of Cu, Nb and Cu-Nb as a function of drawing strain. Also shown is the prediction of the UTS for the Cu-Nb using a rule of mixtures with the data for pure Cu and pure Nb (Spitzig and Krotz, 1987).	13
Figure 2.10	Embury and Fisher's (1966) fit of a Hall-Petch type equation to the strengthening obtained by wire drawing of eutectoid steel.	14
Figure 2.11	Figure 2.11 Use of a modified Embury-Fisher type model to predict the strengthening observed in drawn Cu-Nb and Cu-Ta (Spitzig, 1988). Here $\bar{\lambda}_o$ is the initial spacing between plates, η is the draw ratio and $\bar{t}_o$ is the initial scale of the embedded phase.	15

Figure 2.12	Two dimensional stress state corresponding to uniaxial tension (circle A). Maximum critical tensile stress fracture criteria represented by vertical line and flow criteria represented by horizontal line. Circles B and C show the effect of an increasing superimposed hydrostatic stress.	15
Figure 2.13	Comparison between the tensile behaviour of directionally solidified and conventionally cast Al-Al3Ni (Lemkey, et al., 1965).	17
Figure 2.14	a) Partitioning of strain between α (ε_a^d) and β (ε_a^d) phases (β harder) in a wire drawn Cu-Zn-Al alloy (Adnyana, 1982). b) As for a) but for the Cu-Nb system (Raabe, 1995).	18
Figure 2.15	Strain partitioning between α and β phases in brass deformed by rolling (Engler et al., 1995).	18
Figure 2.16	Measurement of strain partitioning for some simple metal-metal laminates with different ratios of hardness (Ozturk et al., 1994).	19
Figure 2.17	Inverse pole figures showing the effect of added second phase components on the texture development in the matrix phase. Deformation was achieved by wire drawing to a reduction of 95% in all cases (Bergmann et al., 1978).	20
Figure 2.18	Disruption of the plastic flow of the matrix phase by a hard embedded second phase (Bergmann et al., 1978).	20
Figure 2.19	The strength of metallic whiskers as a function of the size. a) Cr b) Cu c) Ni d) Co (from Mehan and Herzog, 1958).	25
Figure 2.20	A series of images taken during the bending of a niobium carbide whisker. Note that the whisker withstands strains of the order of 3 prior to fracture (Salkind et al., 1970).	26
Figure 2.21	a) Strength of extracted Cr whiskers as a function of their cross-sectional dimensions (reproduced from Salkind et al., 1970). b) Stress-strain response recorded during tensile straining of extracted Cr whisker (reproduced from Salkind et al., 1970).	27
Figure 2.22	Stress concentration (K) arising from the presence of a surface step on a whisker. It has been argued that such sub-micron defects may control the strength of fine-scale whiskers (Nohara, 1982).	28
Figure 2.23	Stress-strain curves obtained from Cu whisker tested in a "hard" machine (Yoshida, 1966).	28
Figure 2.24	A series of micrographs taken after measuring amounts of strain on a Cu whisker. The spread of plasticity along the length of the whisker can be seen (Brenner, 1958).	29

Figure 2.25	Markings on an Fe whisker after the onset of plastic deformation. The localization of strain into slip bands at specific points along the length of the fibre reduces the overall ductility (Brenner, 1958).	29
Figure 2.26	The development of internal stresses in a material can occur on different length scales; I macroscopic stresses due to an inhomogeneous applied deformation, II intergranular stresses, III local stresses (Fitzpatrick et al., 1997).	31
Figure 2.27	Schematic stress-strain curve for a hypothetical material that consists of an elastic fibre contained within an elastic/plastic matrix. The elastic properties and the volume fraction are assumed to be the same for the two phases.	32
Figure 2.28	Common parameters used to describe the Bauschinger effect (Abel, 1987).	33
Figure 2.29	Common technique for measuring permanent softening. The reverse flow curve has been transformed into the first quadrant (Abel, 1987).	33
Figure 2.30	The mean internal stress work hardening measured Bauschinger tests in W fibre reinforced Cu at 293K and 77K (Lilholt, 1977b).	35
Figure 2.31	Tension/compression loops for an Al-Al_3Ni directionally solidified eutectic. Plastic flow in compression occurs prior to the applied load becoming compressive (Lasalmonie and Martin, 1974).	36
Figure 2.32	The permanent softening measured by Clark and Lilholt (1975) from the data shown in figure 2.31.	37
Figure 2.33	Stresses deduced from elastic strains by x-ray diffraction for Al-W fibre composites plotted versus the macroscopic strain. The macroscopic (composite) stress-strain curves are shown for comparison (Cheskis and Heckel, 1970).	38
Figure 2.34	Measured lattice strain versus applied stress for Al-Be two-phase material. a) Strains measured parallel to the tensile axis, and b) perpendicular to tensile axis (Carter and Bourke, 2000).	39
Figure 2.35	Residual stresses measured by neutron diffraction for Cu-Nb two-phase material wire drawn to different strains (Han et al., 1999).	39
Figure 2.36	Processes of plastic relaxation that may occur in materials containing equiaxed particles (Brown and Stobbs, 1971).	42
Figure 2.37	Plastic relaxation by a process of double cross-slip in fibre reinforced materials (Lilholt, 1993).	43
Figure 2.38	Secondary slip in the the softer phase (α) of an α–β brass bicrystal in order to partially accommodate the plastic misfit between the two phases (Fat-Halla et al., 1979).	44
Figure 2.39	Schematic showing four possible mechanisms of slip transfer across a phase boundary (Sutton and Balluffi, 1995).	45

Figure 2.40	a) Observation of slip transmission in K-S oriented duplex stainless steel (Verhaeghe et al., 1997). b) Slip transfer across phase interface in K-S oriented γ–β phases in a directionally solidified Ni-Fe-Al alloy.	46
Figure 2.41	TEM micrograph showing dislocations being emitted from the phase boundary in a directionally solidified Ni-W alloy (Garmong, 1976).	46
Figure 2.42	Schematic diagram showing a) bulging of pre-existing interfacial dislocation into a phase and b) nucleation of a dislocation at the phase interface (Louchet, 1998).	47
Figure 2.43	A series of in-situ TEM images taken during tensile testing of a Cu/Ni multilayer showing the bulging of interfacial dislocations in the narrow channels of the Cu phase similar to the processes shown in figure 2.42 (Anderson et al., 1999).	48
Figure 2.44	Atomic positions in atomistic model of a Cu/Ni bilayer showing the position of a dislocation as a function of applied stress (dislocation indicated by vectors) (Rao and Hazzeldine, 2000).	49
Figure 2.45	Measured yield strength of Cr as a function of test temperature (Gilbert et al., 1963).	51
Figure 2.46	Optical micrographs from Hertzberg and Kraft (1963) showing fracture of Cr whisker on surface of bend specimen.	52
Figure 2.47	Schematic illustrating the mode of fracture envisioned by Hertzberg and Kraft to occur in directionally solidified Cu-Cr (Salkind et al., 1970).	52
Figure 2.48	Microstructure of cold rolled Cu-15wt% Cr alloy (hypereutectic) after a 90% reduction (Takeuchi et al., 1989).	53
Figure 2.49	The strength of wire drawn hypereutectic Cu-Cr as a function of imposed drawing strain (Adachi, 1997b).	53
Figure 2.50	a) Starting texture of Cr dendrites. b) Texture developed in Cr dendrites after rolling to a strain of ~90% (Adachi et al., 1997a).	54
Figure 2.51	Damage of Cr phase after tensile testing of swaged Cu-Cr (Lee et al., 2000).	54
Figure 3. 1	Equilibrium phase diagram for Cu and Cr (Chakrabarti and Laughlin, 1984).	56
Figure 3.2	Schematic diagram showing the dimensions of the BN crucible and graphite susceptor used to produce the directionally solidified Cu-Cr alloy.	57
Figure 3.3	a) Schematic diagram illustrating the setup used for directional solidification. Not shown is the vacuum chamber in which this apparatus was situated. b) Photograph of system at temperature taken through front view port.	58
Figure 3.4	Schematic diagram showing tensile specimen used for in-situ straining in the SEM.	62

Figure 3.5	a) Flux distribution from the NRU reactor at Chalk River Laboratories. b) Schematic of NRU floor showing the position of the spectrometers in relation to the reactor.	64
Figure 3.6	Photograph of the experimental setup of the E4 spectrometer equipped for texture measurements.	65
Figure 3.7	Grid of points used for pole figure measurement plotted on a stereographic projection.	66
Figure 3.8	Schematic showing the geometry for in-situ straining experiments at CRL.	67
Figure 3.9	Geometry of tensile specimens used at CRL for in-situ experiments.	68
Figure 3.10	Experimental setup for measurement of lattice strains during in-situ straining. Here, the tensile rig is oriented for measurements of lattice strain parallel to the tensile axis.	68
Figure 3.11	Schematic diagram defining the angles χ and η with respect to tensile specimen.	70
Figure 3.12	Schematic diagram showing the relationship between the tensile axis and the direction of lattice strain measurement when ψ was not set equal to half the Bragg angle.	72
Figure 3.13	Geometry of tensile specimen used at McMaster.	75
Figure 4.1	a) And b) transverse photographs of etched Cu-Cr samples solidified at 57 mm/hr and 6 mm/hr respectively. c) And d) same as a) and b) but from longitudinal sections.	78
Figure 4.2	Transverse photographs from etched samples solidified at a) 57 mm/hr and b) 6 mm/hr.	79
Figure 4.3	Optical micrographs from longitudinal sections of material solidified at 57 mm/hr in a) and b), and 6 mm/hr in (c). a) And b) show regions of well-aligned and misaligned growth respectively.	80
Figure 4.4	Example of a) out-of-plane and b) in plane fibre misorientation for samples solidified at 6 mm/hr. Similar misalignment was observed for samples solidified at 57 mm/hr.	81
Figure 4.5	Deep-etched Cu-Cr specimen solidified at 57 mm/hr showing the scale and morphology of the Cr eutectic phase.	82
Figure 4.6	Longitudinal micrographs showing bands of eutectic fcc material in samples solidified at 6 mm/hr. a) Low magnification showing band crossing several grains. b) Higher magnification view showing flat interface on one side of the band and perturbed interface on other. Solidification direction is to the left.	83

Figure 4.7	a) Plate-like proeutectic Cr phase and b) dendritic Cr exposed by etching away the Cu matrix with 50% HNO_3.	84
Figure 4.8	Representative Cu pole figures as deduced from as-cast specimen a){220}, 57 mm/hr, b){200}, 57 mm/hr, c) {220}, 6 mm/hr, and d){200} 6mm/hr. In all cases the macroscopic growth axis is located at the centre of the pole figure.	85
Figure 4.9	Representative Cr pole figures a) {200}, 57 mm/hr, b) {211}, 57 mm/hr, c){200}, 6 mm/hr d) {211}, 6 mm/hr. As in figure 4.11, the macroscopic growth axis of the ingot coincides with the centre of the pole figure.	85
Figure 4.10	a) Cu {200}pole figure and b) Cr {200}pole figure measured manually by EBSD. Growth axis located at the centre of the pole figure.	86
Figure 4.11	a) Contoured and b) discrete Cu {200} pole figure measured using automated EBSD. Cu Orientation images in b) show the crystallographic directions parallel to the i) growth axis, ii) and iii) directions perpendicular to the growth direction.	87
Figure 4.12	a) BF TEM image of spheroidized Cr particle extracted from Cu matrix. b) Powder diffraction spectra resulting from Guinier x-ray diffraction on extracted spheroidized Cr.	87
Figure 4.13	a) Cr {200} and b) Cr {211} pole figures measured on sample from which thermal residual strains were deduced. Two ideal grain orientations are shown in the {200} pole figures.	88
Figure 4.14	Ideal Position of Cr{211}for a) ideal orientation 1 and b) ideal orientation 2. The filled circles represent the ideal orientations while the open circles (labeled with letters) are positions where peaks were measured experimentally.	88
Figure 4.15	BF TEM image of extracted Cr fibres. Note that the fibres contain no internal defects.	90
Figure 4.16	TEM image showing branched Cr fibre.	90
Figure 4.17	Constrictions in a Cr fibre as viewed a) at low magnification in the TEM. b) High magnification view of one of the constrictions showing the presence of a low angle boundary.	91
Figure 4.18	Transverse BF TEM micrographs from samples solidified at a) 57mm/hr, and b) 6 mm/hr.	92
Figure 4.19	Longitudinal two-beam TEM micrographs from a samples solidified at 57mm/hr. a) BF image showing presence of Cu lattice dislocations at interface. b) DF image showing defects in the interface ($\mathbf{g}$ = [020]). c) As in b) but for $\mathbf{g}$ = [200].	92

Figure 4.20	Two-beam BF TEM images in a sample solidified at 6mm/hr. Beam direction is close to $[110]_{Cu}$ in a) to d) while it is close to $[211]_{Cu}$ in e). a) g = [002] b) g = $[1\bar{1}1]$ c) g =$[2\bar{2}0]$ d) g = $[1\bar{1}\bar{1}]$ e) as d) but tilted approximately 30°. f) SADP at $[110]_{Cu}$. Note the structure of the interface revealed in the inset portion of e).	93
Figure 4.21	BF TEM image from longitudinal sample (solidified at 57 mm/hr) showing dislocation loops bowing out of the phase interface (marked by arrows).	94
Figure 4.22	Overlapping stereographic projections indicating the Kurdjumov-Sachs (K-S) orientation relationship between a body-centred cubic phase (open circles) and face-centred cubic phase (filled circles).	95
Figure 4.23	a) Selected area diffraction pattern (SADP) taken from interface between Cu and Cr in a transverse foil. Beam direction approximately parallel to $[110]_{Cu}$ and $[111]_{Cr}$. b) SADP from phase interface in longitudinal foil. Beam direction approximately parallel to $[1\bar{1}1]_{Cu}$ and $[1\bar{1}0]_{Cr}$. The uneven intensity of the Cr spots indicates that the parallelism is not exact between these directions. c) As in b), but tilted such that beam direction is parallel to $[\bar{1}12]_{Cu}$ and $[11\bar{2}]_{Cr}$. In each case g_1 and g_{2r} refer to parallel crystallographic directions other than those parallel to the beam direction.	95
Figure 4.24	Series of BF images taken at different tilt positions along the common $(1\bar{1}1)_{Cu}\|\|(1\bar{1}0)_{Cr}$ Kikuchi band. The tilt condition on the left, oriented approximately 9° from the common $[110]_{Cu}\|\|[111]_{Cr}$ direction is seen to bring the fibre almost on axis. At the other two tilts, interfaces can be seen at the curved end interfaces (marked by arrows in b and c).	96
Figure 4.25	Cr fibre that exhibits two facets bounded by curved end interfaces. Also shown are the angles that the common close packed plane normals make with the normals to the facets.	97
Figure 4.26	Low magnification BF image showing at least two different variants of Cr fibres.	97
Figure 4.27	Two different variants of fibres. The inset SADP shows that the fibre on the right is oriented such that the beam direction is parallel to the common close packed directions. The fibre on the left shows the same common close packed planes but the beam direction is not parallel to $[111]_{Cr}$. Also note that the fibre on the right is close to end on while interface can be seen on the fibre on the left (marked with arrow).	98
Figure 4.28	Superimposed stereographic projections showing examples of variants of Cr fibres. Common close packed planes and directions noted as CP and CD respectively.	99
Figure 4.29	EDX spectrum collected from a) Cu and b) Cr.	100
Figure 4.30	Stress-strain response of Cu-Cr solidified at 57 mm/hr and tested at 293 K, 223 K, and 77 K.	102

Figure 4.31	Stress-strain response of a series of samples solidified at 57 mm/hr and tested at 293 K showing scatter in the experimental data. Black and gray lines indicate samples with gauge diameters of 5.09 mm and 9.5 mm respectively.	103
Figure 4.32	Work hardening rate (θ) versus strain deduced from data in figure 4.30.	103
Figure4.33	Results of cyclic testing at 293 K and 77 K (Cottrell-Stokes test). Also included are monotonic curves for samples solidified at 57 mm/hr and 293 K (gray lines).	104
Figure 4.34	Photograph showing the change in macroscopic morphology of a tensile specimen after increasing amounts of strain (left to right).	104
Figure 4.35	a) Photographs (rotated 90° between photos) of a sample after testing, but just prior to failure, showing the elliptical cross-section developed. b) Measurements of specimen diameter showing the development of an elliptical cross-section.	105
Figure 4.36	Failure surfaces for sample solidified at 57 mm/hr and tested at 293 K.	105
Figure 4.37	Stress/strain response for samples solidified at 6 mm/hr and tested at a) 293 K, and b) 77 K. Also shown are representative curves for samples solidified at 57 mm/hr (gray lines).	106
Figure 4.38	Hardening rate versus strain for samples solidified at 6 mm/hr and tested at 293 K and 77 K.	106
Figure 4.39	Fracture surfaces from samples solidified at 6 mm/hr and tested at 293 K.	107
Figure 4.40	a) Stress-strain response for sample solidified at 6 mm/hr and tested at 77 K, exhibiting anomalously low ductility. b) Fracture surface of sample in a).	108
Figure 4.41	a) Stress-strain response for hypoeutectic Cu-Cr. b) Longitudinal micrograph after testing showing one large void at centre of sample.	108
Figure 4.42	a) Stress-strain response of conventionally cast Cu-Cr. b) Micrograph showing microstructure after testing at low magnification and high magnification (inset).	109
Figure 4.43	a) Stress/strain response of pure Cu specimens. b) Micrograph showing microstructure prior to straining.	109
Figure 4.44	Low magnification images from samples solidified at 57 mm/hr and tested at a) 293 K, and b) 77 K.	110
Figure 4.45	Higher magnification micrographs from within neck of tensile specimens shown in figure 4.48, showing shear bands and deformation of Cr fibres into shear bands at a) 293 K, and b) 77 K.	111
Figure 4.46	Fracture of coarse Cr particles in a sample solidified at 6 mm/hr and tested at 77 K.	112

Figure 4.47	Development of slip lines on the surface of polished tensile specimen after 10% strain (tensile axis indicated by arrow). Coarse slip bands run across many grains. Little interaction was observed at low strains between Cr fibres and slip traces (inset).	113
Figure 4.48	The morphology of Cr fibres in sample strained to 0.15.	113
Figure 4.49	Series of sequential SEM images taken during in-situ straining of a tensile specimen. The deformation of fibres into shear bands can be followed. Cr fibres are seen to deform extensively into shear bands (e.g. fibre marked by arrow). Strain increases from (a) to (e).	114
Figure 4.50	Low magnification micrographs showing the development of macroscopic shear bands leading to final failure. a) Onset of localized shearing. b) Just prior to final failure.	115
Figure 4.51	Observation of a void formed along a shear band just prior to failure.	115
Figure 4.52	Neutron diffraction results for specimen 1, Cu {331}.	117
Figure 4.53	Neutron diffraction results for specimen 2, Cu {220}.	118
Figure 4.54	Neutron diffraction results for specimen 3, Cu {220}.	119
Figure 4.55	Neutron diffraction results for specimen 4, Cu {220}.	120
Figure 4.56	Neutron diffraction results for specimen 5, Cu {220}.	121
Figure 4.57	Summary of neutron diffraction results showing lattice strain versus applied stress for Cu, including the effect of initial thermal residual stresses. a) Lattice strain versus applied stress. b) Lattice strain versus applied strain.	122
Figure 4.58	Stress-strain response for samples tested in monotonic uniaxial tension (gray line) and after a series of load/unload steps (black lines) at 293 K.	123
Figure 4.59	Hysteresis loops developed on loading and unloading a sample after increasing amounts of pre-strain.	123
Figure 4.60	Schematic diagram illustrating method used to define the reverse flow stress, σ_R.	123
Figure 4.61	Transverse BF TEM images from samples strained a) 0.015, b) 0.12, c) 0.25, and d) 0.9, in uniaxial tension.	124
Figure 4.62	Series of two-beam BF images, ε=0.015. a) g = [002], b) g = $[\bar{1}1\bar{1}]$, c) g = $[\bar{2}20]$, d) g = $[\bar{1}11]$.	125
Figure 4.63	Orientation measurements made around a Cr fibre, ε=0.015. The numbers relate position of measurement and recorded Kikuchi Pattern.	126

Figure 4.64	Series of two-beam images, ε=0.12. a) g = $[1\bar{1}\bar{1}]$, b) g = $[2\bar{2}0]$, c) g = $[1\bar{1}1]$, d) g = [002], e) g = $[0\bar{2}2]$. Beam direction in a) - d) is close to $[110]_{Cu}$. Beam direction in e) is close to $[111]_{Cu}$.	126
Figure 4.65	Orientation measurements made around a Cr fibre, ε=0.012.	127
Figure 4.66	Series of two-beam BF images, ε=0.25. a) g = $[1\bar{1}1]$, b) g = [202], c) g = [111], d) g = [020].	128
Figure 4.67	a) Orientation measurements made around a Cr fibre, ε=0.25. b) Micro-beam diffraction patterns from Cu (top) and Cr (bottom) showing that $[110]_{Cu}$ is no longer parallel to $[111]_{Cr}$.	128
Figure 4.68	DF images showing similar orientation close to all fibres, ε=0.25.	129
Figure 4.69	Images from longitudinal foils showing the heterogeneity of structure at the phase interface at strains of a) 0.12, b) 0.25, c) after necking.	129
Figure 4.70	DF images from a) Cu and b) Cr showing the high dislocation density at the phase interface and the corresponding dislocation activity in the Cr fibre.	130
Figure 4.71	Transverse of BF TEM images from foil cut from neck of tensile specimen. a) Low magnification showing substructure in Cu. b) Cr fibre showing complicated morphology and dislocations.	130
Figure 4.72	BF images of Cr fibres. a) ε=0.12, no dislocations in fibre. b) ε=0.25, dislocations are emitted from the phase interface (marked by arrows).	131
Figure 4.73	Weak beam images from Cr fibre showing dislocation loops being emitted from phase interface.	132
Figure 4.74	BF image showing Cr fibre sheared into shear band.	133
Figure 4.75	Higher magnification view of fibre shown in figure 4.74 showing dislocations in fibre at the point where the fibre is bent into the shear band.	134
Figure 4.76	Hardness measurements on plane strain compressed Cu-Cr.	134
Figure 4.77	Low magnification image of a sample strained to ε=0.95 showing extensive shear banding.	135
Figure 4.78	a) SEM image showing Cr fibres deformed into shear bands. b) SEM images of deep-etched specimens showing segmented fibres within shear band. Note also the fine scale of fibres within shear bands compared to those outside.	136
Figure 4.79	Morphology of fibres after extraction from a sample strained to ε=0.95.	137

Figure 4.80	a) BF TEM image for sample rolled to a strain of ~0.95 viewed parallel to the transverse direction. b) Higher magnification view showing dislocation-free fibre.	138
Figure 4.81	BF TEM images of substructure in a fibre extracted from a sample rolled to a strain of 1.3. a) Low magnification view. b) Substructure in one portion of a fibre.	139
Figure 5.1	a) Schematic illustrating the geometry and crystallography of a typical Cr fibre. F1 and F2 are the two most prominent facets observed on fibres. b) Stereographic projection further illustrating the crystallographic relationship between the two phases. The growth direction is oriented approximately 9° away from the common close packed directions within the common close packed planes.	144
Figure 5.2	a) Measured thermal residual strains in Cr fibres in as-cast samples as a function of angle from angle of measurement from the macroscopic growth axis. b) Simple Eshelby calculation for the normal thermal residual strains for different temperature drops assuming fibres aligned with the macroscopic growth axis. No relaxation in the matrix.	148
Figure 5.3	Punching of non-isoaxial prismatic loops from the sides of a fibre to relax thermal residual stresses (Dunand and Mortensen, 1991b).	150
Figure 5.4	Comparison of experimentally measured thermal residual strains in Cr with models assuming no plastic relaxation in the matrix and plastic relaxation by prismatic punching.	151
Figure 5.5	a) Dislocation loops emitted from phase interface viewed in as-cast longitudinal TEM foil. b) Possible mechanisms for punching of prismatic loops from the sides of a fibre (Dunand and Mortensen, 1991b).	151
Figure 5.6	a) and b) Schematic and stereographic projection showing slip systems in Cu oriented with [110] along the tensile axis (centre of the projection). c) And d) Similar to a) and b) but for Cr crystal oriented with [111] along the tensile axis.	156
Figure 5.7	a) Stereographic projection showing orientation relationship between Cu and Cr and the resulting relationship between the most highly stressed slip systems(tensile axis at centre of projection). Due to texture in Cu, no contraction would be expected along the direction marked "Y". b) Schematic bi-crystal of Cu/Cr showing most highly stressed slip systems across the phase interface. Note that the "interface" in this case (equivalent to F2) is a common slip plane and that the tensile axis (Z) is parallel to a common slip direction.	158
Figure 5.8	Low strain response of Cu-Cr specimens under various test conditions. Also included is the low strain response of pure Cu specimens tested at 293 K and 77 K.	160
Figure 5.9	Elastic loading data for directionally solidified Cu-Cr samples tested at a) 293 K and b) 77 K.	161

Figure 5.10	Standard triangles showing the variation of Young's Modulus for a) Cu and b) Cr at 293 K as a function of position of tensile axis for single crystals.	161
Figure 5.11	a) Low strain work hardening behaviour for directionally solidified Cu-Cr. a) 57 mm/hr b) 6 mm/hr. In both cases θ is the uncorrected hardening rate, $d\sigma/d\varepsilon$.	163
Figure 5.12	Low strain portion of cyclic testing at 293 K and 77 K (Cottrell-Stokes Test).	167
Figure 5.13	Data from Cu phase in specimen #2 during in-situ neutron diffraction experiments. Here, data has only been plotted for the regimes of elastic/elastic and elastic/plastic behaviour.	170
Figure 5.14	Back stress calculated as half the difference in the forward and reverse (offset) yield strength on unloading and reloading of specimens at a) 293 K and b) 77 K.	173
Figure 5.15	Double cross-slip of shear loops around a fibre resulting in a prismatic loop left around the fibre and a prismatic loop in the matrix. Large loops must be produced if cross slip occurs on a system close to the fibre axis. Original shear loop is drawn in black while the two prismatic loops are drawn in gray.	175
Figure 5.16	Stress-strain curves for directionally solidified Cu-Cr showing the response of material tested under various conditions up to the point of macroscopic fibre yielding.	176
Figure 5.17	Data on the size/strength relationship for extracted Cr whiskers (Salkind et al, 1970). Also included is the estimated strength and size range in the materials studied here.	178
Figure 5.18	Schematic illustrating possible mechanisms for nucleation of slip within Cr fibres. a) Homogeneous nucleation within the fibre. b) Nucleation at the phase interface. c) Bowing of a pre-existing boundary defect into the fibre.	179
Figure 5.19	K-M plots for directionally solidified Cu-Cr grown at a) 57 mm/hr and b) 6 mm/hr. Also shown are the K-M curves for pure Cu tested at 293 K and 77 K.	184
Figure 5.20	Comparison between K-M plots for Cu-Cr solidified at 57 mm/hr and 6 mm/hr.	185
Figure 5.21	Cross-sectional area of Cr fibres as a function of imposed tensile strain. The lines indicate the expected change in area from the imposed strain assuming different starting fibre diameters.	186
Figure 5.22	Variation in fibre diameter along the length of a single fibre within the neck of a tensile specimen.	186
Figure 5.23	The transition from brittle to ductile behaviour of cementite in pearlitic steel as the scale of the carbide is reduced (Langford, 1977).	187
Figure 5.24	Representative Lattice strain versus applied stress for in-situ neutron diffraction experiments (specimen 2). Here, the lattice strains developed well into the regime of plastic co-deformation are plotted.	188

Figure 5.25	Back stress measured for samples tested at a) 293 K and b) 77 K. Also included are the monotonic forward flow curves.	191
Figure 5.26	Parameter β as a function of plastic strain for samples tested at a) 293 K and b) 77 K.	191
Figure 5.27	Normalized plastic-plastic hardening rate. If there were no relaxation of the structure developed at the boundary this ratio would equal 1.0. The fact that it varies with temperature suggests a thermally activated mechanism of relaxation.	197
Figure 5.28	DF micrographs taken with the beam direction close to one of the primary slip plane normals showing the lobes of contrast connecting four fibres. a) $g = [\bar{2}20]$, b) $g = [\bar{2}02]$, c) $g = [02\bar{2}]$. d) Same as b) but including Kikuchi patterns taken from different regions. The contrast between the bands is seen to arise from a small (~1 - 2°) rotation between different regions.	199
Figure 5.29	Cottrell-Stokes ratio for Cu-Cr (solidified at 57 mm/hr) compared with that of pure polycrystalline Cu (Bullen and Hutchinson, 1963).	204
Figure 5.30	Predictions of the described model a) for different levels of elastic loading of the fibres (no extra dislocation storage term) and b) comparison of predictions when extra dislocation accumulation is allowed.	209
Figure 5.31	a) Fit of K-M model to directionally solidified Cu-Cr (57mm/hr) at 293 K and 77 K. b) Vocce law fit of pure Cu used in model.	210
Figure 5.32	a) Stress-strain response and b) K-M plot for directionally solidified Ni-W.	211
Figure 5.33	Back stress in austenoferritic stainless steel as a function of plastic strain (Verhaeghe, 1996).	211
Figure 5.34	Hardening behaviour of Cu-Ag eutectic deformed by wire drawing (Frommeyer and Wassermann, 1975).	212
Figure 5.35	Geometry for a fibre rotating into a shear band (Zok, 1988).	215
Figure 5.36	Textural softening parameter for shear at an angle β to the a) tensile axis and b) rolling direction for the Cu in the material studied here. Several minima occur suggesting the possibility for shear localization.	217
Figure 5.37	Orientation measurements made along the length of a Cr fibre deforming into a shear band in the neck of a tensile specimen. {100} pole figure in the upper right hand corner indicates the orientation of the points indicated in the micrograph. The tensile axis is vertical in both cases.	219
Figure 5.38	Measurements of Cr orientation within a shear band. The image quality map for the region analyzed is shown on the left. The texture of the fibres, as indicated by the {100} pole figure on the right shows a weak texture with rotation of the fibre texture approximately about the shear band normal. Note the similarity between the pole figure here and that shown in figure 5.37.	220

Figure 6.1	a) Table summarizing the hardening rate for a number of heavily co-deformed two phase materials. The hardening rate is also given normalized by the volume fraction of embedded phase and elastic modulus of the embedded phase. b) Schematic suggesting the manner in which the hardening rate varies with strain in the materials. It is particularly difficult to make extrapolations due to the lack of knowledge of the behaviour of these materials over the rage of strains between ~ 1.0 and 5.0 (shown as shaded box).	223
Figure 6.2	The strength and conductivity of a number of high strength conductors (Wood et al., 1997).	224
Figure 6.3	Overview BF TEM image showing partially recrystallized Cu-Cr.	225
Figure 6.4	Figure 6.4 BF and DF images (left) at the recrystallization front showing a nuclei situated at the phase boundary. From the Kikuchi patterns and DF image it is clear that the nuclei has an orientation distinct from that of the recrystallized material on the opposite side of the fibre.	225

LIST OF TABLES

		Page
Table 2.1	Processing Routes for Fine-scale Two-phase Materials	5
Table 2.2	Strength of Selected Heavily Co-deformed Two-phase Materials	14
Table 2.3	Strength of Whiskers (From Brenner, 1958)	24
Table 2.4	Strength of Extracted Phases (Webb and Forgeng, 1958)	27
Table 3.1	Impurity Concentrations (in ppm) in OFHC Cu (Lahaie, 1998)	57
Table 3.2	Conditions and Composition of Electroless Ni Plating Solution	60
Table 3.3	Comparison between Ge[115] and Ge[117] Monochromators for Cu and Cr	71
Table 4.1	Measured Scale of Cr Fibres in Directionally Solidified Cu-Cr Eutectic	80
Table 4.2	Peak Positions and Lattice Strains Associated with Thermal Residual Stresses	89
Table 4.3	Various **g.b** Conditions for Cu	93
Table 4.4	Average Angles Between Facet Normals and Common Close Packed Directions	98
Table 4.5	Test Conditions for Neutron Diffraction Experiments	116
Table 5.1	Material Properties used in the Calculation of Thermal Residual Strains via the Eshelby Method	149
Table 5.2	Important Elastic Constants for Cu and Cr	160
Table 5.3	Aspect Ratio of Cr Fibres as a Function of Imposed Tensile Strain	202

1. INTRODUCTION

Most industrially important materials are composed of more than one phase, the purpose being to tailor the engineering properties for a given application. A significant proportion of these multiphase materials are deformed in order to achieve their final bulk properties and form. The prototypical example of an engineering material processed by means of co-deformation is pearlitic (patented) steel wire used in applications ranging from reinforcement in steel belted radial tires, to structural members in suspension bridges. The strength of pearlitic wire can reach 5 GPa and has been attributed to the (poorly understood) mechanisms that allow the metallic and intermetallic components of the microstructure to undergo large strain plastic co-deformation.

More recently, a new class of engineering materials produced by co-deformation has emerged from attempts to produce high-strength electrical conductors. Similar to pearlitic steel in a number of fundamental aspects, these deformed two-phase Cu alloys have been shown to attain strengths approaching the theoretical limit for metals, while retaining adequate ductility and electrical conductivity. Combined with these impressive mechanical properties, some materials within this class have exhibited useful functional properties, and in some cases developed unexpected phases during co-deformation.

Although co-deformation represents an important processing method for a number of materials, very little is understood about the detailed mechanisms that allow for it, particularly in materials containing phases that exhibit very different mechanical properties when tested individually. Recent experiments have focused mainly on attempting to ascertain the important parameters allowing for co-deformation and developing high strengths from samples that have been pre-strained to strains much greater than 1.0. It is difficult to make unambiguous conclusions regarding the mechanisms involved in the strengthening of such materials, as the method of fabrication often necessitates a complicated thermomechanical history. Further insight into this problem may be gained from the vast body of work that was carried out in the 1960's and 1970's on strengthening mechanisms in dispersion and fibre-reinforced metal matrix composites. However, the fact that the majority of this work was restricted to strains of the order of 1%, where the reinforcing phase remained

loaded elastically, restricts the utility of this work with respect to understanding the problem of co-deformation.

As the regime of deformation between strains of 0.01 and 1.0 has received relatively little attention in multiphase materials that undergo co-deformation, this thesis has focused on experiments involving materials at relatively low strains, starting from nearly-equilibrium microstructures. By judicious selection of alloys and production routes, it has been possible to achieve some important similarities to the microstructures found in heavily co-deformed materials; namely fine scale of the phases and a regular interface structure between the constitutive phases. In this way it has been possible to evaluate, in a controlled manner, the importance of the scale of the microstructure, the presence of interfaces between phases, the role of internal stresses, and the general concept of plastic constraint on the co-deformation process. Further, in recognition of the importance of processes occurring on different length scales within these materials, this investigation has sought to evaluate the response of the materials at the macroscopic, microscopic and mesoscopic scales. Because of the importance of the inter-relationship between processes occurring on multiple length scales, the work will be presented with a particular focus on results arising from different length scales.

This thesis is organized in the following manner: first, a brief review of the literature will be made in Chapter 2. The purpose of this section is not to review all literature on the deformation of two-phase materials, but rather to highlight the important issues involved with co-deformation and give examples from various material systems. Following this review, Chapter 3 will describe the experimental methods used in this study. Chapter 4 contains the experimental results of this investigation. The first section of Chapter 4 will be devoted to the description of the as-fabricated material studied while the second section will focus on the observations of the deformation behaviour of this material. In both parts of this chapter the description of the material will follow the above described philosophy of characterizing the material and its behaviour based on length scales. Chapter 5 will be devoted to a discussion of the experimental results presented in the preceding chapter. Some comments are made with respect to the as-cast structure and its relation to the conditions of growth. A general description of the mechanical behaviour of the material in uniaxial tension will be presented, and a simple model will be developed to account for the general features of the experimentally

determined stress-strain response. The mechanisms of plastic deformation in the embedded phase will be discussed with respect to observations on the macroscopic, mesoscopic and microscopic scales. The observed mechanisms of failure will also be discussed. Chapter 6 suggests a number of possible extensions arising out of this work. Finally, Chapter 7 concludes this thesis by summarizing its salient results.

2. LITERATURE REVIEW

2.1 INTRODUCTION

There is an extensive body of literature concerned with the deformation of two-phase materials. This literature spans a vast variety of strain levels, starting microstructures, phase combinations and deformation conditions. Instead of reviewing all of this literature, this chapter will outline salient theoretical and experimental work on the plastic co-deformation behaviour of metallic two-phase materials containing a fibrous embedded phase. This subset of materials will be focused on since the majority of materials that have been examined with regard to co-deformation fall within this class.

Fibrous, fine-scale two-phase materials may be produced via a number of different processes. Three of these processes are compared in table 2.1. Examples of materials produced by the routes in table 2.1 are illustrated in figure 2.1. Each of these routes leads to a material with a different microstructural scale, level of internal stress, and type of phase interface.

In order to organize the wide range of experimental results and theoretical models for the co-deformation of two-phase materials, information will be organized on the microstructural length scale to which it relates (figure 2.2). Following this structure, this literature review is organized into three main sections. In the first, macroscopic mechanical response of fibrous two-phase materials will be described. The term "macroscopic" refers in this context to phase-averaged measurements and models associated with the behaviour of a material on a length scale equal to the specimen dimensions. Next, behaviour on the mesoscopic scale will be reviewed where "mesoscopic" refers to measurements and models associated with processes occurring on the scale of the constituent phases and averaged over each phase separately. Finally,

behaviour at the microscopic scale, e.g. those processes associated with the internal structure developed within phases, will be considered.

Table 2.1 Processing Routes for Fine-scale Two-phase Materials

Processing Route	Methods	Scale of Embedded Phase	Vol. % Embedded Phase	Typical Uses
Phase Transformation: *In-Situ Composites*	Directional solidification, rapid solidification, solid state transformation	100 - 0.01 μm	1 - 50%	Superalloys
Thermomechanical: *Micro-composites*	Rolling, extrusion, wire drawing	100-0.01 μm	1 - 50%	Electrical conductors
Deposition: *Multilayers*	Co-evaporation, electrodeposition, sputtering	100-0.001 μm	1-50%	Electronic devices (e.g. MEMS)

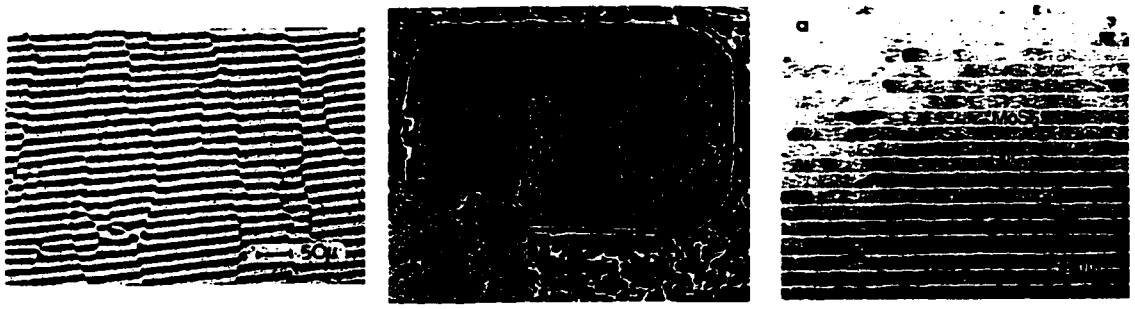

(a) (b) (c)

Figure 2.1 Examples of fine-scale two-phase materials processed by a) solidification (directionally solidified Al-Al_3Ni, Davies, 1971), b) deformation processing (Cu-Nb, Han, 1999), and c) deposition (Kung et al., 1995).

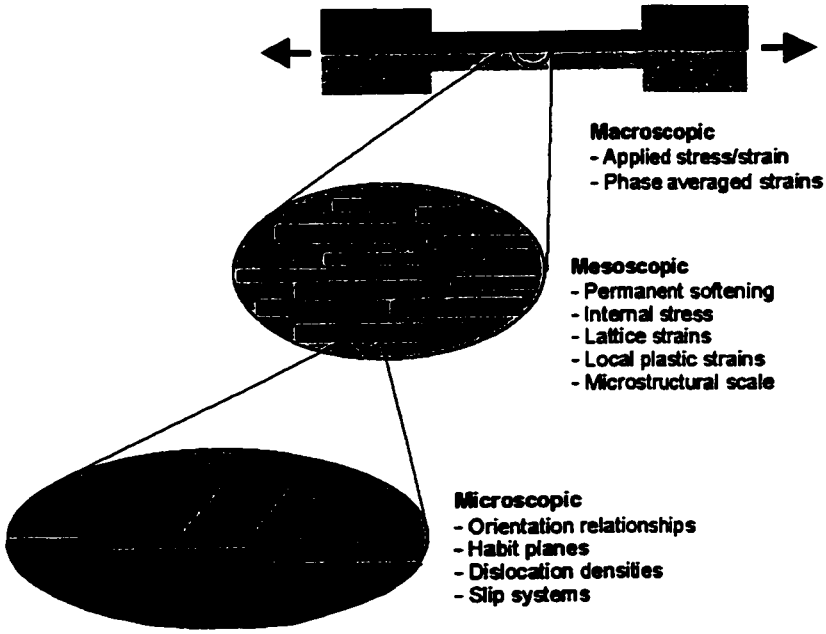

Figure 2.2 Schematic illustration of macroscopic, mesoscopic and microscopic scales along with some of the important variables at each length scale.

2.2 MACROSCOPIC CHARACTERIZATION OF THE CO-DEFORMATION OF TWO-PHASE MATERIALS

At the macroscopic level three types of measurements can be made. Measurements of bulk mechanical response can be determined as a function of imposed strain through uniaxial tensile tests. In conjunction with pre-straining material by wire drawing or rolling, the mechanical behaviour can be tested to large imposed strains. Also, by following the average shape change of the constituent phases observed as a function of applied strain, a measure of strain partitioning can be estimated. Finally, some comments can be made regarding the pattern of flow in the two phases at high strains if the macroscopic texture of the two phases is followed.

2.2.1 Bulk Mechanical Response of Co-deformed Two-phase Materials

A great deal of information can be gathered pertaining to the mechanisms of deformation and the bulk (static) mechanical response of a material by performing simple uniaxial tensile tests. The mechanical properties alone are of practical interest as they comprise an important set of parameters for the design of any engineering structure. It is also possible, through post mortem examination of specimens, to comment on both the macroscopic distribution of strain in the material and the pattern of flow. In many cases this information can give insight into possible mechanisms for the observed mechanical response. A particular problem in analyzing the macroscopic behaviour of co-deformed two-phase materials, however, is that the bulk mechanical response represents an average of the mechanical response of the constituent phases. The individual properties of these phases are often not known ex-situ and so there is ambiguity in how to interpret the data. In order to interpret results, it is often necessary to formulate a theoretical model based on the mechanisms that are assumed to operate.

If a two-phase material is produced by directional eutectic solidification or by the casting of one metal around wires or sheets of a second, the resulting structure is macroscopically similar. In systems of interest to this discussion, either processing route results in an aligned hard phase embedded within a soft, ductile matrix. Testing such a material in uniaxial tension parallel to the direction of aligned rods or plates results in a stress-strain response schematically illustrated in figure 2.3a. The stress-strain curve has historically been associated with four regimes[1] (Kelly and Davies, 1965). At low strains, both phases deform elastically resulting in a linear elastic response for the bulk material. Upon reaching a critical load, the softer phase yields plastically (figure 2.3b). Further straining then results in plastic flow of the matrix and continued elastic deformation of the embedded phase. This regime is characterized by a very nearly linear stress-strain response. Continued straining will subsequently bring the embedded phase to the point of fracture or plastic yield. If possible, further deformation constitutes plastic co-deformation of the two phases up to the point of

1 The term *regime* will be used here to differentiate the macroscopic composite behaviour from the *stages* of deformation typically observed in tensile deformation of single crystals and directly associated with crystallographic slip.

final fracture (considered the fourth regime). Figure 2.4 illustrates this behaviour for selected directionally solidified eutectics. The macroscopic tensile response has been reviewed extensively, both for eutectic alloys

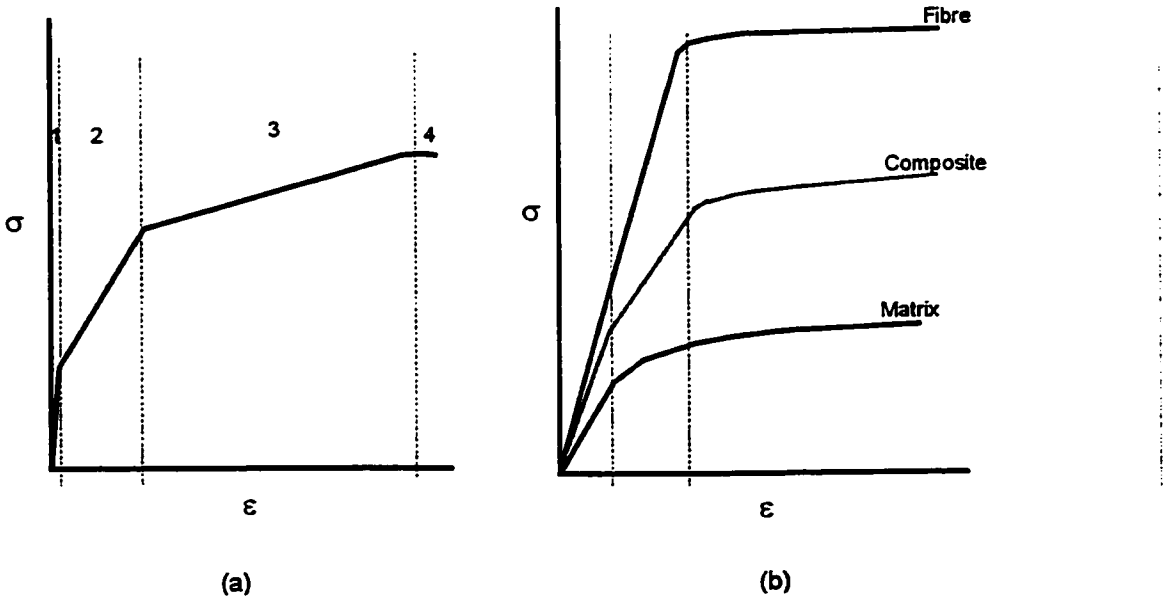

Figure 2.3 a) Schematic stress-strain response for a material reinforced with continuous ductile fibres. b) The first three stages of deformation showing the response of matrix, fibres and overall composite.

(e.g. McLean, 1983, Salkind et al. 1970) and composites produced by solidifying metal matrices around wires (Kelly and Davies, 1965, Kelly, 1972, Kelly, 1971, Kelly and MacMillan, 1986).

The behaviour illustrated in figures 2.3 and 2.4 has often been described using a simple uniaxial stress balance (e.g. see Kelly and Davies, 1965). This approach imagines a material composed of two phases loaded in parallel such that the tensile strains are equal and homogeneous throughout the material. A balance of force along the tensile axis then results in a "rule of mixtures" estimate for the material's response,

$$\sigma_c(\varepsilon) = (1-f)\sigma_m(\varepsilon) + f\sigma_f(\varepsilon) \qquad (2.1)$$

where the subscripts "c", "m" and "f" refer here to bulk, matrix and fibre respectively, ε is the applied strain and f is the volume fraction of the fibrous phase. Differentiation of equation 2.1 with respect to the applied

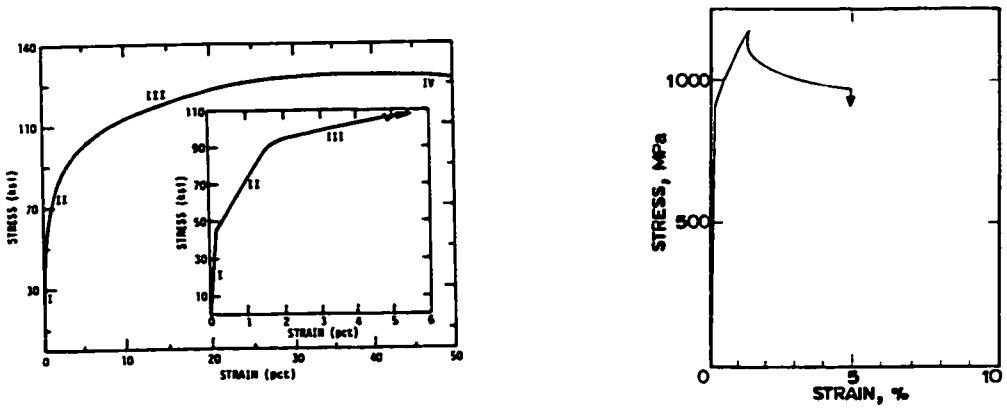

(a) (b)

Figure 2.4 Uniaxial stress-strain response of directionally solidified eutectic alloys. a) Ductile Ni-W (Garmong and Williams, 1975). b) Brittle Ni-Nb_2C (McLean, 1983).

strain predicts the modulus of the flow curve to be equal to the sum of the moduli of the constituent phases weighted by their respective volume fractions. Once the matrix begins to deform plastically, its effective modulus drops significantly compared to that of the still elastically loaded fibres. Thus, often as a first order estimate, the slope of the second section of the stress-strain curve is taken to be linear and equal to the fibre elastic modulus weighted by the volume fraction of fibres. Once the fibres yield plastically, a constitutive response must be assumed for both phases in order to predict any further deformation. This approach, being first order in nature, implicitly ignores any stresses that may arise due to differences in the transverse deformation of the two phases. Kelly (1971) has reviewed the approaches that have been taken into account for differences in Poisson's ratio for the two phases in the calculation of the composite elastic modulus. In general, for metallic systems, these corrections have only a small effect on the overall predicted response, particularly at low strains.

One particular feature that the simple rule of mixtures model is not equipped to deal with is the effect of embedded phase misalignment. For eutectic alloys, the embedded fibrous phase tends to grow along directions of maximum heat extraction. If solidification occurs with a cellular front, the fibres near the cell walls tend to grow perpendicular to the growth front resulting in fibres near the edges of colonies being misaligned with respect to the macroscopic growth direction (figure 2.5). On a more macroscopic scale, growth near the crucible walls is influenced by heat extracted through the walls of the crucible (McLean,

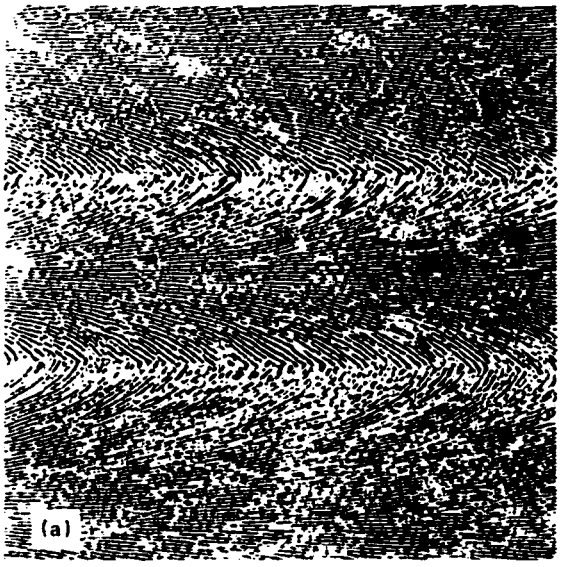

Figure 2.5 Cellular growth in a directionally solidified $Mg_{17}Al_{12}$-Mg eutectic alloy. Near colony boundaries eutectic growth becomes perturbed due to a non-planar interface (Kraft, 1966).

1983). Although it has been suggested (McLean, 1983) that the degree of misalignment typical in directionally solidified eutectics is insufficient for it to have a substantial effect on the macroscopic response. It will have an impact on the local degree of load transfer and plastic flow.

Some work has been done with respect to the measurement of the mechanical properties of samples of eutectic alloys such that the tensile axis is made to vary with respect to the macroscopic growth direction of the sample. Figure 2.6 shows the results of tensile tests on directionally solidified Al-Al_3Ni (George et al., 1968). In this material the Al_3Ni lamella do not deform plastically at room temperature, thus the stress-strain response of the material tested parallel to the lamella (0°) exhibits low ductility. As the tensile axis is rotated relative to the mean fibre axis, the maximum strength of the material drops precipitously while the ductility increases. At 45°, a maximum in ductility and minimum in strength is observed. Fracture of the specimen changes from ductile cup and cone fracture of the 0° sample to predominantly shear at 45° and 90°. Similar

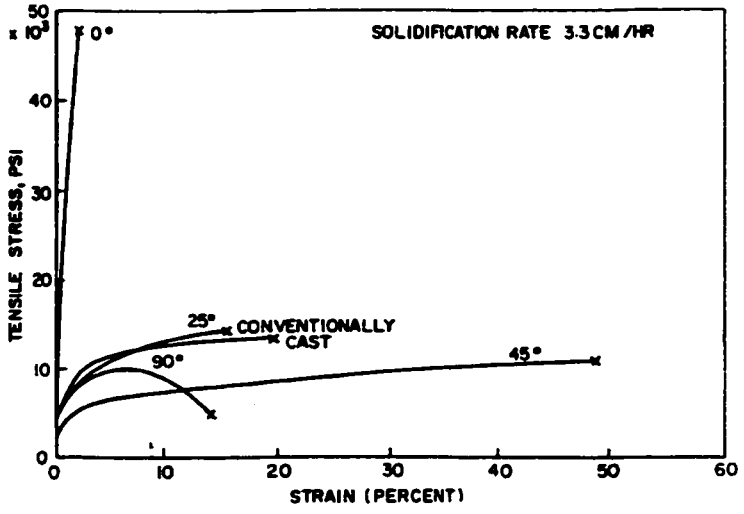

Figure 2.6 Effect of eutectic orientation on the uniaxial stress-strain behaviour of Al-Al_3Ni directionally solidified alloy (George et al., 1968).

observations have been made for other eutectic systems (Hertzberg, 1964, Hertzberg et al., 1965) as well as for materials produced by casting metals around wires (Kelly and Davies, 1965, Cooper, 1966, Jackson and Cratchley, 1966). The effect of fibre orientation on the mechanical response is a direct result of the influence of the fibres on the plastic flow of the matrix. At 45° plastic flow can occur between fibres by shear without directly loading them. At 90° the fibres tend to reduce the ability of the sample to contract along a direction parallel to the fibre axis, thus the sample tends to deform in a mode approaching plane strain. This is borne out by the observation of elliptical cross-sections of previously round specimens tested to failure at this orientation (e.g. Hertzberg, 1964).

To this point, discussion has been limited to the behaviour at relatively low strains. With the exception of a few cases (Williams and Garmong, 1973, Garmong and Williams, 1975, Hertzberg and Kraft, 1963, Strid and Easterling, 1982) most directionally solidified alloys do not show extensive plastic co-deformation during uniaxial tensile tests. This is due to the fact that many of the eutectic systems previously studied have contained an intermetallic embedded phase which, at room temperature, exhibits limited or no plastic behaviour prior to fracture. The tensile test itself is generally limited to low strains due to geometrical instability in the form of necking. To avoid this limitation most work has focused on examining the mechanical response of materials that have been pre-deformed to large strains by routes that are not limited by a geometrical instability (e.g. wire drawing, extrusion, or rolling).

Recently, a large number of studies have been carried out on the mechanical properties of wire drawn Cu-Nb and Cu-Ag two-phase alloys. These systems are currently being developed as high-strength, high-conductivity materials (e.g. see Bevk, 1983). In both cases the materials may be cast as off-eutectic alloys to allow for the tailoring of the proportion of phases. In the Cu-Nb system the material is solidified as a hypereutectic alloy consisting of dendrites of Nb in a eutectic matrix. The Cu-Ag system, on the other hand, is typically solidified as a hypoeutectic alloy and so consists of isolated pockets of eutectic surrounded by Cu dendrites. In both cases, the material initially contains phases that are neither continuous nor necessarily well-aligned with any particular direction. However, a small number of wire drawing passes tends to align the microstructure into nearly continuous, well-aligned rods or fibres. Thus, for the purposes of studying the

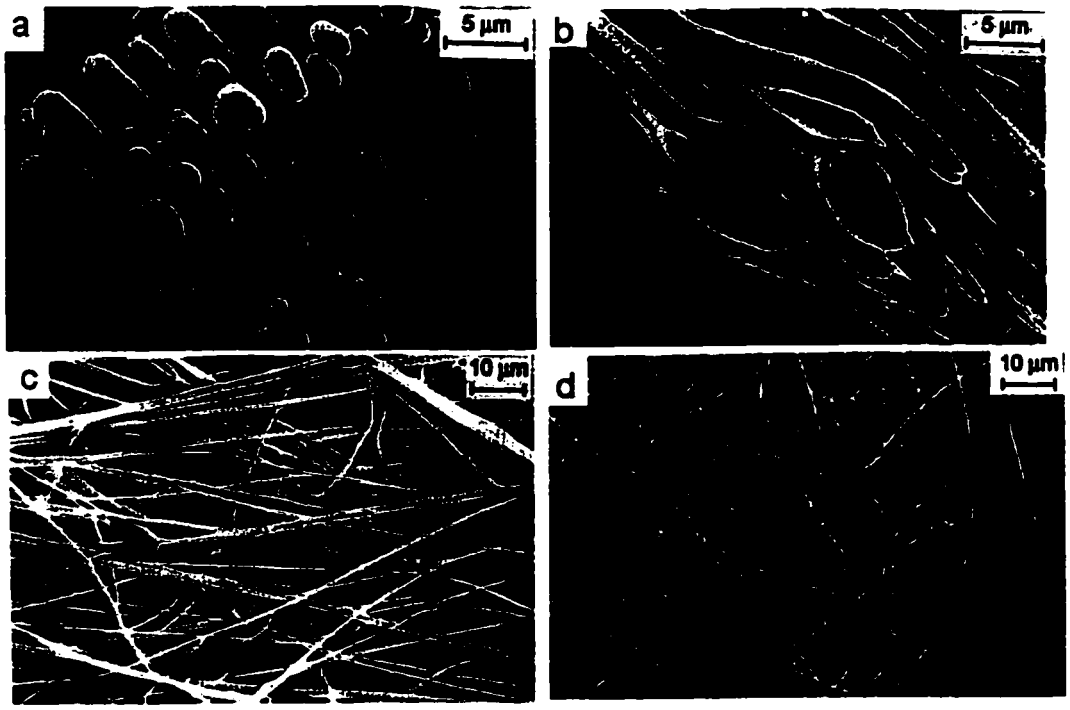

Figure 2.7 Progressive refinement of Nb dendrites with drawing strain (Raabe, 1995). The Nb filaments have been chemically extracted from the Cu after strains of a) 0 b) 88.9% c) 94.8% and d) 99995%.

macroscopic properties of the material after drawing, the structure can be considered similar to that of the directionally solidified eutectic. Figure 2.7 shows a series of images taken from a Cu-Nb alloy after increasing amounts of wire drawing. The progressive elongation of the structure is evident (Raabe et al., 1995).

The stress-strain response for these systems is illustrated by the work of Spitzig et al. (1987) and Frommeyer and Wassermann (1975), shown in figure 2.8 a) and b) respectively. In these figures, the stress-strain response of the material is plotted as a function of drawing pre-strain. The continued drawing of these materials results in the attainment of strengths exceeding those possible in single-phase metals while maintaining reasonable ductility in tension. On loading such pre-deformed samples in tension, the initial three regimes in the stress-strain curve of eutectic materials are replaced by a nearly continuous parabolic curve. It is possible to examine the validity of using a rule of mixtures (equation 2.1) in describing the mechanical response of these materials. Based on equation 2.1, it may be possible to predict the tensile strength of the composite samples with a knowledge of the ultimate tensile strengths of the bulk materials tested separately. Figure 2.9 shows the tensile strength of drawn Cu-Nb composites as a function of the drawing pre-strain

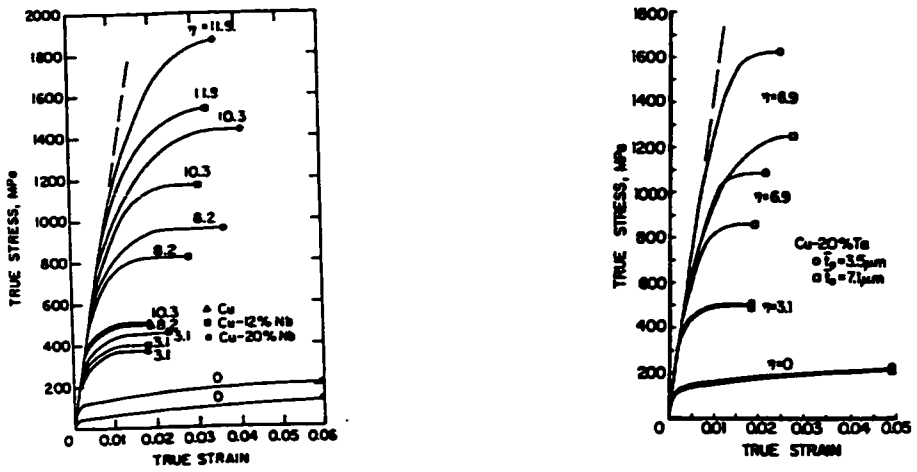

Figure 2.8 a) Stress-strain response of Cu-Nb alloys pre-strained by wire drawing to the indicated reductions in area (η) (Spitzig and Krotz, 1987). b) Similar to a) but for Cu-Ta alloys (Frommeyer and Wasserman, 1975).

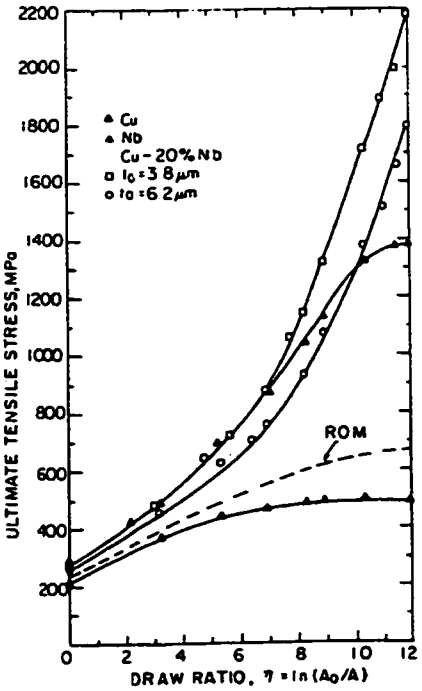

Figure 2.9 Ultimate tensile strength of Cu, Nb and Cu-Nb as a function of drawing strain. Also shown is the prediction of the UTS for the Cu-Nb using a rule of mixtures with the data for pure Cu and pure Nb (Spitzig and Krotz, 1987).

(Spitzig and Krotz, 1987). Also plotted is the prediction of equation 2.1 using data taken from drawn Cu and Nb wires. At all draw ratios the experimental data exceeds the prediction of equation 2.1. At the highest recorded draw ratios the strength of the composite wires exceed that of similarly drawn Nb. Similar observations in heavily co-deformed two-phase materials that far exceed the simple rule of mixtures prediction have now been made in many material systems as shown in table 2.2.

The inability of equation 2.1 to predict the mechanical behaviour of heavily co-deformed two-phase materials has received a great deal of attention. One of the earliest attempts to correct for this was made by Embury and Fisher (1966) to account for the behaviour they observed

Table 2.2 Strength of Selected Heavily Co-deformed Two-phase Materials

Material System	UTS	Drawing Strain	Reference
Cu-15wt%Cr	906 MPa	7.0	Adachi et al., 1997a
Cu-18vol%V	~1850 MPa	11.0	Russell et al., 2000
Cu-30vol%Fe	~1500 MPa	8.5	Russell at al., 2000
Cu-20vol%Ta	1600 MPa	8.9	Spitzig and Krotz, 1988
Cu-20vol%Nb	1400 MPa	6.9	Spitzig and Krotz, 1988
Cu-60at%Ag	1350 MPa	9.3	Frommeyer and Wassermann, 1975
Fe-Fe_3C	4000 MPa	3.0	Embury and Fisher, 1966

in drawn pearlitic steel. Embury and Fisher proposed that a scale-dependent strengthening process, similar to that giving rise to the Hall-Petch effect in single-phase materials, might be important in co-deformed materials. It was proposed that if the microstructure obeys the principle of similitude then it should be possible to correlate the scale-dependent strengthening to the macroscopic reduction in the cross-section of the specimen. Using a Hall-Petch type strengthening law therefore results in a prediction of the strength increase as a function of applied strain (ε).

$$\sigma = \sigma_o + k\exp(-0.25\varepsilon) \qquad (2.2)$$

From a macroscopic viewpoint k is a fitting parameter (similar to the Hall-Petch slope in single-phase materials) and σ_o is a reference strength (taken at the scale independent limit) that is often taken to be equal to equation 2.1. Figure 2.10 shows the good correlation between

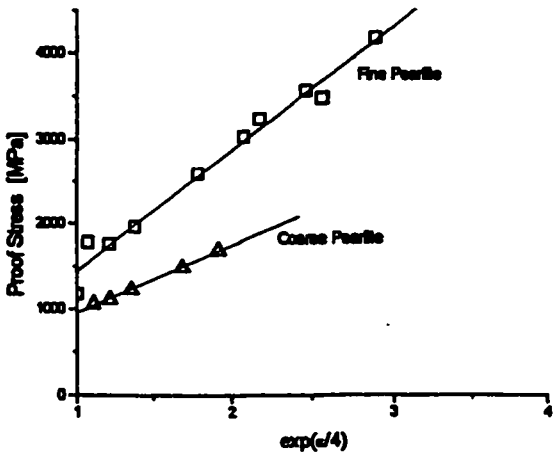

Figure 2.10 Embury and Fisher's (1966) fit of a Hall-Petch type equation to the strengthening obtained by wire drawing of eutectoid steel.

an equation similar to equation 2.2 and the data obtained by Fisher and Embury on pearlitic steel wire. Similar proposals have been made for models with the same theoretical basis in an attempt to explain the strengthening observed in heavily co-deformed copper-based alloys (Spitzig and Krotz, 1987, 1988). An example of the fit of data on the strength of Cu-Nb to a model similar to that of Embury and Fisher is shown in figure 2.11. A problem with models of this type is that they do not provide a clear link to the detailed microstructure of the material. Funkenbusch and Courtney (1989) have argued that, although important, the barrier strengthening model is insufficient to explain the differences in mechanical response between the same material processed in different ways to similar microstructural scales (Everett, 1988).

It was noted above that it is necessary to utilize processes such as rolling or wire drawing in order to avoid geometrical instabilities and allow for large strains to be imposed during co-deformation. These

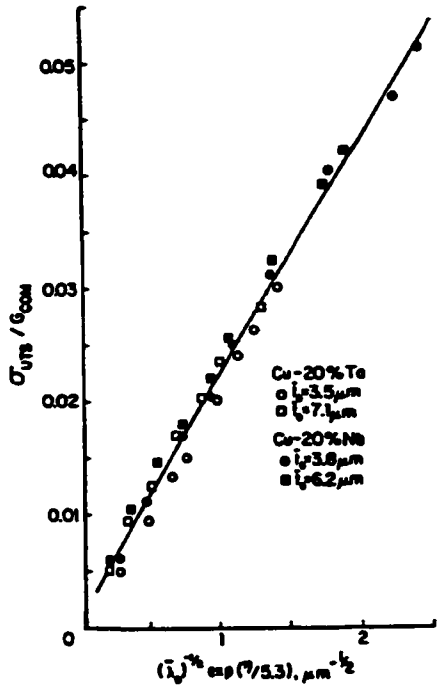

Figure 2.11 Use of a modified Embury-Fisher type model to predict the strengthening observed in drawn Cu-Nb and Cu-Ta (Spitzig, 1988). Here $\bar{\lambda}$ is the initial spacing between plates, η is the draw ratio and $\bar{t}_o$ is the initial scale of the embedded phase.

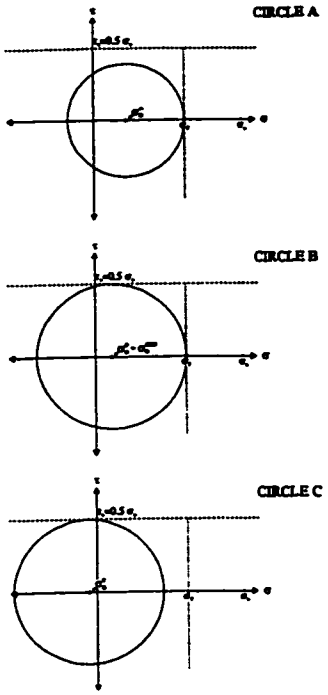

Figure 2.12 Two dimensional stress state corresponding to uniaxial tension (circle A). Maximum critical tensile stress fracture criteria represented by vertical line and flow criteria represented by horizontal line. Circles B and C show the effect of an increasing superimposed hydrostatic stress.

processes may also aid co-deformation by promoting plasticity in phases that are otherwise brittle due to the large hydrostatic pressure inherent in drawing. An example of this is pearlitic steel wire composed of the (nominally brittle) intermetallic Fe_3C in a matrix of ferrite. When these wires are tested in uniaxial tension after drawing, ductile fracture resulting from the fracture of carbides leads to ductility of only a few percent. The same material, however, may be co-deformed by wire drawing to very high strains (> 6) without failure (Langford, 1977). During wire drawing, the material is subjected to a multi-axial state of stress, with a substantial component being hydrostatic. The effect of this is twofold. First, dilatent fracture processes are hindered and the flow of material tends to fill any voids that develop within the material (Zok, 1988). Further, the application of a hydrostatic pressure promotes plasticity in materials that would behave in a brittle manner when tested in uniaxial tension. This is shown in figure 2.12 for a simple two dimensional stress state using Mohr's circle (Lahaie, 1998). If the process of fracture can be attributed to a maximum normal stress, and plasticity to a maximum shear stress, then the competition between these two can be seen schematically by their relative position in the Mohr's circle. In figure 2.12 (circle A) the uniaxial tensile stress has caused the material to reach both fracture and flow criteria simultaneously. If a hydrostatic pressure is now superimposed, the circle is shifted and thus plasticity would be expected to precede fracture (figure 2.12, circles B and C).

2.2.2 Partitioning of Strains and Stresses: The Observation of Morphological Changes

In equation 2.1 it was explicitly assumed that the applied strain was distributed equally and homogeneously throughout the material. Although this satisfies both internal compatibility between phases and external compatibility with the applied strains, it constitutes only one of many possible paths. Since materials tend to minimize the elastic energy stored during deformation, the equal strain assumption is very seldom appropriate. In a material consisting of elastically deforming particles in a plastically deforming matrix, this process of load transfer can be minimized if particle fracture or decohesion occurs or if the matrix is allowed to flow around the particles. For the matrix phase to accomplish this latter process it must undergo extra (redundant) deformation in order to maintain compatibility with the particles. This process becomes more difficult as the aspect ratio of the embedded phase is increased. An analogous situation is found for a

fluid containing rigid cylinders. In this case, the viscosity of the fluid is found to increase as a function of the square of the cylinder's length to diameter ratio (Kelly, 1972). At low strains, the effect of non-equal partitioning of strains between phases is reflected in the tensile response as a loss in the four-regime response observed for continuously reinforced materials. Instead, the overall flow stress of the material is reduced and the transition from elastic deformation to plastic deformation becomes more gradual (figure 2.13). This can be observed experimentally by comparing the tensile response of directionally solidified and conventionally cast eutectic materials.

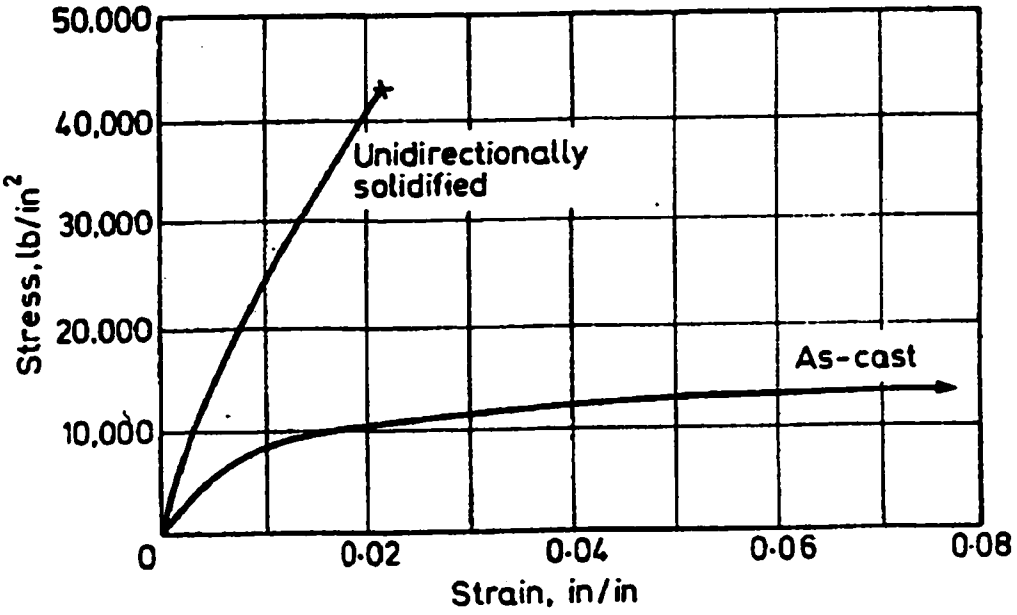

Figure 2.13 Comparison between the tensile behaviour of directionally solidified and conventionally cast Al-Al3Ni (Lemkey, et al., 1965).

It is possible to directly measure the partitioning of plastic strains in a two-phase material by following average shape changes of the phases involved. This has been done for a number of materials deformed both by wire drawing (e.g. Raabe et al. 1995, Adnyana, 1982), and by cold rolling (e.g. Engler, 1995, Ozturk et al., 1984). Figure 2.14 shows the results of measurements on a) the α and β' phases in a copper-zinc-aluminum alloy, and b) for wire drawn Cu-Nb. In both cases it was observed that initially, strains are partitioned quite unequally between phases. For the Cu-Nb alloy this has been attributed to the necessity of bending and

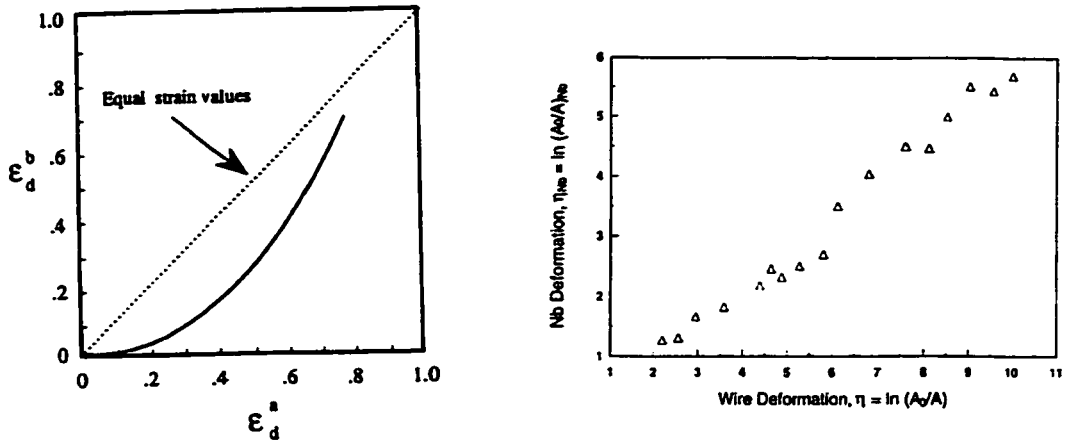

(a) (b)

Figure 2.14 a) Partitioning of strain between α (ε_a^d) and β (ε_a^d) phases (β harder) in a wire drawn Cu-Zn-Al alloy (Adnyana, 1982). b) As for a) but for the Cu-Nb system (Raabe, 1995).

aligning the Nb dendrites into the wire axis. For the Cu-Zn-Al alloy it was suggested that the initial disparity in strains between the two phases was associated with the fact that the softer α matrix initially flows around the harder β' phase. In both cases, continued work hardening of the softer matrix phase tends to result, at high imposed strains, in a more homogeneous pattern of flow. Engler et al. (1995) have studied the strain distribution developed during the rolling of α–β brass (figure 2.15). In this case as rolling proceeds, a comparison of the applied strain to that measured in the matrix suggests that the disparity between the two continues to increase with straining. This can be attributed to the fact that rolling itself tends to be an inhomogeneous process that inherently leads to strain inhomogeneities throughout the specimen. Ozturk et al. (1994) examined this process of strain partitioning during rolling of two-phase materials for a series of idealized metal-metal laminates (figure 2.16). By choosing matrix/embedded phase combinations with

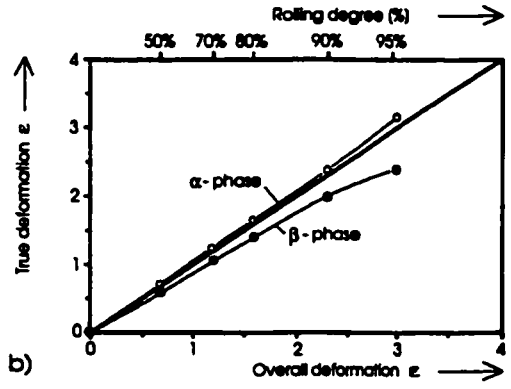

Figure 2.15 Strain partitioning between α and β phases in brass deformed by rolling (Engler et al., 1995).

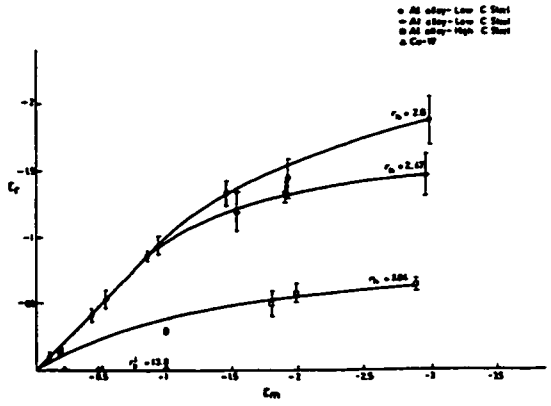

Figure 2.16 Measurement of strain partitioning for some simple metal-metal laminates with different ratios of hardness (Ozturk et al., 1994). The strain in the embedded phase is plotted versus the applied strain.

various ratios of flow strength, a very strong correlation between the homogeneity of strain and the ratio of initial hardness (r_h) of the two phases was found.

2.2.3 Macroscopic Pattern of Flow as Measured by Texture

In the preceding discussion it was emphasized, from a macroscopic point of view, that the addition of a co-deforming second phase may significantly alter the pattern of flow and the partitioning of stresses and strains within a material. This directly influences the bulk mechanical properties measured for a given system because of the degree of the external load that is supported by each phase. The measurement of macroscopic texture can also give insight into strain partitioning and the pattern of flow. Texture arising from plastic deformation is a manifestation of crystallographic slip and the imposed conditions of deformation. Therefore, any process tending to alter the pattern of plastic flow in a material will alter the evolution and/or strength of the texture developed.

The seminal work of Wassermann (Wassermann, 1978, Bergmann et al., 1978) was the first to systematically study the effect of the addition of various embedded phases on deformation texture. Wassermann selected ductile matrices (e.g. Al and Ag) and made additions of i) "un-deformable" or "slightly deformable" particles, ii) particles with nearly equal flow stress as the matrix, and iii) "easily deformable" particles. The final textures of the matrix phase were subsequently compared with the texture of the matrix deformed a similar amount with no embedded phase. The results of these experiments are summarized in figure 2.17. The inverse pole figures for the matrix phase of three composites (left to right) are shown here. The upper inverse pole figure shows the texture of the unreinforced matrix while the lower one shows the

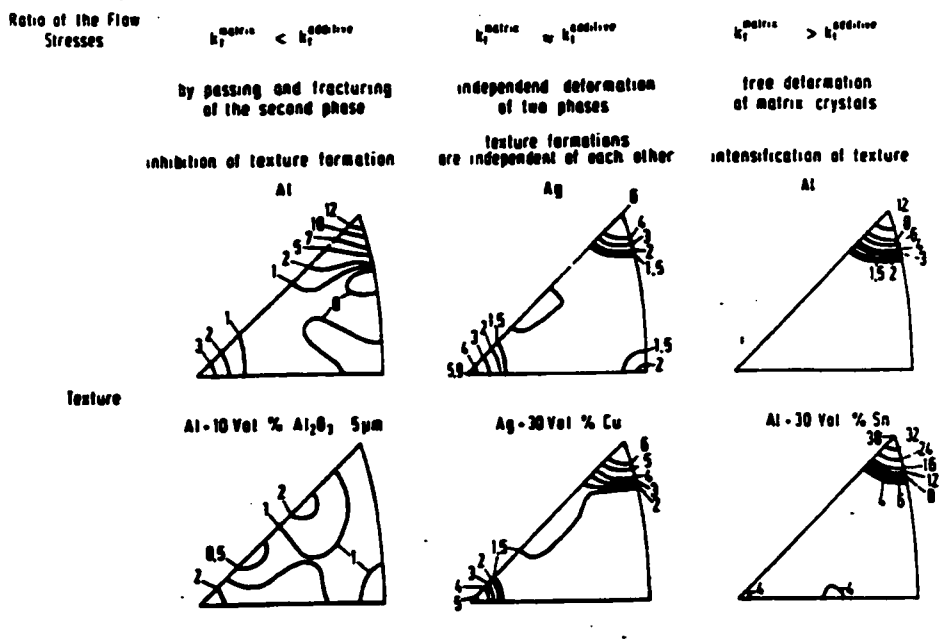

Figure 2.17 Inverse pole figures showing the effect of added second phase components on the texture development in the matrix phase. Deformation was achieved by wire drawing to a reduction of 95% in all cases (Bergmann et al., 1978).

texture taken from the deformed composite. For the case of elastically deforming particles of Al_2O_3 in an Al matrix, the influence was to significantly weaken the matrix texture. Wassermann et al. (1978) attributed this to the disruption of plastic flow around the particles. The picture he envisioned is shown in figure 2.18. For the case of a composite of Cu and Ag (both phases having similar flow strengths) very little changed in the matrix texture, indicating little disruption of flow due to the presence of the second phase. In the final example, soft Sn particles were embedded within an Al matrix. In this case it was found that the strength of the matrix texture substantially increased. This was attributed to the

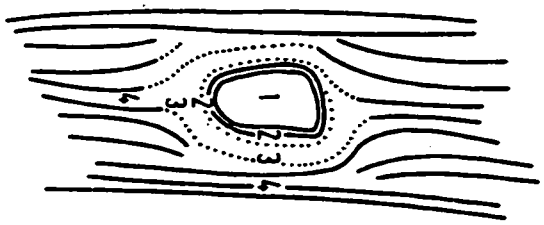

Figure 2.18 Disruption of the plastic flow of the matrix phase by a hard embedded second phase (Bergmann et al., 1978).

presence of the Sn which reduced the constraint that would otherwise be felt due to the presence of adjacent Al grains.

More recently a number of studies similar to Wassermann's have been published (e.g. see Brokmeier, 1994, Bolmaro et al., 1994, Bolmaro et al., 1999) giving similar results. However, these studies have generally lacked a detailed examination of the evolution of texture with strain. In particular, it has been found that for systems containing two phases with similar flow strengths, the texture of the two phases tends to evolve more slowly than if the individual phases were tested separately. This has been observed for drawn Cu-Nb (e.g. Raabe, 1995) and has been attributed to the fact that, in the case of Cu-Nb, a rather complicated pattern of flow must exist initially to align the Nb dendrites. Once aligned, however, the pattern of flow becomes (macroscopically) similar to that expected for the phases separately. For the case of rolled two-phase materials, detailed investigations of texture development coupled with crystal plasticity models based on the Taylor-Bishop-Hill framework have led investigators to postulate that the strains may become more heterogeneously partitioned at high strains due to the relaxation of certain constraints on the deformation of the embedded phase. Raabe et al. (1995) and Engler et al. (1995) in their studies of rolled Cu-Nb and α–β brass concluded separately that the embedded phase behaved more as though it were under conditions of relaxed constraint rather than full (Taylor) constraint. As pointed out by Engler et al. (1995), this constitutes a behaviour of the embedded phase more consistent with an unconstrained single crystal than a constrained particle.

Finally, it is interesting to note that the development of texture, although dictated to a large extent by the imposed strain path, can have a significant influence on the homogeneity of strains within the material. This has been observed in the case of co-deformed fcc-bcc two-phase materials such as Cu-Nb. On drawing, the Nb phase develops a typical bcc <110> fibre texture. However, as Hosford (1964) has shown, it is in fact preferred if <110> oriented bcc crystals deform in plane strain rather than in the imposed axisymmetric mode. In order to accommodate this, the Nb filaments are observed to twist around the wire axis resulting in a complicated "curly" morphology (Bevk et al., 1978). This will be considered later when the detailed mechanisms of strengthening in these alloys are discussed.

2.2.4 Summary

1. The mechanical properties of two-phase materials are sensitive to a number of parameters including volume fraction, aspect ratio of the phases, their continuity and intrinsic properties.

2. If a material consisting of a well-aligned nearly continuous embedded phase is deformed in uniaxial tension a characteristic four regime stress-strain response is obtained. If the phases are not well-aligned and/or they are not continuous, the efficiency of load transfer between phases is reduced and the strength of the material is observed to decrease.

3. A simple rule of mixtures can, in some cases, be used to estimate the mechanical properties of aligned/continuous two-phase materials. This prediction is adequate for the general shape of the stress-strain response at low strains but is unable to predict the strengths that are achieved in heavily co-deformed two-phase materials.

4. The partitioning of strain depends on the morphology and size of the embedded phase, as well as the difference between the mechanical properties of matrix and embedded phase. The inherent inhomogeneity of deformation processes such as rolling must also be accounted for when attempting to quantify the partitioning of strains.

5. The evolution of crystallographic texture in materials that have been heavily co-deformed provides insight into both the pattern of flow and the partitioning of strains. Formation of a preferred texture may also influence the mechanical properties by altering the mode of deformation.

Overall, from the macroscopic vantage, little has been said regarding the in-situ behaviour of the two phases and their interaction. At the macroscopic level, it is often assumed that the in-situ properties of these phases will be the same as those resulting from deformation of the separate phases by testing a homogeneous macroscopic specimen. As will be shown in the following section, this is generally a poor approximation that can result in improper estimates of the bulk response of a material.

2.3 MESOSCOPIC CHARACTERIZATION OF THE CO-DEFORMATION OF TWO-PHASE MATERIALS

In order to understand the bulk properties of materials generated by co-deformation it is necessary to have an understanding of;

i. the degree of load partitioning between the phases

ii. the fundamental mechanical properties of the constituent phases

It was pointed out above that the in-situ mechanical behaviour of embedded phases will be strongly dependent on the effectiveness of load transfer from the surrounding matrix. Although it is found that the upper bound (Taylor) assumption of equal strains gives a reasonable approximation to the behaviour of grains in a single-phase polycrystalline material (e.g. see Kocks, 1970) a hard embedded phase within a soft matrix may choose a path significantly different from that imposed macroscopically. A clear example of this is the observed "curly" Cu-Nb microstructures described above. In this case the assumption that strains in the two phases equal the imposed strain is far from correct. In order to understand the in-situ response of the phases it is necessary to measure and predict the degree of load partitioning between the two phases. Load partitioning, which is a function of both the phase geometry and the mechanical properties of the two phases, can be measured directly if the elastic straining of the two lattices can be followed by diffraction, or can be inferred from forward/reverse flow stress asymmetry as a function of plastic strain. From measurements of the load transfer, inferences can be made about the mechanical response of the two phases. This analysis is normally predicated on an understanding of the ex-situ properties of the two phases. However, in some cases, an extrapolation of the measured behaviour of embedded phases from bulk flow response of samples can yield misleading or erroneous results. This is particularly true in fine-scale embedded phases where a strong size effect on the mechanical response is observed.

In what follows, the experimentally observed mechanical behaviour of fine-scale phases will be reviewed. Of particular interest to this work are experiments that have attempted to determine the mechanical response of fine-scale phases extracted from two-phase materials. Following this, a summary of the experimental and modelling work associated with the determination of load partitioning during deformation of two-phase materials will be presented. Emphasis will be placed on the relationship between load partitioning, measured elastic strains via diffraction and the Bauschinger effect.

2.3.1 The Mechanical Response of Fine-scale Materials

In the Cu-Cr alloy of interest to this work, the Cr phase is present as long fibres with cross-sectional dimensions of the order of ~1 μm. When the minimum dimensions of materials reach the micrometer scale a strong increase in their mechanical strength is observed. This was first demonstrated by Galt and Herring (1952) for 2 μm diameter single crystals of Sn. In this case, the limit of elastic strain prior to failure in bending was observed to be approximately 2%. This is to be compared with the behaviour of bulk Sn which yields at strains typically less than 10^{-4} (Brenner, 1958). This behaviour has subsequently been observed for a wide range of fine-scale metallic and non-metallic single crystals. These observations are generally explained by a

Table 2.3 Strength of Whiskers (From Brenner, 1958)

Material	Maximum Elastic Strain (%)	Method of Growth	Testing Method
Fe	4.9	Halide Reduction	Tension
Cu	2.8	Halide Reduction	Tension
Ag	4.0	Halide Reduction	Tension
Ni	1.8	Halide Reduction	Tension
Co	1.2	Halide Reduction	Tension
Si	2.0	Vapor Condensation	Tension
Sn	2-3	Growth from Solid	Bending
Ge	1.8	Halide Reduction	Bending
Mn	1.5	Halide Reduction	Bending
Graphite	2.0	Vapour Condensation	Tension

lack of internal defects that would, if present, cause either yield or fracture at significantly reduced stress levels. Such defect-free, fine-scale single crystals are typically referred to as whiskers. Table 2.3 gives a compilation of the maximum observed strengths for various metallic and non-metallic whiskers. This demonstrates that elastic strains greater than 1% are typical for such materials. The strength of these whiskers exhibits a strong dependence on the size of the crystals below a cross-sectional scale of ~ 5 μm. Figure 2.19 shows the strength as a function of whisker size for a variety of metallic whiskers. An important point regarding this data is that there is a great deal of variation in the strength. This scatter, however, is artificially

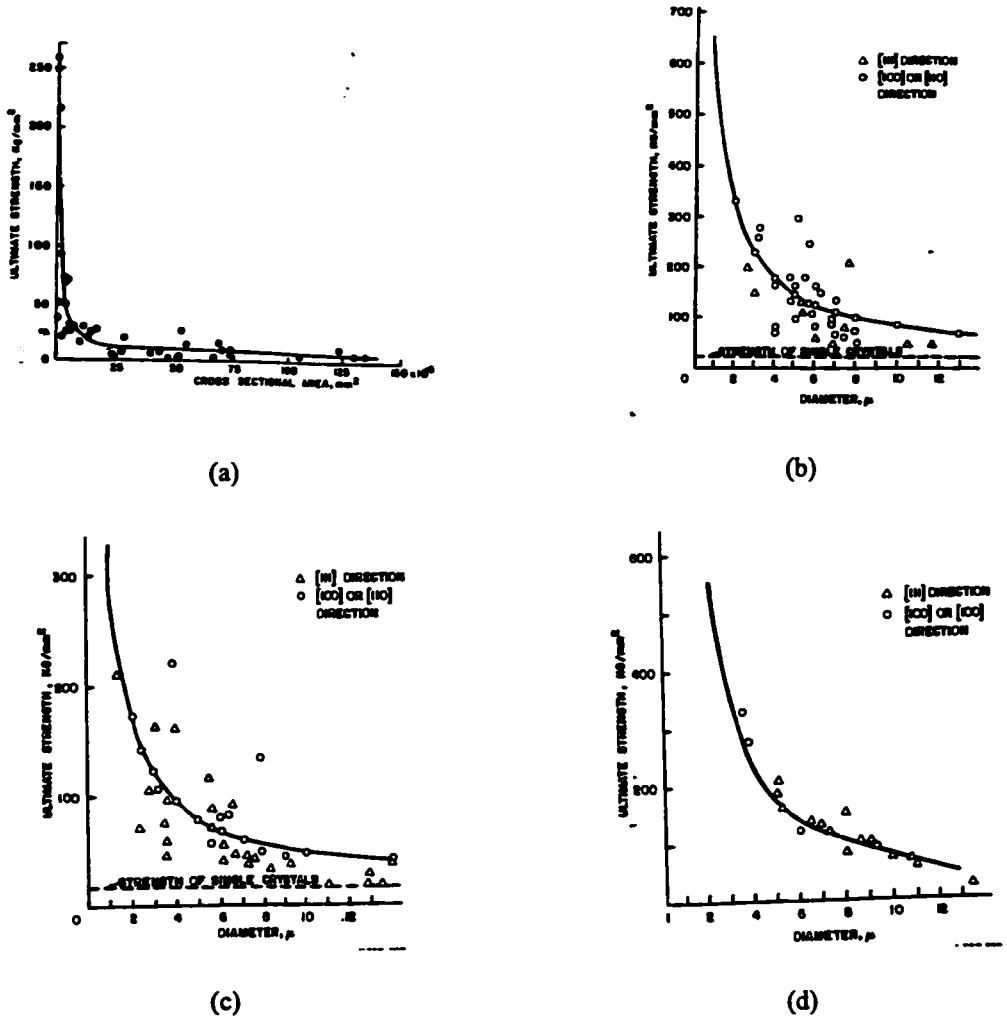

Figure 2.19 The strength of metallic whiskers as a function of the size a) Cr, b) Cu, c) Ni, d) Co, (from Mehan and Herzog, 1958).

low as the typical procedure for testing is associated with the pre-selection of whiskers that exhibit no obvious defects.

The results presented in figure 2.19 arise from materials that have been grown from the vapour state. However, it has been shown that whiskers of strengths equal to, or in some cases surpassing those obtained in vapour grown samples can be produced by solid or liquid state reaction. The work of Webb and Forgeng, (1958) and Salkind et al. (1970) clearly shows this for a variety of extracted phases. Figure 2.20 shows an example of a bend test performed on an extracted Nb_2C fibre. Prior to fracture the whisker supports a tensile strain of the order of 3%. Table 2.4 compiles data from the work of Webb and Forgeng (1958) regarding the strength of fibres extracted from directionally solidified material, including data on Cr fibres extracted from Cu-Cr alloys. Salkind et al. (1970) performed bend and tensile tests on Cr fibres extracted from directionally solidified Cu-Cr. Figure 2.21b reproduces the tensile stress-strain curve for one of the tests performed in this work. Figure 2.21a shows the measured strength of whiskers as a function of their size. It is apparent that the fibre loads in a linear elastic manner to a tensile strain approaching 4% before failure. Failure was reported to occur in the extracted Cr whiskers by localized plastic deformation. This is consistent with the work of Webb

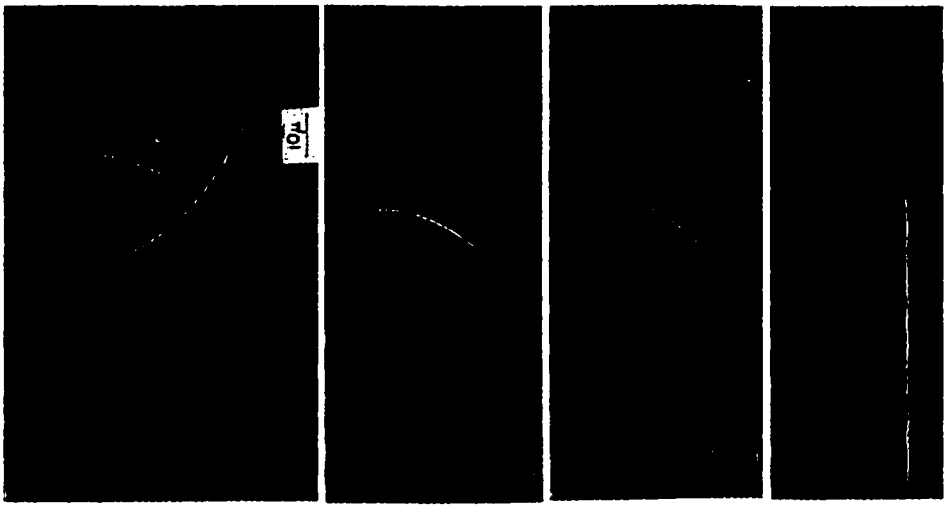

Figure 2.20 A series of images taken during the bending of a Nb_2C whisker. Note that the whisker withstands strains of the order of 3% prior to fracture (Salkind et al., 1970).

Table 2.4 Strength of Extracted Phases (Webb and Forgeng, 1958)

Material	Thickness (μm)	Maximum Strain (%)	Type of Failure
Cr_3O_4	4.7	0.335	plastic deformation
Cr_2N	1.66	1.59	fracture
	1.5	1.64	fracture
Cr	1	3.8	plastic deformation
	1	1.2	fracture at defect
	1	>1.2	plastic deformation
	1	>3.1	-
Fe_3C	1.9	4.7	fracture
	1.45	2.3	fracture
	1.5	2.7	fracture

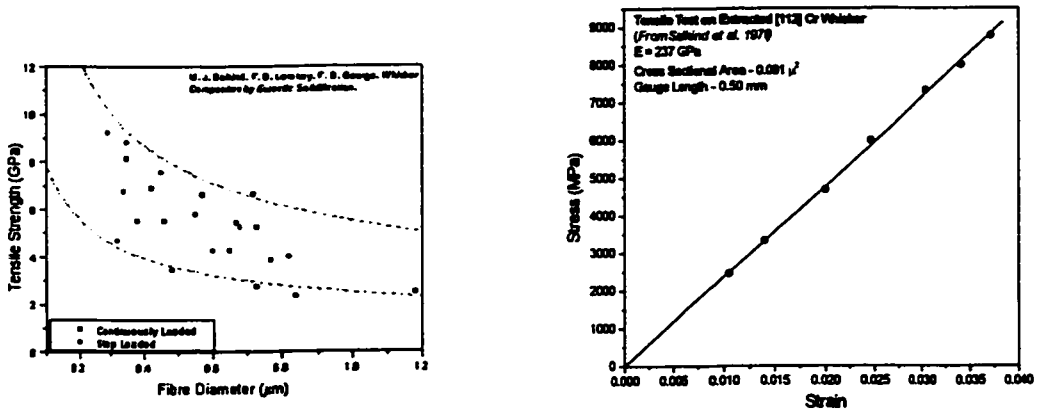

(a) (b)

Figure 2.21 a) Strength of extracted Cr whiskers as a function of their cross-sectional dimensions. b) Stress-strain response recorded during tensile straining of extracted Cr whisker (reproduced from Salkind et al., 1970).

and Forgeng (1958) and Wlodek et al. (1959), although in the latter case it was reported that the Cr whiskers appeared "kinked" after deformation at 77 K.

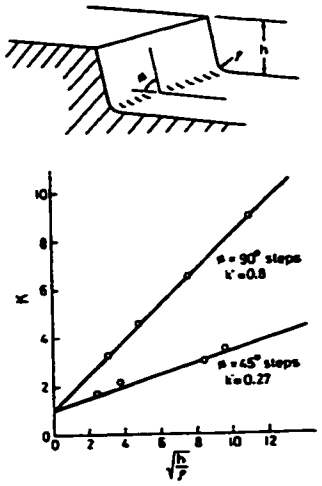

Figure 2.22 Stress concentration (K) arising from the presence of a surface step on a whisker. It has been argued that such submicron defects may control the strength of fine-scale whiskers (Nohara, 1982).

The source of the initial yield or fracture strength of metallic whiskers is still a matter of some controversy (e.g. see Kelly and MacMillan, 1986). What is clear is that the strength of metallic whiskers is intricately linked to the lack of gross imperfections on the surface or in the interior of such crystals and that the strongest approach very close to estimates of the theoretical shear strength (approximately $\mu/30$, Kelly and MacMillan, 1986). It has been argued that the presence of surface steps on the whiskers reduces the apparent yield stress as such steps will act as stress concentrators (Nohara, 1982). The presence of surface steps has also been used to explain the size dependence of the strength of metallic whiskers (figure 2.22) assuming that the height of surface steps depends on the diameter of the whisker.

Most of the early work on testing the mechanical response of whiskers was performed using specialized testing apparatus (see e.g. Kelsey, 1970). Of those tests performed in uniaxial tension, machines of the soft type were typically used, the result being that at the end of elastic loading the sample would fail in a catastrophic manner (e.g. figure 2.21a). Experiments on modified soft machines (Brenner, 1957) or on hard machines (e.g. Yoshida et al., 1966) subsequently showed extensive plastic flow could occur in metallic whiskers after yielding. Figure 2.23 shows the flow curves obtained by Yoshida et al. (1966) on Cu whiskers.

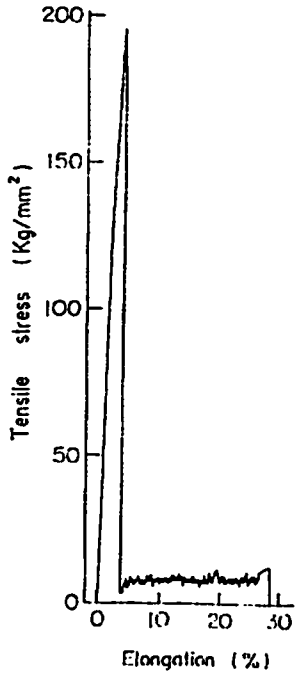

Figure 2.23 Stress-strain curves obtained from Cu whisker tested in a "hard" machine (Yoshida, 1966).

Figure 2.24 A series of micrographs taken after measuring amounts of strain on a Cu whisker. The spread of plasticity along the length of the whisker can be seen (Brenner, 1958).

The measured response clearly shows that, once nucleated, deformation is able to spread quickly throughout the whisker thereby lowering the flow stress of the sample by nearly an order of magnitude. Optical observation of Cu whiskers shows that the initial yield point is associated with the nucleation of a band of deformation which, upon further straining, spreads across the sample (figure 2.24). The explanation given is that a Luders band is formed at the yield point that subsequently propagates along the length of the whisker by a mechanism of double cross-slip (Brenner, 1957, Nittono, 1971). Although a number of metals were shown to exhibit this type of behaviour (e.g. Cu, Zn, and Cd), Fe whiskers exhibit a marked difference. Instead of forming a propagative instability, deformation in Fe whiskers occurred on localized slip bands (figure 2.25). This localization of

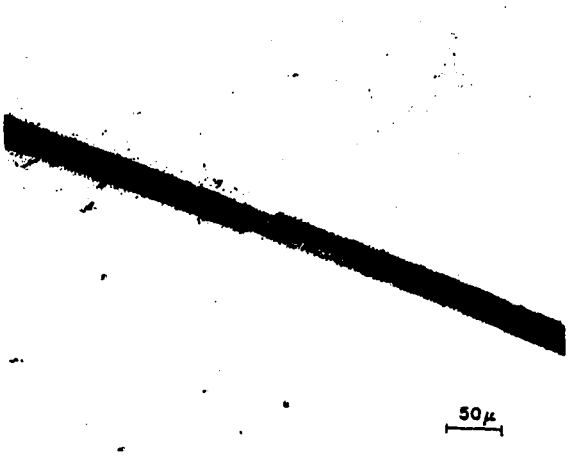

Figure 2.25 Markings on an Fe whisker after the onset of plastic deformation. The localization of strain into slip bands at specific points along the length of the fibre reduces the overall ductility (Brenner, 1958).

strain precluded the development of the large uniform strains observed in figure 2.23.

Reference is often made in the literature on heavily co-deformed material to the whisker-like properties of the fine-scale embedded phases produced by heavy co-deformation (Wood and Embury, 1995, Raabe et al., 1995, Snoeck et al., 1996, Gil Sevillano, 1991, Spitzig et al., 1987). The supposition of whisker-like behaviour in these fine-scale embedded phases is predicated on the observed macroscopic strength of the material and the break down of the rule of mixtures based on the properties of the bulk phases. What is unclear, both in the case of fine-scale embedded phases produced by heavy co-deformation or by eutectic solidification, is what the form of the mechanical response is in-situ when the phases are deformed in the embedded state. If it is to be argued that the embedded phase continues to support very large elastic stresses after heavy deformation the yield drop shown in figure 2.23 cannot occur. Tests on Zn whiskers have shown that the presence of an oxide coating can increase the initial yield point of the whiskers (Cabrera and Price, 1958), suggesting an effect arising from the constraint of the oxide. However to the author's knowledge, there have been no tests carried out to examine the strength of such whiskers beyond initial yield.

2.3.2 Internal Stresses: Measurement, Modelling and Relation to In-situ Deformation Behaviour

In order to understand the in-situ behaviour of phases and their relationship to the bulk mechanical properties of the composite, it is not sufficient to know the mechanical response of the bulk constituents. It is also necessary to know how the imposed stresses and strains are partitioned throughout the microstructure. In a material composed of phases with very different mechanical properties, the applied stresses and strains are partitioned unequally throughout the microstructure. Also, the degree to which the process of load transfer between phases occurs, is sensitive to the geometry of the phases and the mode of deformation. Thus, gradients of stress and strain can be developed on various length scales within a material (figure 2.26). If the mode of imposed deformation is homogeneous (e.g. there are no macroscopically imposed gradients of strain), then the internal stresses must result from the internal inhomogeneity of the material, e.g. the differences in mechanical response of the phases. If means of measuring the degree of load partitioning can be

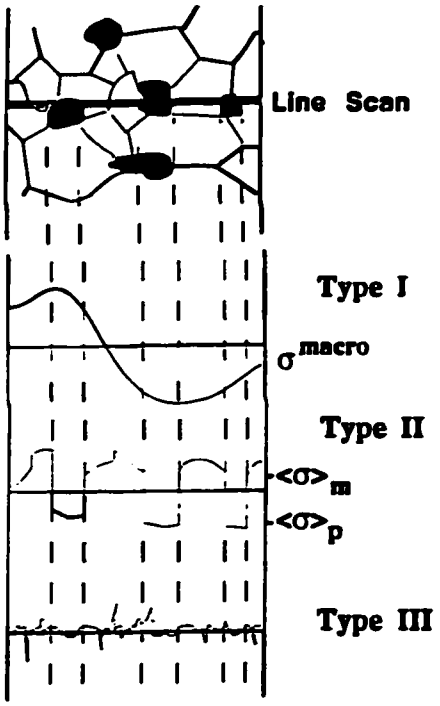

Fig 1. Schematic variation of the type I, II and III stress in a composite material.

Figure 2.26 The development of internal stresses in a material can occur on different length scales; I macroscopic stresses due to an inhomogeneous applied deformation, II intergranular stresses, III local stresses (Fitzpatrick et al., 1997).

devised, comments can be made regarding the in-situ properties of the two phases involved. An example of this is described below.

Following Kelly and MacMillan (1986), consider a material that consists of an infinitely long elastic rod embedded within an elastic/perfectly plastic matrix such that the volume fraction of the two phases are the same. Further, consider that the fibres and matrix share the same elastic properties but that the matrix yields plastically at a stress σ_{ym}, while the fibres continue to deform elastically. If this hypothetical material is strained below the yield stress of the matrix, load is distributed uniformly as the properties are equivalent everywhere and the rate of loading is governed by the modulus of the two phases (E). However, once the matrix yields, it can no longer support an increasing load, and thus any further increase in applied load must be carried by the fibre. The apparent modulus of the material after yielding of the matrix will drop from E to 0.5E. If the material is now unloaded and reloaded in compression, the matrix will yield in compression once the load has been decreased by $2\sigma_{ym}$. However, because the total load carried by the material when the forward test is stopped is greater than σ_{ym} by an amount $\Delta\sigma$ (because of the continued elastic loading of the fibre) yielding of the matrix in compression occurs when the macroscopic stress reaches σ_{ym}- $\Delta\sigma$ (figure 2.27). The inhomogeneous distribution in stresses gives rise to an asymmetry in the uniaxial stress-strain curve that becomes more pronounced the larger the amount of deformation in the forward direction. This asymmetry is often referred to as a *permanent softening* and is due to the inhomogeneous distribution of stresses or, equivalently, due to the presence of an internal stress in the matrix.

The mean internal stress is defined for a phase as the difference between the macroscopically applied stress and the stress carried by the phase. In this case this results in internal stresses of;

$$\langle\sigma\rangle_m = \sigma_m - \sigma_{App} = -0.5E\varepsilon_P = -fE\varepsilon_P$$
$$\langle\sigma\rangle_f = \sigma_f - \sigma_{App} = 0.5E\varepsilon_P = (1-f)E\varepsilon_P \quad (2.3)$$

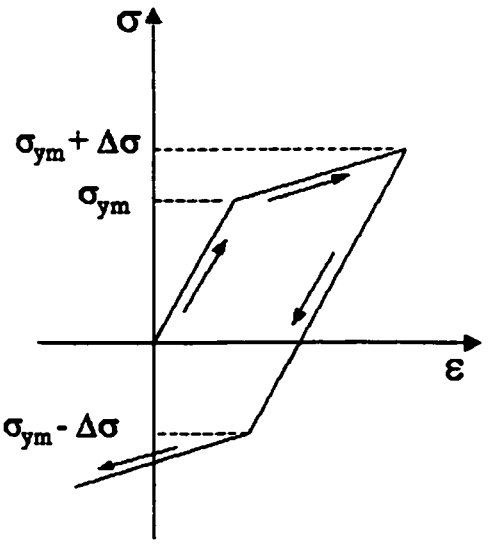

Figure 2.27 Schematic stress-strain curve for a hypothetical material that consists of an elastic fibre contained within an elastic/plastic matrix. The elastic properties and the volume fraction are assumed to be the same for the two phases.

where ε_P is the amount of plastic strain. Thus, it can be seen from equation 2.3 and figure 2.27 that;

i. the mean internal stress in the matrix is half the permanent softening ($\Delta\sigma$)

ii. the internal stresses in the matrix and fibre balance, i.e. $(1-f)\langle\sigma\rangle_m + f\langle\sigma\rangle_f = 0$

iii. although the matrix phase has no ability to work harden alone, the macroscopic flow curve shows a high rate of work hardening due to the elastic loading of the fibres

The observed asymmetry in the uniaxial tension-compression response of materials has been known since the experiments performed by Bauschinger in 1881(Abel, 1987). The *Bauschinger effect* is in fact composed of three phenomena;

i. permanent softening (as described above)

ii. transient softening

iii. a lowering of the initial yield point

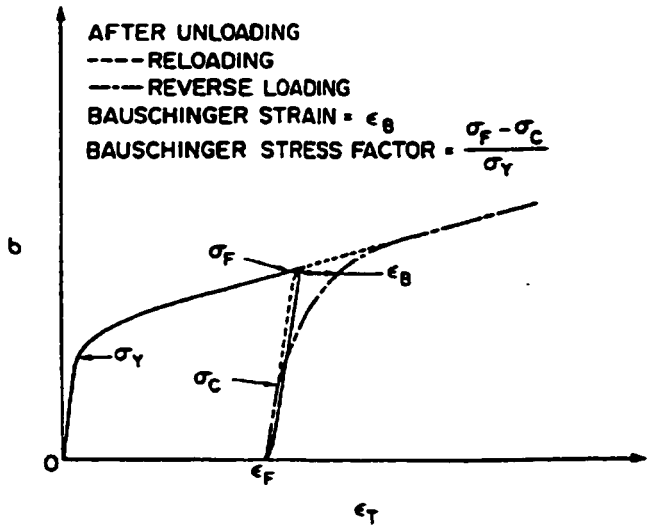

Figure 2.28 Common parameters used to describe the Bauschinger effect (Abel, 1987).

In order for a material to exhibit a Bauschinger effect it is not necessary for it to exhibit all three of these phenomena. In fact many materials have a very strong Bauschinger effect but do not exhibit any substantial permanent softening (e.g. Moan, 1977). A vast number of phenomenological parameters have been forwarded as means of quantifying the Bauschinger effect (Abel, 1987). In all cases, it is necessary to perform some type of uniaxial tension-compression test to determine the flow response of the material in both directions of straining.

Figure 2.28 shows some of the more commonly used measurements of the Bauschinger effect in the standard plot where the compressive response of the material has been transformed into the first quadrant of the stress-strain axes.

The phenomena of permanent softening has been described for a simple case above. In general, the degree of permanent softening is measured by performing a uniaxial tensile test to a given pre-strain followed by a compressive test, where the compressive portion of the test is

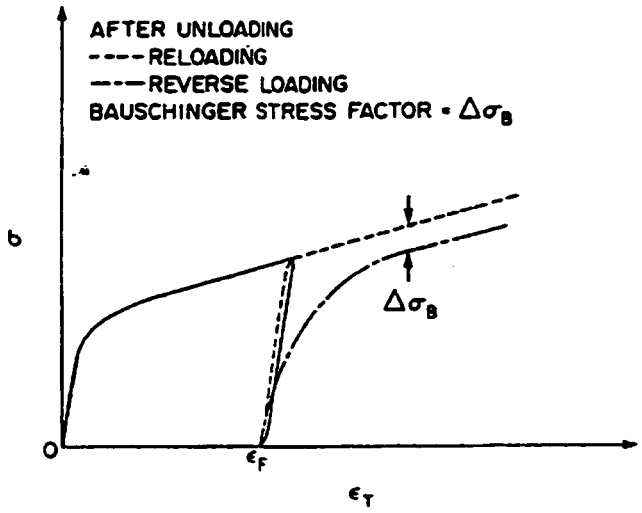

Figure 2.29 Common technique for measuring a permanent softening. The reverse flow curve has been transformed into the first quadrant (Abel, 1987).

taken to large enough strains that the forward and reverse flow curves become parallel. The permanent softening is then obtained by extrapolating the forward flow curve and measuring at the point where the flow curves become parallel (figure 2.29). Although this is the standard method for performing a Bauschinger test to measure the permanent offset, a number of difficulties arise in the interpretation;

i. In order to make the compressive flow curve parallel to the tensile curve, relatively large compressive strains are generally necessary. However, in the compressive direction, strains of the order of 4 -5% can result in buckling of the sample. This limits the amount of forward pre-strain that can be given to the sample as well. Thus, measurements of permanent softening (and in general measurements of the Bauschinger effect) are generally limited to tensile pre-strains of the order of a few percent.

ii. Some (Prangnell et al., 1992, Wilson and Bate, 1986) have questioned the assumption that the two curves should ever become exactly parallel. Experiments by Prangnell et al. (1995) appear to support this view.

iii. Linked to the above point is the assumption that the substructure developed on forward straining does not change on reversing the direction of flow.

Many materials that exhibit a Bauschinger effect do not exhibit a permanent softening. Instead, a process of transient softening is observed. When some materials are deformed in compression after a tensile pre-strain, yielding occurs at a substantially lowered stress. However, unlike the simplistic material shown in figure 2.27, such materials exhibit a very rounded flow curve which may or may not lead to a permanent softening. Two explanations for this effect have been posited. In Orowan's description (e.g. see Brown, 1977) the source of the transient softening is attributable to dislocations piled up against hard obstacles. When the applied stress is removed, these dislocations are able to move away from the obstacles. In this case, a dislocation "sees" a weaker set of obstacles in reverse direction than it does in the forward direction.

Unlike permanent softening, this explanation of transient softening implies that it is independent of the presence of long range internal stresses. Alternatively, it can be imagined that an inhomogeneous distribution of internal stresses may also give rise to transient softening. This is the basis for the simple Masing model

(e.g. see Sowerby et al., 1979) as well as the shake-down model of Cottrell (1964). In both cases it is assumed that the material consists of elements which have different yield strengths. This distribution of yield strengths may be associated with internal stresses developed during pre-straining that vary throughout the microstructure. When such a material is tested in the opposite direction, the first element of material to yield will be that which consists of the largest internal stress acting to aid the applied stresses. As the stress is increased, the material will undergo a gradual transition from the elastic state to the plastic state, during which the fraction of elastic and plastic grains will evolve with the amount of applied stress. This "shake-down" process will lead to a gradual evolution of the flow curve from the elastic response to the fully plastic response giving rise to a transient yield behaviour. Once all elements of the material are plastic, there will be no net permanent offset produced by this mechanism.

Experimental measurements of the Bauschinger effect in fibre reinforced materials have been carried out over the range of strains where the fibres are observed to be loaded elastically. Lilholt (1977a, 1977b, 1993) has performed Bauschinger tests on Cu reinforced with W wires up to the point of fibre fracture. In this material, it was observed that the behaviour of the material actually follows surprisingly closely to the simple model described above for permanent softening. The rate of increase of the mean stress with the volume fraction of fibres for these materials is shown in figure 2.30. As predicted by equation 2.3, the mean internal stress in the matrix is linear in the volume fraction as well as the plastic strain. An interesting feature of this data is that it exhibits a dependence of the rate of internal stress development on the test temperature. Lilholt (1977a) suggested that this is due to a process of

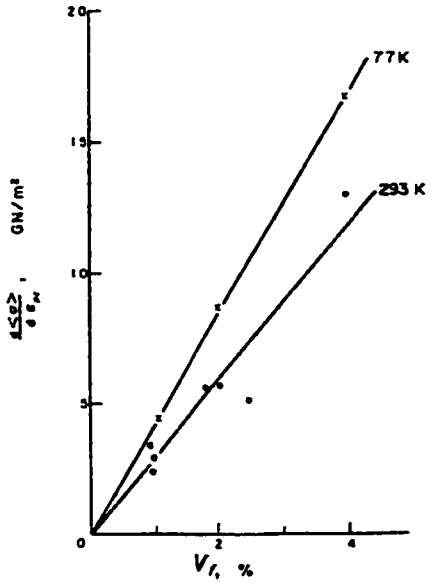

Figure 2.30 The mean internal stress work hardening measured Bauschinger tests in W fibre reinforced Cu at 293K and 77K (Lilholt, 1977b).

plastic relaxation in the Cu matrix, acting to partially relax the stresses in the W fibres (i.e. to allow the matrix to flow around the fibres). This may occur by a number of processes, the most likely being secondary slip close to the fibres or a restricted form of cross-slip around the fibres (Lilholt, 1977b). Brown and Clarke's (1976) analysis of the data collected by Lilholt showed that Eshelby's Equivalent Inclusion Method (Eshelby, 1957,1961) could be used to accurately analyze the development of internal stresses in the Cu-W system. In the notation of Brown and Clarke, the mean internal stress in the matrix developed by the presence of the fibres is given by

$$\langle\sigma\rangle_m = K\gamma\mu f\varepsilon_p \qquad (2.4)$$

where K and γ are constants that depend on the elastic constants of the system and the geometry of the phases and deformation. Note, however, for the simple case were deformation is assumed to occur by multiple slip and the volume fraction of fibres is low, the above equation is approximately equivalent to that given in equation 2.3.

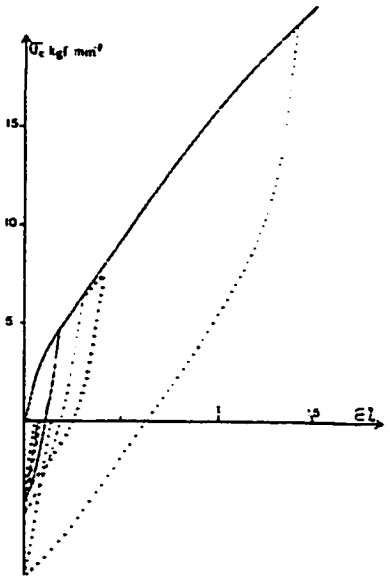

Figure 2.31 Tension/compression loops for an Al-Al_3Ni directionally solidified eutectic. Plastic flow in compression occurs prior to the applied load becoming compressive (Lasalmonie and Martin, 1974).

Bauschinger tests have also been carried out on a directionally solidified Al-Al_3Ni eutectic alloy (Lasalmonie and Martin, 1974). Figure 2.31 shows the stress-strain curves for this material. The internal stresses that tend to aid reverse flow are extremely large. Figure 2.32 shows the amount of permanent softening measured from these curves as a function of plastic strain (Clarke and Lilholt, 1975). As with the Cu-W system, Clarke and Lilholt (1975) were able to show that equation 2.4 fit the experimental data up to the point where either fibre yielding or fibre fracture occurred.

An alternative method for examining the development of internal stresses, and therefore the in-situ loading behaviour, of two-phase materials is to directly measure the elastic strains carried by the two phases in-situ. This can be done using the spacing of atomic planes as a gauge for elastic strains.. An elastic strain will tend to change the interplanar spacings, thus if a material is stretched along a given direction then the change in the spacing of the (hkl) planes perpendicular to this direction can be used to measure the amount of elastic strain carried by that phase along that direction. Analysis of the full stress tensor by such means is cumbersome as it necessitates making at least six independent measurements of strain. Instead, measurements on polycrystalline specimens are normally made in the axial (parallel to the tensile axis) and Poisson (transverse) directions. It is important to distinguish that the strains measured by peak shifts in diffraction experiments are associated with elastic strains. Nothing may be said about the magnitude of the plastic strains simply by measuring peak shifts. There is a strong link between the Bauschinger effect described above and the lattice strains measured by diffraction. Atkinson et al. (1974) realized this and used the diffraction work of Wilson and Konnan (1964) to calibrate the measured permanent softening (as measured in the Bauschinger test) with the magnitude of internal stresses for a dispersion hardened Cu-SiO_2 material. This comparison showed that the permanent softening is generally related to the mean internal stress in the matrix by a factor of approximately two.

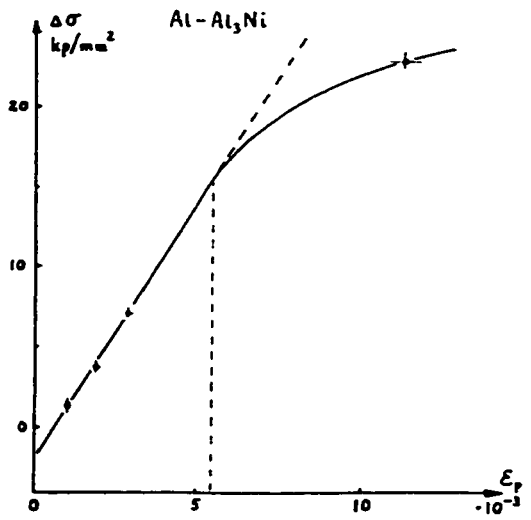

Figure 2.32 The permanent softening measured by Clark and Lilholt (1975) from the data shown in figure 2.31.

Use of the diffraction technique to study the in-situ deformation behaviour of fibre reinforced metals has been carried out by Cheskis and Heckel (1968, 1970) on thin foils of Cu-W, Al-B and Al-W composites. Figure 2.33 shows the deduced stress-strain curves from their x-ray studies on the Al-W fibre reinforced materials. Here, the stress was computed directly from the lattice strains while the strain was measured using

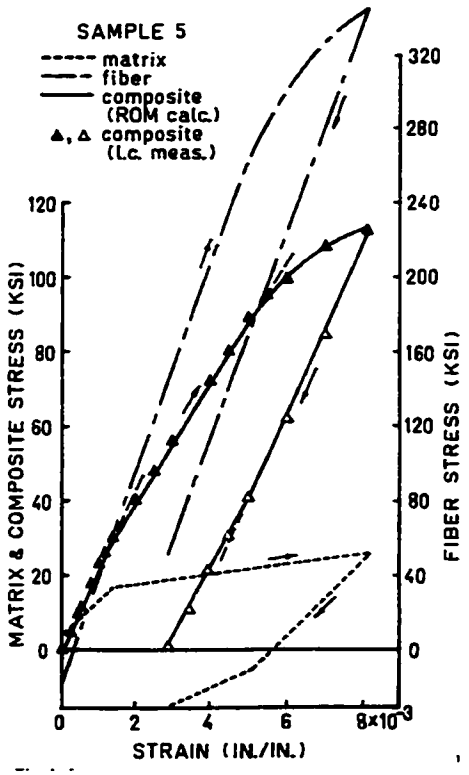

Figure 2.33 Stresses deduced from elastic strains by x-ray diffraction for Al-W fibre composites plotted versus the macroscopic strain. The macroscopic (composite) stress-strain curves are shown for comparison (Cheskis and Heckel, 1970).

a strain gauge attached to the sample. The matrix in this case yields at relatively low stresses while the fibres continue to load elastically to stresses of the order of 2 GPa. As expected, when the samples were unloaded the plastically deformed matrix was left in a state of residual compression and the fibres in a state of residual tension. When the measured stresses in the matrix and fibre were combined using the rule of mixtures the composite flow curve could be predicted with good accuracy.

A number of subsequent experiments have been conducted using both x-ray and neutron diffraction to measure the in-situ response of multiphase materials. Withers et al. (Withers et al., 1989, Allen et al., 1992) have shown that the full tensor Eshelby Method can be used to predict the development of lattice strains in composites consisting of short fibres and particles. However, very little work has been done to examine the in-situ flow behaviour of two-phase materials during co-deformation.

Carter and Bourke (Carter, 1999, Carter and Bourke, 2000) have performed experiments on percolated Al-Be composites in which both phases are able to deform plastically. In this case the Be may be considered the reinforcing phase as it yields at higher stresses than the Al matrix. Figure 2.34 shows the measured lattice strain for the two phases as a function of applied compressive stress both for reflections a) parallel to the direction of applied strain and b) perpendicular to the applied strain. Generally, three regimes could be attributed to these curves associated with i. elastic loading of both phases, ii. elastic loading of the Be/plastic

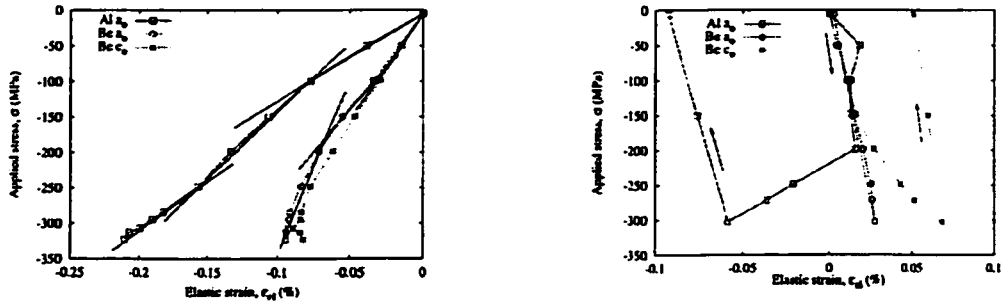

(a) (b)

Figure 2.34 Measured lattice strain versus applied stress for Al-Be two-phase material tested in compression. a) Strains measured parallel to the compression axis, and b) perpendicular to compression axis (Carter and Bourke, 2000).

loading of the Al, and iii. plastic deformation of both phases. Qualitatively, these three regimes can be attributed to the transfer of load between the two phases as deformation proceeds. At the elastic/plastic transition for the Al the slope of the lattice strain versus applied stress for the two phases shifts in opposite directions indicating a strong shift of load from the matrix onto the Be. At the elastic/plastic transition for the Be, the rate of lattice strain accumulation shifts back indicating transfer of load back onto the Al phase.

Measurements of residual lattice strains (i.e. lattice strains measured ex-situ after some amount of plastic deformation) have been performed for very heavily co-deformed two-phase materials by Han et al. (1999) on Cu-Ag and Cu-Nb and Stobbs and Paetke (1985) on pearlitic steel. Figure 2.35 shows the results of Han et al. which indicate that after heavy co-deformation in these Cu based systems, the internal stresses continue to rise. Elastic strains in the Nb phase reach levels in excess of 1%.

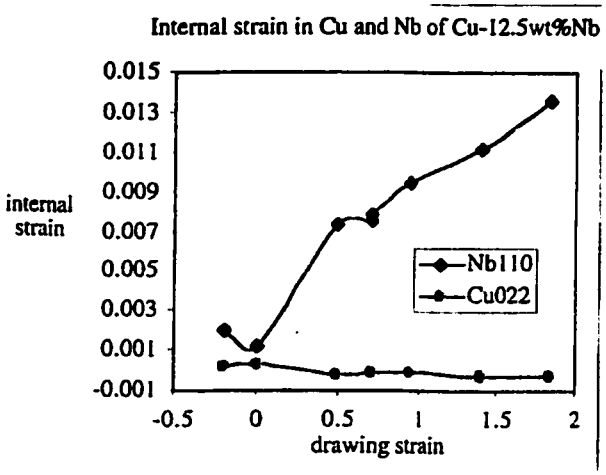

Figure 2.35 Residual stresses measured by neutron diffraction for Cu-Nb two-phase material wire drawn to different strains (Han et al., 1999).

2.3.3 Summary

1. The presence of an inhomogeneous distribution of mechanical properties throughout a material results in an inhomogeneous distribution of stresses and strains. This inhomogeneous distribution may act to aid or hinder plastic flow in the phases.

2. Measurements of long range internal stresses may be made by examining the tension-compression asymmetry in uniaxial deformation. Alternatively, the true in-situ behaviour of phases can be measured if diffraction techniques are utilized.

3. Measurements of internal stresses via permanent softening and the Bauschinger effect have been made on some fibre reinforced materials although the tests are limited to relatively low strains because of the problems with sample buckling in compression. In these tests the mean internal stresses are measured to be very large particularly in directionally solidified eutectic materials.

4. Diffraction measurements of the in-situ deformation behaviour have been successful for materials containing rigid particles, however little work has been done to elucidate the behaviour during co-deformation. The few studies carried out up to this point have been largely limited to ex-situ studies of residual stresses in heavily co-deformed two-phase materials. In these materials very large elastic strains are observed in the embedded phases.

5. In order to be able to properly interpret the measurements made by either of these two techniques it is necessary to have an approximate idea of the mechanical properties of the phases that they contain. In the case of directionally solidified eutectics, the fine-scale eutectic phases may exhibit properties very different from their bulk counterparts. It remains to be seen whether the behaviour of the phases free from their embedded matrix are similar to those observed in-situ.

2.4 MICROSCOPIC CHARACTERIZATION OF THE CO-DEFORMATION OF TWO-PHASE MATERIALS

In two-phase materials that consist of at least one phase that exists at the submicron level, the most predominant feature of the microstructure is the high density of interfaces. In a material that contains 2vol% rods of 0.1 μm diameter the ratio of the internal surface area to total volume is 4×10^5 m^2/m^3. In considering the deformation behaviour of such materials it is impossible to ignore the contribution the interfaces make to the overall behaviour of the material. The presence of a high density of interfaces can influence the overall deformation behaviour of a material in a number of ways. Some of these may include;

i. The need to maintain compatibility between the two phases across the interface can cause deformation to be disturbed in the vicinity of the phase boundary.

ii. The interface can act as a source, sink or barrier for dislocations in the two phases.

iii. The constraint imposed by finely spaced interfaces may induce mechanisms of deformation substantially different from those observed in bulk materials and may alter the competition between plasticity and fracture.

Above, the macroscopic and mesoscopic consequences of an inhomogeneous distribution of mechanical properties throughout a material have been discussed both with regard to the bulk mechanical response and the development of internal stresses. In general, the development of large internal stresses due to differences in flow behaviour between two phases is unfavorable as it results in a high rate of energy storage. In order to reduce the amount of stored elastic energy, the incompatibility between the two phases can be lowered by one phase undergoing extra plastic deformation. This *plastic relaxation* has already been referred to at the macroscopic level as the source of weakened textures in dispersion hardened materials and at the mesoscopic level as reducing the measured Bauschinger effect, or measured internal stress level compared to that predicted based on perfect load transfer. At the microscopic level plastic relaxation occurs due to the glide and storage of extra dislocations in the vicinity of hard particles. The classic example of plastic relaxation can be seen in dispersion hardened materials containing equiaxed particles oriented for single slip and deformed ~2

-5% in tension (Brown and Stobbs, 1971, 1976). Over the first few percent strain, measurements of the internal stress show that it rises in proportion to the plastic strain as would be predicted by the simple models made in the previous section. However, the material can reduce its stored elastic energy if slip processes occur to relax the structure built up around the particles. In terms of dislocation configurations, the initial straining leaves simple shear loops surrounding the particles. When the stress on the particles becomes large enough, these shear loops become unstable and are converted into a lower energy dislocation arrangement. A large number of possible dislocation arrangements have been proposed and reviewed by Brown and Stobbs (1971), the most important of which are shown schematically in figure 2.36. The result of this process of plastic relaxation is twofold. First, the internal stresses are lowered throughout the material, thereby lowering the stored elastic energy. A portion of the stored energy goes into the storage of extra dislocation line length in the vicinity of the particles. Ashby (1971) considered the ideal situation where the internal stresses are reduced to zero by the storage of these extra (or so-called geometrically necessary) dislocations. Brown and Stobbs (1976) showed that this situation is over simplified and that the storage of extra dislocations around the particles will always give rise to some finite long range internal stress in the material.

In the case of equiaxed particles the process of plastic relaxation can be quite efficient at reducing the load transfer to the particles. However, when the embedded phase takes the form of long fibres, plastic relaxation is significantly more difficult. Three of the primary processes of plastic relaxation in particle reinforced materials are observed to be prismatic punching of dislocation loops, double cross-slip and secondary slip. In the case of infinitely long fibres the process of prismatic

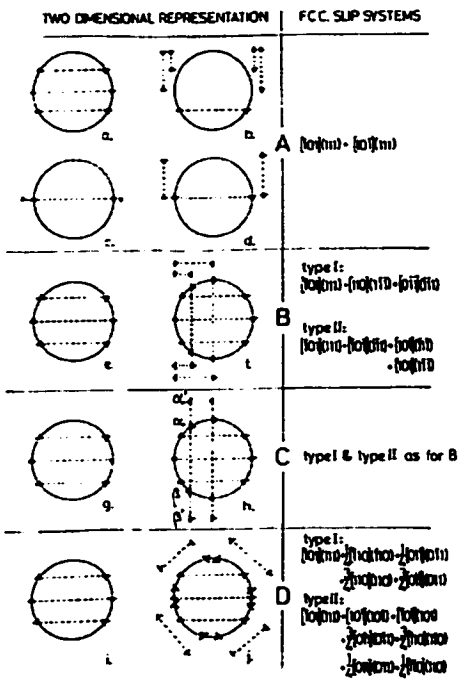

Figure 2.36 Processes of plastic relaxation that may occur in materials containing equiaxed particles (Brown and Stobbs, 1971).

punching is difficult as the length of dislocation line necessary to relax the strain is defined by the fibre length. Alternatively, the process of double cross-slip remains available, however, the process is not nearly as efficient as for equiaxed spheres. Two processes can be imagined in this case (figure 2.37), the ease of each one depending on the orientation of the fibre axis with respect to the cross-slip system. In one case, a shear loop can undergo double cross-slip to convert into two prismatic loops plus a shear loop. In the second case the shear loop can be converted into two prismatic loops. It is also possible in this case that slip on secondary slip systems can help achieve plastic relaxation (figure 2.38). This process is often referred to as the most energetically favorable for fibre reinforced materials (Lilholt, 1993).

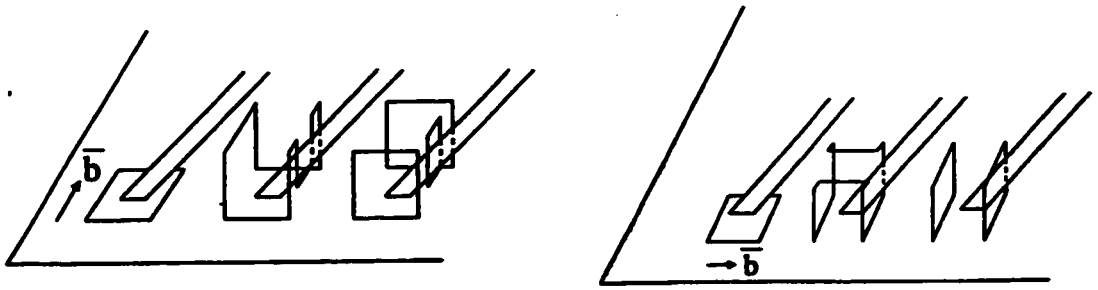

(a) (b)

Figure 2.37 Plastic relaxation by a process of double cross-slip in fibre reinforced materials (Lilholt, 1993).

The above effects are mainly observed at relatively small strains when one phase is deforming elastically and the other is deforming plastically. At higher strains, in materials that undergo a process of co-deformation, the internal stresses can be relaxed more effectively by the plastic deformation of the embedded phase itself. In this case the phase boundary can interact in a number of different ways with the process of co-deformation. One of the most common assumptions is that the phase boundaries act as barriers to slip in one or both of the phases. It is often assumed that the phase interface can be considered as a barrier (of strength τ^*) to slip which dislocations must overcome to pass across the boundary. The applied stress

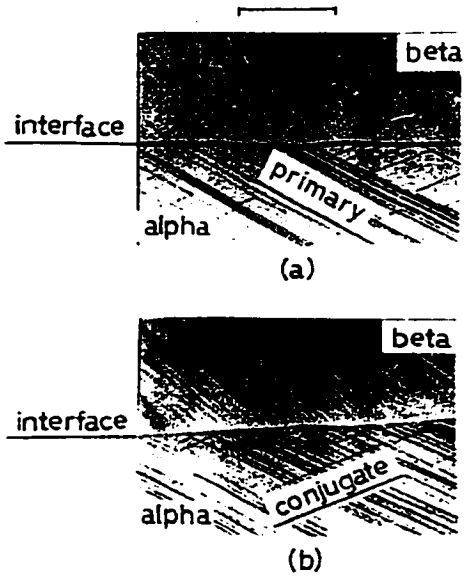

Figure 2.38 Secondary slip in the softer phase (α) of an α–β brass bicrystal in order to partially accommodate the plastic misfit between the two phases (Fat-Halla et al., 1979).

necessary for the first dislocation to pass across the phase boundary is given by the classic Hall-Petch equation,

$$\tau = \tau_0 + \left(\frac{\mu b \tau^*}{\pi \lambda}\right) \qquad (2.5)$$

where λ is the interphase spacing. This model has been used numerous times in attempting to explain the strength (particularly the scale dependence of strength) in co-deforming two-phase materials. Recently, this same general approach has been shown to predict the strength/size dependence in multilayer materials (e.g. Misra et al., 1998, Anderson and Li, 1995, Hazzledine and Rao, 1996). It is somewhat surprising that such a simple approach should give such a good fit to the experimental data for so many different systems. It is clear that phase boundaries can act in many different ways to influence the deformation behaviour of two-phase materials. The basic premise of the Hall-Petch model is that the phase boundary has a finite resistance to the passage of dislocations across it. It is certainly true that dislocation transmission has been observed in many two-phase materials undergoing co-deformation (e.g. Misra et al., 1999, Godfrey et al., 1998, Suri et al., 1999, Fat-Halla et al., 1979, Verhaeghe et al., 1997) however, the process of slip transmission is complicated, thus the ability to attribute a unique barrier strength to boundaries in a material is questionable. Figure 2.39 shows a series of four possible mechanisms for slip transmission. In the first two, transmission occurs directly by cross-slip of the dislocation across the phase boundary, while in the second two transmission occurs indirectly by emission of a dislocation from another position in the phase interface. In all cases, residual dislocations must be left in the boundary with a net Burgers vector equal to the difference in the Burgers vector of the

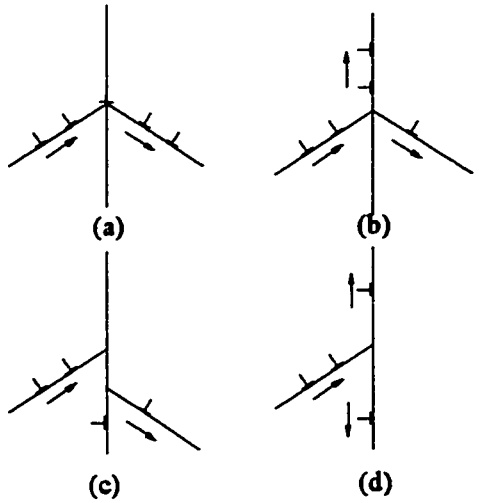

Figure 2.39 Schematic showing four possible mechanisms of slip transfer across a phase boundary (after Sutton and Balluffi, 1995).

incident and transmitted dislocations. Clearly, certain misorientations between phases will lead to easy paths for slip transfer across the phase boundary.

Those misorientations most favorable for slip transmission will tend to have slip systems that are nearly continuous across the phase boundary such that the resolved stress from the incident system is maximized and the magnitude of the residual dislocation left at the boundary is minimized (Sutton and Balluffi , 1995). These conditions are well satisfied in fcc/bcc two-phase materials when the two phases share the Kurdjumov-Sachs (K-S) orientation relationship. In this orientation relationship one slip system is exactly coincident across the phase boundary. Thus, an approximate analysis would suggest that the only barrier to the passage of a dislocation across the boundary is that associated with the energy of the residual dislocation left at the boundary (Sutton and Balluffi, 1995). The transmission on this coincident set of slip systems in K-S misoriented phases has in fact been observed to occur with relative ease. Figure 2.40 shows two examples of slip transmission under these circumstances. The first example is an austenite-ferrite duplex stainless steel where in-situ electron microscopy clearly shows slip transfer on the coincident system (Verhaeghe et al., 1997). The second example is taken from the work of Misra and Gibala (1999) who observed slip transmission between γ and β eutectic phases in a directionally solidified Ni-Fe-Al alloy.

It is also possible that the phase boundaries may help the process of deformation by acting as a source for dislocations. Garmong (1976) observed that in a directionally solidified Ni-W, the Ni/W interface can act as a source of dislocations for the Ni matrix, particularly at low strains. This is illustrated by figure 2.41 which shows dislocations being emitted from a source located within the phase boundary.

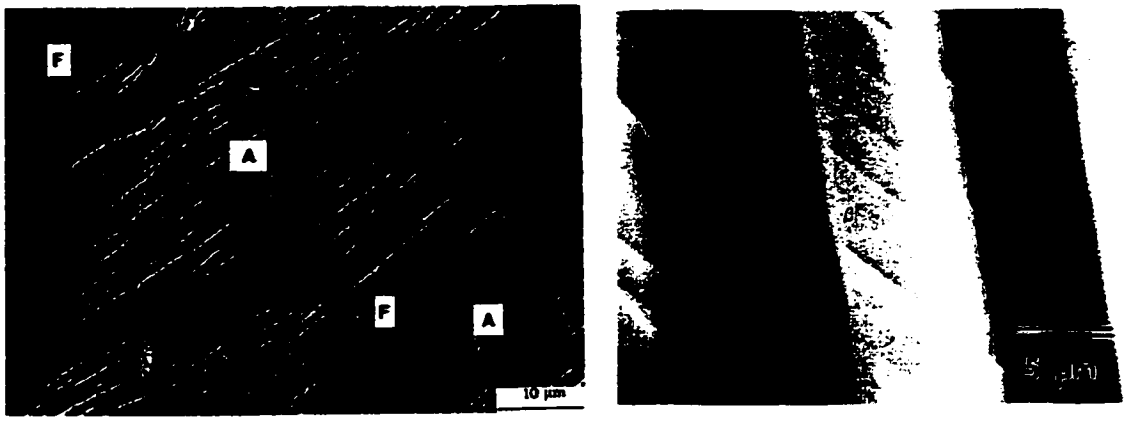

(a) (b)

Figure 2.40 a) Observation of slip transmission in K-S oriented duplex stainless steel (Verhaeghe et al., 1997). b) Slip transfer across phase interface in K-S oriented γ–β phases in a directionally solidified Ni-Fe-Al alloy.

The mechanisms described above are important when the critical length scale in the two phases is larger than ~1 μm. When the minimum length scale within a phase is reduced below this level the implicit assumptions often made in continuum analysis become questionable. In particular, the simplified Hall-Petch law given above begins to predict very large flow stresses when the dimensions of the phases approach the submicron scale. The question that then arises is whether there are other mechanisms that may occur in such systems.

A great deal of work has been carried out recently in an attempt to examine this question for the case of fine-scale multilayers and heavily co-deformed two-phase materials both experimentally (Nix, 1989, Anderson et al., 1999, Janecek et al., 2000, Thilly, 2000) and theoretically (Embury and Hirth, 1994, Anderson et al., 1999, Louchet, 1998, Nix, 1989). It is

Figure 2.41 TEM micrograph showing dislocations being emitted from the phase boundary in a directionally solidified Ni-W alloy (Garmong, 1976).

generally observed that once the interphase spacing reaches a critical level, plasticity occurs by a process that is constrained by the interfaces. Figure 2.42 schematically shows two of the potential processes that may occur. First, in materials that have been heavily co-deformed it is often assumed that the interface will contain a relatively high density of pre-existing sources for dislocations. These sources may then operate by bulging a loop out of one side of the interface and propagating across the phase into the opposite boundary. The portions of the loop left in the phase may then propagate along the length of the phase in the so-called hairpin configuration (Louchet, 1998). Alternatively, if the interfaces are devoid of sources, a loop must be nucleated at the interface. Again, this loop will propagate across one phase until it becomes trapped in the opposite interface. The propagation of the segments of the loop will be limited by the geometry of the channel in which it lies. In most cases it is assumed that the channels are semi-infinite plates in two dimensions, thus the residual segments within the boundary can glide in their slip plane for long distances before reaching a boundary. If, alternatively, the phase in which glide is occurring is cylindrical the amount of strain per dislocation will be limited unless glide occurs on a plane parallel to the cylinder axis. Generally this will not be favorable as the long axis of the phase will either be oriented parallel or perpendicular to the direction of applied stress. Regardless of the geometry of the phases, the common feature in the deformation of sub-micron phases is that it does not occur in bands separated by microns, but instead occurs by the motion of single dislocations on closely spaced planes. The result of this process is that little dislocation storage occurs within the deforming fine-scale phase but instead it occurs at the phase interface. Further, the fine scale of deformation leads to phases that, even after very large plastic strains, remain relatively regular in their cross-sectional dimensions (e.g. Wood, 1994). These

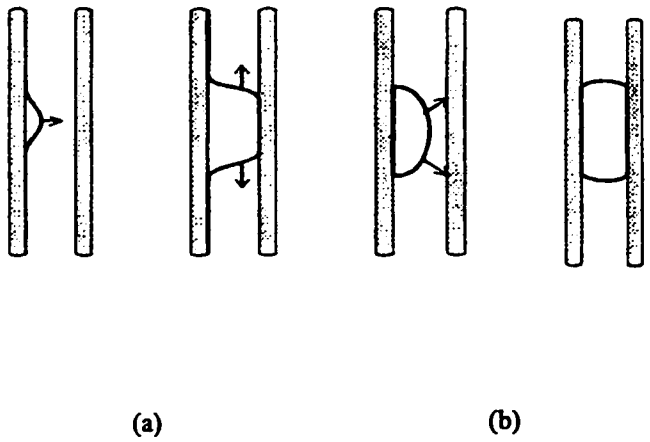

Figure 2.42 Schematic diagram showing a) bulging of pre-existing interfacial dislocation into a phase. b) Nucleation of a dislocation at the phase interface (Louchet, 1998).

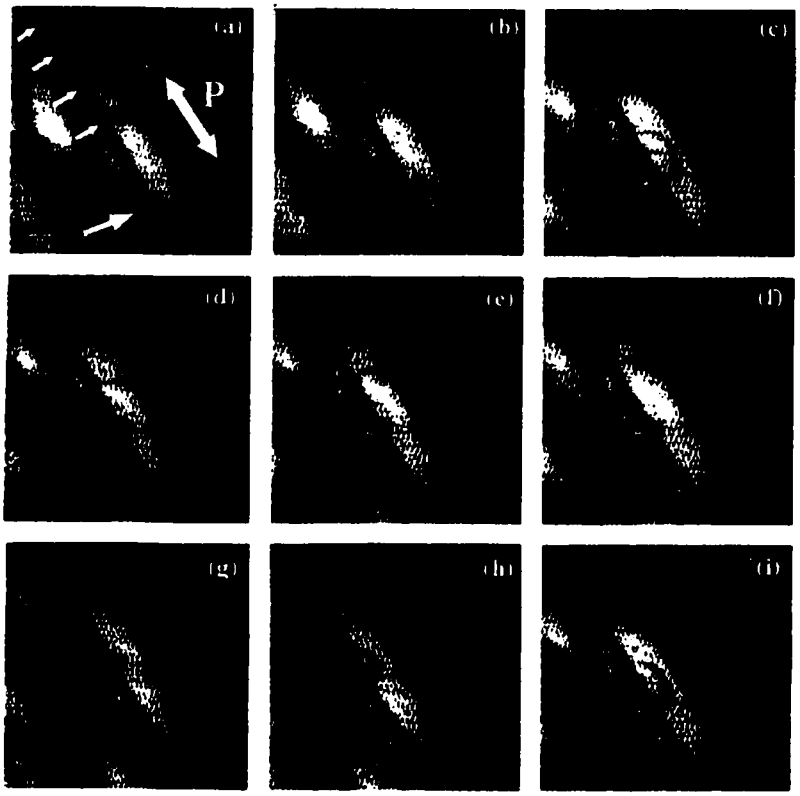

Figure 2.43 A series of in-situ TEM images taken during tensile testing of a Cu/Ni multilayer showing the bulging of interfacial dislocations in the narrow channels of the Cu phase similar to the processes shown in figure 2.42 (Anderson et al., 1999).

processes have been experimentally observed by in-situ TEM observations on strained films of heavily co-deformed Cu/Nb (Thilly, 2000), Fe-Fe_3C (Janecek et al., 1999) and Cu/Ni multilayers (Anderson et al., 1999). Figure 2.43 shows a series of images from the latter work taken in-situ during straining showing dislocations bowing out of the phase interface and subsequently propagating along the length of a Ni nanolayer.

A number of analytical models have been proposed (e.g. Embury and Hirth, 1994, Louchet 1998, Misra et al., 1998, Nix, 1989, Anderson et al., 1999) to explain the mechanical response resulting from the interface constrained deformation described above. In general, these models can be separated into two groups. In one group (e.g. Embury and Hirth, 1994, Nix, 1989, Louchet, 1998) it is assumed that deformation occurs by the motion of dislocations in only one layer (the other layer being elastically loaded) leading to the constrained mode of deformation described above. In the other case, the material is treated using a modified version of the

Hall-Petch equation that accounts for the possible presence of internal stresses due to coherency at the phase interface and stresses arising from the difference in elastic constants across the phase boundary. Both of these approaches are limited to predicting the initial stress necessary to cause bulk yielding of materials with a fine scale; i.e. they assume that by some means (e.g. co-deformation by wire drawing) a certain interphase spacing is produced and that the resulting yield strength of the material in tension is a direct result of this scale. Neither approach gives a complete picture of the behaviour of co-deforming two-phase materials. In the first case, the interface is assumed to be infinitely strong such that deformation in the harder phase will never occur. In the Hall-Petch approach simplifying assumptions about the nature of the barrier stress must be made. In general both approaches, being essentially continuum in nature, necessitate simplifying assumptions concerning the structure and strength of the interphase boundaries.

Recently, efforts have been made to model the low strain deformation processes occurring in fine-scale two-phase materials at the atomistic level (Rao and Hazzledine, 1999, Rao and Hazzledine, 2000, Hoagland, 1999). To date, the most detailed simulations on the interactions of dislocations with interfaces have been carried out by Rao and Hazzledine (2000). Here, simulations were performed on Cu-Ni multilayers in an attempt to understand the barrier strength of the phase interface to dislocation transmission. It was shown that the stress necessary to cause transmission of dislocations across the phase interface is large even for the most favourable of conditions giving transmission stresses of the order of ~μ/100. For example, it was found that at

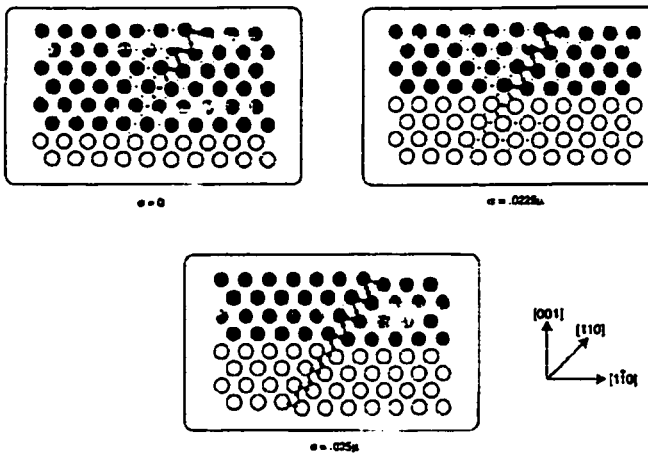

Figure 2.44 Atomic positions in atomistic model of a Cu/Ni bilayer showing the position of a dislocation as a function of applied stress (dislocation indicated by vectors) (Rao and Hazzledine, 2000).

coherent twin boundaries, screw dislocations approaching the interface from Cu find it easier to cross- slip into the boundary rather than transmit across the boundary. This was attributed to the lower stacking fault energy at the interface compared to that within the Ni. Figure 2.44 shows a series of plots indicating atomic positions within a Cu/Ni bilayer. These plots indicate that transmission of a partial dislocation across the phase boundary in the presence of large coherency stresses occurs at an applied stress of 0.024μ, very close to the theoretical shear strength.

Although limited to studies of the interactions of single dislocations with phase boundaries, these calculations give a great deal of detailed information concerning the mechanisms involved in dislocation transmission. Such computational approaches on various two-phase systems could provide valuable information for input into continuum scale models.

2.5 PREVIOUS WORK ON THE DEFORMATION OF CU-CR ALLOYS

The recent interest in co-deformed fcc/bcc materials has been largely due to the observed mechanical behaviour of heavily deformed materials such as Cu-Nb. Although a number of combinations can be imagined as potential fcc/bcc two-phase materials, the requirement that the two components do not form intermediate phases restricts the number of potential systems. Cu-Cr is one combination of an fcc and bcc material that is well suited, as these two components are mutually soluble in the liquid state but nearly insoluble in the solid state. Further, they undergo a eutectic reaction at approximately 1.56 at% Cr and form no intermediate phases. Thus, by solidification it is possible to produce a microstructure either composed of a fine-scale eutectic or to form larger dendrites of one phase embedded in a matrix of the other. The combination of Cu and Cr is also interesting due to the difference between the mechanical properties of bulk Cu and Cr. As a pure single crystal, Cu will yield plastically at stresses of only a few MPa. Further, being an fcc metal, Cu exhibits a relatively small change in flow strength on reducing temperature. Cr, on the other hand, being bcc, has a relatively high flow stress. The extreme sensitivity of Cr to the presence of interstitial solute means that unless great precautions are taken to ensure high purity, Cr will fracture prior to yield at

temperatures substantially above room temperature (Gilbert et al., 1963, Reid et al., 1967). Very careful experiments on single crystals of Cr have shown that under properly controlled conditions, Cr will deform plastically at room temperature prior to fracture. However, its total ductility at this temperature does not exceed a few percent. Unlike fcc Cu, bcc Cr exhibits a strong dependence of the yield stress on the test temperature. Figure 2.45 shows the data compiled by Gilbert (1963) showing that the yield strength of Cr rises by nearly a factor of 4 as the temperature is dropped from 300 K to 77 K. With these substantial differences in bulk mechanical properties it is interesting to examine the properties when these materials are used to form a composite two-phase microstructure.

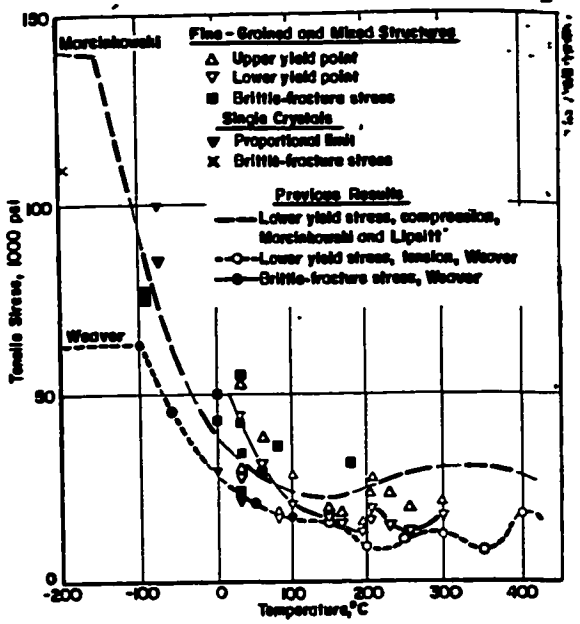

Figure 2.45 Measured yield strength of Cr as a function of test temperature (Gilbert et al., 1963).

Directionally solidified Cu-Cr holds an important place in the history of composite materials as it was the first produced by directional solidification (Salkind et al., 1970) for the purposes of obtaining high mechanical strength. This pioneering work was carried out by Hertzberg and Kraft (Hertzberg and Kraft, 1963, Hertzberg, 1964) on material directionally solidified at various rates. It was the failure behaviour of the material that was the primary interest, as it was expected that fracture of the Cr fibres would lead to substantial damage within the material. Surprisingly it was found that the material was very ductile, undergoing necking prior to failure. Further, optical metallography on sectioned tensile specimens gave little or no indication of damaged fibres outside of the failure surface. However, based on a series of three optical micrographs (figure 2.46) taken from the surface of a specimen viewed during bending, it was concluded that the fibres did in fact fracture in a brittle manner, resulting in the mechanism of final failure depicted in figure 2.47. Although no quantitative data is given for the uniform strain prior to failure, it is clear from the micrographs presented that

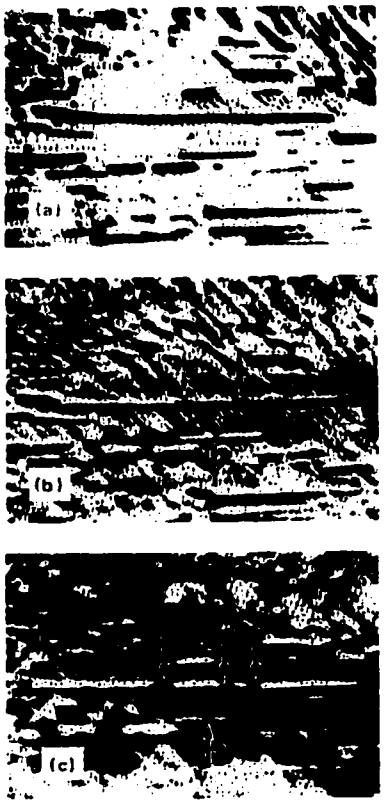

Figure 2.46 Optical micrographs from Hertzberg and Kraft (1963) showing fracture of Cr whisker on surface of bend specimen.

the samples underwent strains > 0.1 prior to failure. No explanation is forwarded to explain how the fibres are able to support such imposed strains prior to failure. The strength of the samples was observed to be approximately 250 MPa when tested in tension parallel to the tensile axis. It is suggested that such strength is not appreciably greater than that obtainable with other Cu based alloys. However, in order to achieve these strengths in conventional Cu alloys a significant reduction in grain size and perhaps alloying would be necessary. Therefore, it appears that the Cr fibres do introduce a significant strengthening effect.

More recently, work on the Cu-Cr system has been focused on the high strain co-deformation behaviour of hypereutectic material consisting of dendrites of Cr within a Cu matrix. In these materials, the Cr dendrites may be deformed extensively by co-deformation in cold rolling (Jin et al., 1998, Jin et al., 1996,

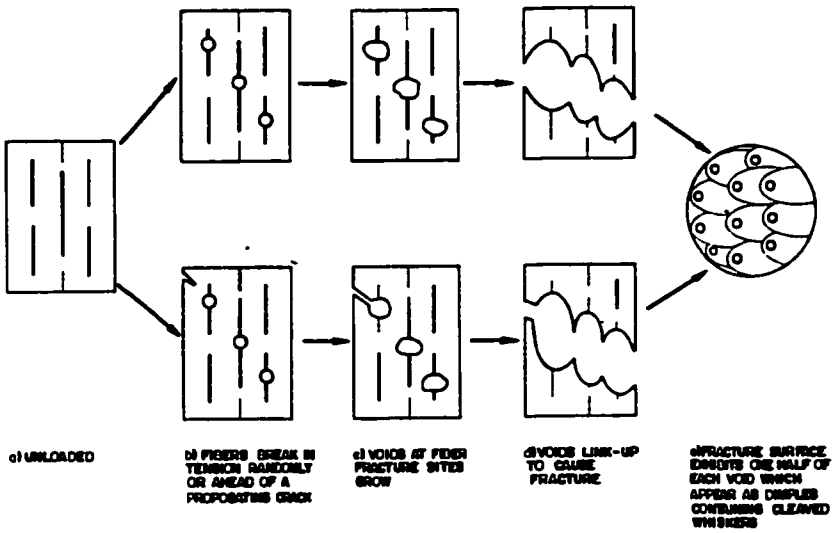

Figure 2.47 Schematic illustrating the mode of fracture envisioned by Hertzberg and Kraft to occur in directionally solidified Cu-Cr (Salkind et al., 1970).

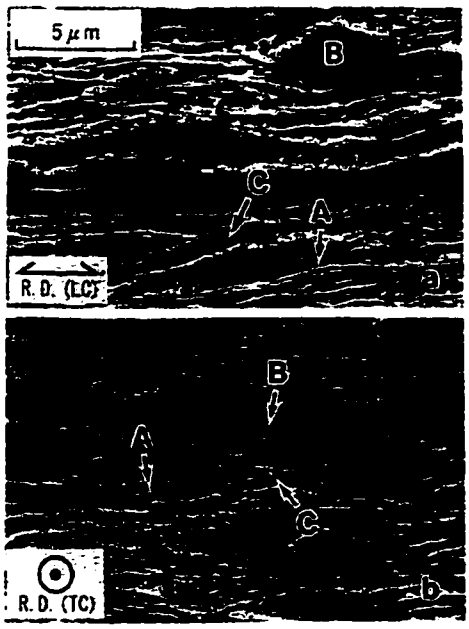

Figure 2.48 Microstructure of cold rolled Cu-15wt%Cr alloy (hypereutectic) after a 90% reduction (Takeuchi et al., 1989).

Adachi et al., 1997b), wire drawing (Adachi et al., 1997a, Takeuchi, 1989, Funkenbusch et al., 1984) and swaging (Lee et al., 2000, Carroll and Whitehouse, 2000). Figure 2.48 shows the microstructure of a Cu-15wt%Cr alloy cold rolled to ~ 90% reduction. Adachi et al. (1997a, 1997b) have performed extensive studies of the strength and deformation mechanisms in this material. Figure 2.49 shows the yield and tensile strength of samples after various amounts of drawing strain showing that significant strengthening continues to occur at high strains. A detailed investigation of the evolution of the Cr phase as a function of drawing strain showed that the ribbons of Cr formed by drawing remained relatively free of substructure throughout the deformation processing (Adachi, 1997a). However, the measured texture of the Cr shows that it develops a typical (001)<110> bcc rolling texture (figure 2.50). This would suggest the Cr dendrites deform by multiple slip, much in the way they would if they were grains embedded within a polycrystal. The plastic deformation of the Cr ribbons may not always be possible. Lee et al. (2000) in studies of the deformation and fracture behaviour of Cu-30vol%Cr material at various temperatures after swaging found that when the swaged material was tested in tension at temperatures below room temperature, fracture of the Cr filaments led directly to failure of the specimens as a whole. At higher temperatures, damage could be seen in the Cr filaments but only close to the fracture surface (figure 2.51).

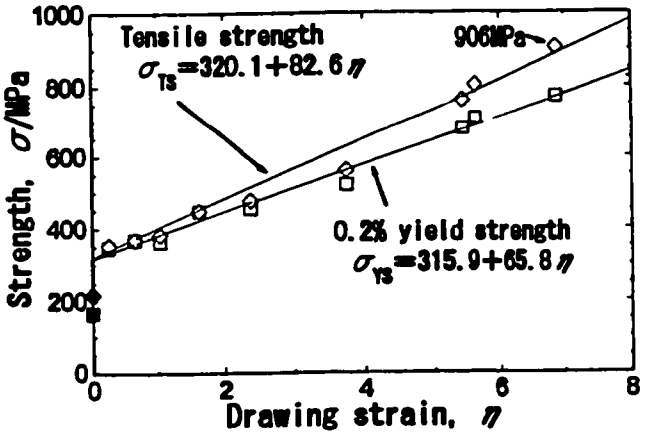

Figure 2.49 The strength of wire drawn hypereutectic Cu-Cr as a function of imposed drawing strain (Adachi, 1997b).

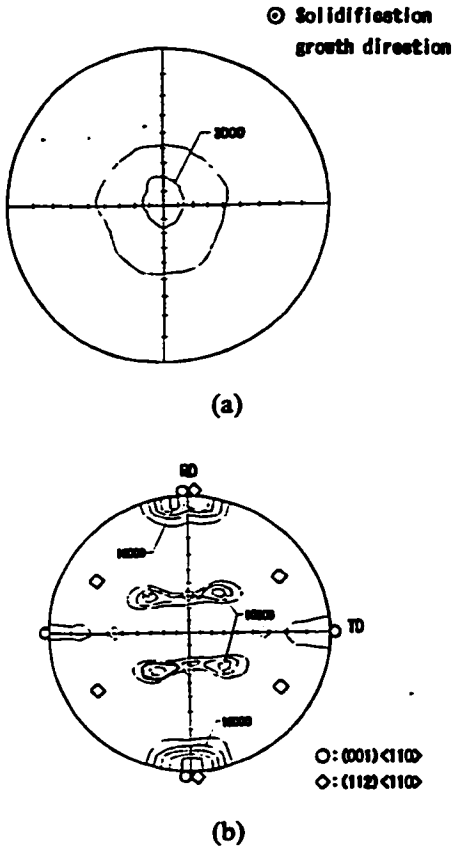

Figure 2.50 a) Starting texture of Cr dendrites. b) Texture developed in Cr dendrites after rolling to a strain of ~90% (Adachi et al., 1997a).

Funkenbusch et al. (1984) further noted that the ability to deform the dendritic Cr phase depends on the volume fraction of Cr present. At high volume fractions the material could not be drawn into wires as fracture of the Cr phase precluded large strain deformation. However, when the volume fraction was reduced below a critical level (the level is not given in the original paper) the Cr phase could be deformed extensively and fine wires could be produced. The explanation given for this behaviour was based on the idea that at high volume fractions a percolated network structure of Cr fibres would be produced. The microstructural constraint associated with the network, and the greater possibility of large flaws either internally (e.g. grain boundaries) or externally (e.g. surface cracks), would be sufficient to significantly reduce the ductility of the Cr phase. Alternatively, it can be imagined that the microstructure under goes a transition from having embedded Cr monocrystals in a soft ductile matrix to a nearly polycrystalline network of Cr grains with isolated pockets of Cu. It is important to note that the Cr filaments in this case are several micrometers in diameter, in contrast to the submicron fibres in the directionally solidified material tested by Hertzberg and Kraft.

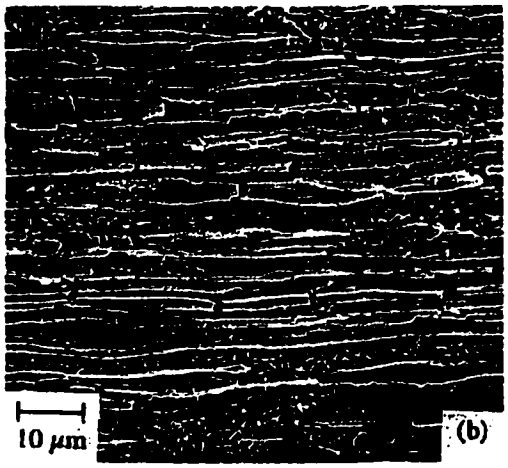

Figure 2.51 Damage of Cr phase after tensile testing of swaged Cu-Cr (Lee et al., 2000).

2.6 SUMMARY OF LITERATURE REVIEW

1. The macroscopic response of co-deforming two-phase materials may be complex as it relates the detailed mechanisms that occur on multiple length scales within the material. Generally, approaches that assume simple distributions of the applied stresses and strains fail to capture the response of the constituent phases. Further, assumptions regarding the mechanical response of the constituent phases tend to be in significant error, particularly when at least one of the phases is submicron in scale.

2. Measurements on the mesoscopic scale can give some insight into the in-situ properties of the phases. In particular, measurements made by diffraction techniques are ideal for the measurement of load partitioning during straining as the actual elastic strains borne by the phases can be followed. Measurements of the internal stresses arising from the presence of fine-scale co-deforming phases indicate very large stresses carried by the embedded phase suggesting of "whisker-like" mechanical properties.

3. At the microscopic level, it is clear that new mechanisms of plastic deformation may occur when at least one of the phases involved exists at the sub-micron level. Measurements made at this scale are often difficult and models based on continuum arguments tend to ignore the important consequences of the detailed atomic nature of the high density of phase interfaces. Atomistic simulations of the interactions between dislocations and interfaces appear to have the potential for helping to interpret the results of experimental measurements made at this scale and for helping to clarify the salient mechanisms that must be included in more continuum models.

3. EXPERIMENTAL METHOD

3.1 DIRECTIONAL SOLIDIFICATION

In order to utilize a system where the geometry of deformation was well controlled, it was decided to focus on the co-deformation behaviour of a directionally solidified Cu-Cr eutectic alloy. The Cu-Cr phase diagram (figure 3.1) may be characterized as a simple binary eutectic with limited mutual solid solubility of the eutectic phases. The eutectic composition is given by Chakrabarti and Laughlin (1984) as 1.56 at% with a eutectic temperature of 1077°C. At room temperature, there is less than 1 at% mutual solubility of the two species.

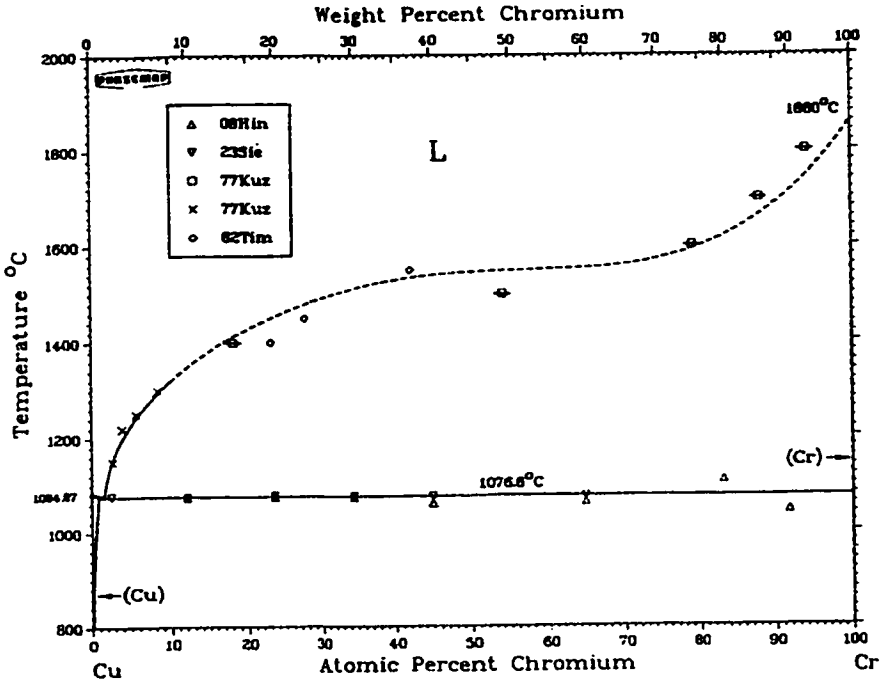

Figure 3.1 Equilibrium phase diagram for Cu and Cr (Chakrabarti and Laughlin, 1984).

Table 3.1 Impurity concentrations (in ppm) in OFHC Cu (Lahaie, 1998).

Bi	Cd	Pb	Hg	O_2	P	Se	S	Te	Zn
<1	<1	4	<1	3	2	<1	9	<1	<1

Directional solidification of a Cu-Cr alloy of eutectic composition was carried out by means of a modified Bridgeman technique. One half inch diameter OFHC Cu, whose composition is given in table 3.1, was initially precast by induction melting into a graphite mold in order to produce a Cu ingot approximately 5 inches in length and 0.5 inches in diameter at its top, with a 1° taper along its length. This step was carried out after evacuating the chamber to better than 10^{-5} torr and then backfilling with argon to -10" Hg. The resulting Cu ingot was subsequently pickled in a solution of 50% nitric acid to remove any surface contamination.

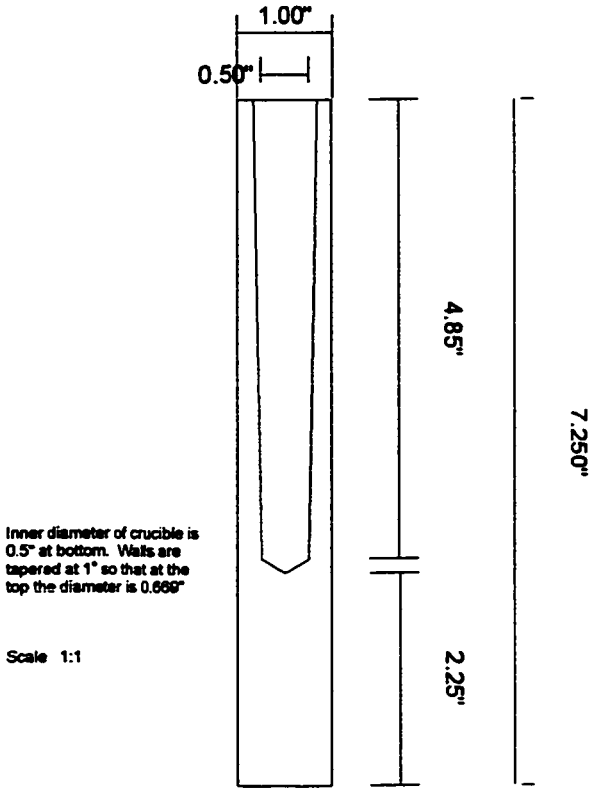

Figure 3.2 Schematic diagram showing the dimensions of the BN crucible and graphite susceptor used to produce the directionally solidified Cu-Cr alloy.

Casting of the eutectic alloy was carried out in a one-piece BN crucible (figure 3.2). The crucible was produced from a single one half inch solid cylinder by means of a tool with a 1° taper and a rounded tip. The purpose of the taper was to ease the removal of the final cast ingot. The rounded tip was meant to reduce the risk of cracking at the base of the hole. This BN crucible was inserted into a graphite crucible with a threaded base. The graphite crucible acted as the susceptor for the system, but also served to improve the life of the BN crucible. The disadvantage of attaching the crucible and susceptor was that the resulting temperature gradient was more gradual than that which would

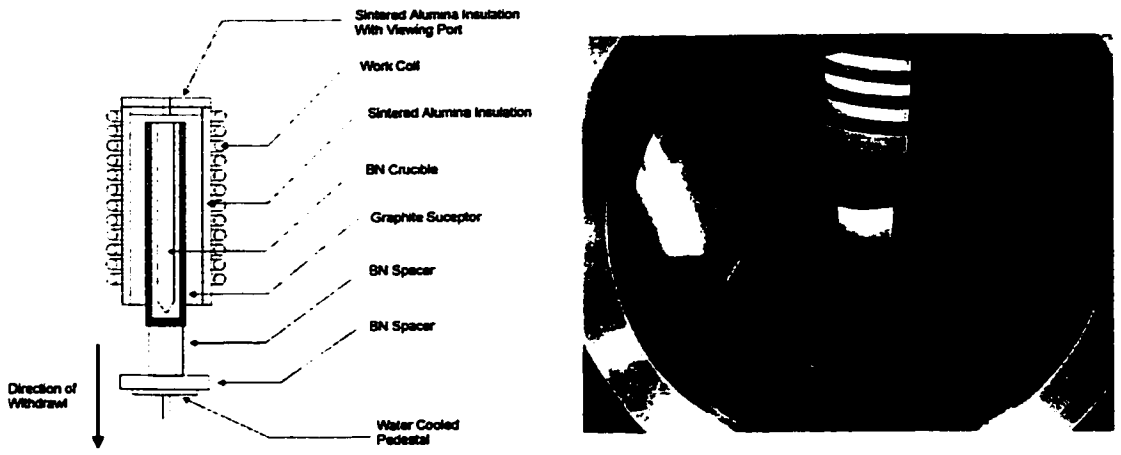

(a) (b)

Figure 3.3 a) Schematic diagram illustrating the setup used for directional solidification. Not shown is the vacuum chamber in which this apparatus was situated. b) photograph of system at temperature taken through front view port.

have been achieved in a setup with a susceptor that remained within the work coil as the crucible was lowered. This setup is illustrated in figure 3.3.

Cr, with a purity of 99.99%, was added to give the eutectic composition and placed at the bottom of the BN crucible. The pre-cast Cu was then added to the top and the assemblage loaded into the vacuum chamber. The chamber was evacuated to better than 10^{-5} torr and backfilled with argon to -10" Hg. It was found that this level of backfilling was sufficient to avoid loss of Cr to evaporation from the melt.

After backfilling, the power to the work coil was gradually increased over 1.5 hours until the sample was molten. The melt was homogenized for approximately 2 hours. Rates of 57 mm/hr and 6 mm/hr were used to solidify the alloy.

After the crucible had fully withdrawn from the work coil, the power was turned off and the system allowed to cool for one hour prior to the chamber being opened.

3.2 METALLOGRAPHY

Samples were sectioned using a high speed cutoff saw and ground using SiC papers to 2400 grit. Polishing was accomplished through two different routes. Mechanical polishing was carried out on cloths impregnated with 6 and 1 μm diamond paste prior to automatic polishing on soft nap cloth with 0.01 μm colloidal silica. In order to produce an adequate surface it was often necessary to iteratively etch the specimen and repeat the final colloidal silica polish numerous times. Following this route samples were suitable for optical examination. Alternatively, electropolishing using a 90% solution of O-Phosphoric acid in water at 2.2 V was used to polish specimens with awkward geometries. This solution was somewhat difficult to control and very sensitive to bath stirring and voltage. Too low a voltage tended to preferentially attack the Cu matrix while too high a voltage tended to preferentially attack the Cr fibres. Pitting was often a problem if the optimal polishing conditions were not reached.

Etching of specimens was carried out with one of two solutions:

i. *10% Ammonium Persulphate in Water*: This rather mild etch was sufficient for etching some grain boundaries and for etching the phase boundaries. This etch also tended to produce etch pits.

ii. *50% Solution of Nitric Acid in Water*: This was extremely aggressive and tended to preferentially etch the Cu while leaving the Cr phase untouched. If diluted and used for very short periods it was possible to etch phase and grain boundaries. Typically, however, this etchant was used for deep etching specimen (i.e. to isolate the Cr fibres) or to produce a continuous etching pattern in the Cu.

For observation of tensile specimens tested to failure, it was necessary to preserve, as much as possible, the fracture surface. To accomplish this, and to improve edge retention, samples had their fracture surfaces plated with Ni from an electroless Ni plating solution. The plating solution consisted of two solutions mixed and then heated to approximately 90°C. Samples were left for several (6-8) hours to allow a thick (100 μm) coating. The details of the solution and its usage are detailed in table 3.2.

Table 3.2 Conditions and Composition of Electroless Ni Plating Solution

Solution A	Solution B
11g $NaC_6H_5O_7$ $5.5H_2O$ (Sodium Citrate)	11g NaH_2PO_2 H_2O (Sodium Hypophosphite)
50g NH_4Cl (Ammonium Chloride)	500 ml Distilled Water
45g $NiCl_2$ $6H_2O$	
500 ml Distilled Water	

A final technique was found to be of use in the optical examination of longitudinal sections of the Cu-Cr alloys. If the alloys were polished and lightly etched (using the ammonium sulphate solution preferably) polarized light microscopy could be used to image the fibres as being bright against a dark Cu background. The fibres were brightest when oriented with their longest direction approximately 45° to the direction of polarization, and darkest when their long axis coincided with the direction of polarization. Although cubic metals do not lend themselves to polarized light microscopy because of their optical isotropy, surface features such as scratches can lead to contrast under polarized light. This attributable to double reflection of the polarized light from the surface of the metal. This technique has been previously used in the study of pearlite (Jones, 1924, Dunsmuir, 1952).

3.3 ELECTRON MICROSCOPY

3.3.1 Transmission Electron Microscopy

Samples were prepared for transmission electron microscopy by first cutting sections from the bulk material using a high speed Accutome saw with a Bakelite bonded alumina blade. The resulting slices were larger than 1 mm in thickness. Next, the cut material was ground on 600 grit SiC paper to 0.2 - 0.3 mm thick using water as a lubricant. These samples were further ground to a final thickness of 0.20 - 0.15 mm on 1200 grit SiC paper. Discs 3 mm in diameter were subsequently cut from this material. Samples were both spark

cut and punched using a mechanical punch. No significant damage from the punching process was observed for foils initially thicker than 0.15 mm.

From this point two routes were attempted for the preparation of TEM foils. First, ion milling was attempted after the disc had been dimple ground to a thickness of approximately 30 μm using 1 μm diamond paste. Unfortunately, ion milling caused significant damage particularly in the Cr phase, making the determination of defect contrast nearly impossible. Therefore, a method for electrolytic preparation of foils was sought. In this case, the as-ground samples were not dimple ground. It was found that adequate foils could be prepared using a similar technique to that described above based on a solution of 90% O-Phosphoric acid in water at room temperature. A Fishcione dual jet electropolishing unit was used to thin the foils. However, with the above solution it was critical to control the voltage within a few millivolts. If the voltage was allowed to rise too high the Cr would be preferentially attacked, whereas if the voltage was too low the Cu was preferentially attacked. Generally, these foils contained only a small thin region close to the perforation. Also, a single foil could take as long as 30 to 40 minutes before perforation, depending on its initial thickness.

A superior method for foil preparation was adapted from that given by Luo et al. (1994) used for the preparation of precipitation hardened Cu-Cr alloys. In this method, a solution containing a ratio of 1 part nitric acid to 7 parts HPLC methanol was cooled to -40 to -30°C using a dry ice and methanol bath. This solution was then jetted onto the foil using the Fishcione jet polishing unit. Below 30 mA the Cr tended not to be attacked, while above 45 mA the rate of attack of the Cr was much higher than that of the Cu. Using this method, a single foil could be prepared in less than 10 minutes.

TEM observation was carried out on a Phillips CM12 STEM operating in TEM mode at 120 KeV, using a double tilt specimen holder. Calibration for the rotation between image and diffraction pattern was obtained in the standard manner (Eddington, 1976) using a MoO_3 crystal. Determination of Burgers vectors in both Cu and Cr phases was carried out using the extinction of contrast observed at $\mathbf{g.b} = 0$ (Eddington, 1976). Crystallographic rotations were measured from Kikuchi patterns by means of the technique described by Young et al. (1973). This technique allows for the accurate determination of orientations to a resolution of

better than 1°. Chemical composition was measured on samples using EDX on JEOL 2010 FEG STEM operating at 200 KeV with a 1 nm probe size. Quantification of compositions from the collected spectrum was done using ZAPF corrections based on a Si standard and assuming a foil thickness of 100 nm.

3.3.2 Scanning Electron Microscopy

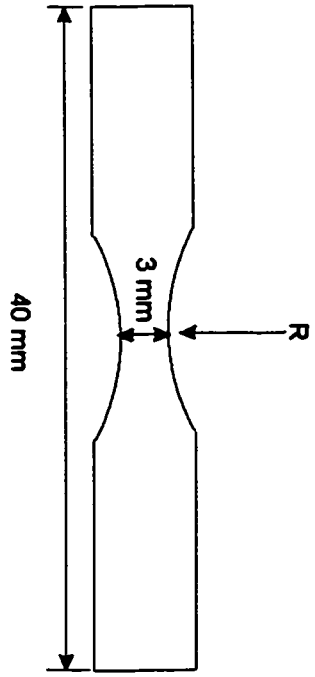

Figure 3.4 Schematic diagram showing tensile specimen used for in-situ straining in the SEM.

Most of the scanning electron microscopy for this work was carried out on an ElectroScan ESEM using a secondary electron detector. Because of the environmental nature of the chamber, it was not essential to remove the specimen from its Lucite, Bakelite or epoxy mount prior to imaging. Optimal contrast and intensity could be obtained from most samples by operating at 30 KeV with a slightly reduced condenser setting (55%).

The above microscope was also outfitted with a screw driven tensile stage that could be used to test small tensile specimen in-situ. The system was controlled by moving the crosshead of the tensile stage manually. It was not possible to collect load or extension data. Figure 3.4 shows the type of specimen used for in-situ tensile tests. An hourglass shaped sample was used so that focus could be made on the central portion of the specimen throughout straining. Samples were prepared by electropolishing followed by mild etching. Similar samples were also used for the observation of slip traces on deformed specimens.

3.4 Electron Backscatter Diffraction

Electron Backscatter Diffraction (EBSD) was conducted at the Center for Materials Science, Los Alamos National Laboratory under the supervision of Dr. O. Engler. The EBSD technique has been described elsewhere (e.g. Randle and Engler, 2000) and so details of the technique will be omitted here. Measurements were made using a Phillips XL30 FEG SEM equipped with TSL OIM software for automated pattern acquisition and indexing. Data collected from this system consisted of Euler angles, confidence index, image quality and measurement position. The former parameter defines the crystallographic orientation of the measurement point while the latter two parameters are associated with the software's ability to index the captured pattern, as well as the quality of the captured pattern. Post processing of this data was carried out using the TSL OIM system and software developed specifically for this project. Where appropriate, the method used to produce data will be mentioned when the resulting data is presented.

Fully automated measurements were made during 12 hour runs. In many circumstances, however, it was necessary to use the system in a semi-automated mode where the user manually positions the beam and accepts or declines the software's indexing of a given pattern. Samples were prepared by the mechanical polishing process described in the metallography section. To remove any surface contamination, a final etch was given to the specimen just prior to viewing in the microscope.

3.5 NEUTRON DIFFRACTION

Neutron diffraction studies were carried out at Chalk River Laboratories (CRL) under the guidance of Dr. K. T. Conlon of the NRC Neutron Program for Materials Research. The neutron source at CRL is the 150 MW NRU experimental reactor. The neutron flux from such a reactor source is thermally moderated and is well represented as a Maxwellian distribution (Bacon, 1975),

$$\varphi(v) \propto v^3 \exp\left(\frac{-mv^2}{2kT}\right) \qquad (3.1)$$

where $\phi(v)$is the flux of neutrons as a function of velocity. The maximum in flux from a thermally moderated neutron source is then associated with a particular velocity, or through the de Broglie relation to a wavelength,

$$\lambda_{max} = \frac{h}{m}\left(\frac{3kT}{m}\right)^{\frac{1}{2}} \quad (3.2)$$

For temperatures near 300 K, equation 3.2 gives an optimal wavelength between 1 and 2 angstroms. Figure 3.5 illustrates the neutron flux from the NRU reactor where the optimal wavelength lies close to 1.54 Å. Unlike conventional laboratory x-ray sources which exhibit very sharp peaks in intensity, it is possible to select a variety of wavelengths from the thermal neutron source by the judicious selection of appropriate monochromators. However, this also typically results in the instrumental resolution being less for neutron diffraction than for x-ray diffraction. Also, the use of wavelengths far from that given by equation (3.2) will be associated with a concomitant drop in flux on the specimen.

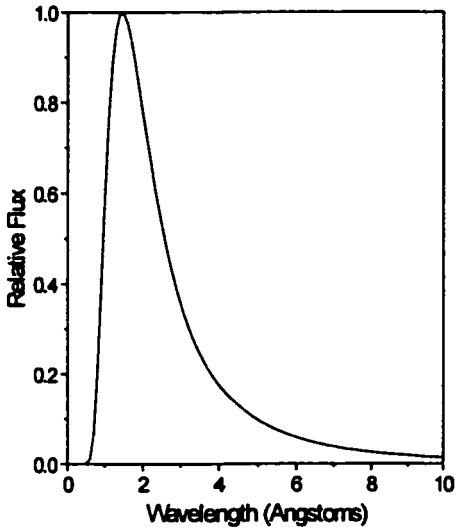

(a)

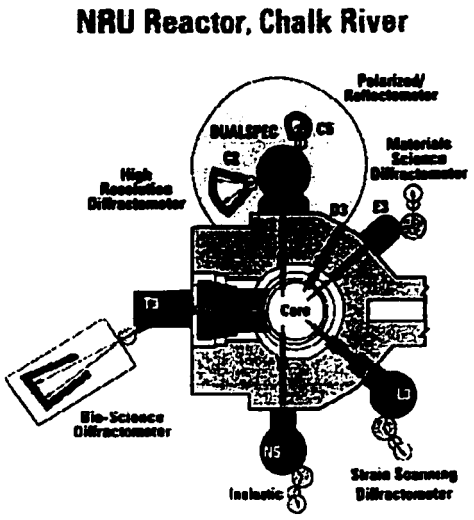

(b)

Figure 3.5 a) Flux distribution from the NRU reactor at Chalk River Laboratories. b) Schematic of NRU floor showing the position of the spectrometers in relation to the reactor.

For the experiments carried out at CRL, intensities were measured using a one-dimensional detector comprised of 32 wires corresponding to a maximum angular range of 2.0°. For measurements of texture the middle 16 wires were typically turned on while for higher resolution strain measurements, only the middle 8 were used. The angular divergence of the incident and diffracted beams was limited by use of Cd coated soller slits and the beam size by Cd beam stops. The spectrometer was controlled by means of a PDP-11 microcomputer connected to a VAX minicomputer. Using the controlling software it was possible to position the detector, experimental apparatus and scattering vector, as well as to define automated scans programmed to run over specified periods of time. Because the flux from the NRU reactor varies substantially over the course of a single experiment, it is not sufficient to simply count for a predetermined amount of time. Instead, the flux of neutrons was constantly monitored by a counter placed in the beam path and the counting period set to correspond to some fixed number of neutrons incident on the counter.

Two types of experiments were carried out at CRL. The details of each of these experiments will be given below.

3.5.1 Texture Measurements

Texture measurement by neutron diffraction has been discussed in detail by Brockmeir (1994). The particular advantages of neutron diffraction over x-ray diffraction for two-phase materials has been summarized by Bunge (1985). The most important advantage of neutrons for this work is the high depth of penetration of neutrons compared to that for x-rays. This allows for the sampling of entire sample volumes in many cases and also avoids problems associated with defocusing at high tilt angles in x-ray diffraction (Kocks et al., 1998), thus allowing for the measurement of complete pole figures.

Texture measurements made on the E4 spectrometer equipped with a 4-axis Eulerian cradle (figure 3.6) at CRL using either a Ge[115] or Ge[117] monochromator. The former results in a wavelength close to the peak flux (at 1.54 Å) while the latter results in a wavelength of approximately 1.10 Å.

The typical setup for texture measurements was to use 20.32 cm long soller slits separated by 2 mm on the scattered side giving an angular resolution of 1.1°. Pole figures were measured on a grid consisting of 1020 points over a full hemisphere (figure 3.7). One pole figure was collected at a 2θ angle far from any possible Bragg peaks in order to provide a background. The measured intensity versus η/χ angles was normalized using software developed at CRL (Root and Holden, 1990) and plotted as standard stereographic projections using a program written for the purposes of this project.

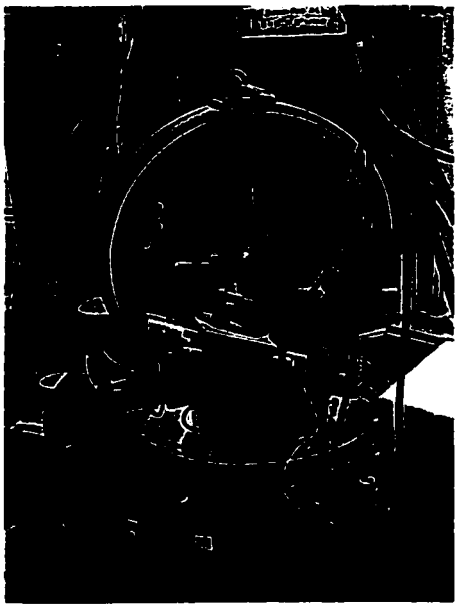

Figure 3.6 Photograph of the experimental setup of the E4 spectrometer equipped for texture measurements.

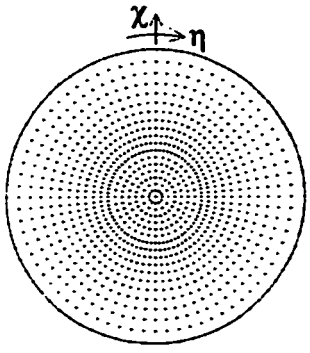

Figure 3.7 Grid of points used for pole figure measurement plotted on a stereographic projection.

3.5.2 Internal Stress Measurements

The use of neutron diffraction for the measurement of internal (elastic) strains has been reviewed extensively (e.g. Allen et al., 1985, Holden, 1999). The basic premise of the technique is that, upon loading, the lattice of the material will be elastically strained. This will affect the diffraction spectrum from a sample by changing the spacing of atomic planes. Using the definition of strain (in the limit of small strains) combined with Braggs Law results in the following equation relating lattice strain to a shift in Bragg angle,

$$\frac{\Delta d}{d_o} = \frac{\sin(\theta_o)}{\sin(\theta)} - 1 \qquad (3.3)$$

where θ_0 is a reference Bragg angle measured in an unstressed lattice and θ is the Bragg angle measured in the strained lattice. In order to measure the strain according to equation 3.3 it is necessary to collect a Bragg peak corresponding to a certain set of {hkl} planes oriented with their normal pointing along a known macroscopic direction. This plane normal is parallel to the scattering vector and thus can be easily deduced from the geometry of the experimental setup (figure 3.8).

In order to collect a Bragg peak, a θ-2θ scan is typically made across the presumed position of the peak in reciprocal space. The resulting counts versus 2θ angle is then subsequently fit to a Gaussian curve with a flat background using a Newton-Raphson iterative calculation. From this Gaussian fit both the full width-half maximum and the integrated intensity were also calculated. The error in the lattice strain as calculated from equation 3.3 was estimated from the error in θ_0 and θ ($\delta\theta_0$ and $\delta\theta$) using,

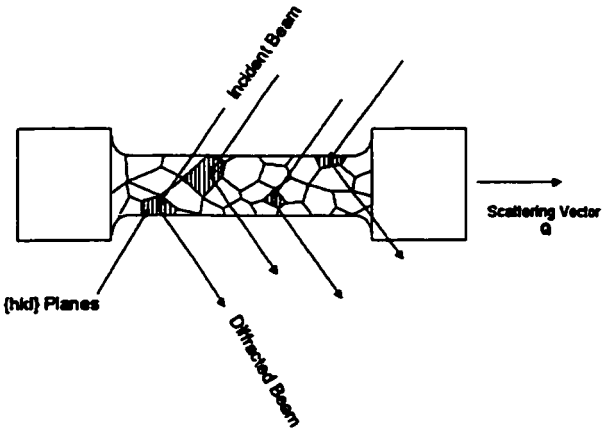

Figure 3.8 Schematic showing the geometry for in-situ straining experiments at CRL.

$$\delta\varepsilon/\varepsilon = \left[\left(\frac{\cos\theta_o}{\sin\theta_o}\delta\theta_o\right)^2 + \left(\frac{\cos\theta}{\sin\theta}\delta\theta\right)^2\right]^{\frac{1}{2}} \qquad (3.4)$$

Experiments aimed at deducing the evolution of lattice strain as a function of applied load or strain were conducted on the L3 spectrometer at CRL equipped with a screw driven mechanical test frame, load cell and MTS strain gauge extensometer. Tensile specimen could thus be loaded within the beam path while measurements of Bragg peaks were made. Figure 3.9 shows the geometry of tensile samples used for these experiments. Large specimen were used in order to provide the largest possible volume for sampling. Some

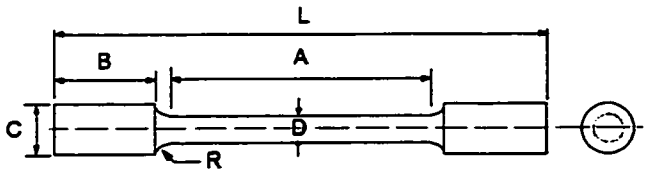

A - Length of reduced section - 1.750 +/- 0.005 in.
B - Length of end section - 0.750 +/- 0.005 in.
C - Diameter of end section - 0.500 +/- 0.005 in.
D - Diameter of gauge section - 0.350 +/- 0.005 in.
R - Radius of fillet, min - 0.250 in.
L - Overall length - 3.500 +/- 0.005 in.

* Diagram not to scale

Figure 3.9 Geometry of tensile specimens used at CRL for in-situ experiments

attempts were made to adjust the gauge diameter and length of the tensile specimen in order to check the effect of these parameters on the signal obtained from the samples. No dependence of the gauge volume on signal was observed.

The setup for in-situ tensile testing is shown in figure 3.10. Here the load frame is oriented such that the tensile axis is located in the horizontal plane. In this manner measurements of lattice strain along the macroscopic tensile axis of the specimen could be made. It was possible to measure lattice strains along other directions located in the horizontal plane by rotating the load frame on the experimental table (figure 3.10). However, such rotations were limited to a maximum of approximately 20°, the exact value depending on the Bragg angle to be measured and the specimen gripping arrangement.

The sequence of an in-situ loading experiment proceeded as follows:

i. Sample was loaded into the tensile rig and extensometer fit onto the gauge length of the tensile specimen using elastic bands. The body of the extensometer was covered with Cd sheet to avoid scattering from the metallic body.

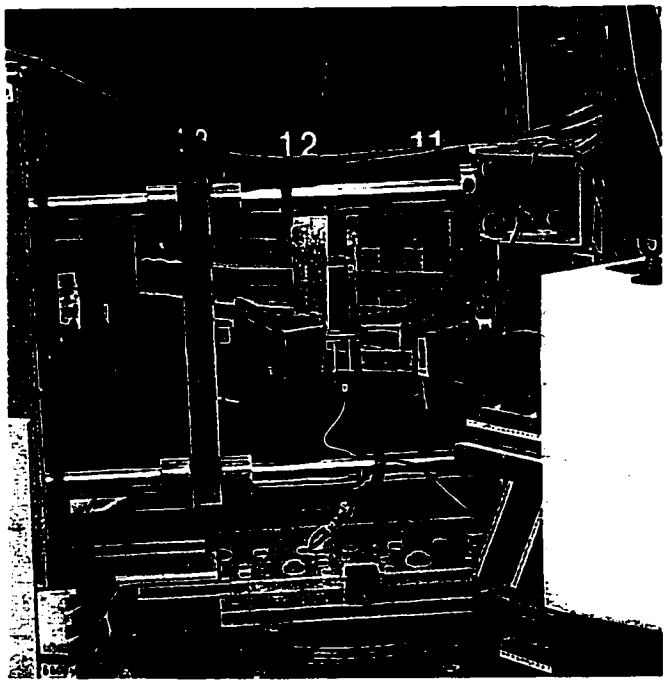

Figure 3.10 Experimental setup for measurement of lattice strains during in-situ straining. The tensile rig is oriented for measurements of lattice strain parallel to the tensile axis.

ii. Sample was loaded either in load or strain control to a predetermined load or strain.

iii. Peaks were measured from Cu and/or Cr phases while load/displacement of sample was held constant

iv. Load/extension of the specimen was incremented to the next predetermined level and held.

v. Steps iii and iv were repeated either until the test was stopped, the specimen failed or the intensity of the diffracted beam dropped below some predetermined level.

Throughout the above steps, the load or strain on the specimen was monitored by the control system. A count inhibit switch was activated if the load/extension dropped below a value set by the user. Similarly, a control limit detector readjusted the load/extension to maintain the applied load/extension within user defined limits.

In polycrystalline single-phase specimens with random crystallographic texture, the experimental setup for measuring lattice strains is relatively straight forward. The textures in the Cu-Cr specimens used in this study are far from random. Due to this, consideration of the crystallographic texture of both phases, and the relationship between the crystallographic texture and the morphology of the microstructure was considered for these experiments. It was necessary to make a number of decisions regarding the initial setup of the sample and beam before measuring a diffraction peak. Once these decisions were made it was then possible to attempt the strain measurement. Here, again, the Cu-Cr specimens produced some concerns that had to be addressed while measurements were being made under load.

3.5.2.1 Preliminary Experiments to Determine Optimum Conditions For Strain Measurement

The preliminary experiments were as follows:

i. Characterization of the Texture of Both Phases: This was done in two steps. First, pole figures for candidate Cu and Cr reflections were collected. Typically two Cu and two Cr pole figures were collected at a time (along with a background measurement), the measurements running for between 12 and 24 hours. Upon completion of these measurements the data was plotted as standard pole figures . Then, both these and the raw

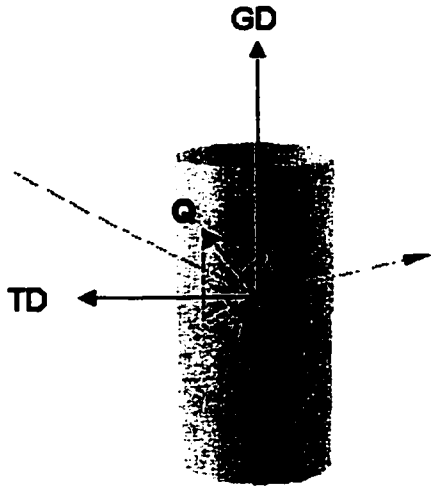

Figure 3.11 Schematic diagram defining the angles χ and η with respect to a tensile specimen. (GD = growth direction, TD = transverse direction)

data files were interrogated for intensity of both Cu and Cr. Figure 3.11 is a schematic diagram illustrating the angles η and χ. Because of the rather coarse step size in the texture measurement (5° over most of the hemisphere but up to 15° at the pole) reduced pole figures were typically conducted within 20° to 30° of the pole. For Cu, {220} and {331} reflections intensity could be found close to the tensile axis. However, the position and intensity of Cr {hkl} was much more difficult to estimate. Therefore, once the reduced pole figure had been collected, any intensity appearing to belong to Cr was checked by collecting and fitting the diffraction peak. This was necessary as anomalously strong backgrounds could be mistaken for intensity from Cr.

ii. Select an Appropriate {hkl} Peak to Follow During Straining for Each Phase and an Appropriate Wavelength for the Straining Measurement: In this study it was necessary to carefully choose the diffraction peaks to follow during straining. A number of factors had to be considered when making this determination. These include:

a) Peak overlap between Cu and Cr

b) Reactor flux for a given wavelength

c) Texture of the two phases and the relation of {hkl}'s to the microstructure

As discussed above, the flux from the reactor follows a Maxwellian distribution with a peak at around λ = 1.53 Å. On either side of this wavelength the flux drops very quickly. This combined with the low volume fraction of Cr phase restricts use of a wavelength close to this value. For these experiments both Ge[115] and Ge[117] monochromators were used, providing beams with wavelengths of 1.53Å and 1.10Å respectively. Although Ge[115] produces more flux on the sample, it also reduces the number of accessible {hkl}'s for the

two phases. Table 3.3 lists the diffracting planes accessible for the strain measurement experiments using these two different wavelengths. With an increased number of available diffracting planes also comes the problem of peak overlap as can be seen in table 3.3

iii. Attempt to Mark the Exact Position of Peak to be Measured and Transfer the Specimen from the Texture Spectrometer to the Straining Spectrometer: It was necessary at this point to mark the position of any Cr peaks that appeared accessible for the strain experiments. This was done by carefully marking the top of the specimen either with a scribe or a fine marker. The sample was then dismounted from the 4-axis cradle on the E4 spectrometer and remounted in the tensile rig on the L5 spectrometer. The mark placed on the end of the

Table 3.3 Comparison between Ge[115] and Ge[117] monochromators for Cu and Cr.

Cu			Cr		
$\lambda = 1.531$ Å (Ge[115])					
{hkl}	2θ	Intensity	{hkl}	2θ	Intensity[1]
{200}	50.113	0.2830	{200}	64.107	0.2795
{220}	73.588	0.3201	{211}	81.081	0.8313
{311}	89.226	0.5237	-	-	-
$\lambda = 1.101$ Å (Ge[117])					
{311}	60.671	0.3377	{211}	55.735	0.5562
{222}	63.676	0.1051	{220}	65.332	0.2210
{400}	75.053	0.0642	{310}	74.235	0.3775
{331}	83.178	0.2327	{222}	82.759	0.1131

[1] Intensity is calculated for a random powder

sample was used to judge the approximate position of the peak previously observed and so acted as a guide when loading the tensile specimen into the tensile rig.

Upon completing the above three steps, the experiment could be started on the spectrometer equipped with the tensile stage. However, before straining could begin, the exact position of the Cu and Cr peaks had to be located. This was accomplished using the following steps:

1. The sample was rotated within the grips to line it up approximately with the previously marked position.

2. The specimen was rotated through approximately ±20° by rotating the table on which the straining rig sat (angle denoted by ψ) while collecting intensity at a given value of 2θ corresponding to the peak of interest. This is shown schematically in figure 3.12. On rotating the angle ψ the direction of the scattering vector with respect to the tensile axis was changed. If ψ was set to equal θ the scattering vector was directed along the tensile axis. The deviation of ψ from this position marked the deviation of the measurement direction from the tensile axis.

3. If no intensity was found during rocking of ψ, the tensile specimen was rotated manually within the grips and step 2 repeated.

Upon finding Cr and/or Cu intensity the above procedure was halted and the spectrometer prepared for the in-situ straining experiment.

3.5.2.2 Experimental Setup for In-situ Straining

For the previously described experiments aimed simply at locating suitable peaks of Cu and Cr, precise setup of the spectrometer was not necessary. However, for high resolution measurement of peak positions the experimental setup became very important. The spectrometer was equipped with soller slits on both incident and diffracted sides that limited the angular

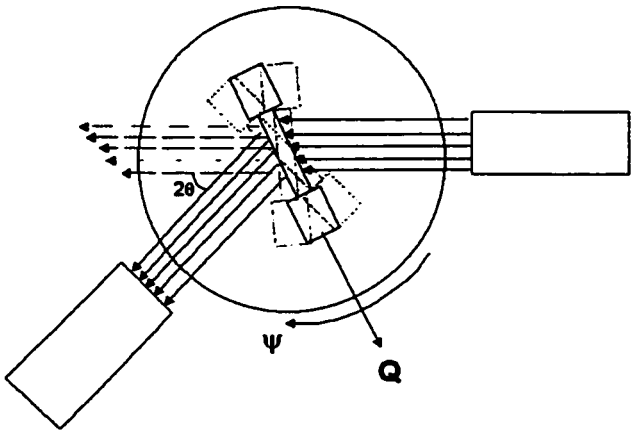

Figure 3.12 Schematic diagram showing the relationship between the tensile axis and the direction of lattice strain measurement when ψ was not set equal to half the Bragg angle.

divergence of the beam to approximately 0.6°. The detector had only the middle 8 wires turned on which meant the detector had a width of approximately 0.5° in the plane of measurement (horizontal) and a 2.5° out-of-plane (vertical) height. Measurements of peaks were then conducted by performing traditional θ-2θ scans. Because of the extremely sharp texture of both the Cu and Cr phases, it was necessary to ensure that the specimen was precisely aligned such that the most intense position of the texture peak corresponded with the maximum of the Bragg peak. This was necessary since the detector "sees" not only 0.5° width in reciprocal space, but also a corresponding volume of material in real space. If the spectrometer is not aligned such that the texture peak corresponds with the Bragg peak the convolution of the two peaks can lead to apparent peak shifts. Two solutions exist to correct for this problem. The first is to simply monitor the position of the texture peak during straining to ensure that the peak does not shift and if it does to re-adjust the alignment to correct for it. The second is to continuously rock the angle ψ by some small amount (typically $\pm$0.5°) to "smooth" the texture peak. The latter solution has two major drawbacks. First, in order to provide enough time for the texture peak to sweep across the full width of the detector long counting times are necessary. Second, by "smoothing" the texture peak the maximum intensity of the Bragg peak is dropped relative to the background. The first of these problems would severely limit the number of points that could be collected in a given period of time while the second creates serious problems for the Cr peaks as their intensities tend to be low under the most optimal of conditions. For these reasons it was decided to monitor the optimal position of the texture peak during straining.

As mentioned above, loading of the specimen could be controlled under either load or strain control (control of the extensometer output voltage). It was most reasonable to control the loading of the specimen under load control up to the point where the Cr fibres yielded. Under load control the specimen was loaded to a predetermined value, a measurement of the load was made and then the load reduced slightly for the measurement of the Bragg peaks to help reduce the possibility of specimen creep. Upon yielding of the Cr fibres it was found that extension of the specimen could no longer be controlled under constant load. Thus, beyond this point strain control was used to increment the deformation of the specimen. Although some unloading of the specimen was observed during peak measurement, under strain control it rarely exceeded 500

N. Periodically the specimen was unloaded to a nominal load of 200 N and peaks measured in order to provide a measure of the residual elastic strains in the two phases. This was accomplished much more easily in load control than strain control. Therefore far more unloading steps were made for the initial part of the stress-strain curve.

3.6 MECHANICAL TESTING

3.6.1 Uniaxial Tensile Testing

Tensile tests were performed on a 100 kN MTS servo-hydraulic load frame controlled by TestStar II on a PC allowing for control of the testing apparatus and data acquisition. Load was measured from a 100 kN MTS load cell while displacements were recorded both by a LVDT attached to the actuator piston and by strain gauge extensometers attached to the gauge length of the specimen. Calibration of the extensometer was checked prior to each test by comparing the extensometer output to that from a shunt resistor. The specimen used for these tests is shown in figure 3.13. This geometry represents a compromise between conservation of material and having a large enough diameter to grain size ratio for the behaviour to represent a polycrystalline average. Tests were conducted at a displacement rate of 0.005 mm/s as measured from the LVDT on the actuator piston. This approximately corresponds to a strain rate of $5 \times 10^{-4}\ s^{-1}$.

Tests were conducted at 293 K, 223 K and 77 K. The latter two test temperatures were achieved by submerging specimens into constant temperature baths of dry ice/methanol and liquid nitrogen respectively throughout the test. For tests at 77 K the specimen and gripping arrangement were fully submerged for approximately 10 minutes before the start of a test to ensure equilibration of the temperature. For tests at 223 K the temperature of the bath and specimen were monitored by a thermocouple attached to the specimen outside of the gauge length. In this case it was observed that the specimen did not vary in temperature by more than 5°C during a test.

Two strain gauge extensometers were used during the course of this study. The first (Instron model 2620-600), with a 12.5 mm gauge length at its zeroed position and ± 4 mm travel could not be used in the low temperature baths, but was favoured for room temperature tests because of its relatively long travel. The second (MTS model 632-13E) was designed for use in low temperature baths. This extensometer also had a 12.5 mm gauge length at its zeroed position with ±1.905 mm travel. The range of travel of this extensometer could be improved if it was initially placed in compression. Often, however, it was found that the ductility exceeded the maximum travel of this extensometer. In this situation the test was stopped and the extensometer was removed, reset and replaced on the specimen or simply removed from the specimen with further strain measured by the LVDT. For temperatures as low as 223 K, the bath apparatus could be moved up and down a post to allow for removal of the specimen from the bath and easy access to the extensometer. At 77 K, however, it was found that icing of the o-rings did not allow for movement of the bath. In this situation the liquid nitrogen had to be drained out of the bath from a hole in the bottom to allow for access to the extensometer. In all cases, the time that the specimen spent outside of the bath was minimized. Load relaxation was observed on stopping of the test but was never observed to exceed 50 N. In all cases the extensometer was removed from the specimen once necking (as evidenced by a continuous load drop) was observed.

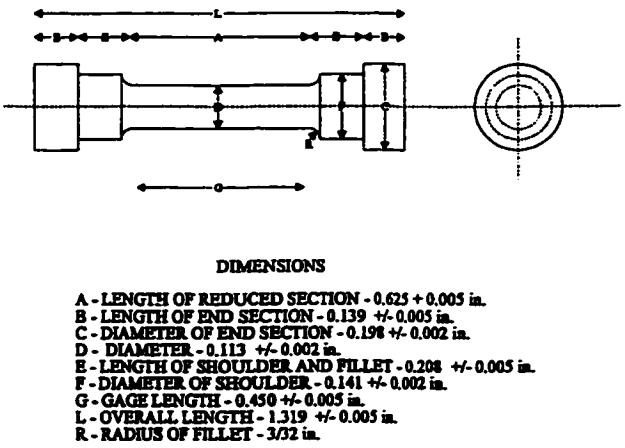

Figure 3.13 Geometry of tensile specimen used at McMaster.

Data obtained from tensile tests is plotted as true stress/true strain plots. In order to investigate the rate of work hardening it is necessary to differentiate this data. Because of the high sampling rate and noise from both load and strain transducers, numerical differentiation of the as-collected data is impossible. In order to obtain

a reasonable estimate of the rate of work hardening it was necessary to smooth the data. This was accomplished by first sampling a proportion of the as-collected data and fitting it to a cubic spline. This spline was then smoothed and differentiated using a Savitzky-Golay filter. The filter parameters were adjusted in order to obtain a curve representative of the collected data. It should be pointed out, however, that this smoothing routine may remove fine details of the collected data and so can at best be considered an approximation of the true behaviour.

3.6.2 Plane Strain Compression

Plane strain compression was carried out to achieve strains beyond those admissible by conventional uniaxial tensile tests. These tests were conducted at room temperature. Details regarding this apparatus may be found elsewhere (Deschamps, 1994). Samples were cut from the as-cast ingot with an aspect ratio of approximately 2.0. These samples were tested with the growth direction oriented along RD. Both specimen and channel walls were lubricated with solid Mo lubricant. Also, Teflon tape was inserted between the specimen and the channel walls. After strains of between 0.1 and 0.2 the test was stopped and the lubrication reapplied. As with the tensile tests, a displacement rate of 0.005 mm/s was used for all tests. The final strain imposed on the specimen was measured using a Von Mises equivalent strain,

$$\varepsilon_{vm} = \frac{2}{\sqrt{3}} \ln(1+r) \qquad 3.5$$

$$r = \frac{\Delta t}{t_0}$$

where r is the percentage reduction in height of the specimen.

4. EXPERIMENTAL RESULTS

4.1 INTRODUCTION

Following the methodology of previous chapters, this chapter will set out to describe the structure and properties of a directionally solidified Cu-Cr eutectic alloy at the macroscopic, mesoscopic and microscopic scales. In this chapter the results of these experiments will be described. Discussion of the implications of these results on the mechanisms and modes of deformation will be dealt with in Chapter 5. The results of experiments performed to characterize the as-cast material will be dealt with first, followed by the presentation of results on the behaviour during deformation. Experiments performed in order to study the stability of deformation and the deformed state will conclude this section. The salient features of all results will be summarized at the end of the chapter as a starting point for the discussion that will follow in Chapter 5.

4.2 THE AS-CAST STATE OF A DIRECTIONALLY SOLIDIFIED CU-1.56AT%CR EUTECTIC ALLOY

Experimental work performed to characterize the as-cast Cu-Cr alloy will be presented here. These results will be separated into those that characterize the material at the macroscopic, mesoscopic and microscopic levels. At the macroscopic level, the general morphology and scale of the constituent phases, as well as the existence of preferred crystallographic orientation (texture) of the Cu and Cr phases will be dealt with. At the mesoscopic level, measurements aimed at deducing the level of residual stresses due to thermal misfits will be examined. At the microscopic level, the detailed crystallographic relationship between phases will be addressed. Orientation relationships, habit planes, and crystallographic growth directions will all be

described. Also, observations of growth imperfections in the Cr phase will be described together with the chemical composition of the constituent phases.

4.2.1 MACROSCOPIC CHARACTERIZATION OF AS-CAST CU-1.56AT%CR EUTECTIC ALLOY

4.2.1.1 Morphology and Scale of Cu Grains

The Cu-Cr eutectic alloy was produced as ingots approximately 12 cm long and 1.75 cm in diameter. Figure 4.1a and b are low magnification images of the as-cast macrostructure of samples solidified at 57

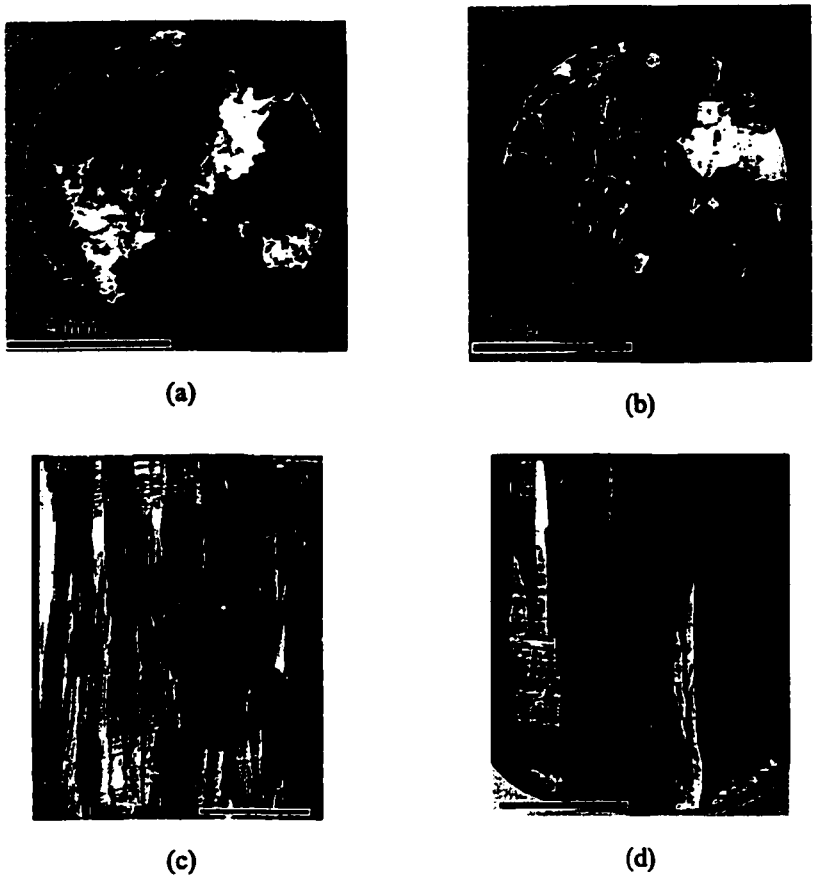

Figure 4.1 a) And b) Transverse photographs of etched Cu-Cr samples solidified at 57 mm/hr and 6 mm/hr respectively. c) and d) same as a) and b) but from longitudinal sections.

mm/hr and 6mm/hr, viewed in a section transverse to the macroscopic growth axis. The longitudinal structure is similarly shown in figure 4.1c and d. In both cases the coarse, columnar nature of the Cu grains is revealed. Observation of the grain structure of these samples was difficult as adjacent grains tend to etch in a similar manner. While it is difficult to make an exact measurement, it is clear from the images in figure 4.1 that the grains are several hundred μm in length and of the order of a hundred μm in diameter

4.2.1.2 Morphology, Scale and Alignment of Cr Phase

The Cr phase developed during directional solidification takes the form of long rods or laths. Figure 4.2 shows transverse optical micrographs obtained from samples solidified at 57 mm/hr and 6 mm/hr. The transverse size of the fibres was measured from TEM micrographs using digital image analysis (ImageTool, 1996). The measured distribution of fibre size is given in table 4.1.

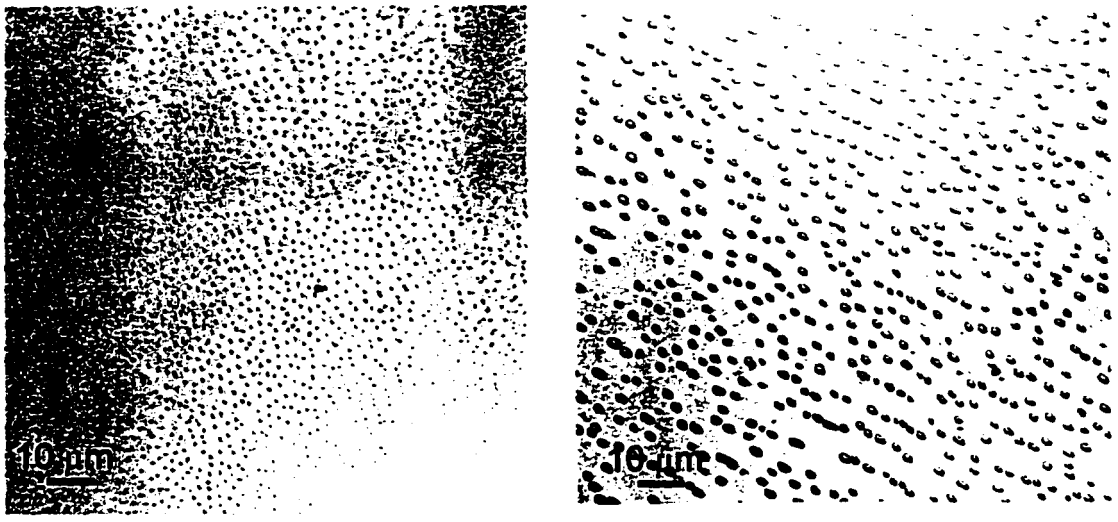

(a) (b)

Figure 4.2 Transverse photographs from etched samples solidified at a) 57 mm/hr and b) 6 mm/hr.

In viewing the microstructure in longitudinal sections (figure 4.3) the fibres, which are observed to be truncated by sectioning, are oriented differently in different grains but aligned roughly within 20° of the macroscopic growth axis of the ingot. The misalignment of Cr fibres was quantitatively characterized in a manner proposed by Yurgartis (1987). Longitudinal optical micrographs were analyzed in order to deduce i)

Table 4.1 Measured Scale of Cr Fibres in Transverse Section of Directionally Solidified Cu-Cr Eutectic

Growth Rate	Mean Minimum Dimension	Standard Deviation	Mean Maximum Dimension	Standard Deviation	Ratio of maximum to minimum dimensions	Standard Deviation
57 mm/hr	0.174 μm	0.050 μm	0.390 μm	0.089 μm	2.106	0.378 μm
6 mm/hr	0.403 μm	0.057 μm	1.001 μm	0.188 μm	2.608	0.660 μm

the truncated length of the Cr fibres and ii) the angle of the fibre axis from the macroscopic growth direction. Measurement of the distribution in the angle between the longest axis of truncated fibres and the macroscopic growth direction of the ingot gives a direct measure of the degree of in-plane misorientation. The truncated length of the fibre was used to compute the out-of-plane misorientation (ω) of the fibres via,

$$\sin \varpi = d/l \qquad (4.1)$$

where d is the average fibre diameter, l is the measured fibre length and w is the average angle between the fibre axis and the cutting plane. To calculate the fraction of fibres with a given misorientation, the stereological relationship

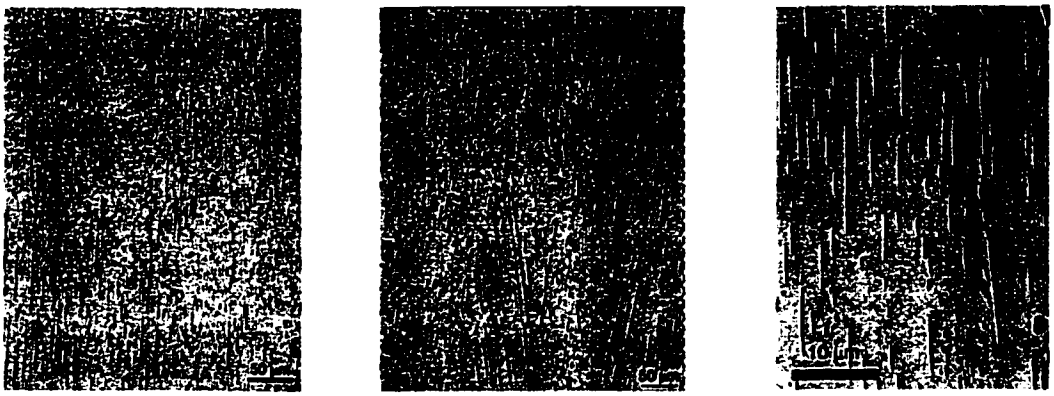

(a) (b) (c)

Figure 4.3 Optical micrographs from longitudinal sections of material solidified at 57 mm/hr a) and b) and 6 mm/hr c). a) and b) show regions of well-aligned and misaligned growth respectively.

$$f_v(\omega) = \frac{N_i}{\tan(\omega_i)} \Big/ \sum_i^n \left(\frac{N_i}{\tan(\omega_i)} \right) \quad (4.2)$$

can be used to account for the fact that the probability of cutting a fibre is zero when the fibre is parallel to the growth axis and 100% when oriented perpendicular to the growth axis. Figure 4.4 shows an example of the results of the independent measurements of in-plane and out-of-plane fibre orientation measurements for one sample solidified at 6 mm/hr. The results shown in figure 4.4 are typical of all samples measured, regardless of solidification rate.

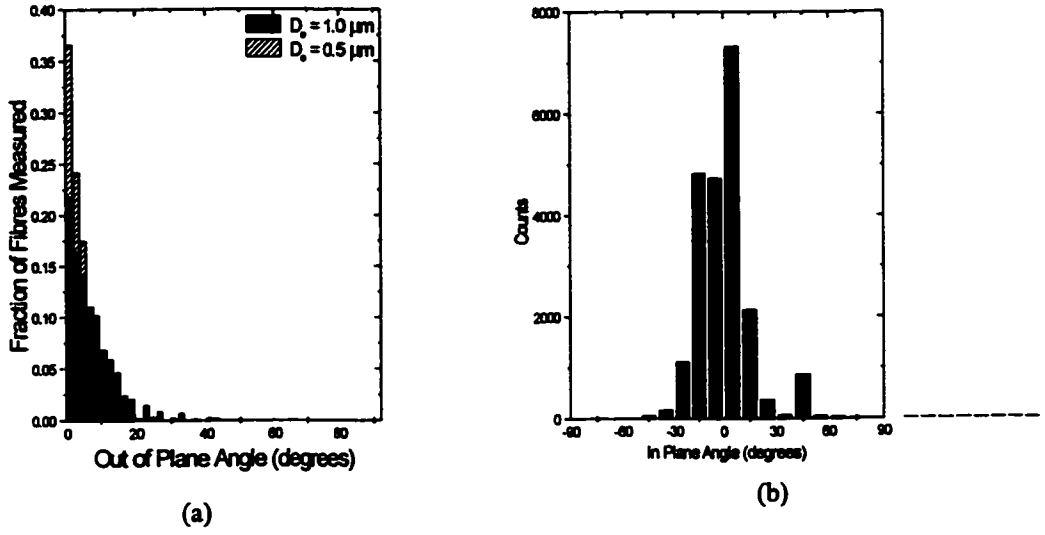

Figure 4.4 Example of a) out-of-plane and b) in plane fibre misorientation for samples solidified at 6 mm/hr. Similar misalignment was observed for samples solidified at 57 mm/hr.

The true morphology of the Cr fibres is seen if the Cu matrix is etched away (figure 4.5). The fibres are very long, in essence reflecting the Cu grain size. The cross-section is lath-like with one or more predominant flat facet bounded by curved end interfaces. The most striking feature of these fibres is their consistent morphology.

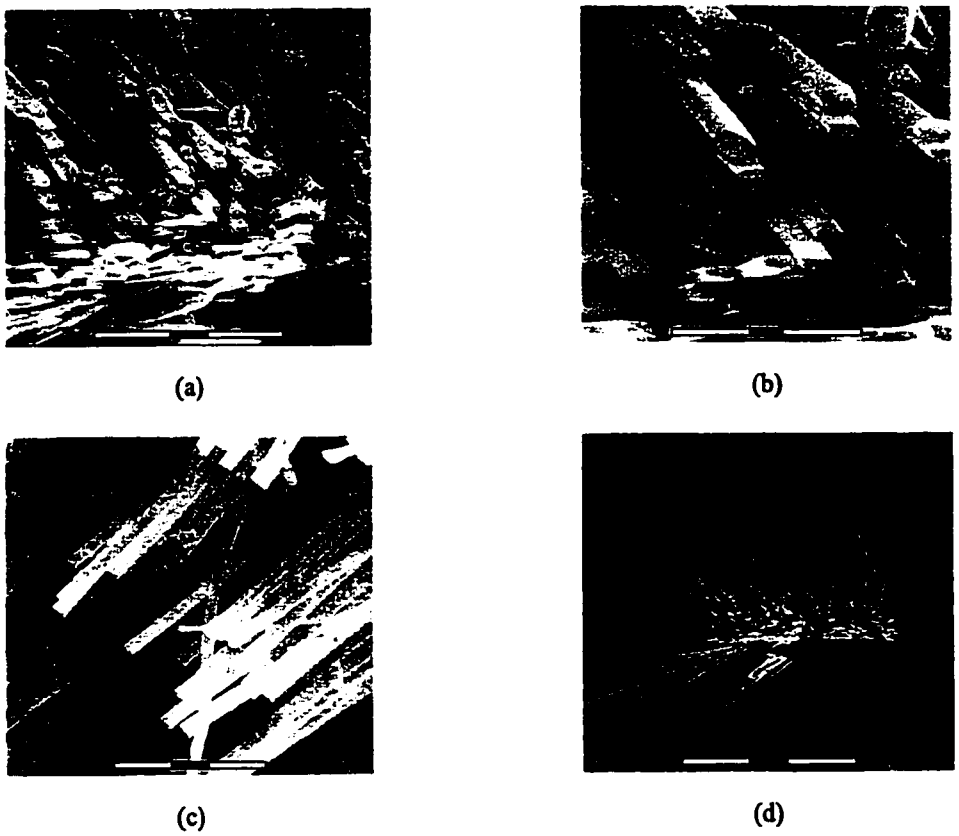

Figure 4.5 Deep-etched Cu-Cr specimen solidified at 57 mm/hr showing the scale and morphology of the Cr eutectic phase.

4.2.1.3 Macroscopic Defects Associated with Solidification

Although the process of directional solidification was observed to produce the well-controlled microstructure described above, growth imperfections were observed in both the Cu and Cr phases. Characterization of these defects is important as they impact on the macroscopic mechanical response of the material.

Although never observed in samples solidified at 57 mm/hr, all samples solidified at 6 mm/hr were observed to contain (to a varying extent) bands of eutectic-free Cu. Figure 4.6 illustrates this for a sample solidified at 6 mm/hr, viewed in the longitudinal section. These bands cross the entire thickness of the

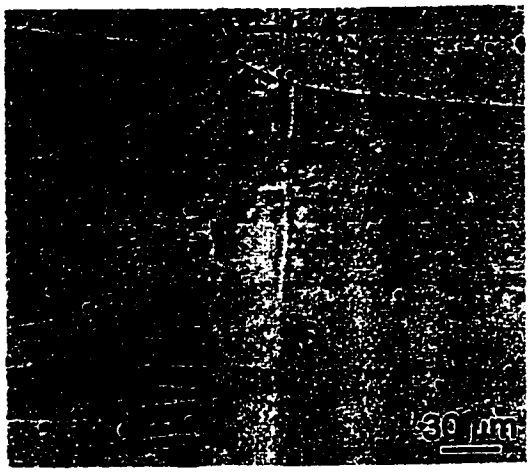

(a)

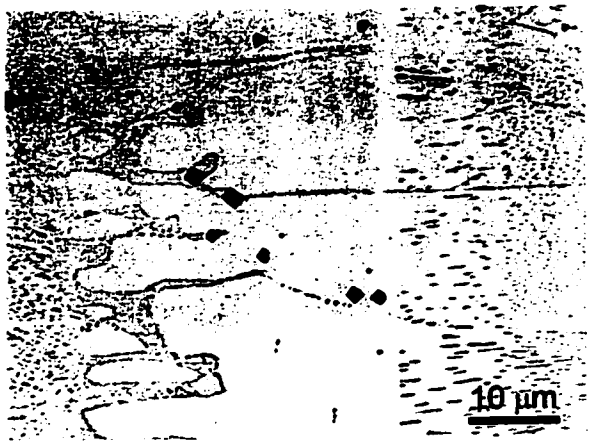

(b)

Figure 4.6 Longitudinal micrographs showing bands of eutectic fcc material in samples solidified at 6 mm/hr. a) Low magnification showing band crossing several grains. b) Higher magnification view showing flat interface on one side of the band and perturbed interface on other. Solidification direction is to the left.

specimen and have thicknesses (along the growth axis) as large as ~40 μm (figure 4.6a). The transition from eutectic to eutectic-free band was found to be planar while the transition from eutectic-free band to eutectic was found to be perturbed (figure 4.6b). Isolated Cr particles were often situated within grain boundaries crossing the bands or as dendrites within the bands. Macroscopically, no periodicity could be associated with the position of the bands along the length of an ingot. Samples with volume fractions of eutectic-free bands exceeding 5% were discarded.

Samples solidified at 6 mm/hr show more evidence (compared to samples solidified at 57 mm/hr) of coarse proeutectic Cr phases. The morphology of these Cr particles varied but could generally be described as plate-like (figure 4.7a) or dendritic (figure 4.7b). The characteristic scale of these phases was > 10 μm. This is to be compared with the eutectic Cr phase which has a cross-sectional dimension at least an order of magnitude smaller.

Other forms of defects observed in directionally solidified specimens included Cu dendrites and eutectic growth instabilities at cell boundaries. The former was primarily due to the evaporation of Cr from the top of

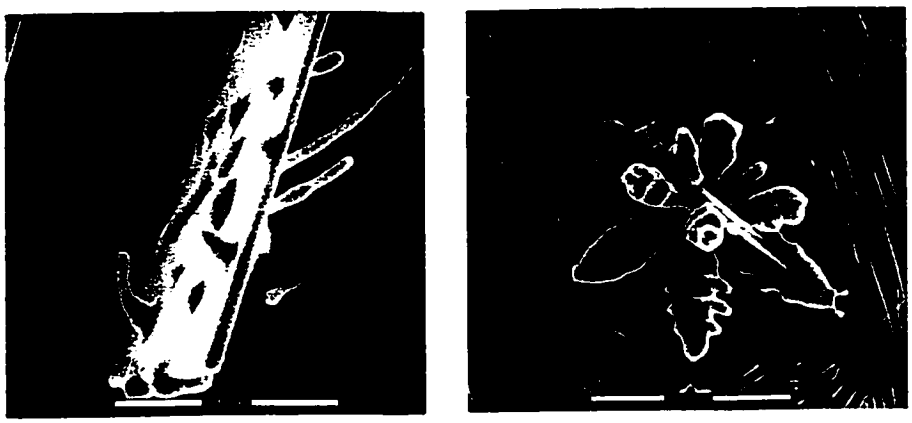

(a) (b)

Figure 4.7 a) Plate-like proeutectic Cr phase and b) dendritic Cr exposed by etching away the Cu matrix with 50% HNO_3.

the melt and could be controlled by backfilling with argon. The latter proved impossible to control but was considered a minor problem in most cases, due to the large cell size.

4.2.1.4 Crystallographic Texture

Both Cu and Cr phases exhibit a very high degree of crystallographic texture resulting from solidification. Figure 4.8 shows representative {220} and {200} pole figures for the Cu phase as deduced from neutron diffraction. The high degree of texture with a strong {220} texture along the macroscopic growth axis is evident. The {220} pole figure appears not to show proper crystallographic symmetry. This effect can be traced to the use of a relatively coarse counting mesh (5° intervals) in conjunction with a highly textured material. Pole figures for Cr were more difficult to measure due to the combination of a very high degree of texture and low volume fraction of Cr phase. Figure 4.9 shows representative Cr {200} and {211} pole figures collected from samples solidified both at 57 mm/hr and 6 mm/hr. Again, an apparent lack of crystallographic symmetry in some pole figures can be attributed to the relatively coarse grid size compared to the strength of the texture.

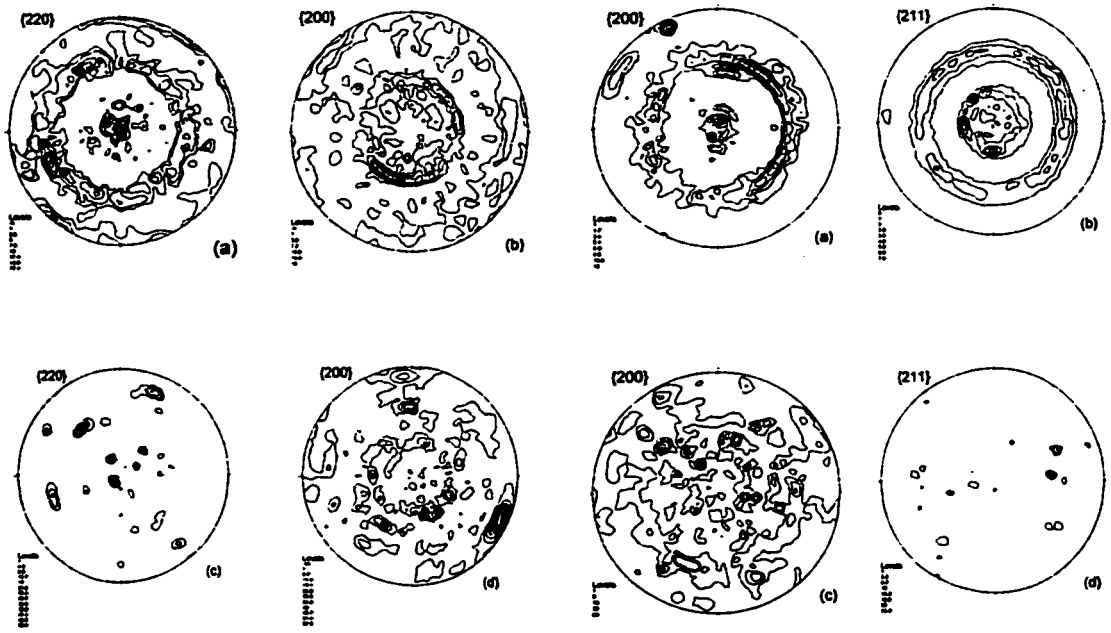

Figure 4.8 Representative Cu pole figures as deduced from as-cast specimen a){220}, 57 mm/hr b){200}, 57 mm/hr c) {220}, 6 mm/hr d){200} 6mm/hr. In all cases the macroscopic growth axis is located at the centre of the pole figure.

Figure 4.9 Representative Cr pole figures a) {200}, 57 mm/hr b) {211}, 57 mm/hr c){200}, 6 mm/hr d) {211}, 6 mm/hr. As in figure 4.11, the macroscopic growth axis of the ingot coincides with the centre of the pole figure.

Electron backscatter diffraction (EBSD) was also used to study the as-cast crystallographic texture in both Cu and Cr phases. Although this technique is limited to sampling a much smaller volume than neutron diffraction, it allows individual phases to be directly targeted for measurement and therefore overcomes problems associated with low volume fraction of phases. Figure 4.10 shows both Cu and Cr pole figures as measured for a sample solidified at 57 mm/hr. This data was collected by manually moving the beam across the sample while randomly selecting points for measurement. For each point measured in Cr, a measurement was made in the adjacent Cu. Figure 4.11 shows the results of an automatic scan run over a 24-hour period. In this measurement a coarse (25 μm) step size was used and only Cu data was collected. The Cu texture is qualitatively similar to that measured by neutron diffraction. Figure 4.11 also shows reconstructed orientation maps made from this data. This plot shows the crystallographic orientation of the measured region i) parallel to the growth direction, ii) perpendicular to the growth direction (parallel to the direction of measurement),

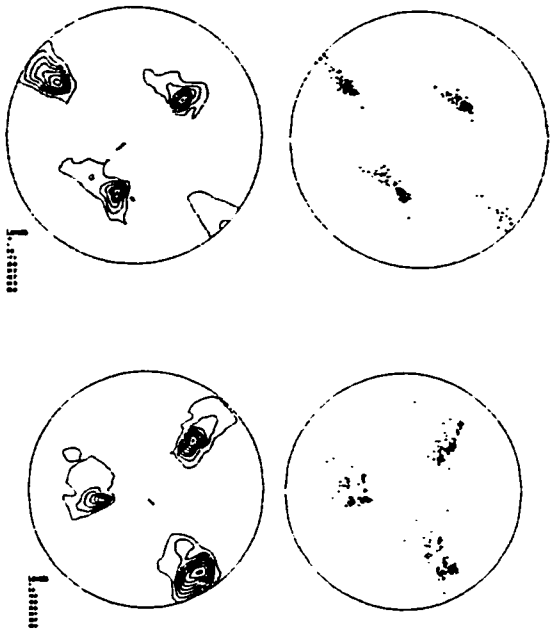

Figure 4.10 a) Cu {200}pole figure and b) Cr {200}pole figure measured manually by EBSD. Growth axis located at the centre of the pole figure.

and iii) perpendicular to the previous two directions. This view of the microstructure is also instrumental in pointing out the very large Cu grain size and low degree of misorientation between adjacent Cu grains.

4.2.2 Mesoscopic Characterization of As-cast Cu-1.56at% Cr Eutectic Alloy

The behaviour of the individual phases during deformation depends on the residual stress state produced in-situ during the solidification of the sample. These thermal residual stresses develop due to differences in the thermal contraction of the two phases during cooling. To investigate the presence of thermal residual stresses, neutron diffraction was used to determine elastic strains in the Cr phase of a sample solidified at 6 mm/hr. In order to calculate an accurate value of the elastic strains in the Cr it was necessary to determine a zero-stress reference lattice parameter.

A reference zero-stress lattice parameter for the Cr phase was determined by Guinier x-ray diffraction on Cr particles extracted from directionally solidified Cu-Cr samples. For the purpose of fitting the experimentally determined spectrum, it was necessary to provide a texture-free specimen. In order to ensure this, a sample of Cu-Cr was rolled to approximately 50% reduction and subsequently annealed under vacuum for approximately 72 hours. This process resulted in the spheroidization of the Cr fibres (figure 4.12a). These spheroidal Cr particles were then extracted from the copper matrix using a solution of 50% HNO_3. The powder

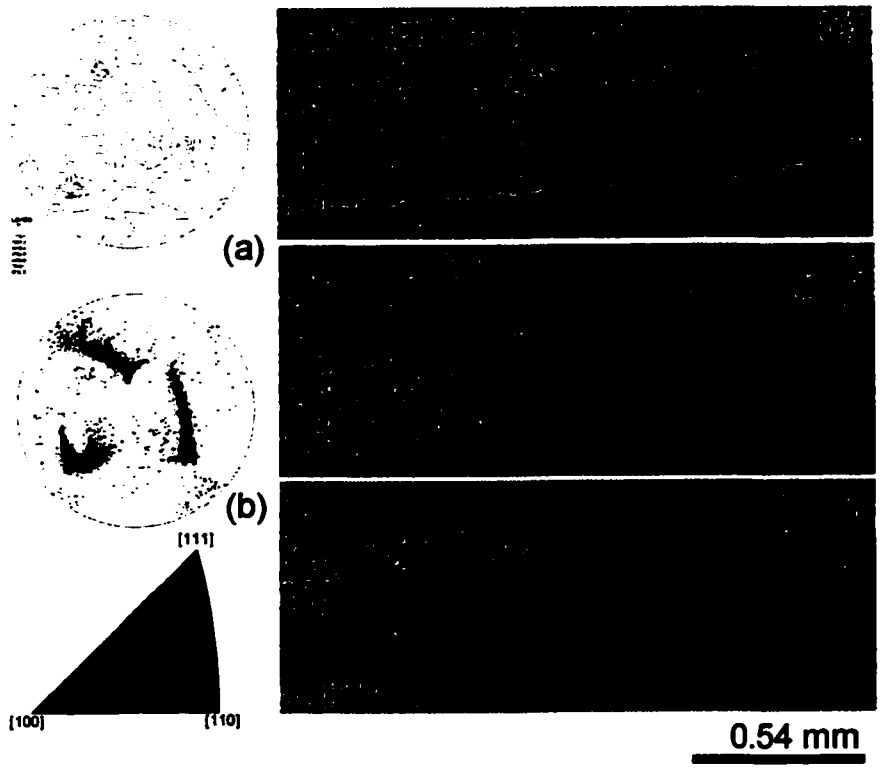

Figure 4.11 a) Contoured and b) discrete Cu {200} pole figure measured using automated EBSD. Cu Orientation images in b) show the crystallographic directions parallel to the i) growth axis, ii) and iii) directions perpendicular to the growth axis.

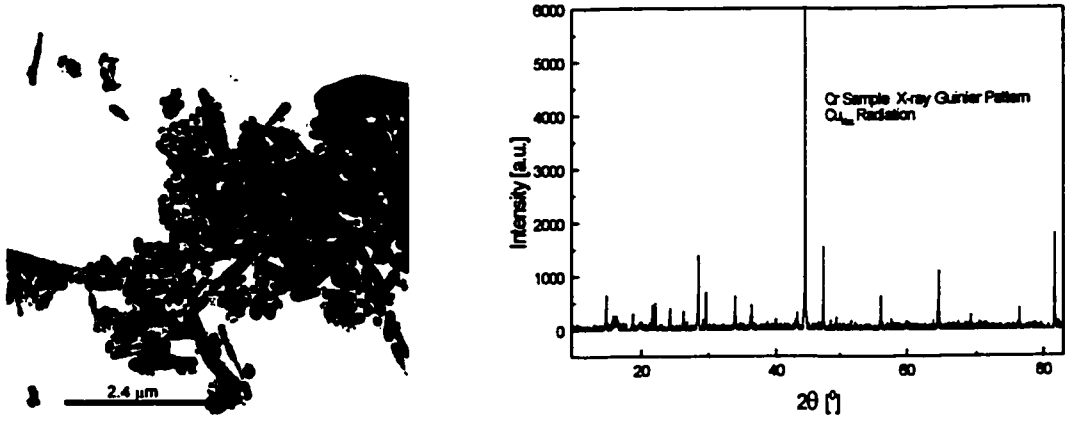

Figure 4.12 a) BF TEM image of spheroidized Cr particle extracted from Cu matrix. b) Powder diffraction spectra resulting from Guinier x-ray diffraction on extracted spheroidized Cr.

diffraction pattern resulting from these Cr particles is shown in figure 4.12b. The lattice parameter obtained by fitting this pattern was 2.8848 ± 0.0001 Å.

The setup used on the E3 spectrometer at CRL for determining thermal residual strains is the same as that shown in figure 3.11. Figure 4.13 shows the {200} Cr and {211} Cr pole figures for the sample on which measurements were made. From the Cr {200} pole figure it was possible to find two strong orientations of the

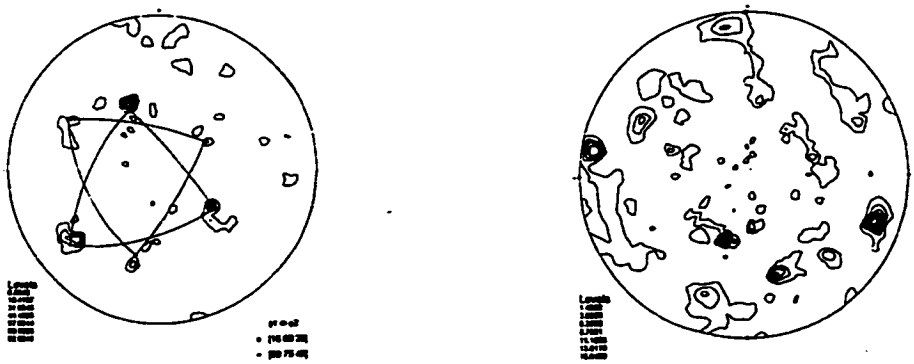

(a) (b)

Figure 4.13 a) Cr {200} and b) Cr {211} pole figures measured on sample from which thermal residual strains were deduced. Two ideal grain orientations are shown in the {200} pole figures.

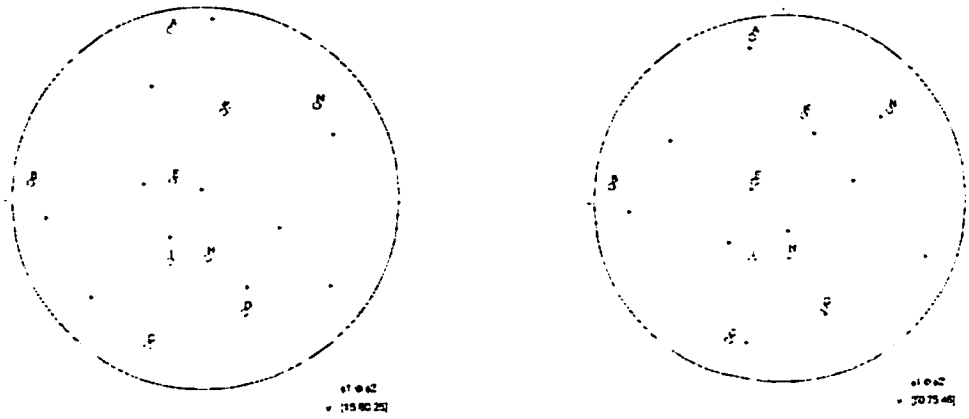

(a) (b)

Figure 4.14 Ideal Position of Cr{211} for a) ideal orientation 1 and b) ideal orientation 2. The filled circles represent the ideal orientations while the open circles (labeled with letters) are positions where peaks were measured experimentally.

fibres (with some scatter about the mean position) as shown in figure 4.13. The specimen was tilted to allow for the measurement of the Bragg peaks associated with these six texture maxima. A more difficult task was finding Cr {211} peaks suitable for measurement. In an attempt to find peaks consistent with the fibre orientations deduced from the {200} pole figure, the position of the Cr {211} texture peaks were predicted

Table 4.2 Peak Positions and Lattice Strains Associated with Thermal Residual Stresses

{hkl}	η (°)	χ (°)	2θ (°)	error	ε (10^{-4})	error (10^{-4})
{200}	21.2	50.5	64.6955	0.0037	-7.59	1.02
{200}	-122.4	47	64.6851	0.0045	-6.16	1.24
{200}	65.5	63.6	64.6792	0.003	-5.33	0.83
{200}	-49.5	38.8	64.7304	0.0065	-12.39	1.79
{200}	170.2	64.5	64.6945	0.0065	-7.45	1.79
{211}	10	83.7	81.731	0.0027	8.61	0.54
{211}	56.5	20	82.061	0.0070	-24.56	1.40
{211}	-14	50.5	81.8458	0.0384	-2.95	1.43
{211}	-50.3	74.5	81.7814	0.0071	3.53	2.42
{211}	-160	64.75	81.803	0.0049	1.34	0.99

from the two ideal Cr orientations shown in figure 4.13a. Figure 4.14 shows the ideal position of Cr {211} poles associated with a) fibre orientation 1 and b) fibre orientation 2.

Table 4.2 lists the best fit peak position (in 2θ) for the Cr peaks measured and the calculated lattice strains. Using the stress-free lattice parameter measured via x-ray diffraction as a reference it was possible to compute the lattice strain (using equation. 3.3) from each peak. This data is tabulated in table 4.2.

4.2.3 Microscopic Characterization of As-cast Cu-1.56at%Cr Eutectic Alloy

4.2.3.1 Microstructure and Defect Content of Cr Fibres

In order to fully characterize the structure (internal and external) of the Cr fibres it was useful to extract fibres from the surrounding Cu matrix. Figure 4.15 shows a number of fibres prepared in this way and viewed

Figure 4.15 BF TEM image of extracted Cr fibres. Note that the fibres contain no internal defects.

in the TEM. It is apparent that the fibres are uniform in size and morphology and exhibit a large aspect ratio. At higher magnifications the fibres appear to be largely free of internal and surface defects. In a small fraction of the fibres, however, growth defects could be observed. One common defect was branching of the fibres (figure 4.16). The presence of branches was not accompanied by internal defects in the fibres, as can be seen in figure 4.16.

A second common form of growth defect in the Cr were constrictions along the length of fibres. Figure 4.17a shows a low magnification TEM image of a Cr fibre exhibiting a large number of these constrictions. Viewed in the TEM, these constrictions are often associated with internal defects typically in the form of low-angle subgrain boundaries (figure 4.17b). These boundaries exhibit very small misorientations (< 5°) between the material on either side.

Figure 4.16 TEM image showing branched Cr fibre.

Finally, some small proportion of the Cr phase was also observed as nearly equiaxed

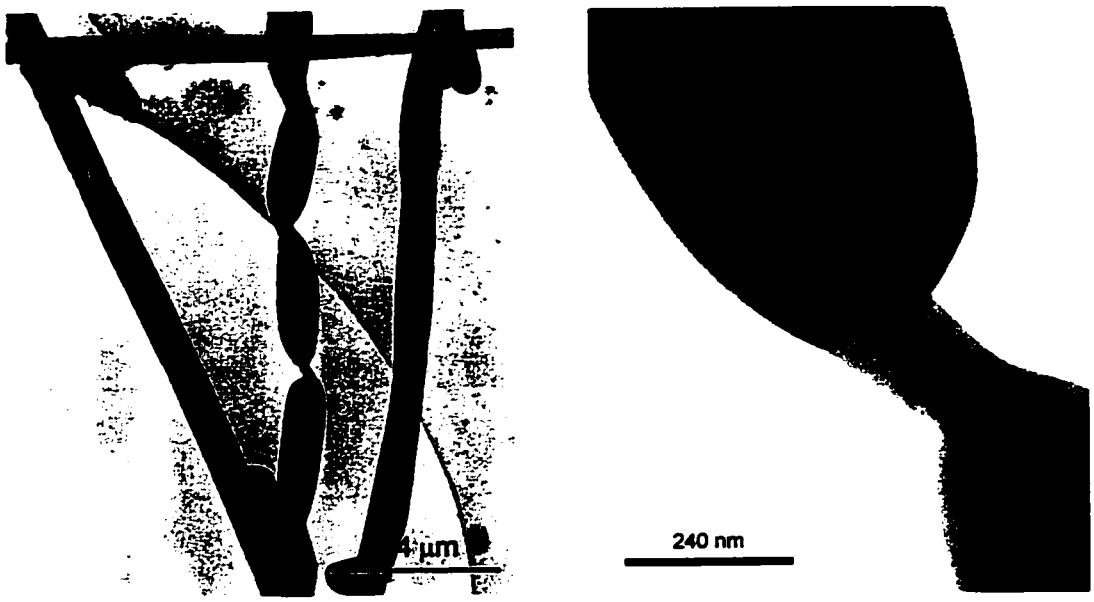

(a) (b)

Figure 4.17 Constrictions in a Cr fibre as viewed a) at low magnification in the TEM. b) High magnification view of one of the constrictions showing the presence of a low angle boundary.

particles. The dimensions of these particles appeared similar to that of the cross-sectional diameter of the fibres. The equiaxed Cr particles were typically observed to be preferentially situated near cell boundaries where the growth and orientation of fibres was generally observed to break down. Some of these particles can be seen in figures 4.15 and 4.16.

Although observed in all samples produced, these three types of defects were found to be associated with only a small minority (<< 1%) of the total population of Cr.

4.2.3.2 Substructure in As-cast Cu-Cr

If instead of viewing the Cr fibres after extraction from the Cu, the microstructure was viewed as thin foils in the TEM, a more complete picture of the relationship between the two phases could be determined. Figure 4.18 shows typical images from transverse foils of as-cast Cu-Cr solidified at a) 57 mm/hr and b) 6 mm/hr with the foil tilted such that the beam direction is within a few degrees of the growth direction of the fibres. Figure 4.19 shows a longitudinal micrograph taken from a sample solidified at 57 mm/hr, where the

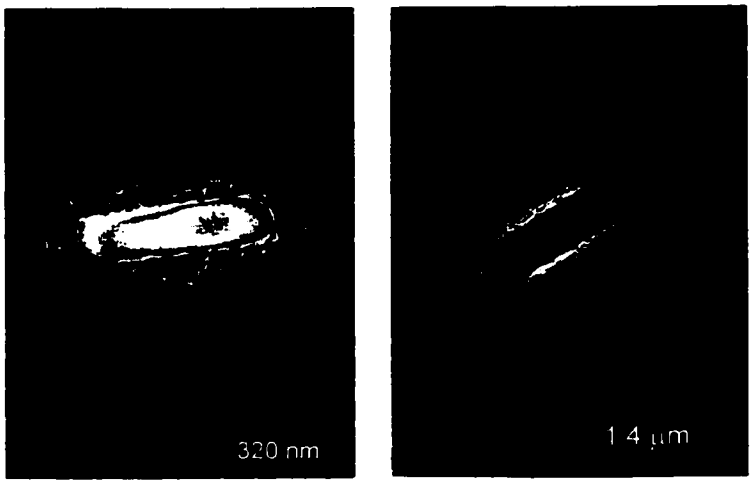

(a) (b)

Figure 4.18 Transverse BF TEM micrographs from samples solidified at a) 57mm/hr, and b) 6 mm/hr.

fibre growth axis is now nearly entirely contained in the plane of the foil. Figure 4.19 b and c show two-beam images illustrating the interfacial structure along the fibres. No dislocations were ever observed in the Cr fibres in as-cast foils, supporting the claim made in the previous section that the fibres are largely perfect single crystals. In both longitudinal and transverse foils a relatively high density of dislocations was observed in the matrix surrounding the fibres. These dislocations form loose tangles around

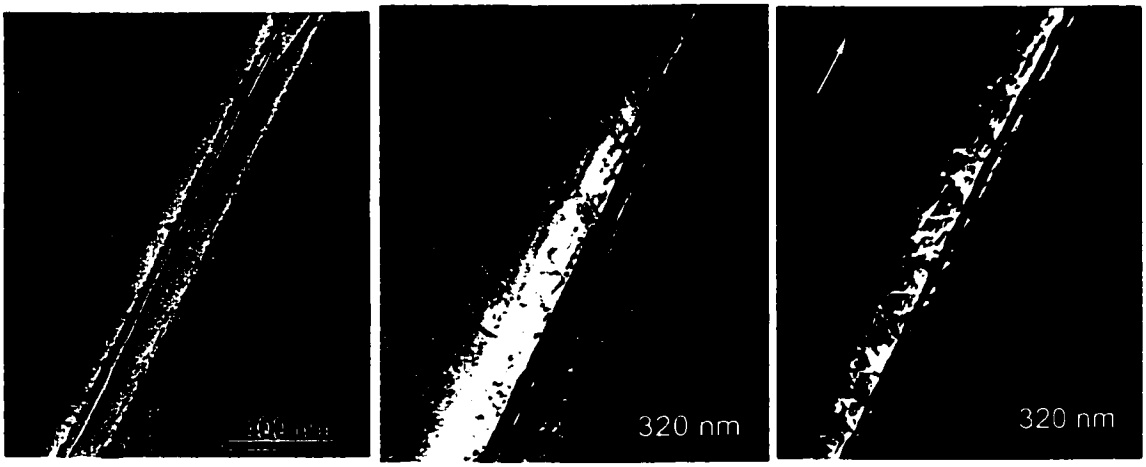

(a) (b) (b)

Figure 4.19 Longitudinal two-beam TEM micrographs from a samples solidified at 57mm/hr. a) BF image showing presence of Cu lattice dislocations at interface. b) DF image showing defects in the interface (**g** = [020]). c) as in b) but for **g** = [200].

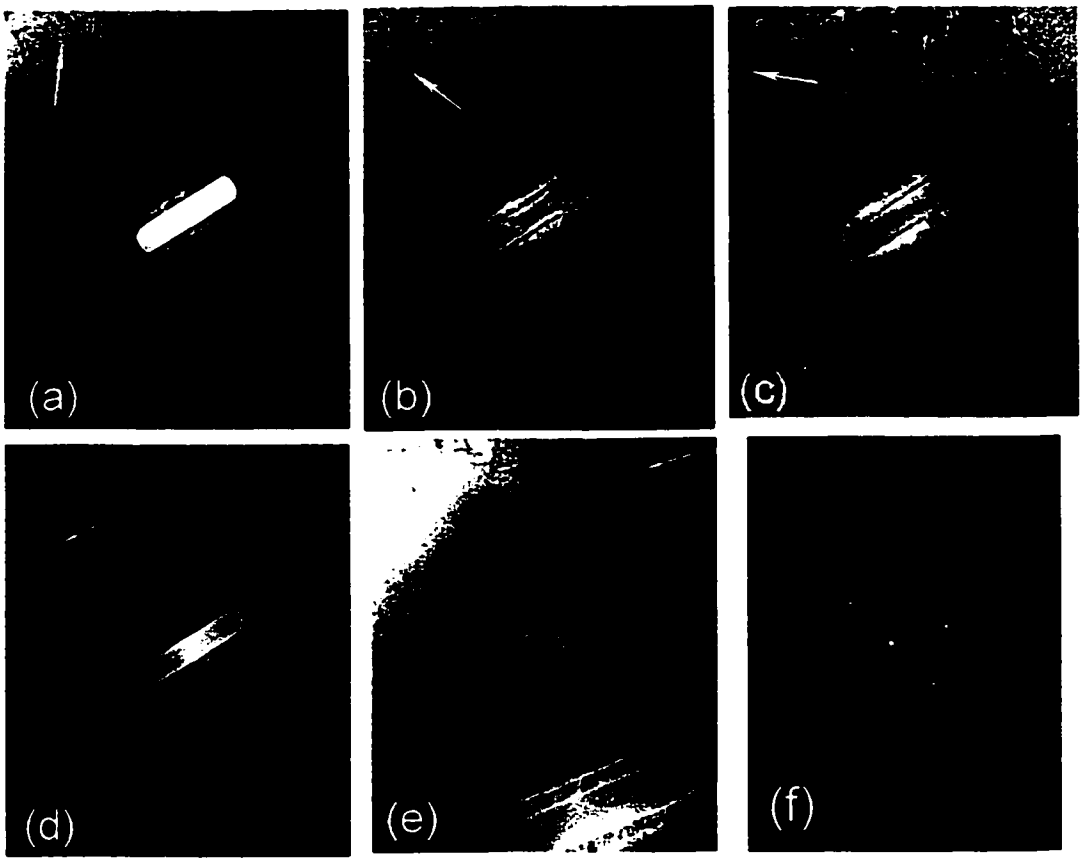

Figure 4.20 Two-beam BF TEM images in a sample solidified at 6mm/hr. Beam direction is close to $[110]_{Cu}$ in a) to d) while it is close to $[211]_{Cu}$ in e). a) $\mathbf{g} = [002]$ b) $\mathbf{g} = [1\bar{1}1]$ c) $\mathbf{g} = [2\bar{2}0]$ d) $\mathbf{g} = [1\bar{1}\bar{1}]$ e) as d) but tilted approximately 30°. f) SADP at $[110]_{Cu}$. Note the structure of the interface revealed in the inset portion of e).

Table 4.3 Various g.b Conditions for Cu

b / g	$\bar{1}11$	$1\bar{1}1$	$\bar{2}20$	002	$\bar{1}13$	$1\bar{1}3$
a/2[110]	0	0	0	0	0	0
a/2[$\bar{1}$10]	+1	-1	+2	0	+1	-1
a/2[101]	0	+1	-1	+1	+1	+2
a/2[10$\bar{1}$]	+1	0	+1	+1	+2	+1
a/2[011]	+1	0	+1	+1	+2	+1
a/2[01$\bar{1}$]	0	+1	-1	+1	+2	+2

the fibres and appear similar for both solidification rates. Burgers vector analysis was carried out for dislocations surrounding fibres in a sample solidified at 6 mm/hr. Figure 4.20 shows a series of bright field images taken using a variety of two-beam conditions in Cu. Table 4.3 lists the values of **g.b** for each of the conditions used. From this analysis it is found that all six possible Burgers vectors exist in the structure around the fibre.

Figure 4.21 BF TEM image from longitudinal sample (solidified at 57 mm/hr) showing dislocation loops bowing out of the phase interface (marked by arrows).

Longitudinal sections exhibit similar features to those observed in transverse foils. However, in longitudinal foils it was possible to observe what appeared to be dislocation loops emitted from the phase interface into the Cu (figure 4.21). Observations on longitudinal foils were made more difficult due to the fact that the foil surface cut fibres at an angle resulting in only short lengths of fibre for analysis. Those foils that did contain fibres with their growth axis nearly lying in the plane of the foil contained few fibres within the thin regions.

4.2.3.3 Crystallography of Cu and Cr Phases

From the regular appearance of the Cr fibres and the strong macroscopic texture of both Cu and Cr phases, it might be expected that a preferred crystallographic relationship exists between the two phases. It was found that the vast majority of fibres could be described as sharing the Kurdjumov-Sachs (K-S)

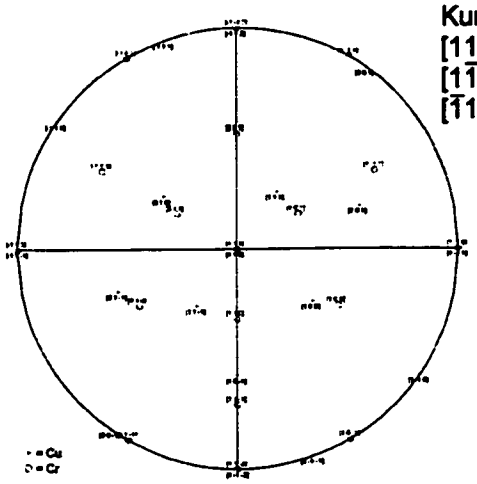

Figure 4.22 Overlapping stereographic projections indicating the Kurdjumov-Sachs (K-S) orientation relationship between a body-centred cubic phase (open circles) and face-centred cubic phase (filled circles).

Kurdjumov-Sachs orientation relationship with the neighbouring Cu matrix. This orientation relationship is defined by parallelism between the close packed planes and close packed directions for the two phases, e.g.

$$[111]_{Cr} \| [011]_{Cu} \quad (a)$$
$$[1\bar{1}0]_{Cr} \| [1\bar{1}1]_{Cu} \quad (b) \qquad 4.1$$

This orientation relationship is illustrated in figure 4.22 as overlapping stereographic projections for the two phases. The parallelism indicated by 4.1a could be found readily in transverse TEM foils by tilting to the closest $[110]_{Cu}$ zone axis. Selected area diffraction patterns (SADP) taken from the interface between the Cu and Cr phases at this position show the parallelism

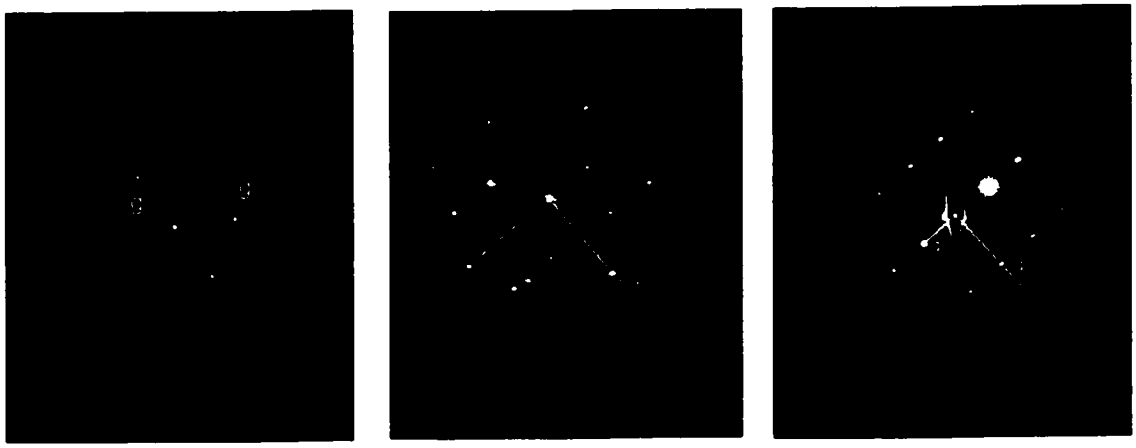

(a) (b) (c)

Figure 4.23 a) Selected area diffraction pattern (SADP) taken from interface between Cu and Cr in a transverse foil. Beam direction approximately parallel to $[110]_{Cu}$ and $[111]_{Cr}$. b) SADP from phase interface in longitudinal foil. Beam direction approximately parallel to $[1\bar{1}1]_{Cu}$ and $[1\bar{1}0]_{Cr}$. c) As in b), but tilted such that beam direction is parallel to $[\bar{1}12]_{Cu}$ and $[11\bar{2}]_{Cr}$. In each case g_1 and g_{2r} refer to parallel crystallographic directions other than those parallel to the beam direction.

described above (figure 4.23a). In longitudinal foils it was often possible to find the corresponding parallel $<110>_{Cr}||<111>_{Cu}$ or $<112>_{Cr}||<112>_{Cr}$ zone axes. Examples of SADP showing this parallelism from longitudinal foils are shown in figure 4.23b and c.

The consistent morphology of the Cr phase and orientation relationship between Cu and Cr suggests the possibility that the axis of the fibres may be indexed crystallographically. From transverse foils it was found that the fibre axis lay close to the common close packed directions ($[110]_{Cu}||[111]_{Cr}$). However, fibres viewed with the sample tilted to this position exhibited their end interfaces inclined. Tilting the foil slightly about the normal to the common close packed planes, $(1\bar{1}1)_{Cu}||(1\bar{1}0)_{Cr}$, was found to bring all facets to a nearly "end on" condition. Figure 4.24 shows an example of a tilting experiment where the foil was tilted to either side of

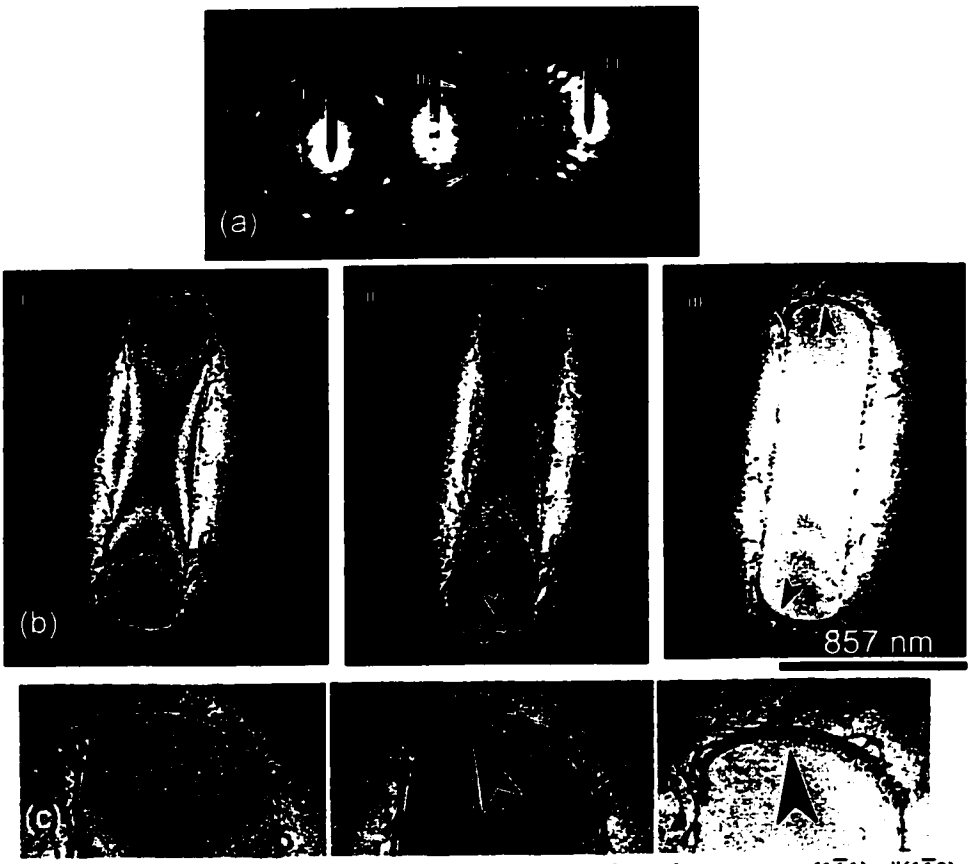

Figure 4.24 Series of BF images taken at different tilt positions along the common $(1\bar{1}1)_{Cu}||(1\bar{1}0)_{Cr}$ Kikuchi band. The tilt condition on the left, oriented approximately 9° from the common $[110]_{Cu}||[111]_{Cr}$ direction is seen to bring the fibre most nearly on axis. At the other two tilts interface can be seen at the curved end interfaces (marked by arrows in b and c).

$[110]_{Cu}\|[111]_{Cr}$ along the common $(111)_{Cu}\|(110)_{Cr}$ planes. The interfaces all appear nearly edge-on after a tilt of approximately 9° from $[110]_{Cu}\|[111]_{Cr}$ towards $[1\bar{1}2]_{Cu}$.

Attempts to make a more accurate determination of the fibre growth axis by the methods outlined by Luo et al. (1994) on longitudinal foils failed. In this method it is necessary to accurately determine the projected axis of the fibre at different tilts about the common close packed directions. Accurate measurements of the projected fibre axis necessitates the use of completely embedded fibres. As opposed to the solid state precipitates studied by Luo, the fibres in this case are thicker than the foil and so precluded proper analysis.

The above evidence supports the assertion that the fibres and matrix share an orientation relationship approximately described as K-S. The lath-like cross-sectional shape of the fibres also indicates the possible presence of preferred facets on the Cr fibres. Fibres exhibited as many as three facets although most showed only one or two (figure 4.25). Again, following the method proposed by Luo et al. (1994), transverse foils were used to examine the crystallography of the facets. Foils were tilted to bring the beam direction parallel to

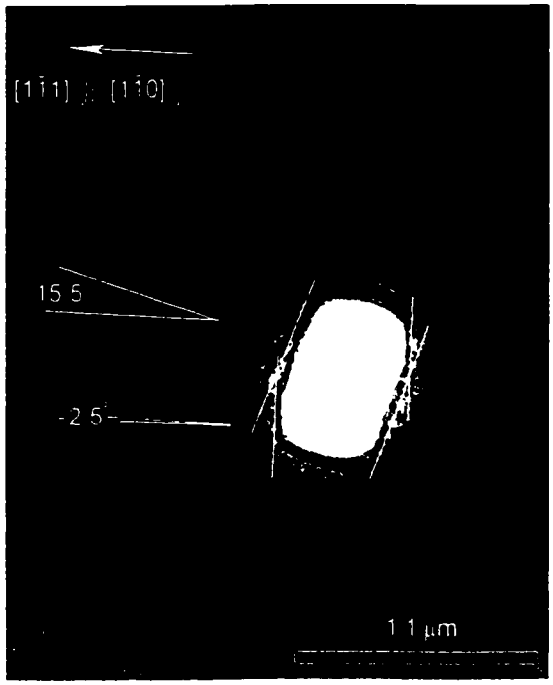

Figure 4.25 Cr fibre that exhibits two facets bounded by curved end interfaces. Also shown are the angles that the common close packed plane normals make with the normals to the facets.

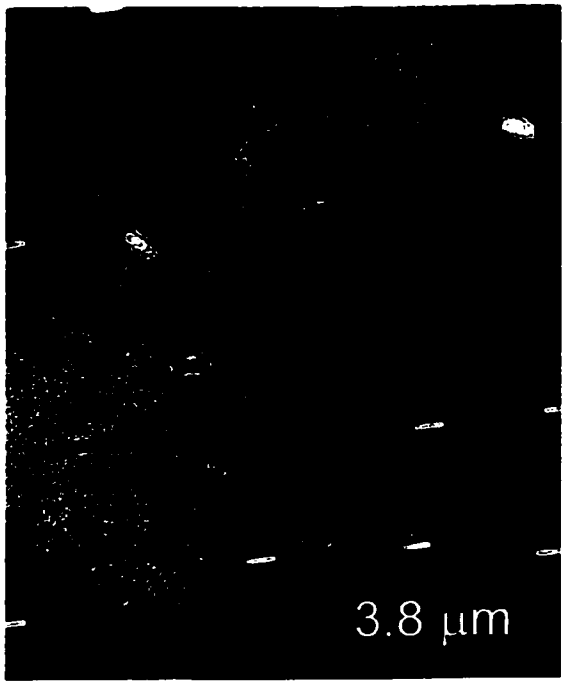

Figure 4.26 Low magnification BF image showing at least two different variants of Cr fibres.

the common close packed directions. In this condition, superimposed diffraction patterns and images were taken of the fibres and matrix. The angles between the facets and the normal to the common close packed

Table 4.4 Average Angles Between Facet Normals and Common Close Packed Directions

	Facet Type #1	Facet Type #2	Facet Type #3
Angle	16.33°	-2.57°	-19.91°
Standard Deviation	1.63°	2.69°	2.98°
Number Measured	18	8	4

planes was measured and recorded. The results of these measurements are tabulated in table 4.4. The measured angles fall roughly into three groups associated with the three observed facets.

The above description defines the general crystallography exhibited between a single fibre and the adjacent matrix. Within a single Cu grain, however, it was often possible to observe more than one variant of fibre. Figure 4.26 is a low magnification BF TEM micrograph from a transverse foil showing differently oriented Cr fibres in the same grain. Three situations were encountered;

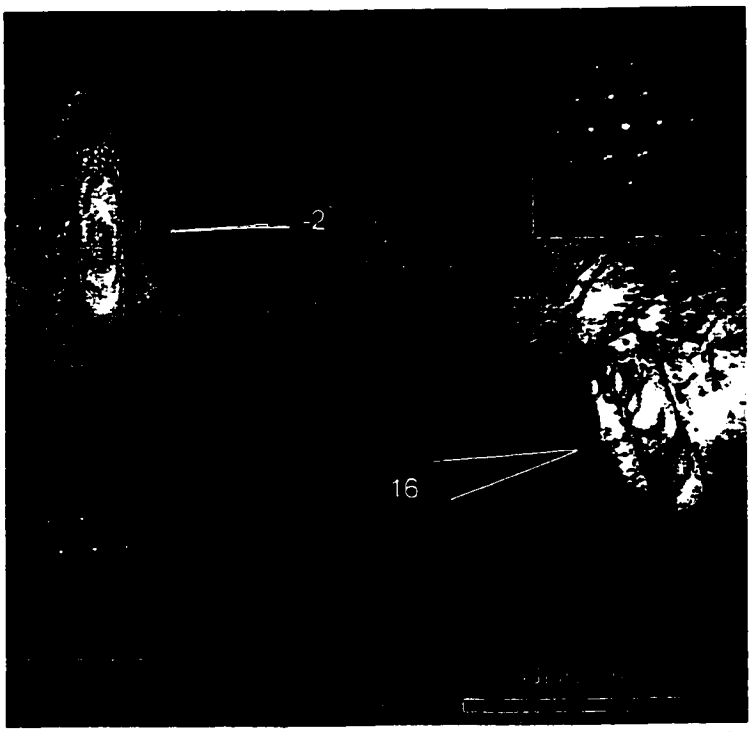

Figure 4.27 Two different variants of fibres. The inset SADP shows that the fibre on the right is oriented such that the beam direction is parallel to the common close packed directions. The fibre on the left shows the same common close packed planes but the beam direction is not parallel to $[111]_{Cr}$. Also note that the fibre on the right is close to end on while interface can be seen on the fibre on the left (marked with arrow).

i) *Both fibres have the same common directions but different common planes:* In some cases it was possible to find adjacent fibres

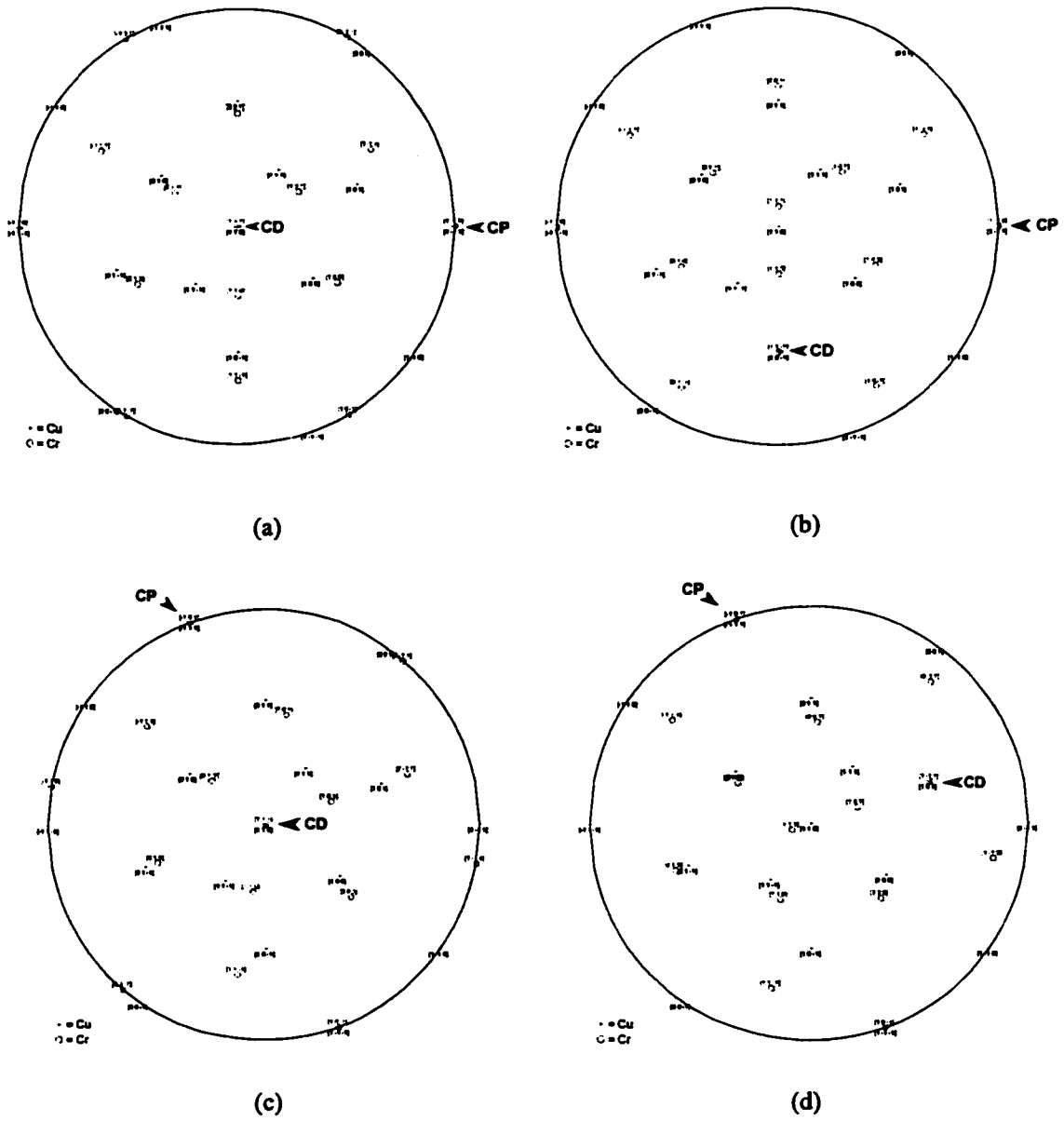

Figure 4.28 Superimposed stereographic projections showing examples of variants of Cr fibres. Common close packed planes and directions noted as CP and CD respectively.

that appeared rotated with respect to one another although they shared the same common close packed directions. Close examination of the SADP from the interface for the two fibres, however, showed different parallel common planes.

ii) *Fibres have different common direction but same common plane:* In some cases fibres within the same grain appeared to share a similar morphology at low magnification. However, upon tilting to the common close packed directions for one fibre, the second fibre was found to be tilted off axis. An example of this situation is shown in the image and SADP patterns of figure 4.27. Here one fibre is close to being end on, while the other is tilted such that the interface on the end facet can be seen.

iii) *Fibres have different common close packed planes and directions:* If one fibre is tilted to the common close packed directions the other fibre is found to be tilted along the normal to the close packed planes such that the beam direction is far from the common close packed directions.

Figure 4.28 summarizes examples of the above variants as superimposed stereographic projections. The majority of fibres within a single grain tended to have the same growth direction. This is consistent with observations in figure 4.4 that showed most fibres aligned closely with the macroscopic growth direction of the sample.

4.2.3.4 Chemistry of Cu and Cr Phases

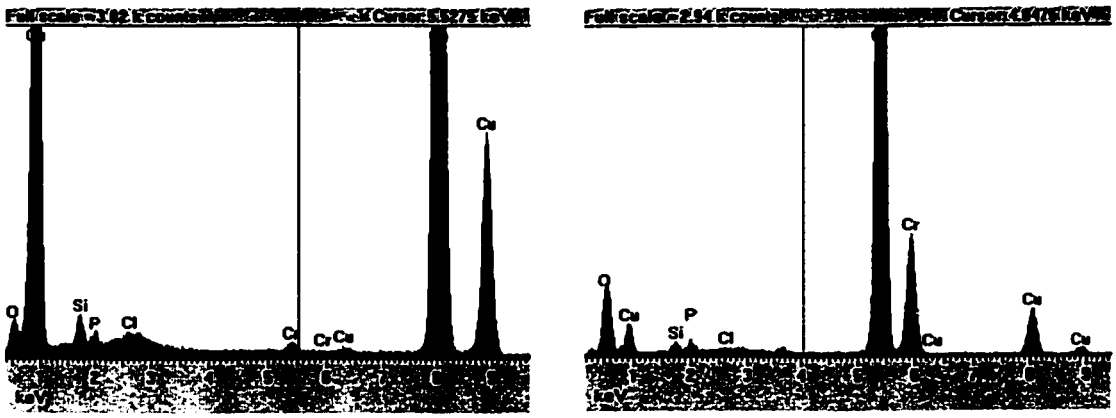

(a) (b)

Figure 4.29 EDX spectrum collected from a) Cu and b) Cr (1 nm spot size) .

The equilibrium binary Cu-Cr phase diagram (figure 3.1) predicts less than 1 at% mutual solubility for the Cu and Cr phases at room temperature. In order to experimentally estimate the chemistry of the phases quantitative EDX analysis was used on transverse thin foils of as-cast samples. Figure 4.29 shows representative spectrum from Cu (far from Cr) and Cr phases. The average measured solubility of Cu in Cr was 4.91 at% while the solubility of Cr in Cu was 0.18at%. The measured solubility of Cu in Cr is higher than predicted by the phase diagram shown in figure 3.1. Others, however, have measured similarly high concentrations of Cu in dendrites of Cr (Jin et al., 1996).

4.3 THE DEFORMATION BEHAVIOUR OF A DIRECTIONALLY SOLIDIFIED CU-1.56AT%CR EUTECTIC ALLOY

The deformation behaviour of the material characterized in the preceding section has been studied using a number of different experimental techniques. In the following sections the observed behaviour will be described. First, the behaviour at the macroscopic scale will be treated. The results of uniaxial tensile tests at various temperatures will be described for directionally solidified and conventionally cast samples. Following this, the evolution of the morphology and scale of both the bulk test specimen and the microstructure as a function of imposed strain will be treated. At the mesoscopic scale, focus will be on the results from tests aimed at deducing the internal stress developed during uniaxial tensile tests. Descriptions of experimental results from in-situ neutron diffraction experiments will be complemented with results from loading/unloading tests in uniaxial tension. At the microscopic scale, the development of substructure in both Cu and Cr phases will be described as a function of test conditions and imposed strain. Of particular interest is the characterization of dislocation activity in the Cr phase, local lattice rotations around Cr fibres in the Cu matrix and evidence of the influence of the Cr phase on the deformation behaviour of the Cu. Finally, because of the importance of large strain deformation in many applications, experiments have been conducted to test the deformation behaviour of this material in plane strain compression up to strains of 1.3. A brief description

of the results of these tests will be presented in terms of the development of phase and specimen morphology after testing, strength as measured by hardness as a function of imposed strain and crystallographic texture.

4.3.1 Macroscopic Characterization of Cu-1.56at%Cr Eutectic Alloy Deformed in Uniaxial Tension

In order to probe the mechanical response of Cu-Cr, uniaxial tensile tests were performed at 293 K, 223 K and 77 K on samples that were solidified at 57 mm/hr and 6 mm/hr. Further, some tests were performed on samples that had solidified either with a hypoeutectic microstructure (Cu rich), or had been conventionally cast. The results of tests on directionally solidified material will be described based on the rate of solidification of the sample tested. For both solidification rates the tensile response will be presented, followed by a description of the evolution of the microstructure and the mode of final failure. Following this, the results of tests on pure Cu, hypoeutectic material and conventionally cast specimens will be presented.

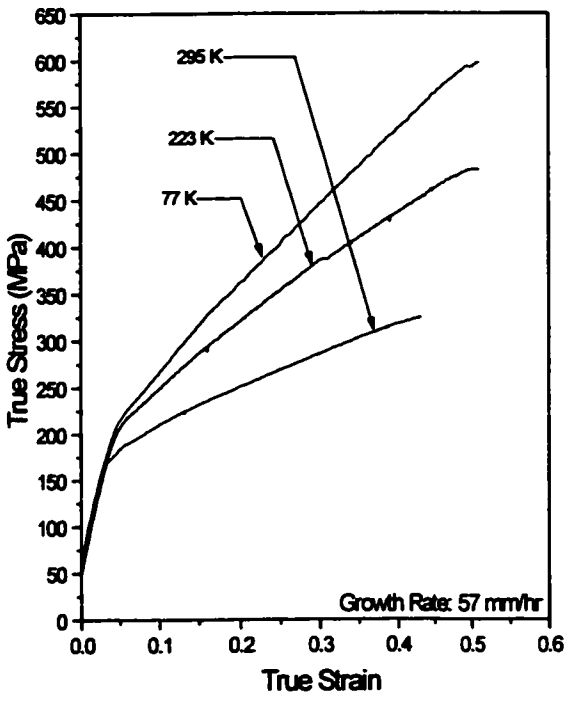

Figure 4.30 Stress-strain response of Cu-Cr solidified at 57 mm/hr and tested at 293 K, 223 K, and 77 K.

4.3.1.1 Mechanical Response of Material Solidified at 57 mm/hr

The majority of samples tested were solidified at a rate of 57 mm/hr. Figure 4.30 shows three representative flow curves measured for samples tested at 293 K, 223 K and 77 K. In all three cases the three regime behaviour characteristic of fibre reinforced composite materials is observed. Comparison of similar samples tested under the same conditions showed a degree of scatter, presumably due to the relatively coarse grain size and high texture. Figure 4.31 shows the magnitude and sense of this scatter for a number of flow curves measured for

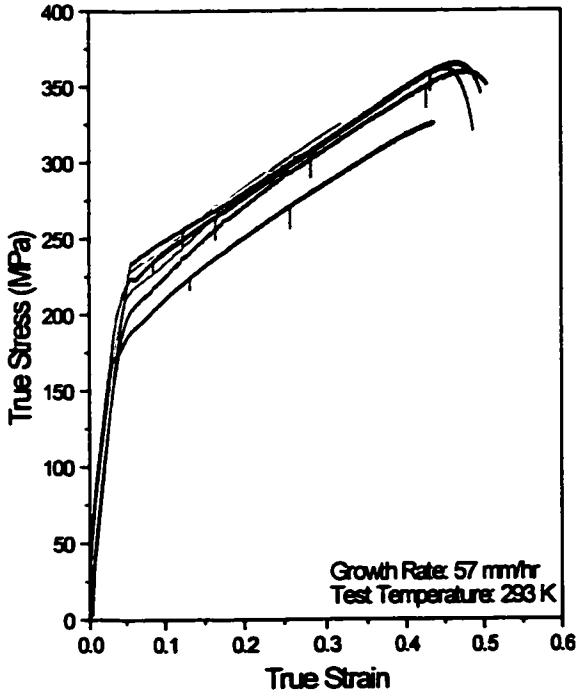

Figure 4.31 Stress-strain response of a series of samples solidified at 57 mm/hr and tested at 293 K showing scatter in the experimental data. Black and gray lines indicate samples with gauge diameters of 5.09 mm and 9.5 mm respectively.

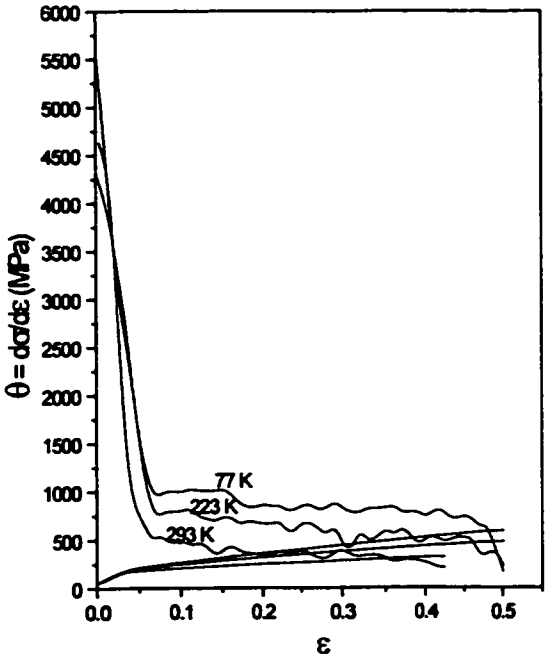

Figure 4.32 Work hardening rate (θ) versus strain deduced from data in figure 4.30.

samples solidified at 57 mm/hr and tested at 293 K. In order to ensure the scatter could not be attributed to an insufficient ratio of grain size to specimen diameter, samples with larger gauge diameters were tested. Comparison of the response of specimens with gauge diameters of 5.05 mm and 9.5 mm indicated that this was not an issue.

The tensile data plotted in figure 4.30 was differentiated and plotted as the rate of work hardening (θ) versus applied strain and applied stress in figure 4.32. For the sake of comparison, figure 4.32 includes the flow curves for the three test temperatures.

A final test performed on samples solidified at 57 mm/hr was to pre-strain the material at 293 K and subsequently test the flow stress at 77 K. The results of such a test (Cottrell-Stokes Test) are shown in figure

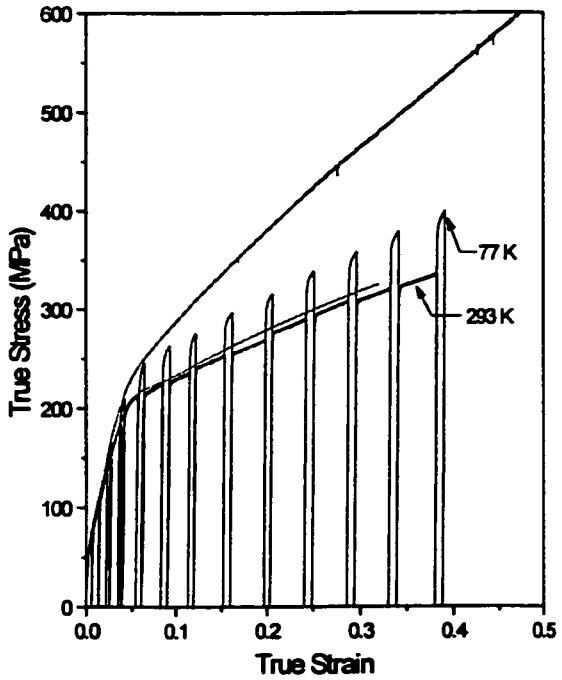

Figure4.33 Results of cyclic testing at 293 K and 77 K (Cottrel-Stokes test). Also included are monotonic curves for samples solidified at 57 mm/hr and 293 K.

4.33. The flow curve resulting from iteratively testing at 293 K and 77 K is shown here, along with monotonic curves from samples tested at 293 K and 77 K.

It was important to follow the macroscopic evolution of sample morphology with strain in order to judge the macroscopic homogeneity of deformation. Figure 4.34 shows a series of photographs taken in-situ during the tensile deformation of a specimen at room temperature. At strains above 0.2 roughening associated with surface grains occurs. As straining continues, surface striations develop roughly perpendicular to the tensile axis. As necking initiates, one or two of these striations develop preferentially and failure occurs by shear along (predominantly) one of the resulting macroscopic shear bands. Further, it was found that deformation of the sample was not purely axisymmetric as expected for isotropic polycrystalline specimens. Figure 4.35a illustrates a sample that was strained beyond the onset of necking at 293 K (ε =0.32). It is clear that this sample has deformed into an elliptical

Figure 4.34 Photograph showing the change in macroscopic morphology of a tensile specimen after increasing amounts of strain (left to right).

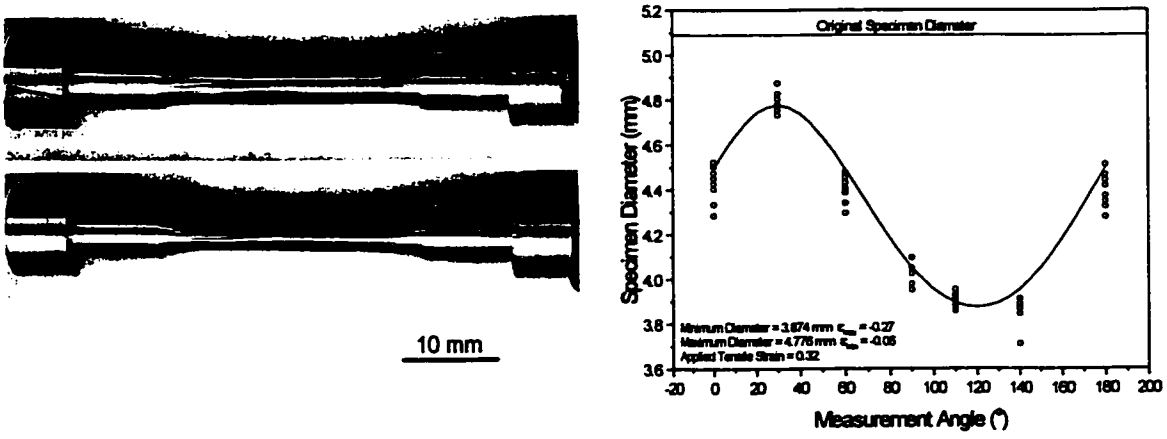

(a) (b)

Figure 4.35 a) Photographs (rotated 90° between photos) of a sample after testing, but just prior to failure, showing the elliptical cross-section developed. b) Measurements of specimen diameter showing the development of an elliptical cross-section.

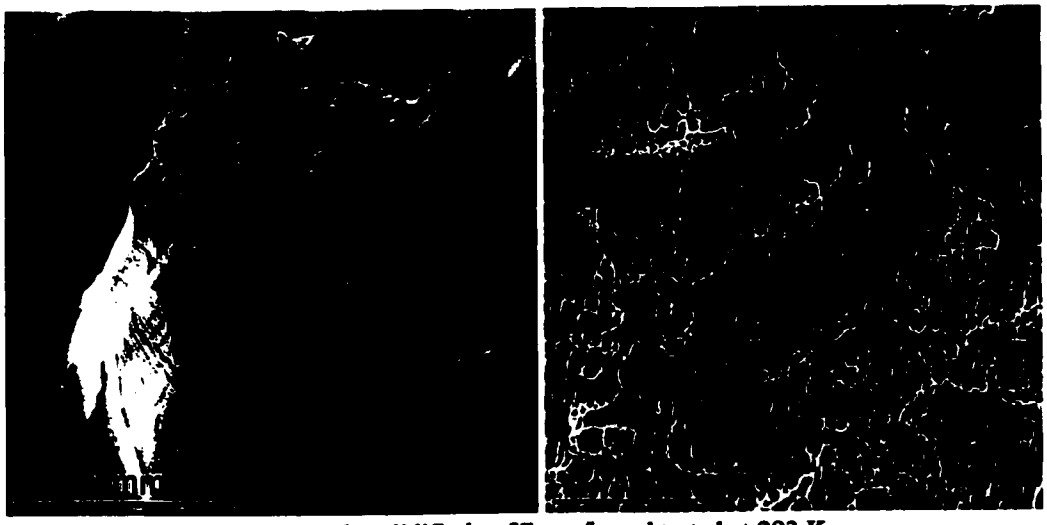

Figure 4.36 Failure surfaces for sample solidified at 57 mm/hr and tested at 293 K.

cross-section. The degree to which the cross-section became elliptical was quantified by measuring the diameter of a specimen rotated about its axis. Fitting an ellipse to the measured points gives major and minor strains of-0.27 and -0.06 respectively. This indicates a nearly plane strain condition. Fracture surfaces in

samples tested at all temperature were consistent with failure by localized shear (figure 4.36). Elongated dimples are the predominant feature in all cases.

4.3.1.2 Mechanical Response of Material Solidified at 6 mm/hr

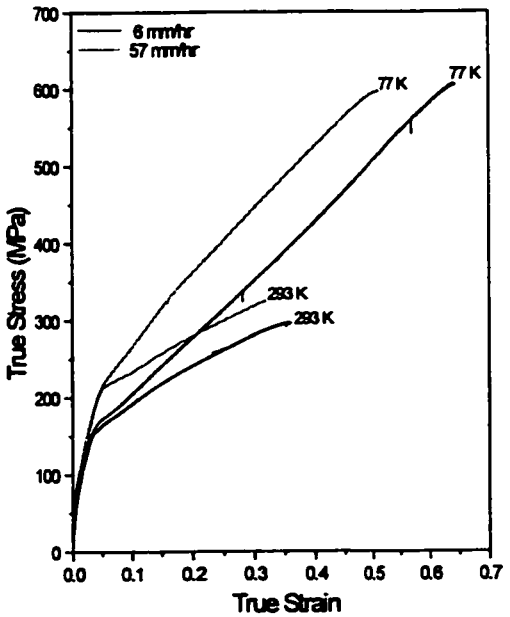

Figure 4.37 Stress/strain response for samples solidified at 6 mm/hr and tested at a) 293 K, and b) 77 K. Also shown are representative curves for samples solidified at 57 mm/hr.

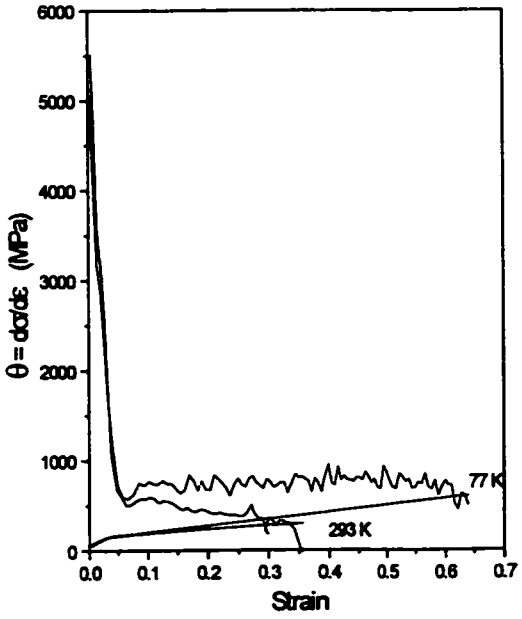

Figure 4.38 Hardening rate versus strain for samples solidified at 6 mm/hr and tested at 293 K and 77 K.

Figure 4.37 shows the results of uniaxial tensile tests performed on samples solidified at 6 mm/hr and tested at 293 K and 77 K. For the purposes of comparison, representative flow curves for samples solidified at 57 mm/hr and tested at 293 K and 77 K (from figure 4.35) are included. As with the samples solidified at 57 mm/hr, scatter in the mechanical response at all temperatures was evident.

Figure 4.38 reports the calculated rate of work hardening derived from the curves in figure 4.37 as a function of applied strain.

Similar to samples solidified at 57 mm/hr, the fracture surfaces of most samples were composed of elongated dimples consistent with localized shear as a mode of failure (figure 4.39). When compared with

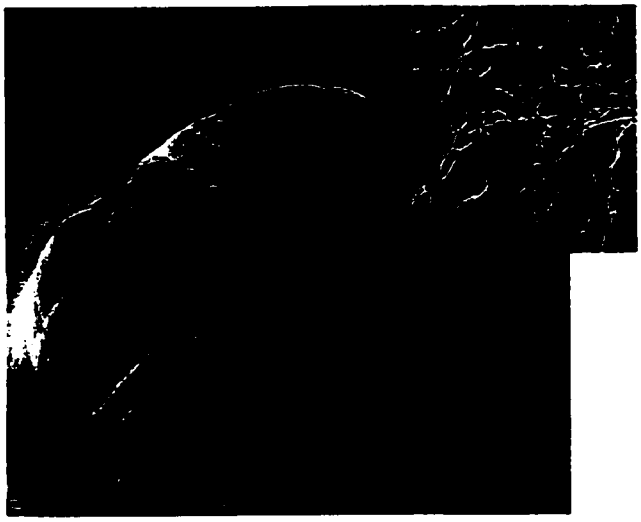

Figure 4.39 Fracture surfaces from samples solidified at 6 mm/hr and tested at 293 K.

samples solidified at 57 mm/hr, however, the fracture surfaces tended to be composed of a higher density of equiaxed dimples associated with failure outside of shear bands.

One group of samples solidified at 6 mm/hr and tested at 77 K were found to possess anomalously low ductility (figure 4.40a). These anomalous specimens were machined from the bottom of ingots where the presence of proeutectic Cr phases were known to be present in the microstructure. Figure 4.40b shows an SEM image of the fracture surface from one such specimen. The predominant features of the fracture surface are equiaxed dimples surrounding relatively flat cleavage facets associated with proeutectic Cr particles. A further discussion of the source of fracture in these specimens will be reserved for section 4.3.1.3, where the detailed microstructural features will be discussed.

4.3.1.3 Mechanical Response of Other Materials Tested

Uniaxial tensile tests were performed on specimens solidified at off-eutectic compositions. Due to difficulty controlling the homogeneity of such samples only a single tensile specimen could be machined from an ingot. Lack of material thus resulted in tests being performed only at room temperature. Figure 4.41a shows the tensile response of a specimen consisting of approximately 10% eutectic, while figure 4.41b shows a composite longitudinal micrograph from this specimen after testing. Although the test was stopped prior to final failure, a shear induced void is seen to have opened at the centre of the specimen.

Material produced by conventional casting was also tested in tension. Instead of slowly lowering the specimen from the work coil, this material was produced by leaving the molten charge within the work coil and shutting off the power. The resulting shrinkage cavity at the top of the ingot precluded the production of more than a single tensile specimen from an ingot, thus tests were conducted at 293 K only. Figure 4.42a

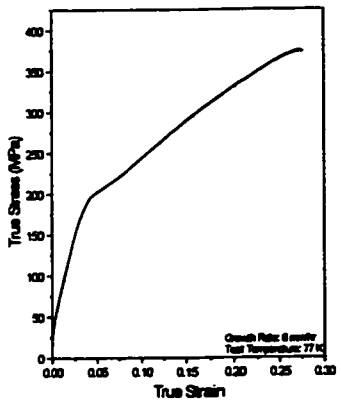

(a)

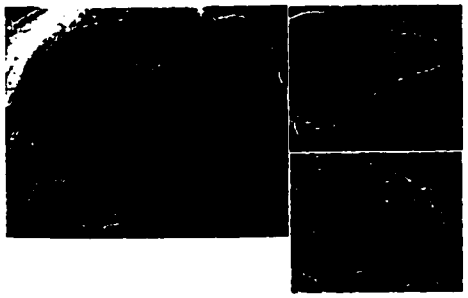

(b)

Figure 4.40 a) Stress-strain response for sample solidified at 6 mm/hr and tested at 77 K, exhibiting anomalously low ductility. b) Fracture surface of sample in a).

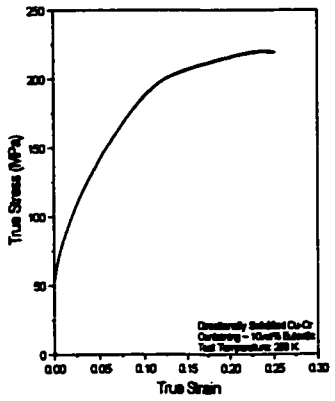

(a)

(b)

Figure 4.41 a) Stress/strain response for hypoeutectic Cu-Cr. b) Longitudinal micrograph after testing showing one large void at centre of sample.

shows the tensile response from such a specimen while figure 4.42b shows a series of optical micrographs taken from the longitudinal section after testing.

Finally, for the purpose of comparing the above tensile data from Cu-Cr alloys with the behaviour of unreinforced Cu, pure Cu specimens were prepared and tested at 293 K and 77 K. In order to have samples with a grain size comparable to that in the directionally solidified material, a thermomechanical treatment was

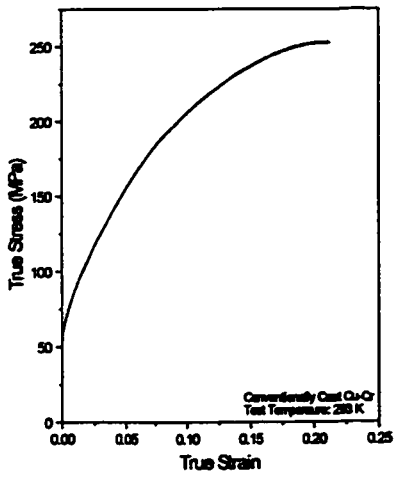

(a)

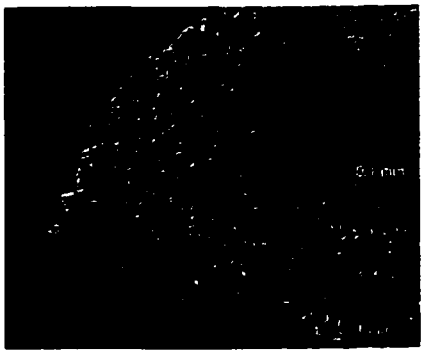

(b)

Figure 4.42 a) Stress-strain response of conventionally cast Cu-Cr. b) Micrograph showing microstructure after testing at low magnification and high magnification (inset).

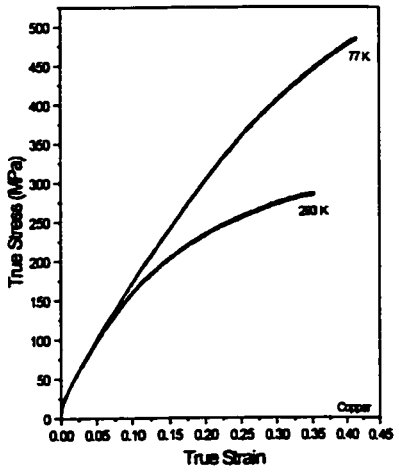

(a)

(b)

Figure 4.43 a) Stress-strain response of pure Cu specimens. b) Micrograph showing microstructure prior to straining.

given to bulk OFHC Cu. The same material used in the production of the Cu-Cr alloys was rolled to approximately 50% reduction and subsequently annealed under an argon atmosphere at 650°C for 72 hours. This material was then rolled to a further 50% reduction, tensile specimen cut parallel to the rolling direction, and the above heat treatment reapplied. The resulting microstructure (shown in figure 4.43b) resulted in a grain size of approximately 150 µm. The tensile response of this material at 293 K and 77 K is shown in figure 4.43a.

4.3.1.4 Morphological Evolution of Specimens and Microstructure as a Function of Strain

The effect of tensile deformation on the evolution of the microstructure was evaluated in three ways. First, after failure, samples were cut and observed metallographically in longitudinal sections. Observations were made by both optical and scanning electron microscopy. Second, uniaxial tensile specimen were polished prior to straining in order to observe slip traces. Finally, in-situ tensile tests were carried out in an SEM. While the first method of characterization was applied to samples solidified at 57 mm/hr and 6 mm/hr and tested at 77 K, 223 K and 293 K, the latter two techniques were applied to samples solidified at 57 mm/hr and tested at 293 K.

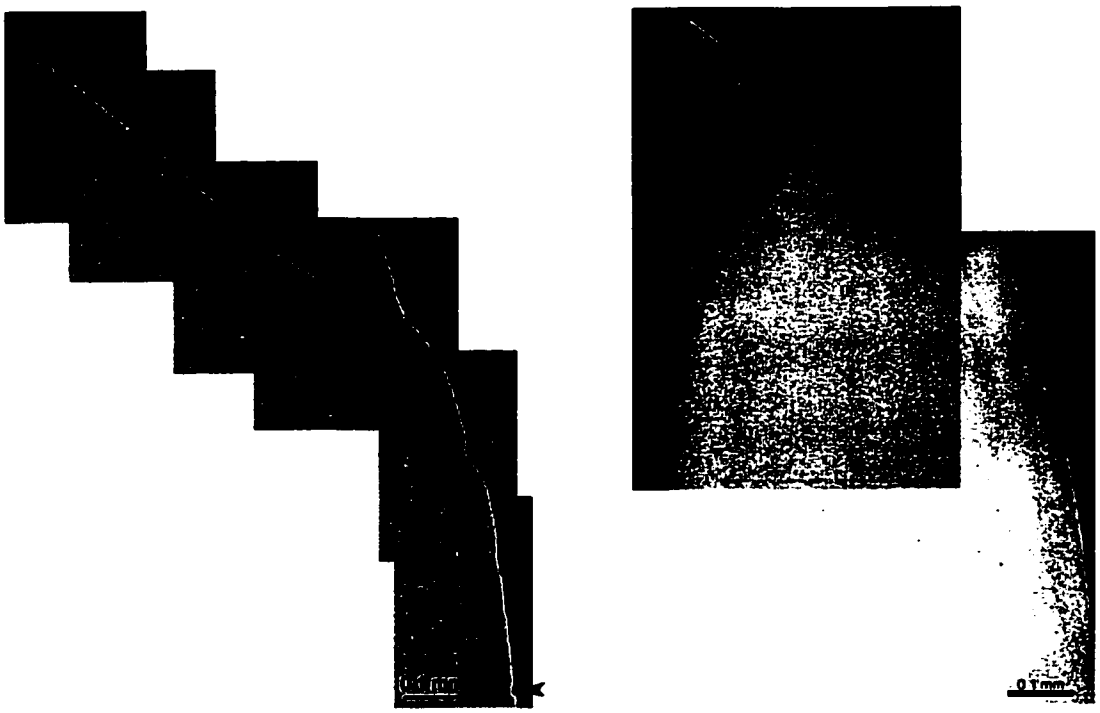

(a) (b)

Figure 4.44 Low magnification images from samples solidified at 57 mm/hr and tested at a) 293 K, and b) 77 K.

Figure 4.44 shows low magnification optical micrographs taken from longitudinal sections of tensile specimens (solidified at 57 mm/hr) tested to failure at a) 293 K and b) 77 K. All samples failed by localized shear along one or two predominant shear bands. Along the length of the samples, shear offsets can be seen along the surface (marked with arrows). Although these shear offsets were observed on samples solidified at all test temperatures, they were most prominent on samples tested at 293 K. These shear offsets could be identified with the transverse markings observed on the surface of tensile specimen during testing (cf. section 4.3.1.2). Evidence for fracture of the eutectic Cr phase was never observed optically for any test condition.

Close observation of the microstructure within the necked portion of samples tested to failure showed the presence of shear bands both at, and below the fracture surface. Compared to samples tested at 293 K, samples tested at 77 K exhibited fewer shear bands beyond those that resulted in final failure (figure 4.45). The Cr fibres deform extensively within the shear bands. Fibres appear to be sheared into the bands, resulting in short segments of reoriented fibres oriented along the direction of shear. This can be seen clearly if polarized light is used in the manner discussed in chapter 3. The shear bands, and therefore the fibres lying therein, are situated at angles between 35° and 55° from the tensile axis. If the sample is oriented such that this

(a) (b)

Figure 4.45 Higher magnification micrographs from within neck of tensile specimens shown in figure 4.44, showing shear bands and deformation of Cr fibres into shear bands at a) 293 K, and b) 77 K.

band is approximately 45° from the direction of polarization, double reflection results in the fibres within the bands appearing bright. If the sample is rotated through 90°, so that the fibres outside of the bands are roughly lying at 45° to the polarization direction, the fibres within the bands appear dark while those outside of the bands appear light. Figure 4.45 shows this technique used to examine the region just below the fracture surface in samples solidified at 57 mm/hr and tested at a) 293 K, and b) 77 K.

Samples solidified at 6 mm/hr also tended to fail by localized shear. However, the eventual mode of failure was strongly sample dependent such that the degree of shear localization varied from sample to sample far more than for samples solidified at 57 mm/hr.

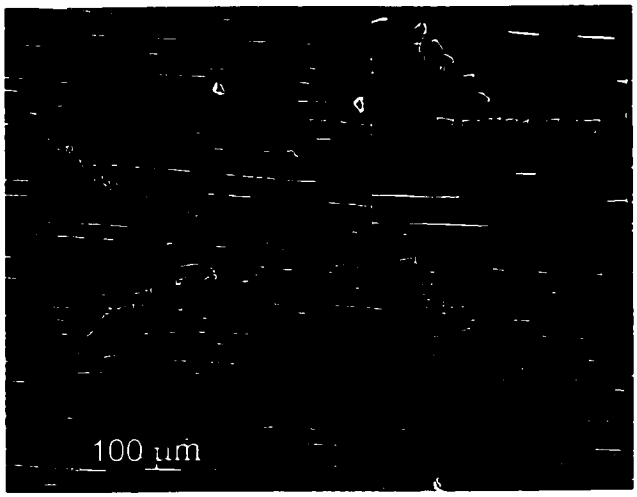

Figure 4.46 Fracture of coarse Cr particles in a sample solidified at 6 mm/hr and tested at 77 K.

As previously mentioned (cf. section 4.3.1.2), some samples solidified at 6 mm/hr exhibited anomalously low ductility when tested at 77 K. Longitudinal sections revealed fractured coarse Cr particles, located both at, and below the fracture surface (figure 4.46). No evidence of the fracture of eutectic Cr fibres was observed. The scale of the fractured particles was >> 1 µm, in contrast to the cross-sectional dimensions of the fibres which were an order of magnitude smaller.

In order to observe the spatial homogeneity of plastic deformation and the interaction between flow in the Cu matrix and Cr fibres, slip traces were observed on the surface of polished flat tensile specimens. As described in section 3.3 the samples were machined into an hourglass shape localizing the bulk of strain into a narrow region of the specimen. Samples were pre-strained in tension, unloaded and electropolished. The same sample was then further strained 2-5% in tension in order to produce slip traces on the polished surface. This process was repeated several times for the observation of slip distribution as a function of pre-strain.

Figure 4.47 shows a series of composite micrographs showing a low magnification view of slip traces on the surface of specimen strained 10%. At low strains the slip distribution is relatively inhomogeneous. Slip

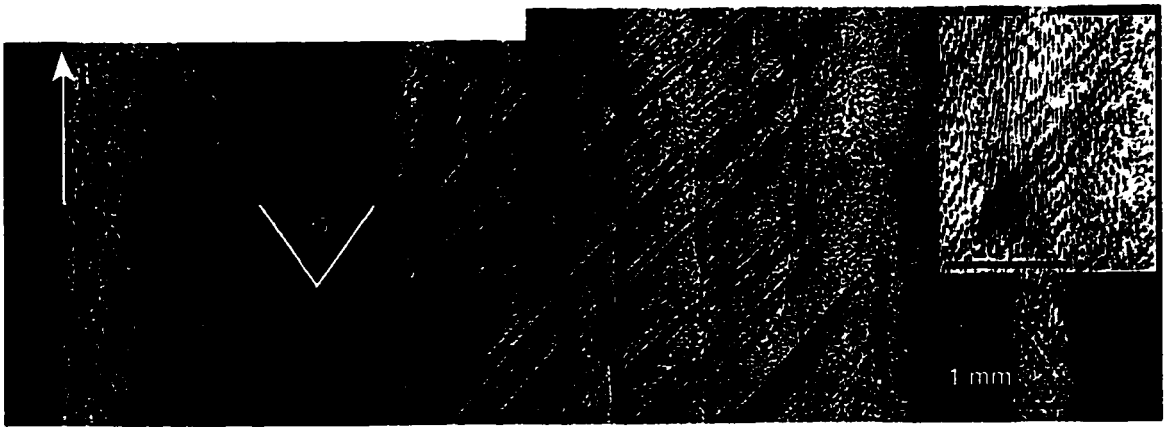

Figure 4.47 Development of slip lines on the surface of polished tensile specimen after 10% strain (tensile axis indicated by arrow). Coarse slip bands run across many grains. Little interaction was observed at low strains between Cr fibres and slip traces (inset).

bands, consisting of many slip lines, run nearly unobstructed across several grains, consistent with the strong texture of the sample. As the amount of pre-strain was increased, slip became more homogeneous, although macroscopically coarse slip bands were still obvious. The onset of necking coincided with the development of a single predominant set of slip bands, oriented at an angle between 35° and 55° to the tensile axis and crossing the entire sample.

In order to explore the process of co-deformation at a finer scale, in-situ SEM tensile tests were conducted using the same samples as used for the above described observations of slip traces. At low strains, few modifications to the microstructure were observed. Slip traces were observed in the Cu but little evidence of extensive plasticity in the Cr

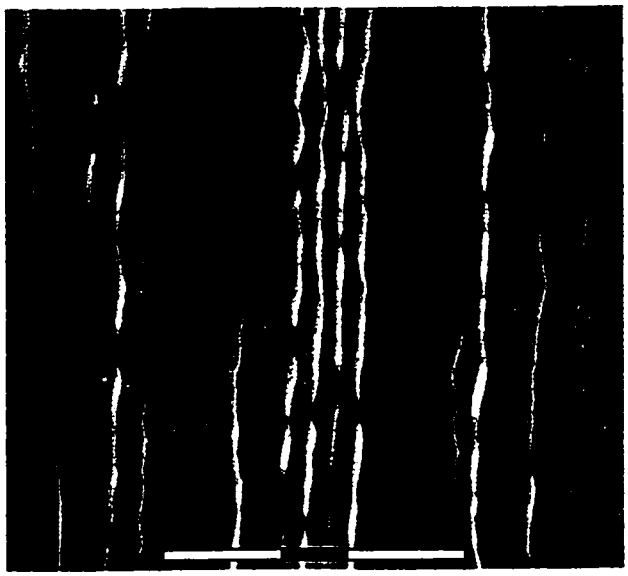

Figure 4.48 The morphology of Cr fibres in sample strained to 0.15.

Figure 4.49 Series of sequential SEM images taken during in-situ straining of a tensile specimen. The deformation of fibres into shear bands can be followed. Cr fibres are seen to deform extensively into shear bands (e.g. fibre marked by arrow). Strain increases from (a) to (e).

fibres can be observed. At strains close to the onset of necking the morphology of the fibres changed drastically. Figure 4.48 shows a micrograph taken from a sample strained to approximately 0.3(at the point of necking). The previously homogeneous Cr fibres have become extensively deformed in an inhomogeneous manner (sample was pre-strained and electropolished prior to viewing). This sample was deformed further in-situ to follow the continued deformation of the fibres. Figure 4.49 shows a series of sequential micrographs from a single region with increasing strain. The interaction of slip bands in the Cu interacting with the Cr fibres can be observed. Those fibres intersected by slip bands are deformed extensively in the bands. As straining continued fibres sheared apart with no evidence of voiding or cleavage at the point of rupture. With further straining, fibres within a shear band were observed to become oriented along the direction of shear. Further deformation resulted in strain becoming localized into two predominant macroscopic shear bands. The localization of strain within these bands then led to the final failure of the specimen. Figure 4.50 shows a series of composite micrographs at low magnification showing this localized shear band and the initiation of

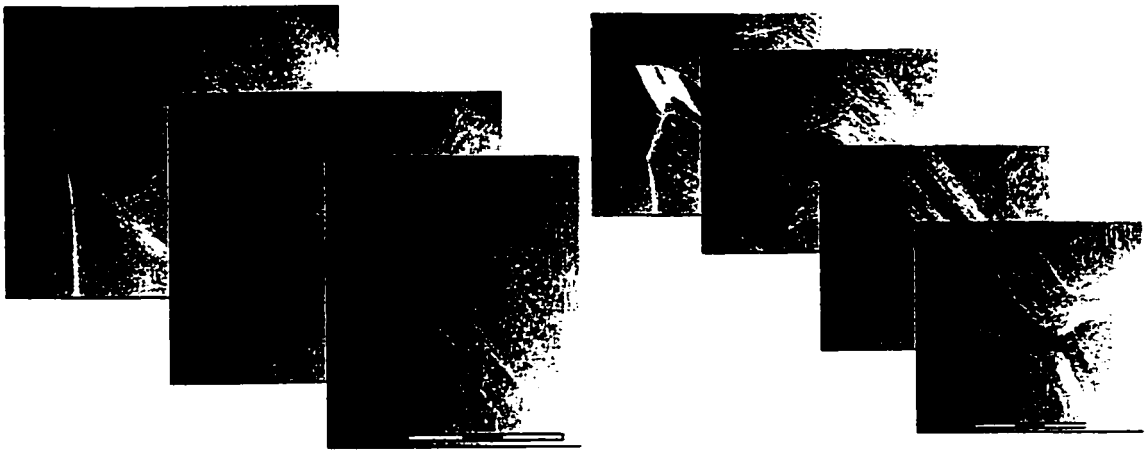

(a) (b)

Figure 4.50 Low magnification micrographs showing the development of macroscopic shear bands leading to final failure. a) Onset of localized shearing. b) Just prior to final failure.

failure at increasing applied strain. On a microscopic scale, voids began to appear on the shear band just prior to final fracture (figure 4.51). These voids were not associated with Cr fibres on the surface of the sample. As with conventionally tested specimen, the fracture surface is characterized largely by elongated dimples.

Figure 4.51 Observation of a void formed along a shear band just prior to failure.

4.3.2 Mesoscopic Characterization of Cu-1.56at%Cr Eutectic Alloy Deformed in Uniaxial Tension

The in-situ response of the Cu and Cr phases during deformation were probed using two experimental techniques. In this section, results from neutron diffraction experiments will be presented first, followed by results from loading/unloading uniaxial tensile tests.

4.3.2.1 In-Situ Measurement of Lattice Strains via Neutron Diffraction

Five tensile specimen were tested in-situ in tension. Table 4.5 gives a summary of the specimen tested, the total strain to which the measurements were made, the peaks measured, and the wavelength of the incident beam. Although the measurement of Cu peaks was relatively straight forward, problems were encountered with measurements on the Cr fibres. Because of the low volume fraction of fibres and the high degree of

Table 4.5 Test Conditions for Neutron Diffraction Experiments

Specimen	Growth Condition	λ	Cu Reflection	Angle from TA	Total Applied Strain
1	57 mm/hr	1.101Å	{331}	0°	0.117
2	57 mm/hr	1.531Å	{220}	0°	0.041
3	57 mm/hr	1.531Å	{220}	0°	0.150
4	57 mm/hr	1.531Å	{220}	0°	0.289
5	57 mm/hr	1.531Å	{220}	0°	0.344

crystallographic texture, finding Cr peaks was very difficult. When peaks were found at the proper Bragg angle they were often poorly resolved against the background. Although attempts were made to follow several peaks, the declining quality of the peaks with straining and the weak signal made accurate fitting difficult. For these reasons, only data from the Cu will be presented here.

The results from each of the above specimens are presented in figures 4.52, 4.53, 4.54, 4.55, and 4.56. At the end, the data from different specimens will be directly compared (figure 4.57). For figures 4.52-4.56 six plots showing the variation of lattice strain, peak FWHM, residual lattice strain and mean peak position as a function of applied stress and/or applied strain are presented along with the macroscopic stress/strain data. In each case, the first measured point is assumed to correspond to the "stress -free" state, i.e. it is assumed that the sample prior to straining contains no residual stresses. This is accounted for in figure 4.57.

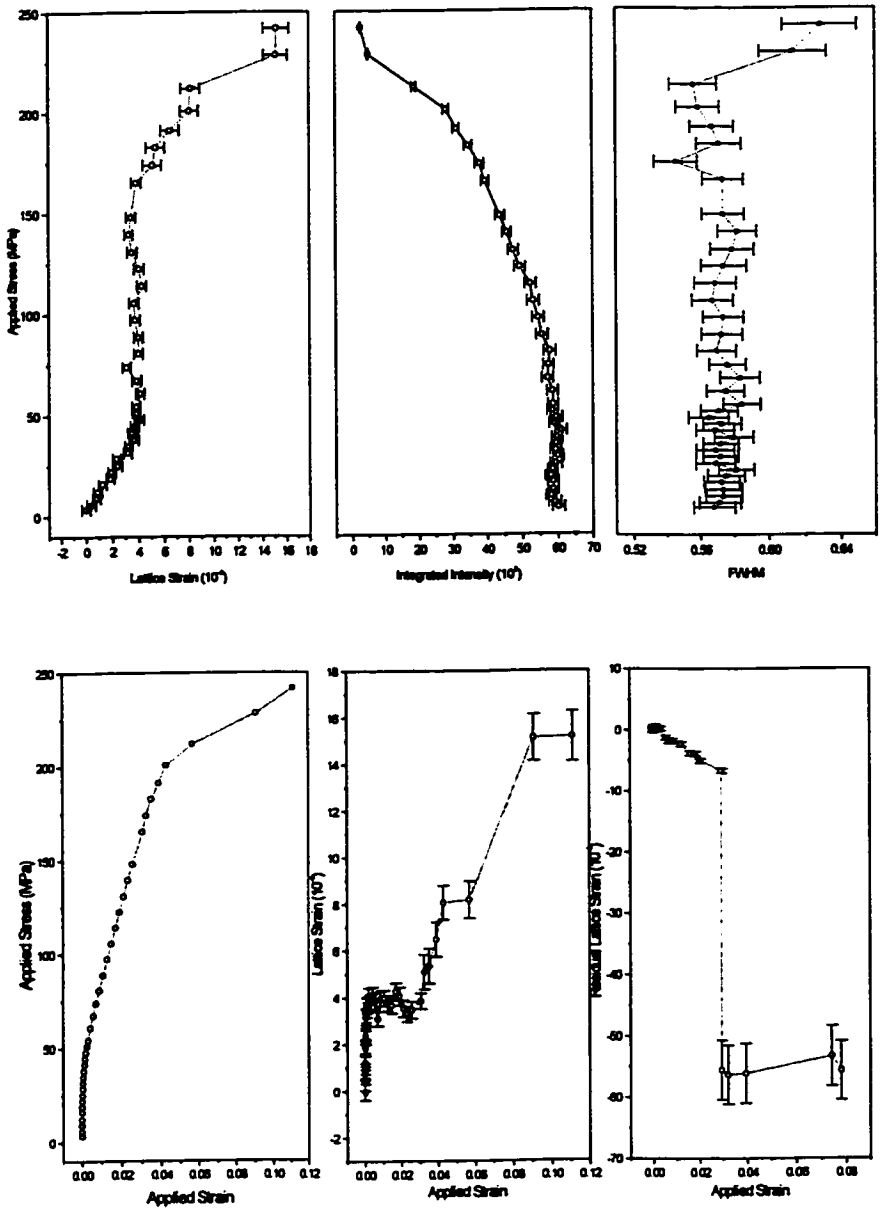

Figure 4.52 Neutron diffraction results for specimen 1, Cu {331}.

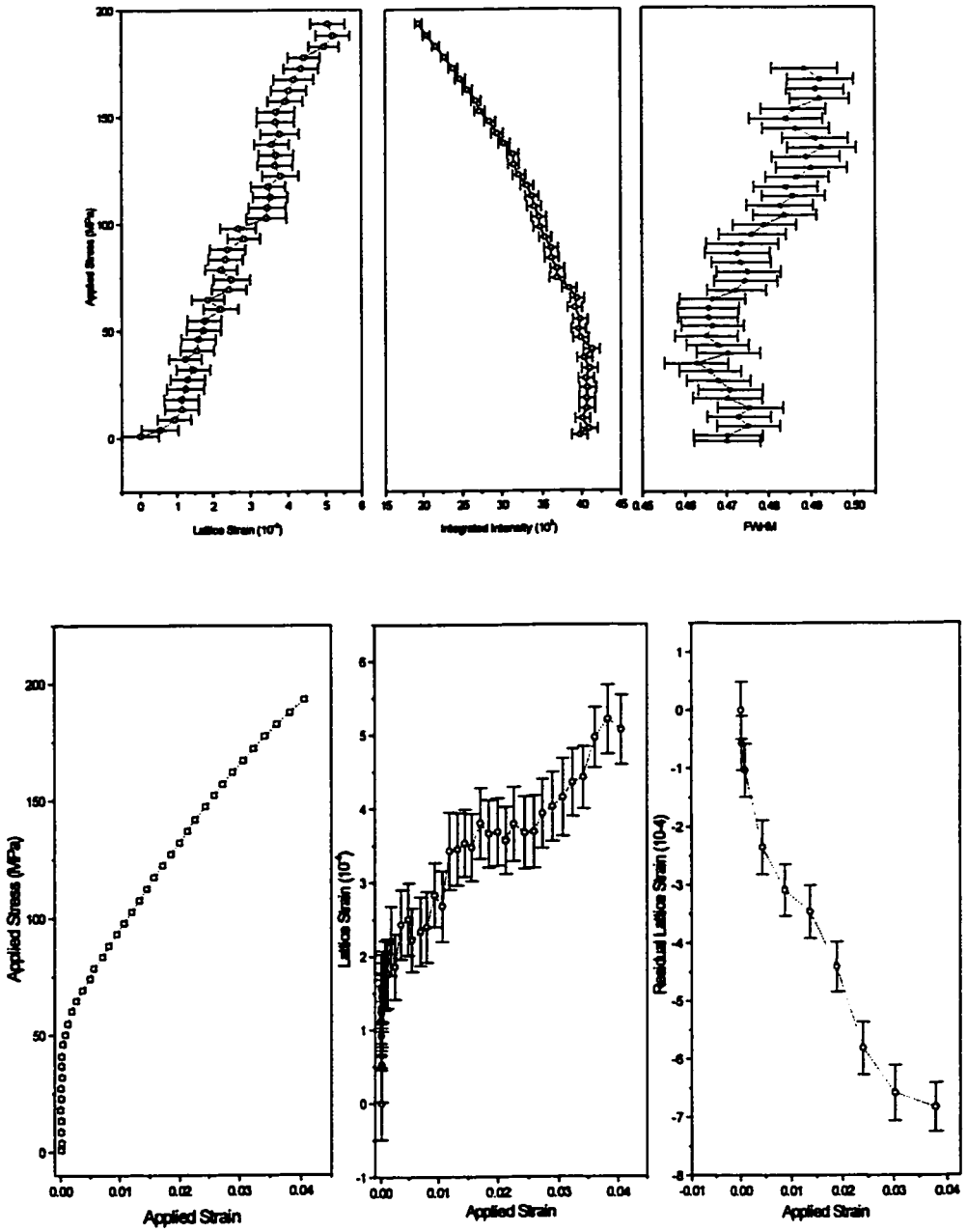

Figure 4.53 Neutron diffraction results for specimen 2, Cu {220}.

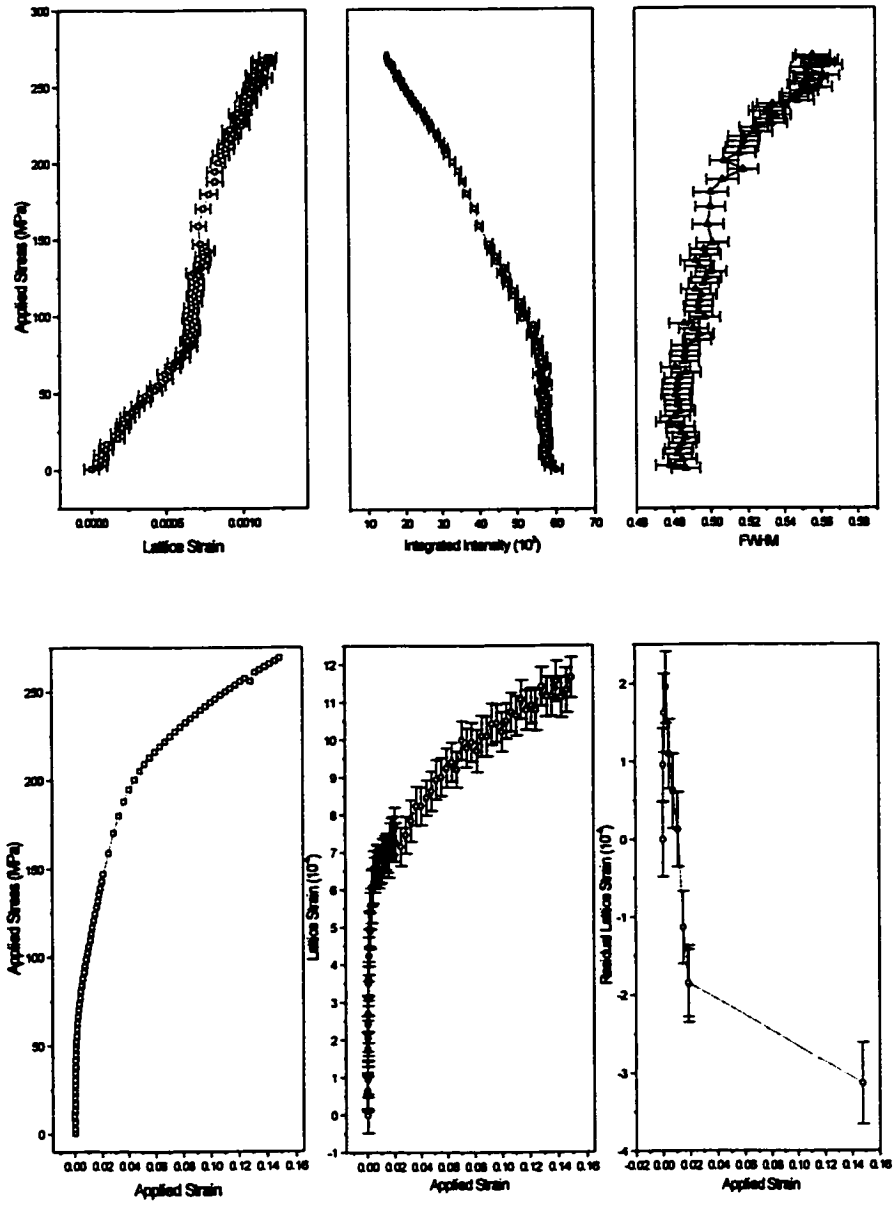

Figure 4.54 Neutron diffraction results for specimen 3, Cu {220}.

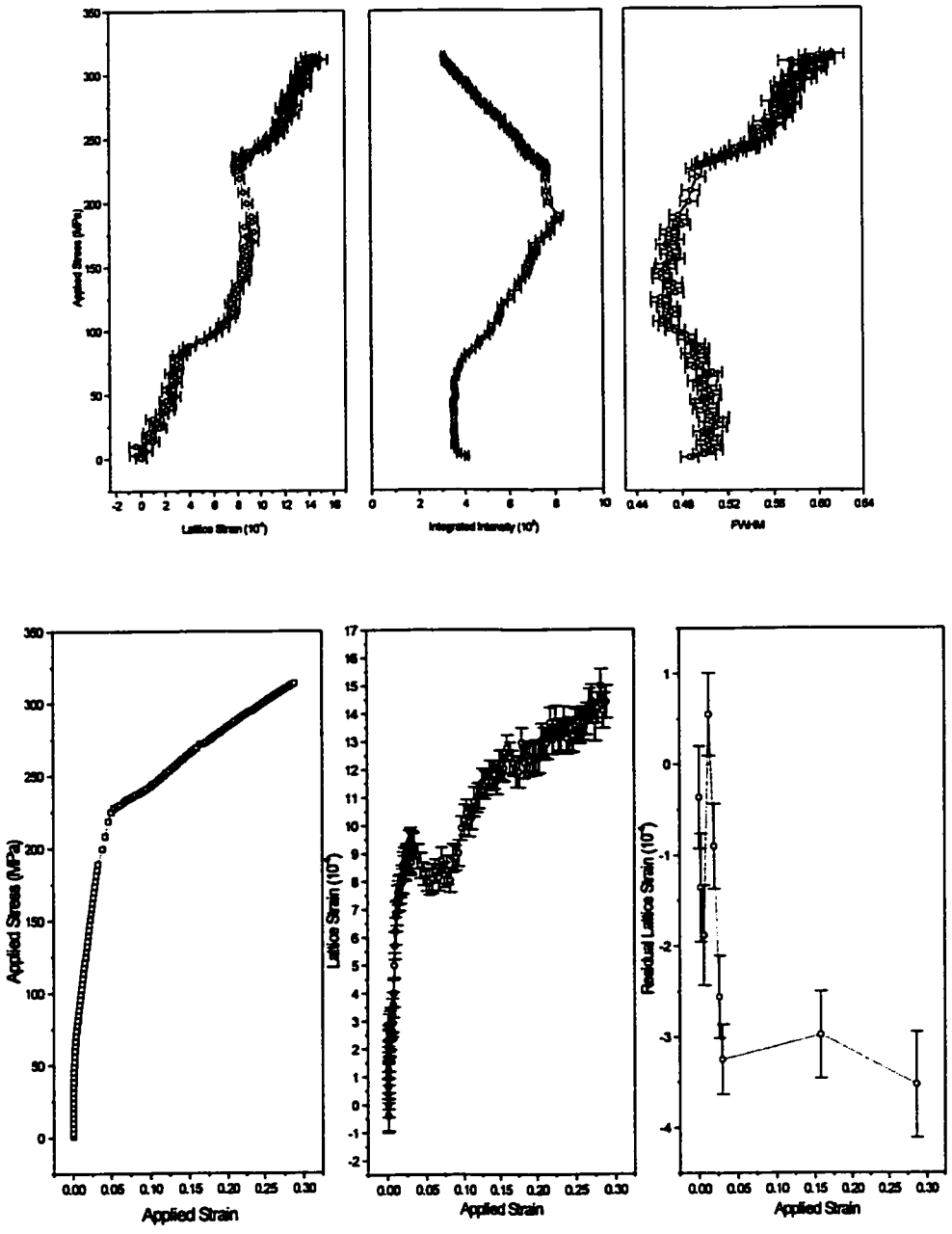

Figure 4.55 Neutron diffraction results for specimen 4, Cu {220}.

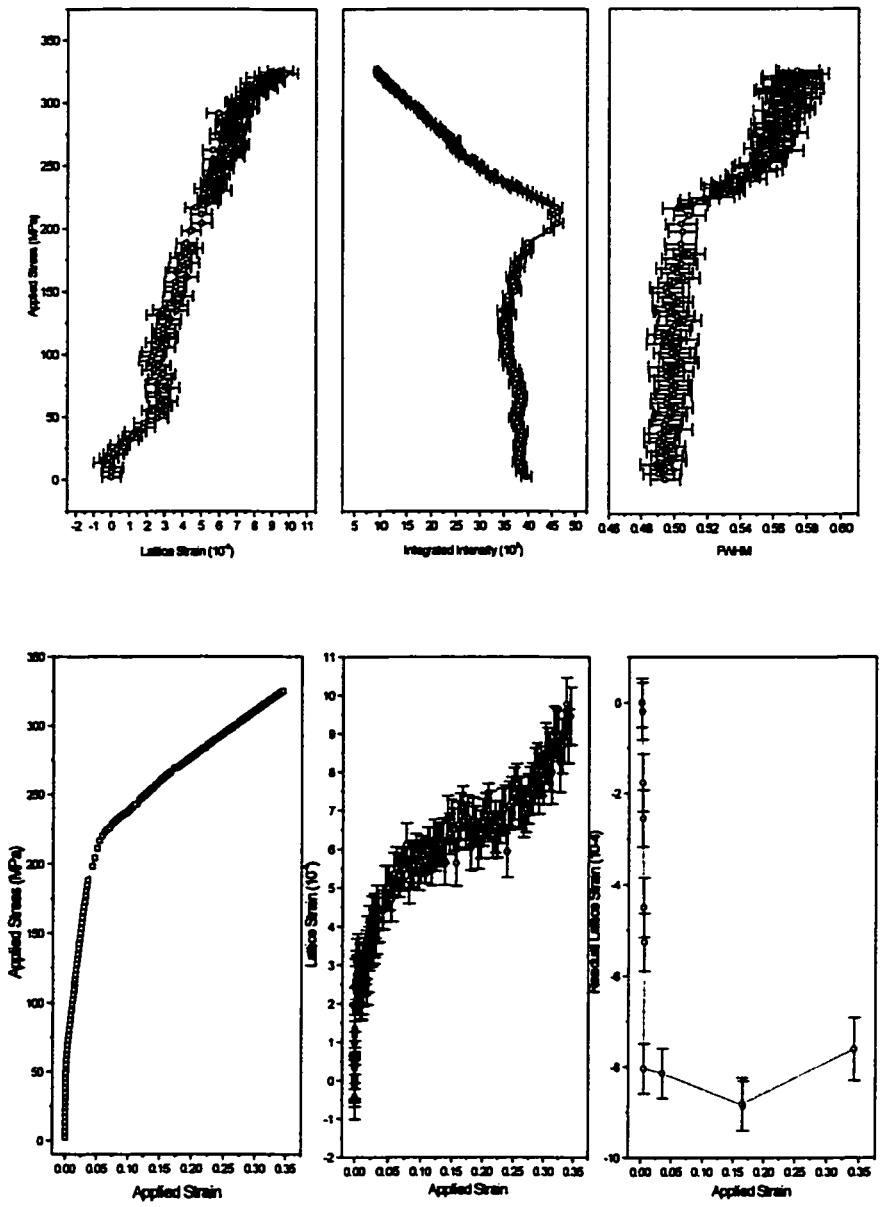

Figure 4.56 Neutron diffraction results for specimen 5, Cu {220}.

In order to predict the initial residual lattice strain, a reference lattice parameter has been selected. Because of the low concentration measured within the Cu matrix by EDX (section 4.1), the lattice parameter given for pure Cu of 3.6105 Å (Pearson,1967) will be used here as a reference.

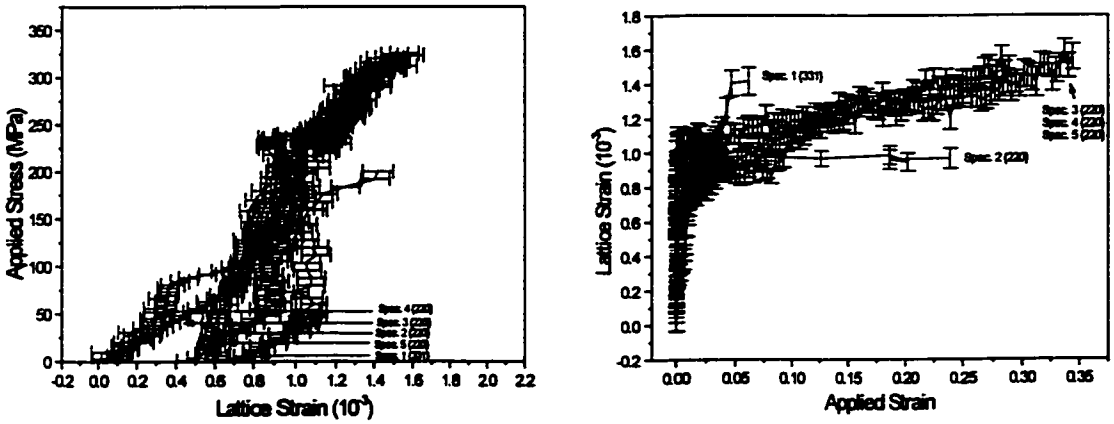

(a) (b)

Figure 4.57 Summary of neutron diffraction results showing lattice strain versus applied stress for Cu, including the effect of initial thermal residual stresses. a) Lattice strain versus applied stress. b) Lattice strain versus applied strain.

Figure 4.57 summarizes the collected Cu lattice strain data as a function of imposed strain and stress for samples 1, 2, 3, 4, and 5. All samples show similar trends, although significant differences in starting residual stresses exist between the different samples.

4.3.2.2 Reversible Plastic Deformation and Internal Stresses Estimated by Loading/Unloading Experiments in Uniaxial Tension

Further insight into the distribution of internal stresses and strains during tensile straining was obtained through the use of simple tests where samples were iteratively pre-strained plastically in uniaxial tension, unloaded and then re-loaded to the prior flow stress . The resulting loading/unloading curves show hysteresis associated with the internal stress distribution developed in the initial tensile deformation. Figure 4.58 shows tensile curves with loading/unloading steps for samples solidified at 57 mm/hr and deformed at 293 K. No significant difference between the flow curves from the cyclic tests and those obtained from monotonic tests

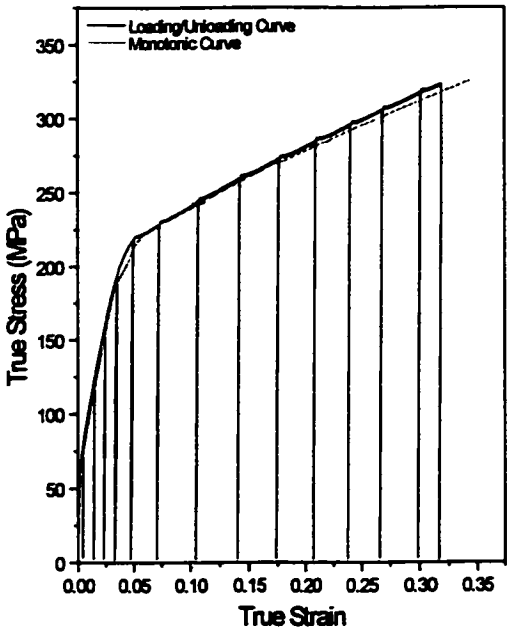

Figure 4.58 Stress-strain response for samples tested in monotonic uniaxial tension (gray line) and after a series of load/unload steps (black lines) at 293 K.

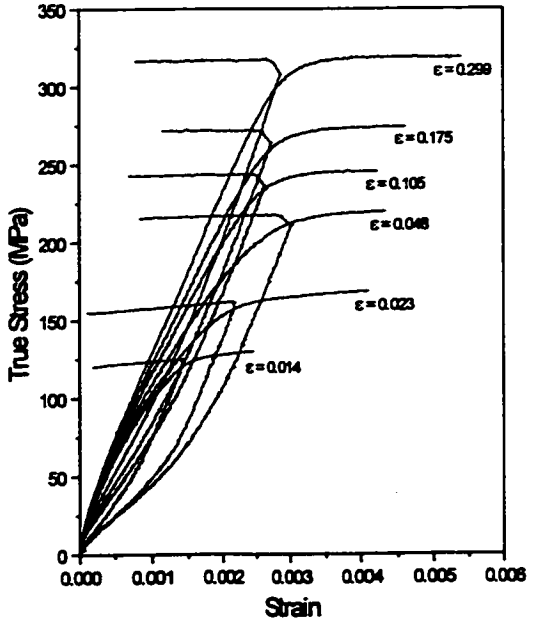

Figure 4.59 Hysteresis loops developed on loading and unloading a sample after increasing amounts of pre-strain.

was observed. Only a slight overshoot of the yield stress above the previous flow stress was observed on re-loading the sample.

Figure 4.59 gives an example of a series of loading/unloading curves obtained from a single sample as a function of tensile pre-strain. All curves have been normalized such that zero applied load corresponds to zero strain. The degree of hysteresis grows substantially as the level of pre-strain increases within the regime where fibres are loaded elastically and the matrix is deforming plastically. At pre-strains beyond the macroscopic strain corresponding to yielding of the fibres, the hysteresis is observed to decrease

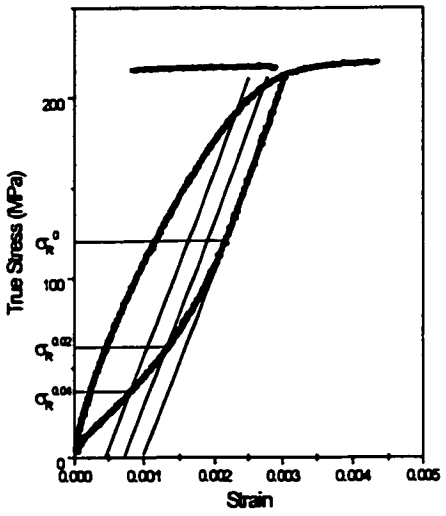

Figure 4.60 Schematic diagram illustrating method used to define the reverse flow stress, σ_R.

and saturate. In order to quantify the degree of hysteresis, the reverse flow stress was measured using different offsets, as shown in figure 4.60.

4.3.3 Microscopic Characterization of Cu-1.56at%Cr Eutectic Alloy Deformed in Uniaxial Tension

The evolution of the dislocation substructure of Cu-Cr specimens tested in uniaxial tension has been followed by means of transmission electron microscopy. In the following sections this structural evolution will be described for the Cu matrix and the Cr fibres. Further, measurements of local misorientations in the Cu surrounding Cr fibres will be discussed. Finally, interaction between Cr fibres and shear bands at high strains will be described. These observations have been made on samples solidified at 57 mm/hr and tested at 293 K. The general features presented here are similar to those observed in samples solidified at 6 mm/hr and tested at 77 K and 223K.

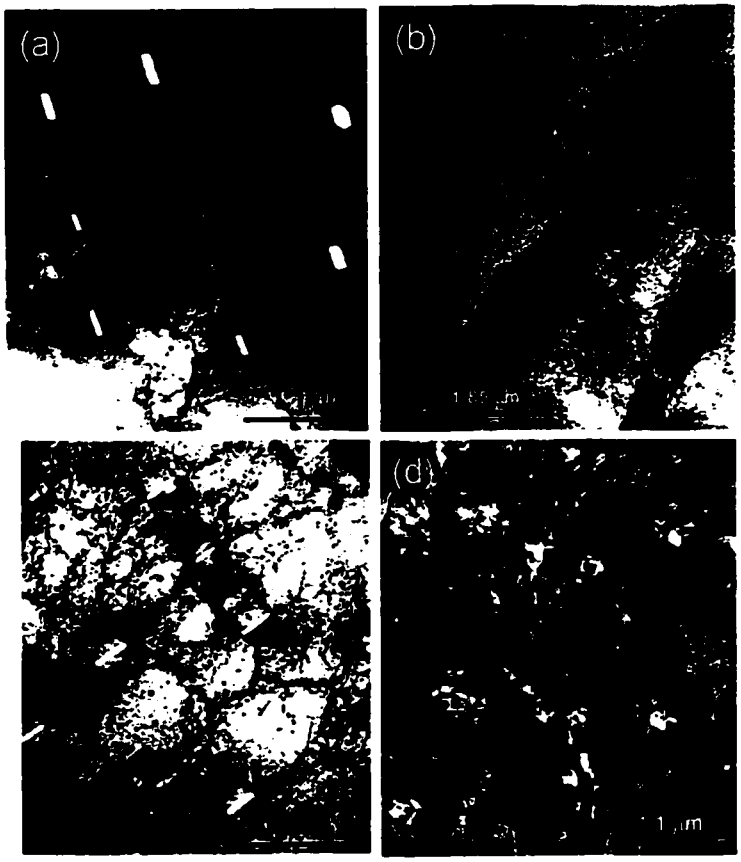

Figure 4.61 Transverse BF TEM images from samples strained a) 0.015, b) 0.12, c) 0.25, and d) 0.9, in uniaxial tension.

4.3.3.1 Development of Substructure in Cu as a Function of Strain

Figure 4.61 shows a series of transverse BF TEM micrographs taken from specimens strained various amounts. These structures will be investigated in detail below.

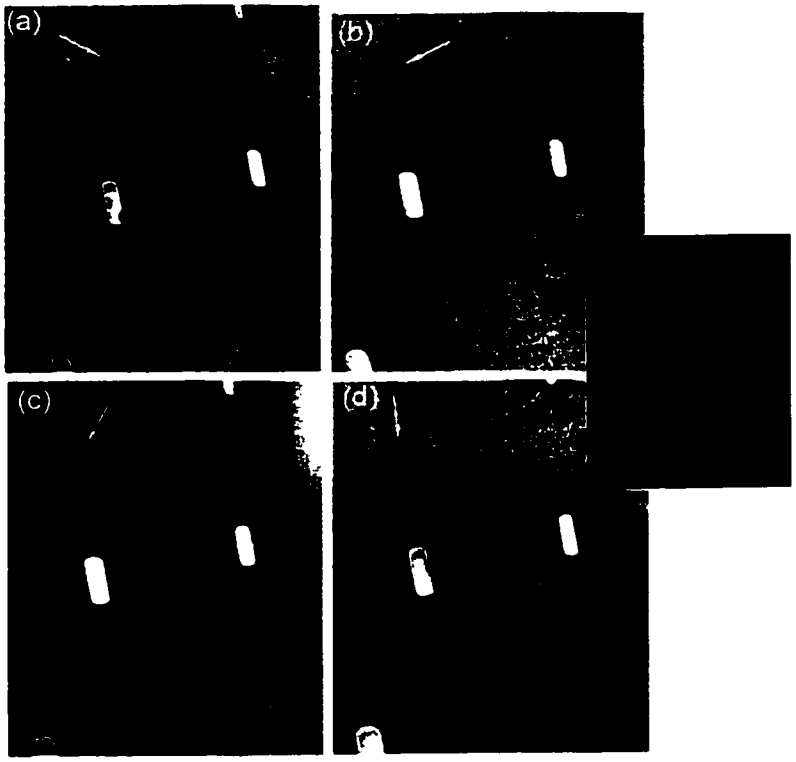

Figure 4.62 Series of two-beam BF images, ε=0.015. a) $\mathbf{g} = [002]$, b) $\mathbf{g} = [\bar{1}1\bar{1}]$, c) $\mathbf{g} = [\bar{2}20]$, d) $\mathbf{g} = [\bar{1}11]$.

At strains below the macroscopic yield point of the Cr fibres, tangles of dislocations surround the Cr fibres. Figure 4.62 shows a series of two-beam BF TEM images taken from around the same Cr fibres in a sample strained to $\varepsilon = 0.015$. From these images it can be determined that all six Burgers vectors are present around the fibres. Individual loops can not be resolved at the phase interface. At lower magnifications the background structure in the Cu is observed to contain a low density of dislocations that appear to form no particular long range pattern (figure 4.62).

Figure 4.63 shows orientation measurements made in the Cu around the fibre as indicated by the numbered positions within the micrograph. Each of these positions is associated with a Kikuchi pattern. No misorientation is observed between Cu close to the phase interface and Cu far from the interface. This is also evidenced by the fact that the orientation relationship between Cu and Cr is approximately retained at these low strains (figure 4.63).

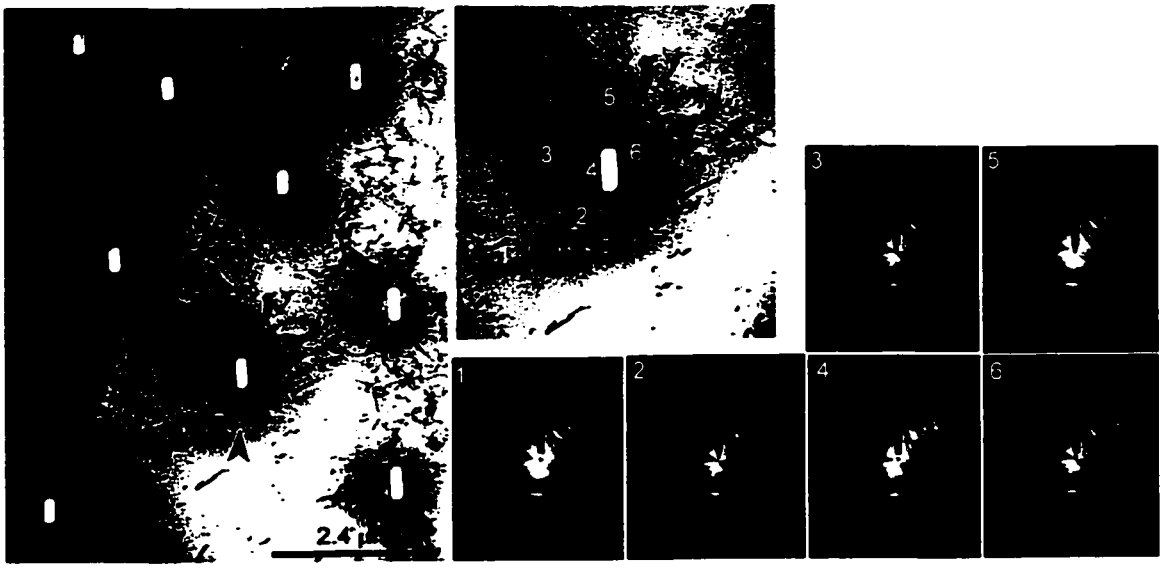

Figure 4.63 Orientation measurements made around a Cr fibre, ε=0.015. The numbers relate position of measurement and recorded Kikuchi Pattern.

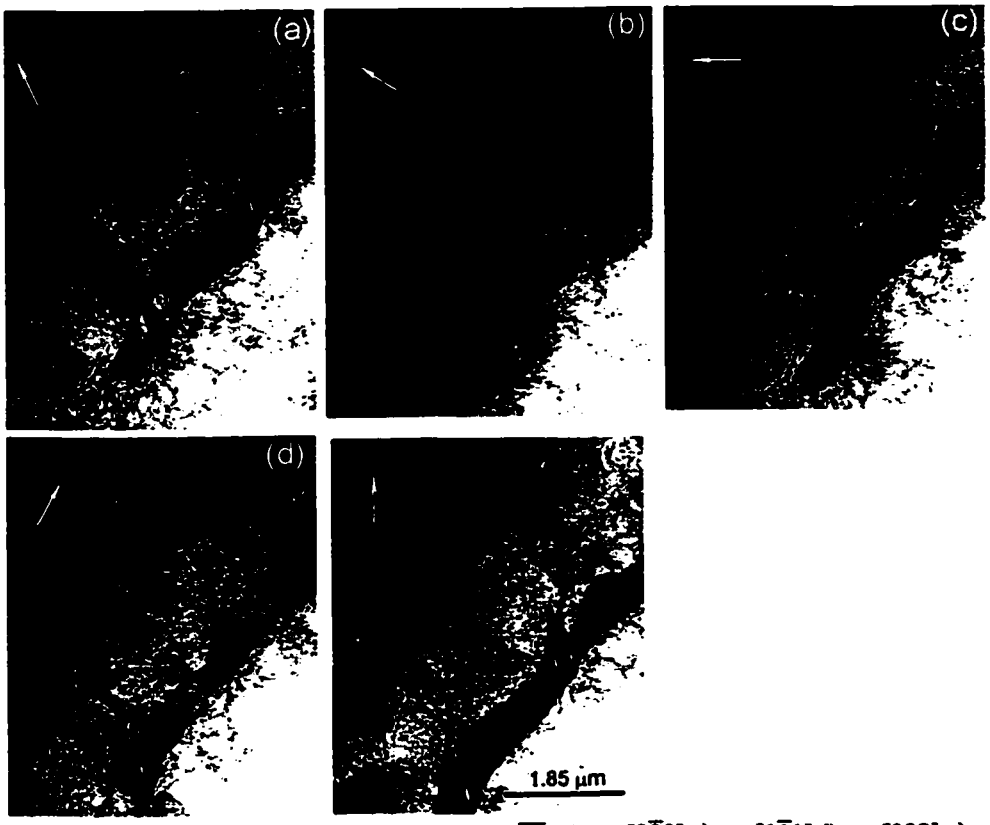

Figure 4.64 Series of two-beam images, ε=0.12. a) $\mathbf{g}=[1\bar{1}1]$ b) $\mathbf{g}=[2\bar{2}0]$ c) $\mathbf{g}=[1\bar{1}1]$ d) $\mathbf{g}=[002]$ e) $\mathbf{g}=[0\bar{2}2]$. Beam direction in a) - d) close to $[110]_{Cu}$. Beam direction in e) is close to $[111]_{Cu}$

As the level of strain was increased, a well-defined structure began to develop within the Cu. Figure 4.64 shows BF TEM images from a sample strained to 0.12. The loose tangle of dislocations surrounding the Cr fibres in the sample strained 1.5% is replaced by a structure that is roughly organized into cells. A particular structure appears to be associated with the presence of the Cr fibres.

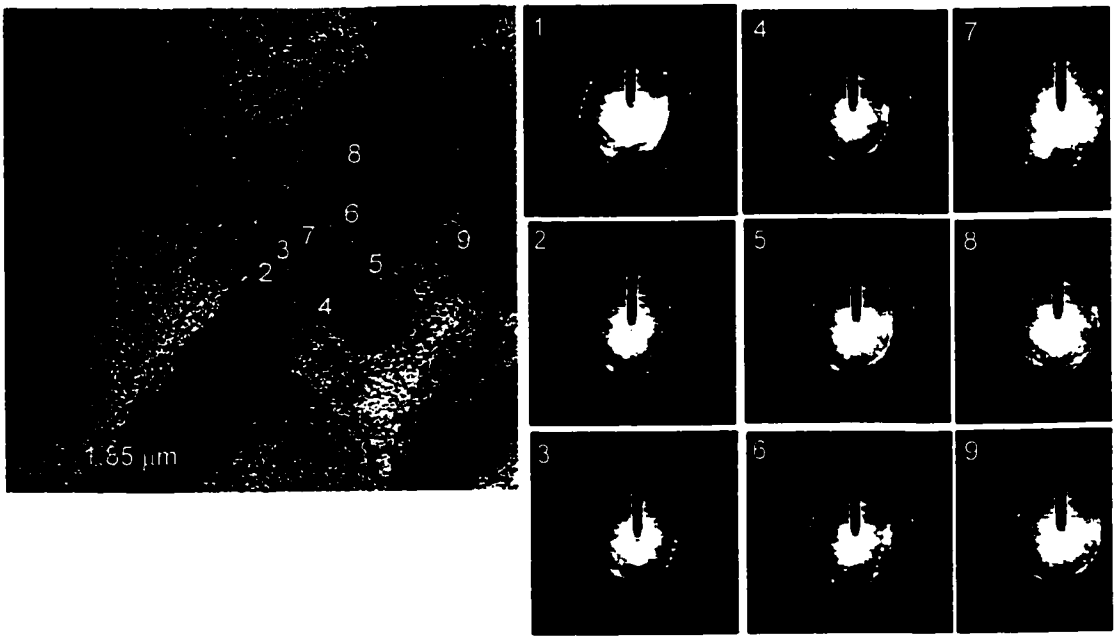

Figure 4.65 Orientation measurements made around a Cr fibre, ε=0.012.

Figure 4.65 shows the results of measurements of misorientation in the Cu surrounding a Cr fibre. As with the measurements in figure 4.63, very little misorientation is observed to be associated with the regions surrounding the Cr fibres. However, at positions close to the phase interface, small misorientations of the order of ~5° are observed.

At still higher strains, the above described dislocation structure in the Cu developed into a well-defined substructure consisting of dislocations organized into cell walls. Figure 4.66 shows a series of BF TEM micrograph taken from a sample strained to approximately 0.25. Along with the typical cell structure observed in single phase Cu samples, the banded regions connecting adjacent Cr fibres continue to persist. At lower magnifications, the structures developed around all the Cr fibres within the same region are similar.

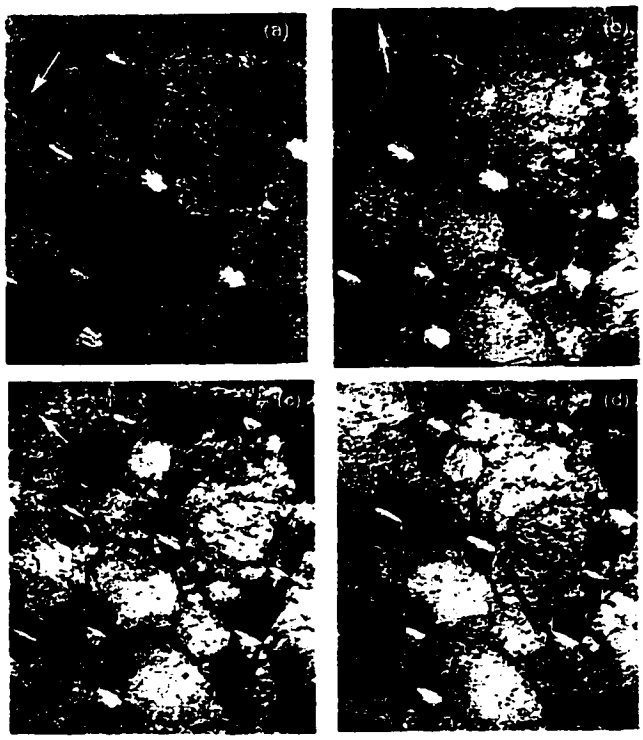

Figure 4.66 Series of two-beam BF images, ε=0.25. a) $\mathbf{g} = [1\bar{1}1]$ b) $\mathbf{g} = [\bar{2}20]$ c) $\mathbf{g} = [\bar{1}11]$ d) $\mathbf{g} = [00\bar{2}]$.

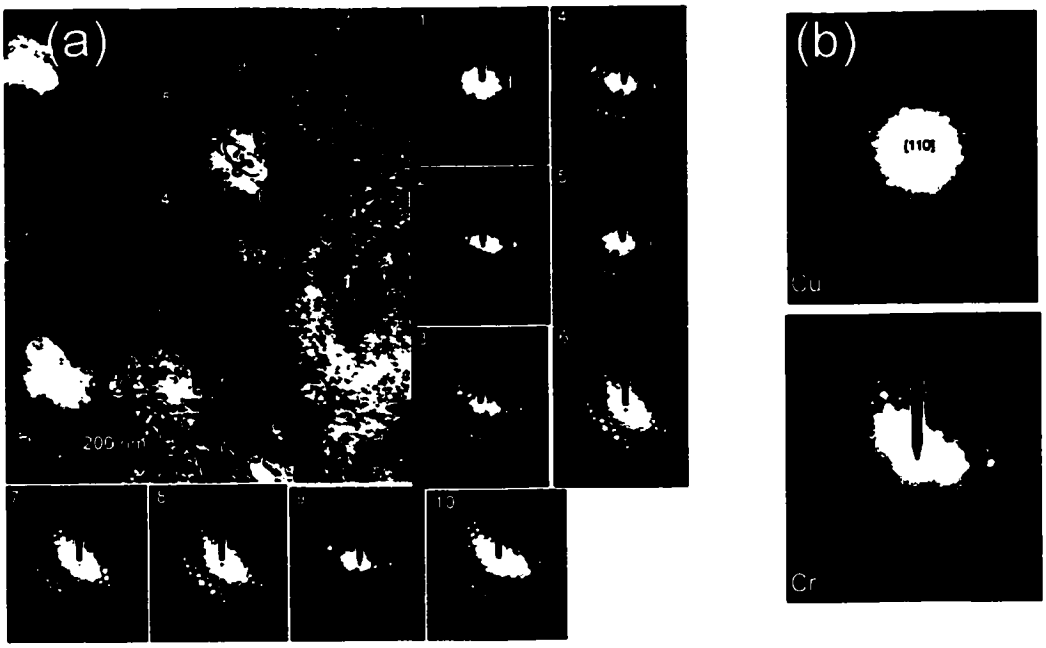

Figure 4.67 a) Orientation measurements made around a Cr fibre, ε=0.25. b) Micro-beam diffraction patterns from Cu (top) and Cr (bottom) showing that $[110]_{Cu}$ is no longer parallel to $[111]_{Cr}$.

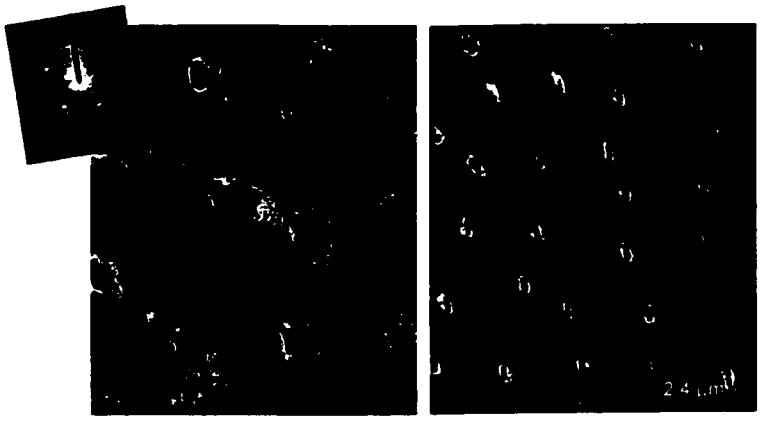

Figure 4.68 DF images showing similar orientation close to all fibres, ε=0.25.

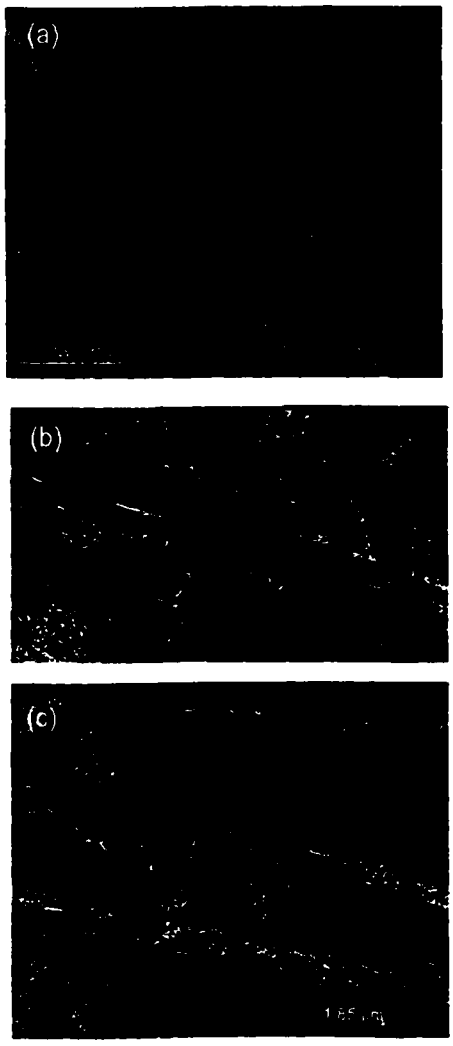

Figure 4.69 Images from longitudinal foils showing the heterogeneity of structure at the phase interface at strains of a) 0.12 b) 0.25 c) after necking.

The detailed nature of the orientation around these fibres was measured as shown in figure 4.67. Local lattice rotations are observed close to the phase interface. Although the maximum measured misorientation is only ~5°, the misorientation drops to approximately zero in less than 200nm from the phase interface. Further, the starting K-S orientation relationship between the two phases has also been destroyed (figure 4.67b). Although the misorientations are small around the fibres, the structure developed close to the interface appears to be consistent from fibre to fibre. Figure 4.68 shows a dark field image using a two-beam condition established within the region adjacent to the phase interface. All fibres show similar orientations (as evidenced by the similar contrast) at the phase interface.

Figure 4.69 shows longitudinal images from sample strained to 0.12, 0.25 and beyond necking in tension. The primary feature of the structure observed in the longitudinal foils is the relatively high density of

Figure 4.70 DF images from a) Cu and b) Cr showing the high dislocation density at the phase interface and the corresponding dislocation activity in the Cr fibre.

Figure 4.71 Transverse of BF TEM images from foil cut from neck of tensile specimen. a) Low magnification showing substructure in Cu. b) Cr fibre showing complicated morphology and dislocations.

dislocations at the phase interface. Further, one can see that the structure is heterogeneous along the length of a fibre. Regions of high dislocation density could often be associated with dislocation activity in the Cr fibre. This is illustrated in figure 4.70 which shows defects in both the Cu and Cr phases close to the phase interface.

Finally, figure 4.71 shows the structure observed in samples cut from the neck of tensile specimens. A complicated cell structure in the Cu with large misorientations between cells can be seen (e. g. inset SADP). Further, the morphology of the Cr fibres becomes complex, and in some cases dislocations are observed to thread across the fibre (figure 4.70b).

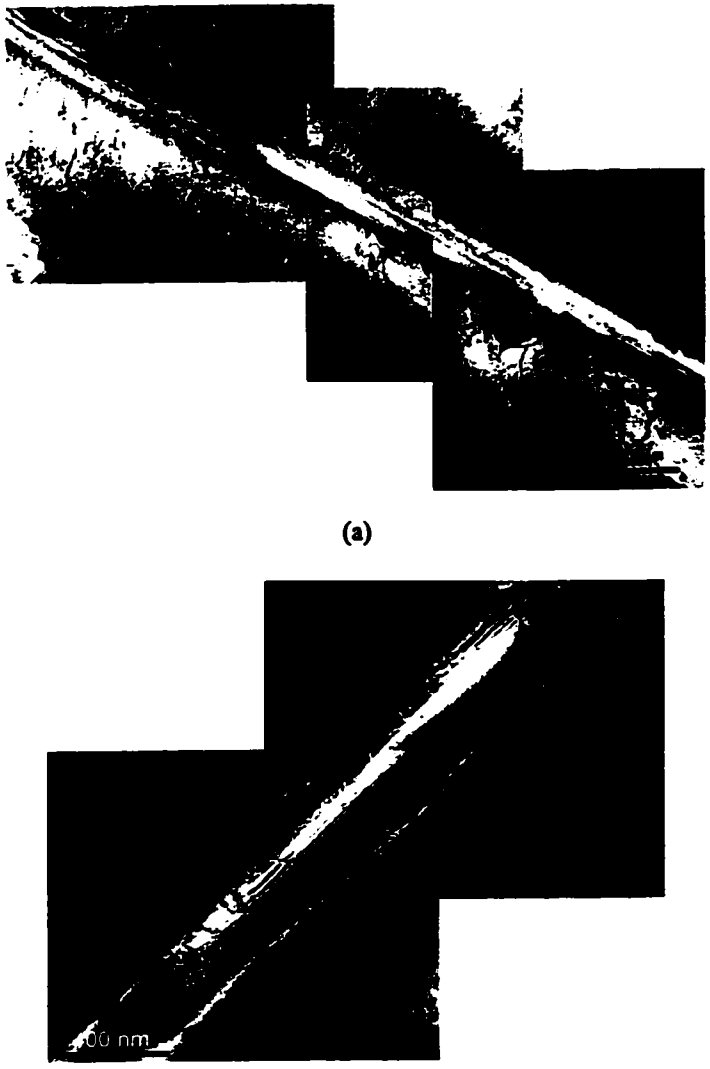

Figure 4.72 BF images of Cr fibres. a) ε=0.12, no dislocations in fibre b) ε=0.25, dislocations can be seen to be emitted from the phase interface (marked by arrows).

4.3.3.2 Observation of Dislocation Activity in Cr and its Relation to the Substructure in Cu

Dislocation activity in the Cr fibres was difficult to observe. This was largely due to the fact that, in order to view a significant length of a Cr fibre, it was necessary to prepare longitudinal foils. Longitudinal foils, however, tended to contain many fewer fibres than similar foils prepared from transverse samples.

Observations on foils cut from samples deformed just beyond the point of macroscopic yielding of the Cr showed no dislocation activity within the Cr. Figure 4.72a shows longitudinal BF TEM images from one such foil showing a representative Cr fibre. The fibre's morphology appears constant and similar to that observed in as-cast foils. No dislocations are observed within the fibre but variations in contrast along the length of the fibre suggest inhomogeneous variations in elastic stresses along the length of the fibre.

Foils cut from samples deformed to strains of the order of 0.15 - 0.2 begin to exhibit signs of dislocation

Figure 4.73 Weak beam images from Cr fibre showing dislocation loops being emitted from phase interface.

activity within the Cr fibres. Figure 4.72b shows a BF longitudinal TEM micrograph exhibiting the type of dislocation structure observed within fibres. Individual dislocations can be observed within the fibre. Each dislocation appears to have its ends embedded within the phase interface and appears to belong to the same slip

system. However, the spatial inhomogeneity in the dislocation structure is obvious since no dislocations can be observed to the left or right of the central portion of this micrograph.

A more detailed examination of fibres like that in figure 4.72b revealed a slightly more complicated structure. Figure 4.73 shows a series of weak beam images taken from the same Cr fibre. Dislocation loops are nucleated from the phase interface. These loops appear to expand into the fibre with both ends remaining in the phase interface. Burgers vector analysis of the dislocations within this region shows all dislocations to be of the same Burgers vector. It was common to observe only one or two Burgers vectors within segments of fibre several microns in length.

The general features of the dislocation structure within Cr fibres was observed to change little with straining up to the point of necking (cf. section 4.3.3.3). Also, similar structures were observed in samples tested at 77 K and in samples solidified at 6 mm/hr. The latter samples were difficult to analyze because the Cr fibres in longitudinal electropolished samples tended to be much thicker than in samples solidified at 57 mm/hr.

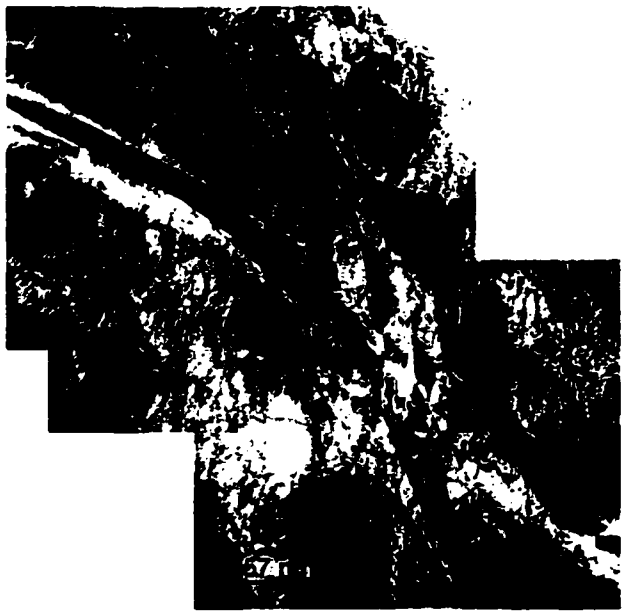

Figure 4.74 BF image showing Cr fibre sheared into shear band.

4.3.3.3 Interactions Between Shear Bands and Cr Fibres

Although the dislocation structure in the Cr fibres changed only slightly from the point of their yield to macroscopic necking, a significant change in morphology and defect content was associated with shear bands within necked portions of tensile specimen. Figure 4.74 is a low magnification micrograph taken from a longitudinal foil. This micrograph shows a Cr fibre sheared by a shear band in the Cu. Within this fibre a

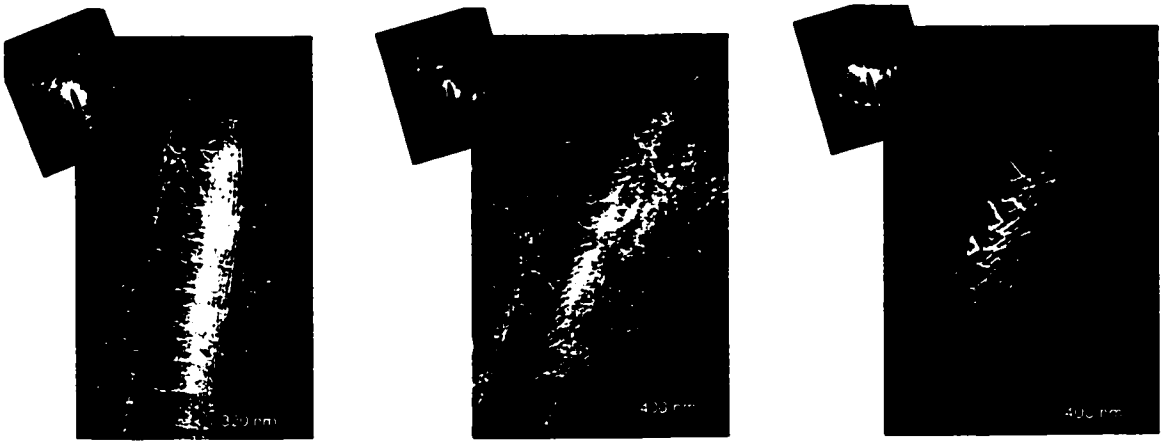

Figure 4.75 Higher magnification view of fibre shown in figure 4.74 showing dislocations in fibre at the point where the fibre is bent into the shear band.

relatively high dislocation density (compared to homogeneously deformed fibres) was observed in the region close to the point of shear band/fibre intersection. Figure 4.75 shows the structure observed in the fibre. Dislocations in this case appear to be arranged into a simple structure. Burgers vector analysis showed that most dislocations shared a common Burgers vector.

4.3.4 Characterization of Cu-1.56at%Cr Eutectic Alloy Deformed in Plane Strain Compression

4.3.4.1 Macroscopic Flow Stress and Hardness at Large Strains

In order to extend the observations on deformation behaviour to higher strains, tests were conducted in plane strain compression on samples solidified at 57 mm/hr. In all cases, plane strain compression was undertaken with the macroscopic growth axis of the sample aligned along the direction of free expansion in the channel die

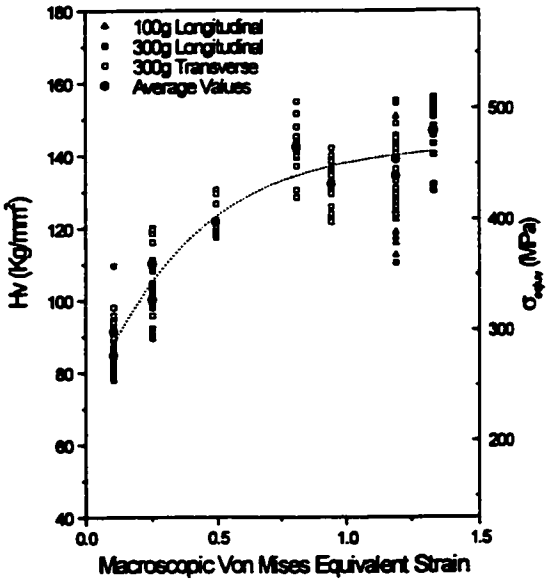

Figure 4.76 Hardness measurements on plane strain compressed Cu-Cr.

compression rig. Samples were lubricated after an imposed reduction in thickness of ~10% using both Teflon tape and Molykote lubricant as described in section 3.5.

Hardness measurements were made on samples pre-strained various amounts. Figure 4.76 shows the measured hardness on the longitudinal and transverse face of the sample (parallel to the channel) as a function of pre-strain, up to a maximum strain of 1.3. While hardness is plotted on the left hand axis of these figures, the approximate flow stress (calculated using $3\sigma = Hv$) is plotted on the right hand axis. At least 10 hardness measurements were made at each strain. All measurements were made using a 300 g load and 15s dwell time on the polished section of specimens.

4.3.4.2 Evolution of Microstructure with Imposed Strain

The morphology and scale of the microstructure has been followed as a function of pre-strain in plane strain compression. Observations of samples strained to < 0.5 indicate relatively homogeneous deformation. At strains > 0.5 two important processes begin that strongly influence continued deformation. First, due to the friction of the top and bottom platens and the decreasing height to diameter aspect ratio, the deformation becomes ever more inhomogeneous. On the macroscopic scale, this can be linked to the observed "bending" of grains at either end of the specimens when viewed in the longitudinal section. The second feature of the microstructure which develops significantly at strains > 0.5 are macroscopic shear bands. The shear bands can

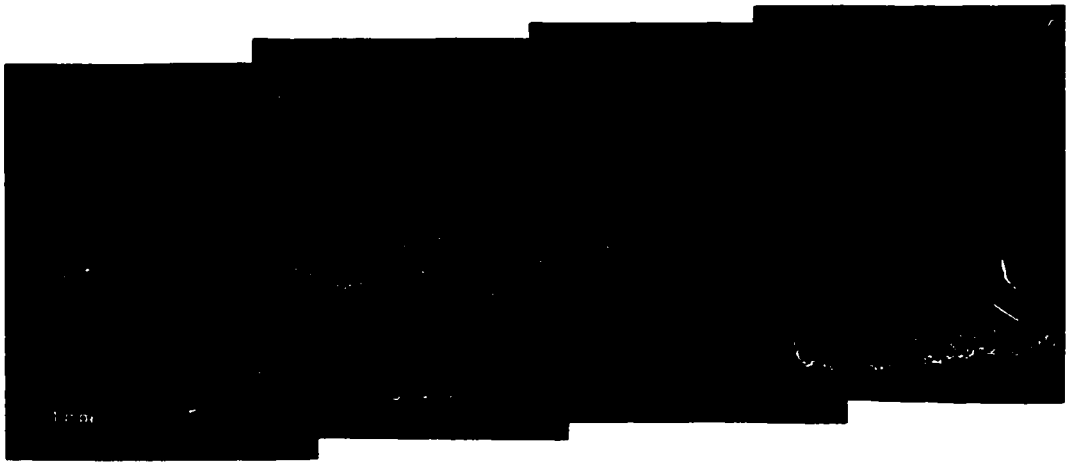

Figure 4.77 Low magnification image of a sample strained to ε=0.95 showing extensive shear banding.

be imaged clearly if polarized light is used (figure 4.77). At lower strains these shear bands can often be associated with grains near the top or bottom surface of the specimens. Shear bands in these samples tend to be isolated within single grains. At higher strains large numbers of shear bands propagated across the entire microstructure. Some are nucleated near the sample surfaces while others are located within the central region of the specimens. Typically, in a given region one set of shear bands tends to dominate the microstructure making an angle of between 50° and 35° with the direction of free expansion. However, observations over the entire longitudinal section indicate that two different sets of shear bands operate.

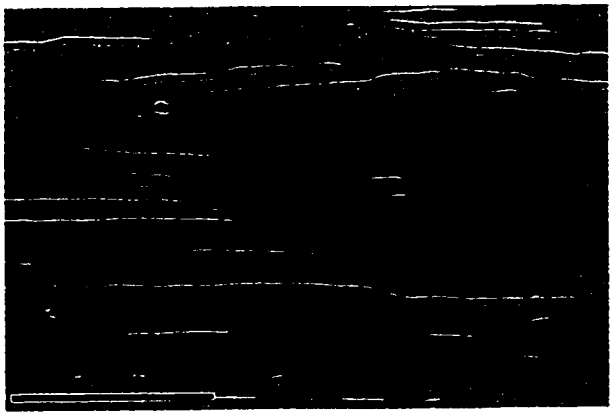

(a)

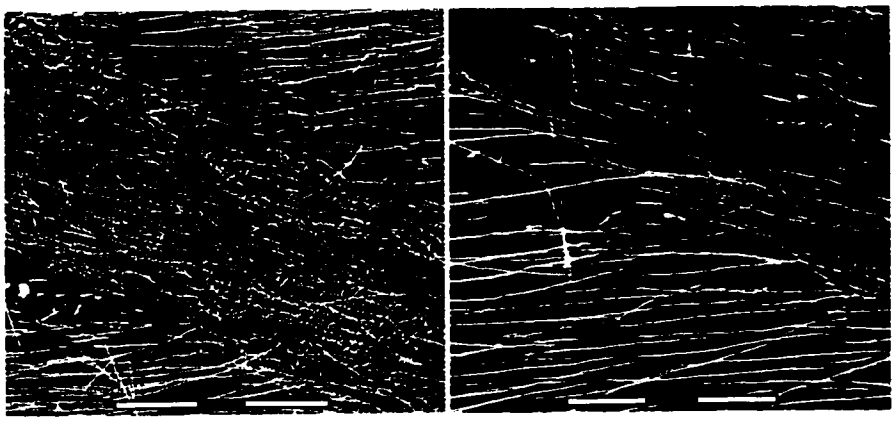

(b)

Figure 4.78 a) SEM image showing Cr fibres deformed into shear bands. b) SEM images of deep-etched specimens showing segmented fibres within shear band. Note also the fine scale of fibres within shear bands compared to those outside.

As observed with shear bands formed in uniaxial tension, the interaction between shear bands in the Cu and the Cr fibres results in the Cr fibres becoming plastically sheared parallel to the bands. Figure 4.78a shows SEM micrographs from plane strain compressed specimens showing the influence of shear bands on the Cr fibres. At imposed strains of the order of 0.9 the fibres shear into short segments which become aligned with the direction of shearing. This can be seen most clearly if the Cu matrix is etched away and the fibres exposed. Figure 4.78b shows such an etched section. The fibres have clearly been sheared into short segments within the shear band ,while outside they remain relatively long. It is also apparent that the fibre segments within this

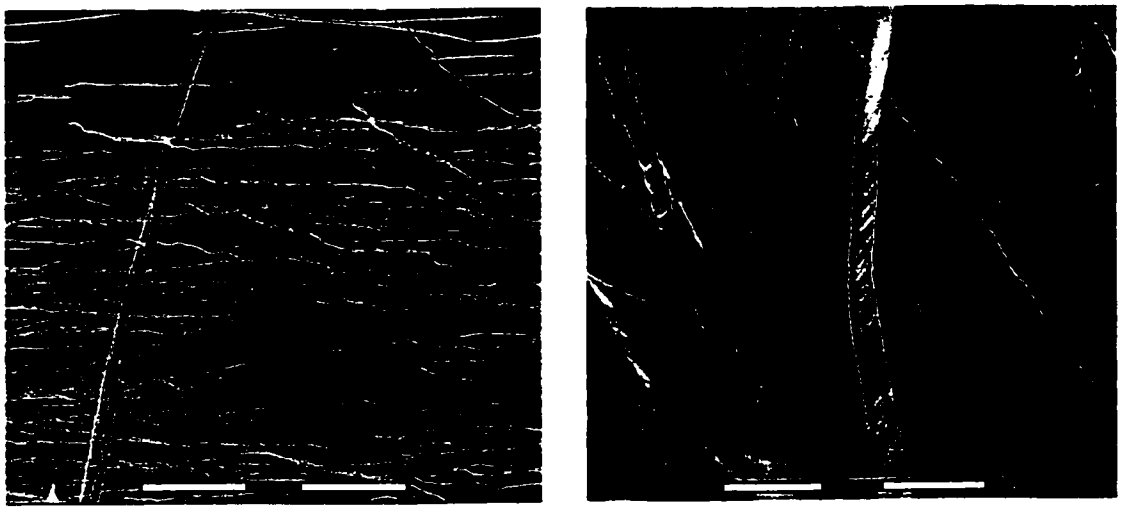

(a) (b)

Figure 4.79 Morphology of fibres after extraction from a sample strained to ε=0.95.

shear band have suffered larger strains as they are thinner in cross-section than those outside of the bands. At higher magnification extracted fibres show that the deformation at high strains is inhomogeneous (figure 4.79) even outside of shear bands. Fibres that appear very regular in morphology in the as-cast state appear inhomogeneous after large strains.

4.3.4.3 Substructure in Cu and Cr Phases at High Strains

At high strains it was found that the substructure in the Cu was similar to that which would be expected for pure Cu deformed to similar strains (Humphreys and Hatherly, 1995). Figure 4.80a shows a TEM micrograph that illustrates the substructure in Cu and a corresponding SADP taken from a sample strained to 0.95. Even in samples strained to these levels, large areas of defect-free Cr could be observed. Figure 4.80b shows a fibre that contains no dislocations after a strain of 0.95. Figure 4.81 shows a micrographs taken from a fibre extracted from a sample strained to a strain of 1.3 and placed on a holey carbon film. In general, extracted fibres showed the structure in the fibres to be very inhomogeneous with long, defect-free lengths separated by regions containing loose tangles.

Measurements of texture were attempted both using neutron diffraction and EBSD on samples rolled to a strain of 0.95. In both cases the results show that the Cu develops a strong Cu rolling texture as would be expected. It was not possible to make measurements of bulk texture on the Cr fibres but EBSD results suggest that the texture of the Cr becomes weaker with straining but does not develop a characteristic bcc rolling

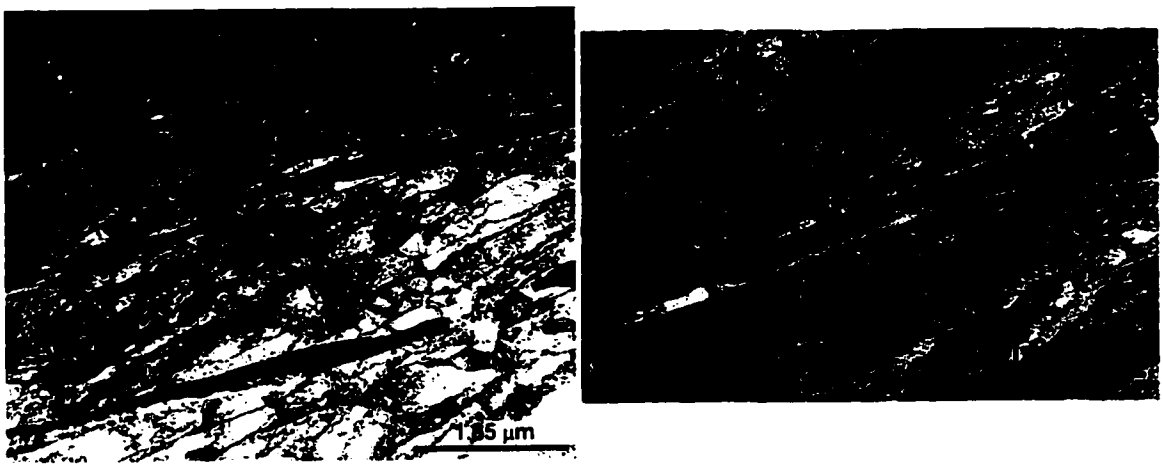

(a) (b)

Figure 4.80 a) BF TEM image for sample rolled to a strain of ~0.95 viewed parallel to the transverse direction. b) Higher magnification view showing dislocation-free fibre.

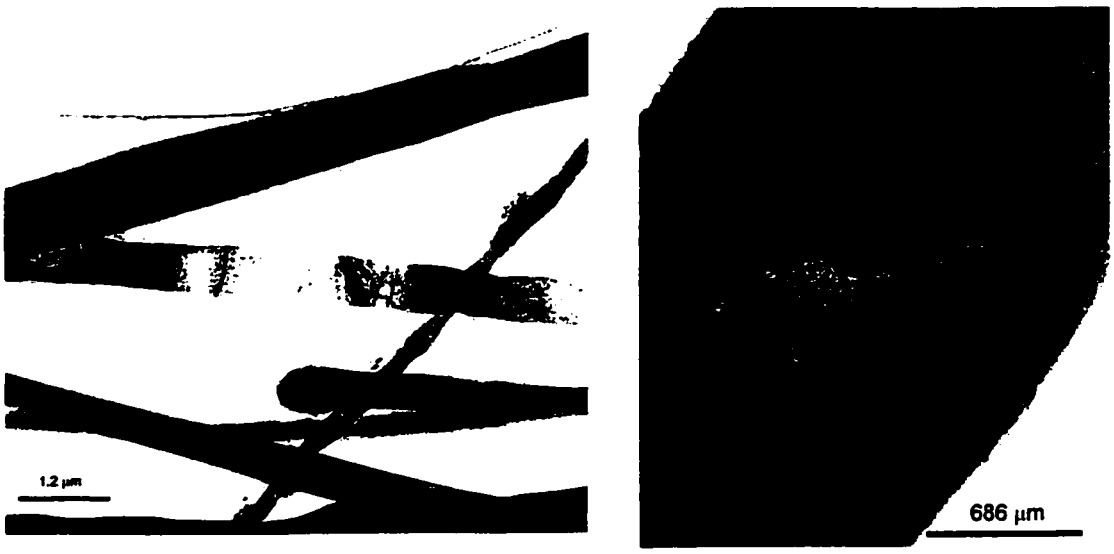

(a) (b)

Figure 4.81 BF TEM images of substructure in a fibre extracted from a sample rolled to a strain of 1.3. a) Low magnification view. b) Substructure in one portion of a fibre.

texture as would be found in similarly strained polycrystals. This will be examined further in the following chapter.

4.4 SUMMARY OF SALIENT EXPERIMENTAL RESULTS

4.4.1 As-cast Material

i. The as-cast sample has been characterized as a multicrystal composed of a nearly pure Cu matrix containing fine-scale Cr fibres which appear largely defect free. By changing the growth rate, the scale of the fibres can be changed. By decreasing the rate of solidification from 57 mm/hr to 6 mm/hr the size of the Cr fibres can be increased by approximately a factor of two.

ii. The Cu and Cr phases exhibit a strong preferred orientation relationship approximately described as Kurdjumov-Sachs. Associated with this orientation relationship, the facets on the fibres and the growth axis

may be consistently indexed. The preferred crystallography of the two phases is reflected in the strong crystallographic texture measured for the two phases.

iii. Internal stresses exist in the Cu and Cr phases due to differences in thermal contraction during solidification.

An understanding of the detailed nature of the starting crystallography of fibres and the internal stress distribution in both phases is key to understanding to processes that occur when the material is deformed. For this reason, these two aspects of the as-cast material will be focused on in the following discussion.

4.4.2 Deformation Behaviour

i. Deformation in these materials must be considered in terms of three stages of deformation: both phases deform elastically, Cu deforms plastically/Cr deforms elastically, and both phases deform plastically.

ii. All evidence points to the development of very large elastic strains during the deformation of the two phases.

iii. Detailed examination of the dislocation structure developed in the Cu as a function of tensile straining shows that it is influenced locally by the presence of Cr fibres. However, at large strains, the bulk of the specimen seems to develop a substructure similar to that observed in single phase Cu. The Cr fibres store very few dislocations even at high strains. Dislocations appear to be introduced into the Cr fibres by sources operating from the phase interface, thus resulting in an inhomogeneous distribution of the small number of dislocations that are stored.

iv. At higher strains, homogeneous deformation of the specimen gives way to inhomogeneous deformation due to the development of macroscopic shear bands. Cr fibres deform readily into these shear bands, eventually becoming sheared into short segments aligned along the direction of shearing. Shear bands limit the ductility of specimens deformed both in uniaxial tension and plane strain compression.

It is necessary in the following discussion to build a quantitative understanding of the behaviour of this material that encompasses the deformation behaviour at all levels of strain. In order to do this each stage of the macroscopic stress-strain response will be discussed in reference to the available experimental data. In particular, this discussion will focus on the inhomogeneous nature of the elastic/elastic-plastic transition marking the onset of co-deformation and the stability of plastic flow that is associated with continued plastic flow. Finally, the interaction between the process of flow localization and the presence of Cr fibres will be discussed.

5. DISCUSSION

5.1 INTRODUCTION

This chapter will discuss the salient features of the results presented in the previous chapter. First, a discussion of the as-fabricated material will be presented. This will be followed by a discussion of the mechanical response focused on the behaviour of the material up to the point of the onset of co-deformation, through the regime of stable co-deformation in tension, and to the point of tensile instability and failure.

5.2 THE AS-CAST STATE

In order to understand the deformation behaviour of this Cu-Cr eutectic alloy it is necessary to define the starting condition of the material. This section will discuss the experimental results in terms of the morphology and scale of the microstructure, the crystallography and crystallographic relationships of the Cu and Cr phases, and the thermal residual stresses present in the as-cast material.

5.2.1 Scale, Morphology and Defects in the As-cast Microstructure

It has been shown that the scale of the Cr fibres can be reduced from approximately 1.0 μm to 0.5 μm by changing the rate of crucible withdrawal from the work coil from 6 mm/hr to 57 mm/hr. The inter-fibre spacing in directionally solidified eutectics is normally found to obey the relation,

$$\lambda^2 G = \text{constant} \qquad (5.1)$$

(Zener, 1946) where λ is the inter-fibre spacing and G is the rate of solidification. Assuming regularly spaced fibres, values of 114 and 147$\mu m^3/s$ are obtained for samples solidified at 57 mm/hr and 6 mm/hr respectively. This is in relatively good agreement with values of 281 and 253$\mu m^3/s$ deduced from the work of Hertzberg and Kraft (1963).

The absence of dislocations in the as-grown Cr fibres is in accord with the observations of others on the directionally solidified Cu-Cr eutectic (Clarke and Stobbs, 1974 and Lavelle, 1987) and in other systems (e.g. Hertzberg, 1993). The defects that do exist in the Cr fibres are similar to those reported by Lavelle (1987) in directionally solidified Cu-Cr eutectic material.

5.2.2 Crystallography of the As-cast Eutectic alloy

A summary of the results of the orientation relationship, fibre growth axis, and fibre facets determined in this work are illustrated in figure 5.1. The main points to highlight from this are;

i) *Orientation Relationship*: Most fibres were observed to exhibit the K-S orientation relationship ($[110]Cu \| [111]Cr$, $[1\bar{1}1]Cu \| [1\bar{1}0]Cr$) to within ~ 1° error.

ii) *Axis of Fibres:* The axis of the fibres was relatively high index in both the Cu and Cr phases. The fibre axis was situated approximately 9° away from the common close packed directions tilted about the common close packed planes. Indexing this gives a growth axis of $[561]_{Cu}$.

iii) *Habit Planes:* Most fibres exhibited one or more (up to three) sets of well-defined habit planes. The most predominant sets have normals parallel to $[1\bar{1}1]_{Cu}$ and $[3\bar{3}5]_{Cu}$.

iv) *Interfacial Structure:* The defects in the Cu near the interface made observation of the interfacial structure difficult. The structure that was observed in the boundary appeared to consist of more than one set of Burgers vectors.

This work differs from that obtained in other studies of directionally solidified Cu-Cr eutectics in terms of the measured orientation relationship, growth axis, and predominant facets. Clarke and Stobbs (1974)

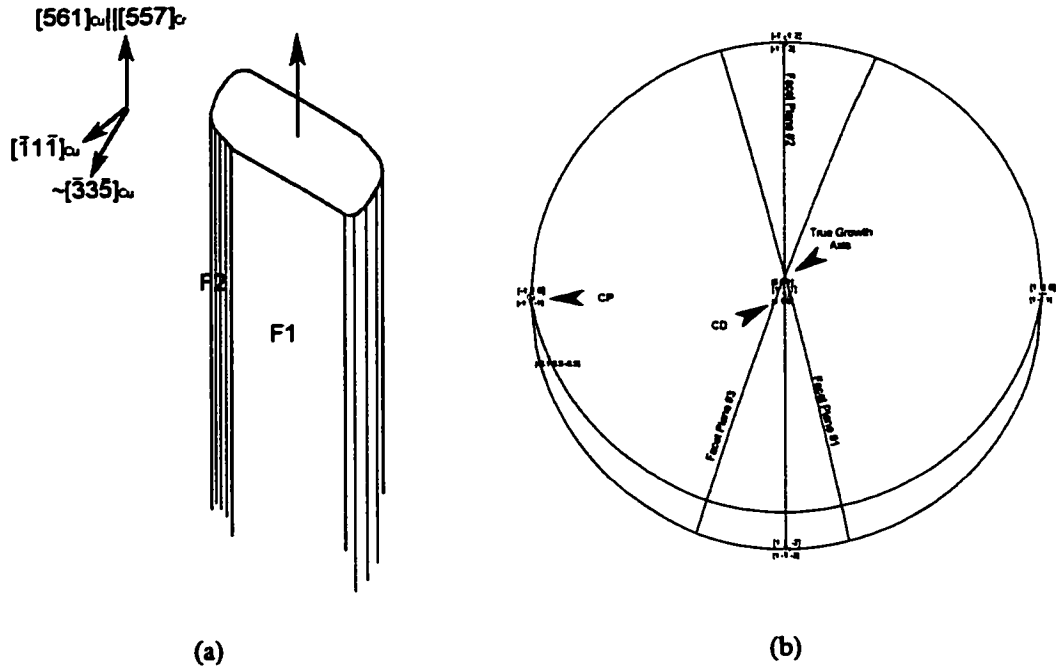

(a) (b)

Figure 5.1 a) Schematic illustrating the geometry and crystallography of a typical Cr fibre. F1 and F2 are the two most prominent facets observed on fibres. b) Stereographic projection further illustrating the crystallographic relationship between the two phases. The growth direction is oriented approximately 9° away from the common close packed directions within the common close packed planes.

reported Cr fibres with a (transverse) appearance very similar to those found in this study. The growth axis was determined in this work to be close to $<111>_{Cr}||<110>_{Cu}$, while the predominant facet was indexed as $<211>_{Cu}$. Although the results of this work could be described in terms of variants of K-S with a wide statistical scatter, Clarke and Stobbs found that the scatter could be reduced if the results were separated into two different orientation relationships; the exact Kurdjumov-Sachs relationship and an inverse Nishiyama-Wassermann relationship given by,

$$\begin{aligned}&[111]_{Cr}||[0\bar{1}1]_{Cu}\\&[\bar{1}01]_{Cr}||[100]_{Cu}\\&[1\bar{2}1]_{Cr}||[011]_{Cu}\end{aligned} \quad (5.2)$$

The work of Lavelle (1987) found this to be the principle orientation relationship between fibres and matrix, but also found a wide variety of fibre morphologies, facets, and growth axes.

The results found in this work bare more resemblance to the careful work carried out recently on the crystallography of solid state precipitation in the Cu-Cr system (Weatherly et al., 1979, Luo et al., 1994 and 1998, and Fujii et al., 2000). The observation that the axial view of the Cr fibres occurred when the foil was tilted approximately 9° from the common directions about the normal to the common planes is consistent with the measurements of both Weatherly et al. (1979) and Luo et al. (1994). The axis in this case may be indexed approximately as $[561]_{Cu}$. Further, the measurements given in tables 4.4 of angles between habit plane normals and common close packed planes are in exact agreement with those made by Luo et al. (1994). This indicates that two predominant facets may be indexed as $(\overline{3.1}\ 3.5\ \overline{5.5})$Cu and $(1\bar{1}1)$Cu.

The results of the crystallographic analysis on solid state Cr precipitates in Cu has been shown to obey the predictions of the invariant line strain model (Luo et al. 1994, 1998). The basis for this model is associated with the idea of a transformation strain that may be used to transform one lattice (e.g. the fcc lattice) into the second (e.g. the bcc phase) (Dahmen, 1981a, 1981b, 1982, Weatherly and Zhang, 1994). In fcc/bcc systems this transformation may occur through the Bain strain, normally associated with the martensitic transformation in Fe. Dahmen (1981b) suggested that a precipitate will attempt to minimize its energy by selecting a transformation that gives a boundary between phases that contains directions of good fit. It is possible to achieve this by applying a transformation strain modified from the Bain strain by rigid body rotations about the principle axes, such that the close packed planes are brought into parallelism and one direction remains both unextended and unrotated after the transformation. This direction is the invariant line and the transformation strain which produces the invariant line, an invariant line strain. The process of applying an invariant line strain to produce a precipitate results in the prediction of a particular orientation relationship between phases. For the Cu-Cr system, the invariant line is found when the orientation relationship is a slightly modified version of Kurdjumov-Sachs, where the close packed directions ($[110]_{Cu}$, $[111]_{Cr}$) are misoriented from perfect coincidence by 0.5°. Further, it is predicted that the invariant line direction for Cu-Cr is 0.14° from a $[561]_{Cu}$ direction. Predictions of preferred habit planes based on the extension of this analysis (Luo et al., 1994) matches the experimental observations to within $\pm 1°$.

It is interesting to note that the crystallographic analysis of eutectic phases in directionally solidified materials and solid state precipitates in similar systems have developed quite independently. Preferred orientation of eutectic phases in directionally solidified materials has been long known (e.g. see Hogan et al., 1971) and has been associated with the material "seeking out" conditions in which the solid-solid interface is of low energy (Hertzberg, 1993). The results of this work suggest that this is the case for directionally solidified Cu-Cr at both rates of solidification studied here. The significant differences in the analysis presented here and that presented by Clarke and Stobbs and Lavelle is, however, somewhat surprising. The results of Clarke and Stobbs are considered more reliable than those of Lavelle, since the latter focused on fibres with complex morphologies and defects and did not describe the exact method by which orientation determinations were made. The fibre axis being parallel to the close packed directions could be quite easy to wrongly identify if the true axis was $[561]_{Cu}$ due to the relative proximity of these two orientations. Further, the predominant habit plane of $(112)_{Cu}$ is most likely the $\{112\}_{Cu}$ located ~5° from the $\{335\}_{Cu}$ reported here as the predominant facet on the fibres. Although the accuracy of the technique employed by Clarke and Stobbs was reported to give results to within ~2°, some alternative sources of error can be suggested. First, the authors allude to the fact that there was a high density of dislocations present in the Cu surrounding the fibres. The presence of a high density of dislocations at the phase interface makes exact determination of the axial condition for the fibres quite difficult. Also, it is possible that local rotations around the fibres may have been produced by the local dislocation density, thereby reducing the accuracy of the determination of the orientation relationship. This would be consistent with the wide scatter in orientation relationships measured. These factors could lead to erroneous measurements to within a range consistent with the difference between these results, the results presented here and the results presented on solid state precipitates.

A final possibility for the differences in reported crystallography of directionally solidified eutectic also exists. Although the most recent work on solid state precipitates (discussed above) suggests a single preferred orientation relationship, and a small number of reproducible habit planes, earlier studies (Hall et al., 1972, 1986, Weatherly et al., 1979) found a range of fibre axes and orientation relationships. Dahmen et al. (1988) have attributed this variation to the method of heat treating to produce the precipitates. Quenching and aging

tends to result in consistent results while cooling from the solutionizing temperature to the precipitation temperature directly, tends to lead to variable orientation relationships and growth axes. It is possible that differences in the route of production of the eutectic material, as well as in the purity of the precursor material (Luo et al., 1991) may significantly affect the proportion and type of orientation relationships.

Finally, it is significant in the context of understanding the deformation behaviour of this material to examine the interfacial structure of the Cu and Cr phases. As was shown in figure 4.20, a relatively high density of dislocations exist adjacent to the phase interface in the as-cast material. The interaction of these dislocations with the phase interface appear to modify its appearance compared to that observed in solid state precipitates. In materials that exhibit a growth direction parallel to an invariant line, a series of parallel misfit dislocations are predicted to exist in the phase interface running parallel to the invariant line direction (Luo et al., 1994). These are probably the defects seen in the interface in figure 4.20e. However, due to the dislocations surrounding the fibres in this case, other defects are also observed in the interface. In figure 4.19 a series of dislocations running approximately perpendicular to the fibre axis exist at the boundary. Although it was not possible to determine the Burgers vectors of these defects, they would be consistent with dislocations lying on one of three possible Cu slip planes. The interface structure in these samples is thus quite complicated even prior to imposed deformation.

5.2.3 Thermal Residual Stresses and Plastic Relaxation

The high density of dislocations surrounding the Cr fibres in as-cast specimens may arise from the relief of residual stresses developed during solidification. To clarify the results tabulated in table 4.2, the data is plotted as the elastic lattice strain as a function of angle from the macroscopic axis of the sample in figure 5.2a. These lattice strains arise from differential contraction of the two phases during cooling after solidification. The magnitude of the shape misfit that arises between the two phases on cooling is given by

$$\varepsilon^{T^*} = \left(\alpha_m - \alpha_f\right)\Delta T \qquad (5.3)$$

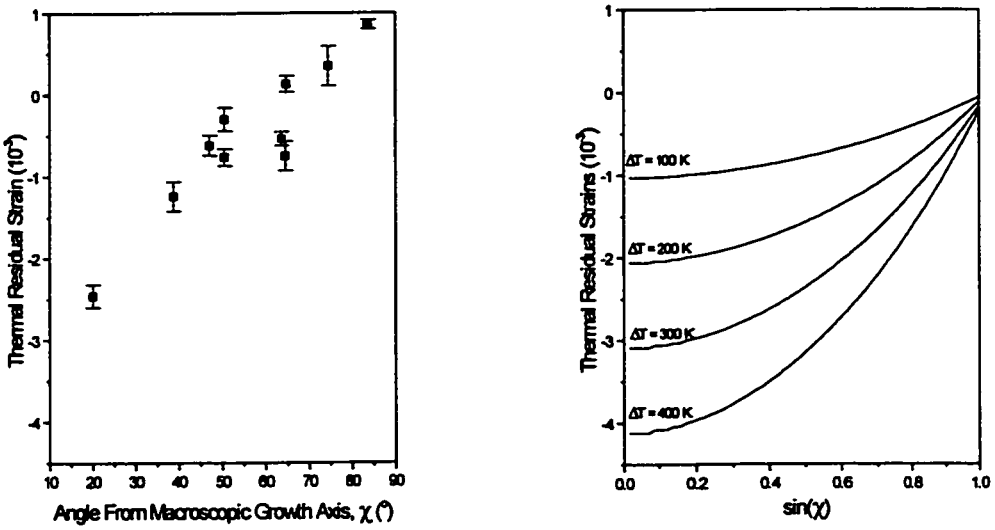

Figure 5.2 a) Measured thermal residual strains in Cr fibres in as-cast samples as a function of angle from angle of measurement from the macroscopic growth axis. b) Simple Eshelby calculation for the normal thermal residual strains for different temperature drops assuming fibres aligned with the macroscopic growth axis. No relaxation in the matrix.

where α_m and α_f are the coefficient of thermal expansion for the matrix and fibre and ΔT is the temperature change. Cooling in this case occurs from the solidification temperature to 293 K. However, over some portion of this temperature drop, the matrix will be able to alleviate the differential contraction by diffusion and/or creep. Below a critical temperature, these processes will become ineffective and another means of relaxation must be sought out. Plastic deformation of the matrix is the most likely alternative. In the case of very long, stiff fibres with a coefficient of thermal expansion lower than the matrix, large compressive elastic strains will accumulate along the fibre length. Smaller compressive strains will develop in the transverse direction. This is easily observed if Eshelby's equivalent inclusion method is used to calculate the full strain tensor resulting from a temperature drop ΔT. The equation that relates the strain (dilation) resulting from a temperature drop is given by (clyne and Withers, 1993)

$$\langle \varepsilon \rangle_M = f(S-I)\left[\left(C_M - C_F\right)\left[S - f(S-I)\right] - C_M\right]^{-1} C_F \varepsilon^{T^*} \qquad (5.4)$$

Table 5.1 Material Properties used in the Calculation of Thermal Residual Strains via the Eshelby Method

	Young's Modulus, E	Poisson's Ratio, ν	Coefficient of Thermal Expansion, α
Cu	130 GPa [a]	0.369 [a]	16.5 με/K [b]
Cr	255 GPa [a]	0.186 [a]	6.2 με/K [b]

a Hirth and Loethe, 1986.
b ASM Handbook, 1990.

Where C_m and C_f are the stiffness tensors for matrix and fibre, and S is the Eshelby tensor. Using the data given in table 5.1 and the tabulated values for the entries in S for infinitely long fibres (Clyne and Withers, 1993) gives the results shown in figure 5.2b.

In order to compare with the measured lattice strains, the data is plotted as normal strains as a function of the angle from the fibre axis.

Figures 5.2 a and b show that the trend predicted for the lattice strains (figure 5.2b) is similar to the trend in the measured data (figure 5.2a). However, the unrelaxed model always predicts compressive strains in the transverse direction while the measured data shows tensile strains in this direction. One possible reason for this contradiction may arise from plastic relaxation in the matrix.

Dunand and Mortensen (1991a, 1991b, 1991c) have described a number of potential mechanisms by which plastic relaxation may relax thermal residual stresses in fibre reinforced materials. In the current situation, the fibre axis lies nearly parallel to a matrix slip system. Thus, one method for relaxing the large thermal residual stresses along the axis of the fibre would be to punch dislocation loops from the ends of the fibre. The number of loops necessary to completely relax the axial stresses would be

$$n = \frac{\varepsilon L}{b} \qquad (5.5)$$

where L is the fibre length. As the fibre becomes very long this mechanism becomes more difficult owing to the large number of loops that must be punched (Dunand and Mortensen,1991a). Similarly, the smaller transverse thermal residual stresses may be relaxed by slip on a system transverse to the fibre direction. However, slip will generally occur on more than just these systems. Relaxation may occur by slip on systems

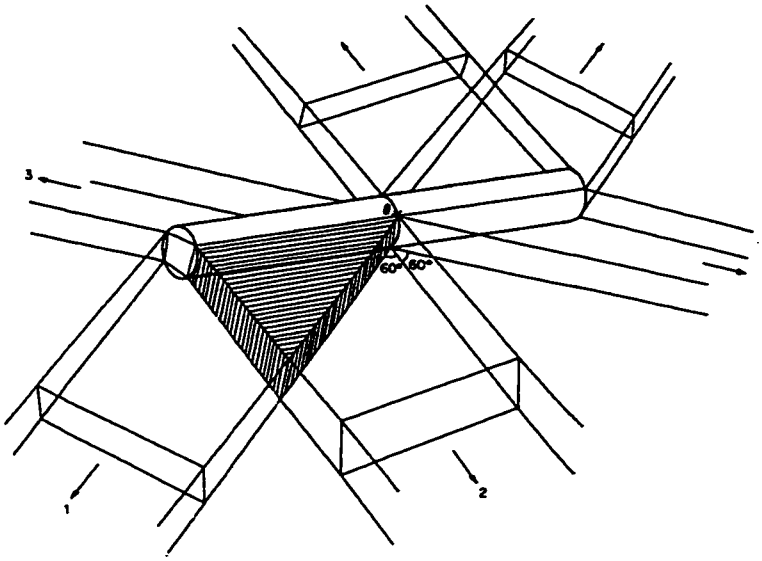

Figure 5.3 Punching of non-isoaxial prismatic loops from the sides of a fibre to relax thermal residual stresses (Dunand and Mortensen, 1991b).

oriented at an angle to the fibre axis (figure 5.3). In this case, each loop punched form the interface will give rise to a displacement $b\cos\theta$ parallel to the fibre axis, and $b\sin\theta$ perpendicular to the fibre axis. Because of the differences in longitudinal and transverse thermal residual stresses, this process may continue beyond the point where the transverse fibre stresses have been reduced to zero. Thus, in order to continue to reduce the longitudinal thermal residual stresses the transverse stresses will become tensile.

In the current situation slip may occur on two symmetrically disposed slip planes in the matrix oriented ~55° from the fibre axis. Equivalent slip on these two systems will give rise to relaxation along the fibre axis and one transverse direction, resulting in a non-axisymmetric strain distribution in the transverse plane. Accounting for slip on these two symmetrically disposed systems in the Eshelby equation gives the results shown in figure 5.4. The best fit of this model to the experimental data occurs for a temperature drop of 300 K and a strain of 5×10^{-6} on the two slip systems.

Up to this point, it has been implicitly assumed that the experimental measurements in figure 5.2a could be associated with fibres aligned directly along the macroscopic growth axis. The orientation of the two ideal families of grains shown in figure 4.13 suggests, however, that the angle between the closest $[111]_{Cr}$ and the

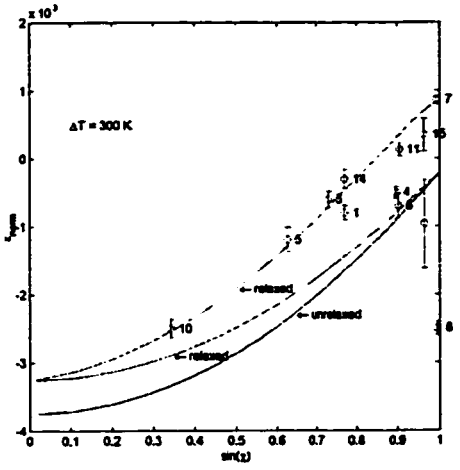

Figure 5.4 Comparison of experimentally measured thermal residual strains in Cr with models assuming no plastic relaxation in the matrix and plastic relaxation by prismatic punching. Numbers correspond to data in Table 4.2.

macroscopic growth axis was ~17° for the two families. This simply shifts the predicted curves left or right and does not change the maximum/minimum predicted thermal residual stress or the overall shape of the curves.

The relaxation of the thermal residual stresses in the Cr fibres by plastic flow from the phase interface is consistent with the picture that is obtained via electron microscopy. Figure 4.20 illustrates the typical structure observed to surround the fibres when the as-cast material is viewed in transverse sections. It is clear that some form of plastic relaxation

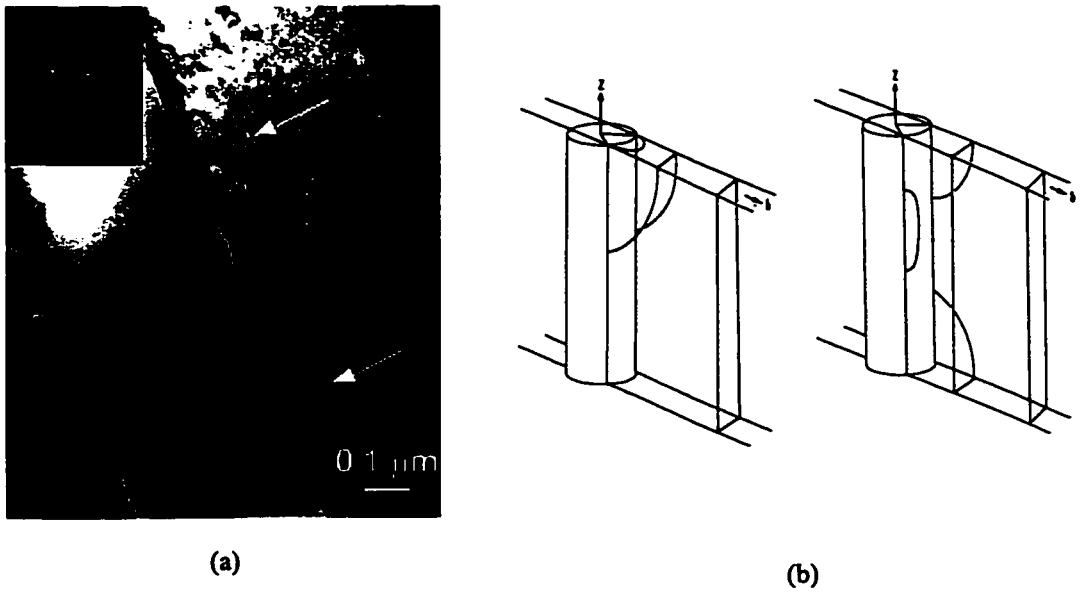

(a) (b)

Figure 5.5 a) Dislocation loops emitted from phase interface viewed in as-cast longitudinal TEM foil. b) Possible mechanisms for punching of prismatic loops from the sides of a fiber (Dunand and Mortensen, 1991b).

takes place at the phase interface, although due to the complicated nature of the structure (all possible Burgers vectors are present) it is difficult to decide on a single mechanism. Observation of longitudinal foils provides a somewhat simpler picture. Figure 5.5a shows the interface observed in an as-cast longitudinal foil. Dislocation (shear) loops can be seen still partially embedded within the phase interface. These loops are bowing out of the interface and into the matrix (marked by arrows). These shear loops may be the precursor to prismatic loops. Figure 5.5b shows a possible mechanism for punching prismatic loops from the interface of fibres. Here, a glide loop is nucleated out of the interface. Screw segments then cross-slip until the end of the fibre is reached, or some obstacle is encountered.

5.3 Deformation Response of the Cu-Cr Eutectic Alloy in Uniaxial Tension

The above discussion illustrates that the Cu-Cr system represents a well-characterized starting system for examining the co-deformation of two-phase materials. In discussing the mechanical response of directionally solidified Cu-Cr a comprehensive approach will be adopted. The macroscopic mechanical response of the composite will be related to the in-situ behaviour of the individual phases as deduced from observations of the microscopic mechanisms that operate in each phase during deformation. Following a brief discussion of general issues influencing all stages of deformation in the Cu-Cr system, a detailed analysis of the specific stages of deformation will be made. In order to accomplish this, the discussion will be separated into sections related to the deformation behaviour in uniaxial tension. These sections are,

i) *The Behaviour of the Material at Low Strains:* This section will deal with the behaviour of the material during the elastic/elastic regime, the elastic/plastic regime, and the transition to the plastic/plastic (co-deformation) regime. During these regimes (up to strains of ~0.05), the most important factor contributing to the overall mechanical response will be shown to be due to direct load transfer to the Cr fibres.

ii) *Continued Co-deformation Beyond the Plastic/Plastic Transition:* Within this regime of deformation (from strains of ~ 0.05 to 0.5), it will be shown that the Cr fibres continue to influence the overall mechanical response, but by means of a slightly different mechanism than at low strains.

iii) *Stability of Plastic Flow and Large Strain Behaviour:* Of particular relevance is the interaction between fibres and macroscopic shear bands. The discussion will also aim to link the results on the high strain behaviour of the Cu-Cr alloys to the behaviour of other heavily deformed two-phase materials.

5.3.1 Preliminary Issues

5.3.1.1 Differentiating Strengthening Mechanisms from Experimental Techniques Employed

Overall, it has been the aim of this work to deduce the mechanisms that operate to give the observed mechanical response of the directionally solidified Cu-Cr. In order to do this it is necessary to be able to clarify mechanisms that operate to change the mechanical response of the material. In particular it is necessary to be able to separate effects due to changes in the flow behaviour of the Cu due to the presence of the Cr fibres and direct loading of the Cr fibres.

This is made difficult because of a number of factors, including the low volume fraction of fibres, the difficulty in obtaining a direct measure of the in-situ response of the fibres and matrix separately, and the interaction of the fine-scale fibres with the detailed local mechanisms of deformation in the Cu. In an attempt to separate the various possible mechanisms for deformation in this material a number of experimental techniques have been used. These include,

i) *Methods Aimed at Deducing the Level of Internal Stresses:* This has primarily been carried out by measurements of the reverse yielding behaviour on unloading of tensile specimens as well as by inferences made from elastic strains made on Cu during neutron diffraction experiments. In the first case, some comments regarding the level of internal stresses can be made by examining the asymmetry of the flow behaviour in tension and compression. Although , as discussed in chapter 2, it is ideal to make measurements when the forward and reverse flow curves become parallel this is impossible for large tensile pre-strains. Thus

the measurements here include the effects of local stresses and the possible instability of the substructure to reverse deformation. In the case of neutron diffraction, by examining the variation of the measured elastic strains with respect to the applied stresses a direct measure of the degree of load transfer between phases can be made.

ii) *Methods Aimed at Understanding the Substructure Development in Cu and Cr Phases:* Transmission electron microscopy was the primary means of deducing the substructure developed within the two phases as a function of strain. This technique suffers in this case because reverse plastic flow occurs prior to unloading of the specimens. Thus, the structure developed under load will not be the same as the one observed in post mortem TEM foils. This technique, does, however allow for some general comments to be made. Cottrell-Stokes tests (Cottrell and Stokes, 1955) were also carried out and the results compared to the behaviour of pure Cu specimens. This technique allows testing of the nature of the structure developed with straining and whether the nature of the structure changes with increased straining.

In combination with the above mentioned techniques, the complementary observations of the scale, morphology and defect structure in pre-deformed samples will be correlated with the above measurements and the macroscopically observed mechanical behaviour of the material.

5.3.1.2 Crystallographic Texture and its Influence on the Mechanical Response of Directionally Solidified Cu-Cr

Crystallographic texture influences both the elastic and plastic response of anisotropic materials. Normally, the effect of texture on the behaviour of tensile tested as-cast polycrystals is relatively small due to the nearly random distribution of the orientation of grains. However, due to the high degree of crystallographic texture observed in the directionally solidified materials studied here, a significant influence on the mechanical response of the material is to be expected. Therefore, before presenting a detailed analysis of the mechanical response of this material, the influence of the observed texture will be discussed.

Figure 4.8 shows representative Cu pole figures from a sample solidified at 57 mm/hr. The strong <110> component located along the macroscopic growth axis of the sample can be understood in relation to

the crystallographic relationship between Cu and Cr discussed above. A first order approximation would describe the Cu as having a <110> direction oriented approximately along the tensile axis, a fact that can be rationalized quite easily with reference to the crystallographic relationship found between Cu and Cr. However, in the transverse plane the sample is also observed to be strongly oriented, resulting in a spotty texture that appears to result from a finite number of grain orientations. The fact that the grains do not solidify to produce every orientation about the <110> growth axis probably reflects a process of orientation selection from the melt that depends on the orientation of the grains at the liquid/solid interface. To a first order approximation we can consider (at least when examining the effect of texture) that the material is made of a small number of grain orientations with the same crystallographic direction along the macroscopic growth axis, with only a few different rotations about that axis.

One of the features of the observed deformation behaviour that can be explained via the macroscopic texture is the development of an elliptical cross-section after plastic deformation. When deformed in uniaxial tension, randomly oriented polycrystals of cubic metals are observed to deform in such a manner that the cross-section reduces equally about the circumference thereby resulting in axisymmetric deformation. Thus, when describing the strain path associated with uniaxial tension the approximation

$$\frac{1}{2}d\varepsilon_z = -d\varepsilon_x = -d\varepsilon_y \quad (Z \,||\, tensile\ axis) \qquad (5.6)$$

is normally obeyed. However, figure 4.35 shows that this does not hold for the deformation of samples tested here. Instead of reducing equally about its circumference (as equation 5.6 requires), the samples develop an elliptical cross-section, the degree of ellipticity increasing with increasing strain. The source of this anisotropy can be envisioned quite easily if one imagines the ideal case of a single crystal oriented with [110] along the tensile axis (figure 5.6a). For the typical case of <110>{111} slip for fcc crystals, this orientation results in four equally stressed systems; $(111)[10\bar{1}]$, $(111)[01\bar{1}]$, $(11\bar{1})[101]$, $(11\bar{1})[011]$. The other eight systems experience no resolved shear stress as the slip planes or directions are parallel or perpendicular to the tensile axis. In figure 5.6a a coordinate system is defined such that the Z-direction (tensile axis) is parallel to [110] and the X and Y directions are parallel to the [001] and $[\bar{1}10]$ directions respectively. The macroscopic

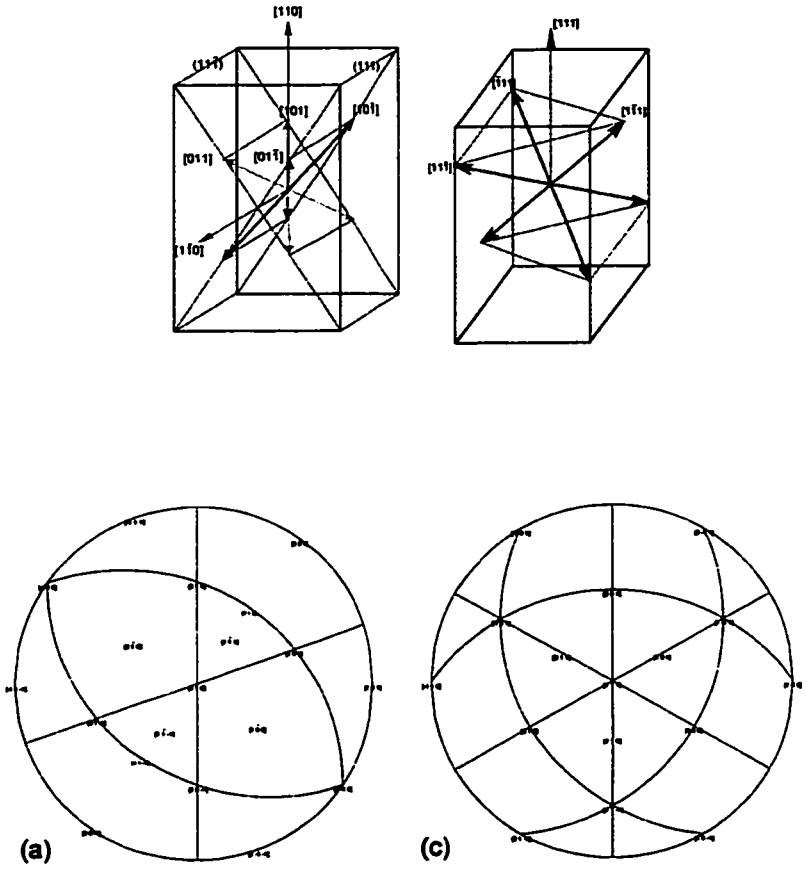

Figure 5.6 a) and b) Schematic and stereographic projection showing slip systems in Cu oriented with [110] along the tensile axis (centre of the projection). c) And d) Similar to a) and b) but for Cr crystal oriented with [111] along the tensile axis.

strains along the X, Y, and Z directions ($d\varepsilon_x, d\varepsilon_y, d\varepsilon_z$) may be related to the sum of the shear strains ($d\gamma$) on the four equally favoured slip systems as,

$$d\varepsilon_z = \frac{1}{\sqrt{6}} d\gamma$$
$$d\varepsilon_y = 0 \qquad (5.7)$$
$$d\varepsilon_x = -\frac{1}{\sqrt{6}} d\gamma$$

The operation of these four slip systems produces a condition of plane strain; i.e. no contraction is experienced parallel to $[\bar{1}10]$. In order for the sample to undergo axisymmetric deformation, some combination of the other eight slip systems would have to operate thus requiring higher stresses and more work to be done on the sample.

The factor,

$$M = \frac{d\gamma}{d\varepsilon_z} = \frac{\sigma}{\tau} = \sqrt{6} = 2.45 \quad (5.8)$$

that arises from equation 5.8 (referred to as the Taylor Factor), is an average measure of how the applied strains ($d\varepsilon$) and stresses (σ) are resolved onto the active slip systems to give the shear strains ($d\gamma$) and stresses (τ) when more than one system operates. If a condition of axisymmetric deformation were imposed on the crystal illustrated in figure 5.6a, a Taylor Factor of M = 3.67 would be required (Hosford, 1964). This is to be compared with the average value of M = 3.06 for a random polycrystalline aggregate tested in tension (Taylor, 1938).

The above discussion has centered around the deformation behaviour of a single crystal. In the case of the directionally solidified Cu-Cr eutectic alloy, the material may be better described as a multicrystal with some scatter from the ideal orientation. This is reflected in the fact that the deformation of the directionally solidified eutectic is observed to fall somewhere between being plane strain and axisymmetric. The analysis of the ellipticity of a sample strained to 0.32 at 293 K (figure 4.35) gave a strain of -0.06 along the minor axis and -0.27 along the major axis of the ellipse. This indicates that the deformation is closer to plane strain tension than to axisymmetric tension. Thus, for the remainder of this discussion the results of tensile tests on Cu-Cr will be referenced against a Taylor Factor of M = 2.45.

The preferred orientation of the Cr fibres, unlike the Cu matrix, allows for relatively easy axisymmetric deformation. Figure 5.6b illustrates the arrangement of the slip directions in relation to the tensile axis. This shows that one of the four potential slip directions is unavailable as it is aligned along the tensile axis. Due to

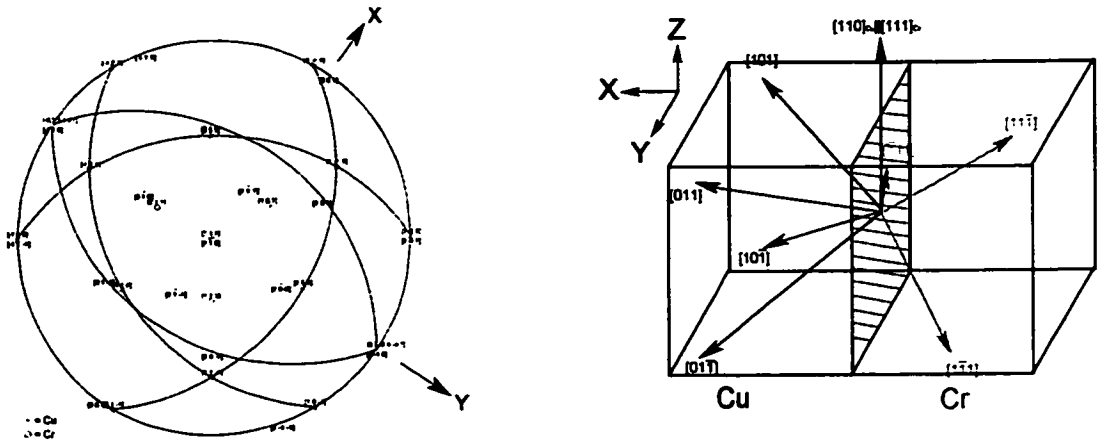

(a) (b)

Figure 5.7 a) Stereographic projection showing orientation relationship between Cu and Cr and the resulting relationship between the most highly stressed slip systems (tensile axis at centre of projection). Due to texture in Cu, no contraction would be expected along the direction marked "Y". b) Schematic bi-crystal of Cu/Cr showing most highly stresses slip systems across the phase interface. Note that the "interface" in this case

the possibility of pencil glide in bcc metals, a large number of possible slip planes are available. If only <111>{110} slip is considered, axisymmetric deformation with <111> as the tensile axis results in a value of M = 3.67. If, however, the deformation of the Cu matrix is assumed to be plane strain then this must be considered with relation to the deformation of the Cr. For zero contraction along the $[1\bar{1}0]_{Cu}$ direction there must equivalently be zero contraction along the $[8.1\ 3.4\ 4.7]_{Cr}$ direction due to the orientation relationship between the phases (figure 5.7a). The Taylor Factor for this imposed strain in the Cr is M = 4.90.

Before moving on, it is important to point out that although the K-S orientation relationship between Cu and Cr results in one slip system in each phase being exactly parallel across the phase interface, this "coincident" slip system is oriented parallel to the tensile axis in the case of Cu-Cr (figure 5.7b). Because of this, there exists no "easy" path for dislocations to be transmitted from the Cu into the Cr across the phase interface, as there is in duplex steel and Ni-Fe-Al eutectic discussed in chapter 2.

5.3.1.3 Influence of Grain Size on Deformation

The very large grain size of the samples studied here introduces some difficulty in terms of examining the macroscopic response of the material. First, differences in texture from sample to sample may result from not enough grains available to provide a statistically averaged response. This is compounded by the fact that the mechanical response of individual grains will be sensitive to how the Cr fibres are oriented within a grain. Second, the large grain size to specimen diameter used for tensile tests means that a significant fraction of the grains in the sample reside at the surface of the specimen. Grains at the surface are less constrained compared to their neighbours in the interior of the specimen and so are able to undergo shape changes more freely. This is evidenced by surface roughening (the so-called orange peel effect in metal forming). A significant amount of surface roughening (appearing as ridges running parallel to the tensile axis) occurred during testing. Tests conducted on samples with a larger gauge diameter did not show a significant difference from those conducted on smaller samples (figure 4.31). However, less variability was observed in the results from larger samples. Kocks (1970) has pointed out that it is necessary to have a specimen diameter at least 30 times the grain size to ensure that less than 10% of the grains in a specimen are located at the free surface. The larger samples tested here meet this requirement easily while the smaller samples are close to this ratio. Thus, in the following discussion the effect of grain size is an important , particularly with reference to the variability of the test results.

5.3.2 Deformation Behaviour at Low Strains: Elastic/Elastic and Elastic/Plastic Response

The salient points to be considered in the deformation of directionally solidified Cu-Cr up to strains of ~0.1 are i) the elastic response of the composite and its relation to the elastic response of the constituent phases, ii) the onset of plasticity in Cu and load transfer to the Cr fibres, and iii) the elastic/plastic transition of the Cr fibres and the onset of co-deformation. The results from each of these portions of the tensile response will be dealt with below.

5.3.3 Matrix Elastic/Fibres Elastic

The elastic response of continuously reinforced fibrous composites is a mature topic. It has not been the focus of this study to provide a comprehensive evaluation of the elastic properties of the directionally solidified Cu-Cr alloy, however a brief discussion will be included here as the composite modulus will play an important role in the subsequent analysis.

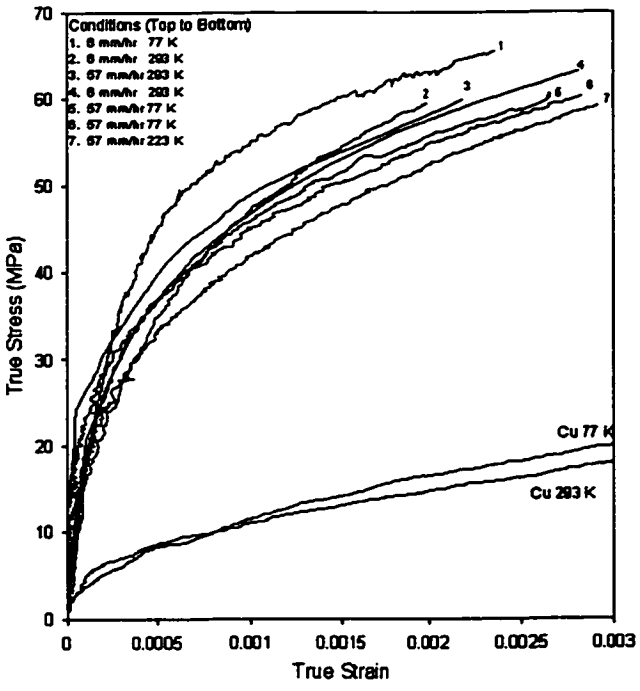

Figure 5.8 Low strain response of Cu-Cr specimens under various test conditions. Also included is the low strain response of pure Cu specimens tested at 293 K and 77 K.

Figure 5.8 shows representative flow curves for directionally solidified Cu-Cr specimens plotted to strains of 0.3%. The curves show an initial linear elastic response that exhibits a gradual transition to plastic behaviour. Because of the low yield stress of the Cu matrix and the corresponding rounded flow curve it is difficult to define an elastic modulus from plots of the initial loading response of the composite. Thus, the elastic modulus of the material was estimated from the linear portions of loading and unloading curves such as those shown in figure 4.58. Figure

Table 5.2 Elastic Constants for Cu and Cr

	μ (polycrystal)			E (polycrystal)	$E_{[100]}$	$E_{[111]}$	$E_{[110]}$
	293 K	223 K	77 K	293 K			
Cu	42.2 GPa [a]	44 GPa [a]	46.3 GPa [a]	109 GPa [b]	66.7 GPa	191.6 GPa	130.5 GPa
Cr	-	-	-	255 GPa [b]	333 GPa	265.6 GPa	248.8 GPa

[a] Mecking et al., 1986
[b] Hirth and Loethe, 1986

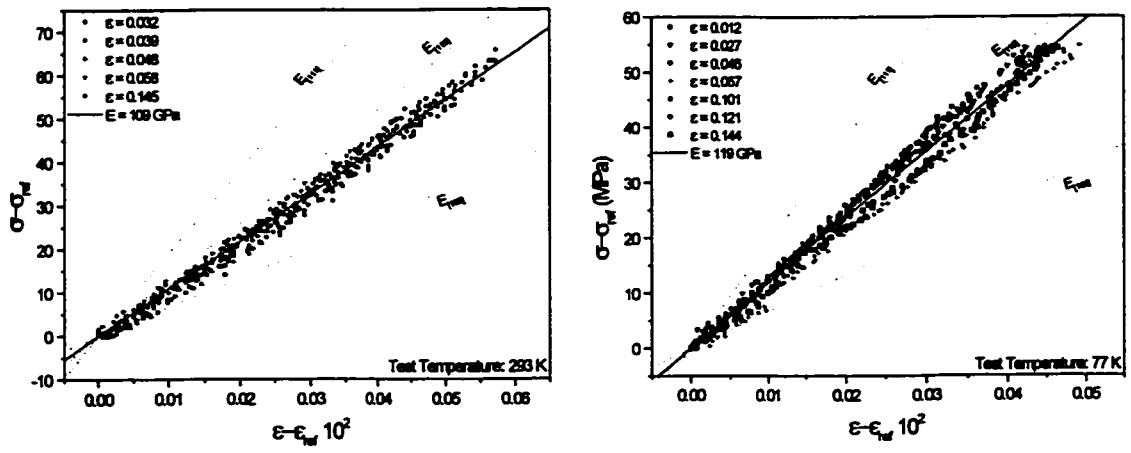

(a) (b)

Figure 5.9 Elastic loading data for directionally solidified Cu-Cr samples tested at a) 293 K and b) 77 K.

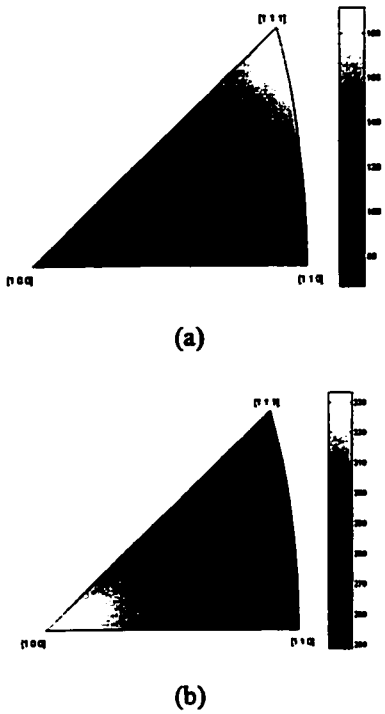

(a) (b)

Figure 5.10 Standard triangles showing the variation of Young's Modulus for a) Cu and b) Cr at 293 K as a function of position of tensile axis for single crystals.

5.9 shows representative data taken from the unloading portion of curves for samples solidified at 57 mm/hr and tested at a) 293 K, and b) 77 K. Here, data taken from samples unloaded after various pre-strains have been plotted on the same graph to show that there is little variation in the modulus as a function of prestrain. Also plotted on these charts are the absolute upper and lower limit moduli for Cu corresponding to single crystals oriented along the <111>, <110>, and <100> directions. The values of these and other important elastic constants are given in table 5.2. Although the strain gauge extensometer used is not ideally suited for the measurement at high accuracy necessary for unambiguous determination of elastic constants, the measured moduli are reproducible for a given

temperature and can be estimated as 109 GPa for samples tested at 293 K and 118 GPa for samples solidified at 77 K.

The values of the elastic moduli measured above can be directly compared to the elastic moduli of Cu and Cr. The single crystal elastic constants give the maximum possible range of permissible elastic constants for the single-phase materials. These single crystal elastic constants are represented in the standard triangles of figure 5.10. It is apparent, with reference to both figure 5.9 and table 5.2, that the measured moduli are relatively low (particularly compared to Cr) and that they tend to fall close to the values for pure Cu. This could be associated with poor alignment of Cr along the macroscopic growth axis of the sample. However, from the analysis of the degree of alignment given in figure 4.4 it would seem that this should enter as a second order effect.

As mentioned above, estimates of the elastic moduli of continuously reinforced fibre composites are highly developed (e.g. see Rosen and Friedman, 1970). One method that predicts the elastic properties of transversely isotropic composites particularly well is that developed by Hashin and Rosen (1964). For the purposes of this work the most important quantity to examine is the longitudinal Young's modulus,

$$E = fE_f + (1-f)E_m + \frac{4f(1-f)\left(\nu_m - \nu_f\right)^2}{\left(f/K_m\right) + \left((1-f)/K_f\right) + \left(1/\mu_m\right)} \qquad (5.9)$$

Here, f is the volume fraction of fibres, K_i is the bulk modulus (i = m, f corresponding to matrix or fibres), μ_m is the shear modulus of the matrix, and E_i and ν_i are the Young's moduli and Poisson's ratios of the matrix (i = m) and fibres (i = f). The third term on the right hand side of equation 5.9 arises due to differential transverse contraction arising from differences in the Poisson's ratio between the two phases and normally can be ignored compared to the first two terms. Focusing on these first two terms it is evident that the term corresponding to the matrix will tend to dominate for low volume fractions. This is true for the case of Cu-Cr where the volume fraction of Cr ($f = 0.02$) is much smaller than the maximum possible ratio of matrix to fibre moduli ($E^{Cu}_{[100]} / E^{Cr}_{[100]} \approx 0.2$). The result of this is that, as observed, the modulus of the composite should be

approximately that of pure Cu considering the appropriate average over the sample texture. This result also applies to the temperature dependence of the elastic modulus in that the composite modulus should have the temperature dependence of pure Cu. The results from the two tests above tend to support this claim as the ratio of moduli at 77 K and 293 K ($E_{77}/E_{293} = 1.092$) is close to the ratio of moduli at 77 K and 293 K quoted for polycrystalline Cu by Köstor (1948) and Mecking et al. (1986).

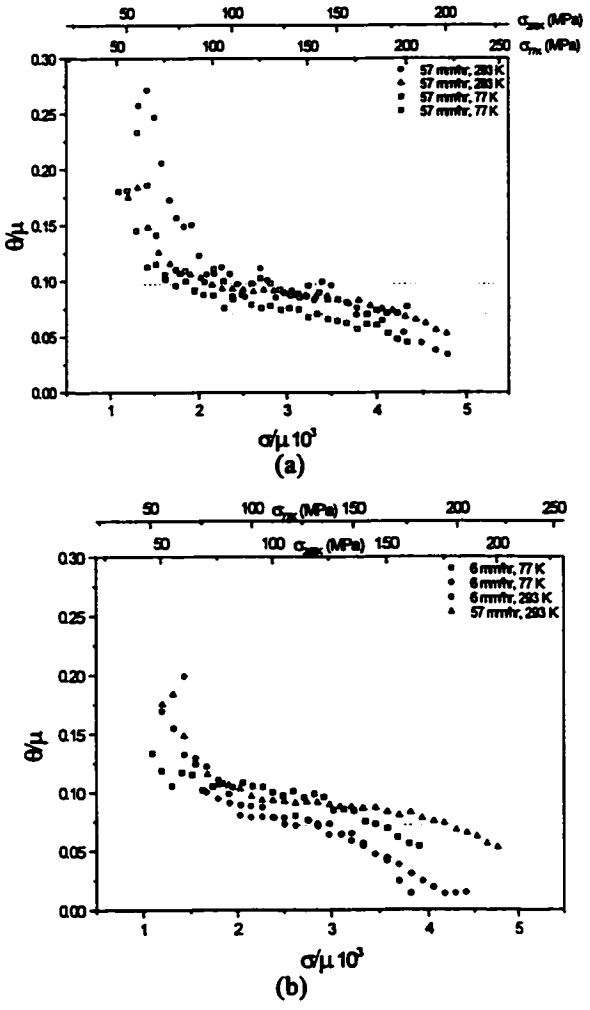

Figure 5.11a) Low strain work hardening behaviour for directionally solidified Cu-Cr. a) 57 mm/hr b) 6 mm/hr. In both cases θ is the uncorrected hardening rate, dσ/dε.

In the following discussion it will often be necessary to compare data collected at different test temperatures from different materials. The typical method for comparing the mechanical response from such different sources is to normalize the data by the temperature dependent shear modulus of the material (as well as by the Taylor Factor to correct for differences in texture). From the above discussion it is apparent that it is an appropriate approximation to use the temperature dependent shear modulus of pure Cu in place of that of the composite. For the purposes here, the shear modulus of pure Cu at 293 K and 77 K quoted by Mecking et al. (1986) (see table 5.2) will be used as a scaling factor for the mechanical response.

5.3.4 The Elastic/Elastic - Elastic/Plastic Transition and Elastic/Plastic Response

In figure 5.8 a series of low strain tensile curves from samples grown and tested under various conditions was plotted. Yielding of the

Cu matrix is evidenced by the gradual transition from the initial linear elastic response to the nearly linear portion of the curve associated with fully plastic behaviour of the Cu and elastic loading of the Cr fibres. The progressive nature of yielding in the Cu makes determination of a unique yield stress from the macroscopic flow curve difficult. In order to examine the mechanical response during this portion of the flow curve the flow curves of several specimens have been differentiated with respect to strain to give the work hardening rate ($\theta = d\sigma/d\varepsilon$). This has been plotted against the applied stress in figure 5.11. As described above, these plots have been normalized with respect to the temperature dependent shear modulus for Cu. These plots allow for easy recognition of the progressive yielding of the Cu as the initial transient associated with the initial rapid drop in θ. For the purposes of defining an applied stress associated with yielding of the Cu, a 0.1% offset has been used on the data plotted in figure 5.8, including the low strain flow curves for the pure Cu specimens tested. This method gives an approximate proof stress of 50 ± 5 MPa for the onset of plastic flow in the eutectic alloys. From both figure 5.8 and figure 5.11 there appears to be no systematic variation of the yield stress with temperature or growth rate of the sample apart from of the sample to sample variations resulting in the scatter evident in figures 5.8 and 5.11. Measurement of a similar 0.1% offset yield stress for the pure Cu specimens (figure 4.3 and figure 5.8) resulted in an average measurement of 12 ± 2 MPa.

It is apparent that the incorporation of the Cr fibres into the Cu matrix raises the yield stress of the matrix. Care must be taken in defining the actual stress carried by the matrix as the above measurements have been made on the composite flow curve. A simple approximation under the conditions where the matrix is deforming plastically and the fibres are deforming elastically is to use the rule of mixtures (assuming aligned fibres) and the composite 0.1% proof stress,

$$\sigma_m = \frac{\sigma_c - f E_f \varepsilon_c}{1 - f} \qquad (5.10)$$

where ε_c is the composite strain. When the strains are low (e.g. close to the point of matrix yield) the load carried by the fibres is small (compared to that carried by the matrix) due to the low volume fraction of fibres. Thus, at the point of yield (as defined above) the stress carried by the fibres is higher than that measured from

the flow curve by only ~ 1 MPa. However, as will be shown, as straining continues load is partitioned more heavily onto the fibres during deformation within the elastic/plastic portion of the curve.

Three factors must be considered in regard to the rounded portion of the flow curve corresponding to the yielding of Cu. First, the presence of the Cr fibres acts as possible obstacles to the long range motion of dislocations through the matrix. In order for flow in the Cu to occur, dislocations must bend between fibres, thereby increasing their line length. The limit of this process, given by the stress at which dislocations are able to just bow between the fibres, is the Orowan stress,

$$\sigma \approx M \frac{\mu b}{2\lambda} \ln\left(\frac{\lambda}{2d_o}\right) \qquad (5.11)$$

where M is the Taylor factor, μ is the shear modulus of Cu, b is the magnitude of the Burgers vector d_o is the core cutoff, and λ is the spacing between fibres in the slip plane. Assuming a homogeneous distribution of fibres of radius r and volume fraction *f* such that the approximate inter-fibre spacing is given by,

$$\lambda = \left(\frac{1}{\sqrt{f}} - 1\right) r \qquad (5.12)$$

gives an increase in flow strength of $\Delta\sigma \approx 20$ for $r = 0.1\,\mu m$ ($\lambda = 0.6\,\mu m$) and $\Delta\sigma \approx 2$ MPa for $r = 1.0\,\mu m$ ($\lambda = 6\,\mu m$). This represents an upper limit to the possible contribution from an Orowan process for the two growth rates studied here and alone is insufficient to explain the increase in observed flow stress. Furthermore, this explanation would predict a growth rate dependent yield stress for the Cu, a fact that has not been observed experimentally.

The residual stresses developed during cooling of the casting from the solidification temperature would also be expected to influence the initial yielding of the Cu. As was shown in section 4.3.2.1, these thermal residual stresses are tensile in the Cu suggesting that their influence would be to lower the stress needed to cause yielding of the Cu. Large variations in the initial thermal residual stresses in the Cu were observed (figure 4.57) in the samples studied by neutron diffraction. This is most likely due to grain statistics associated

with where in the microstructure the signal was received from. Samples exhibiting very large starting residual stresses may be associated with measurements taken from grains located near the machined surface. Further, the difficulty in defining a reference lattice parameter suggests relatively large errors in the predicted magnitude of the starting thermal residual strain.

Although the influence of the thermal residual stresses themselves on the initial yielding behaviour of the Cu should decrease the applied stress necessary to reach the flow stress of Cu, it is also observed that in order to locally relieve some proportion of these stresses there is plastic flow in the Cu close to the fibres. This was shown by TEM observations and the measurements of the thermal residual strains in the Cr fibres (cf. section 5.2.3). This increase in dislocation density close to the fibres would raise the local flow stress of the Cu. A simple estimate of the dislocation density necessary to give the observed rise in the initial yield stress of the Cu is given by,

$$\rho = \left(\frac{\Delta\sigma}{M\alpha\mu b} \right)^2 \approx 5x10^8\, cm^{-2} \qquad (5.13)$$

with $\alpha = 0.5$ and $\Delta\sigma = 38$ MPa, which is reasonable considering the observations presented in chapter 4. This explanation would also account for the progressive nature of yielding as flow would initiate in the vicinity of fibres and propagate outwards in a manner analogous to the "shakedown model" of Cottrell (1964). This effect would be approximately independent of both the growth rate and the testing temperature.

A further factor that will influence the nature of the macroscopic elastic/plastic transition in this material is the texture associated with the as-cast material. Variation in fibre orientation from grain to grain will result in an inhomogeneous distribution of stresses and strains on the scale of individual grains. The variation in strain was observed in the distribution of slip lines on the surface of polished and strained specimens (figure 4.47) and is expected to provide the most significant source of scatter in these measurements as discussed in section 5.3.1.2.

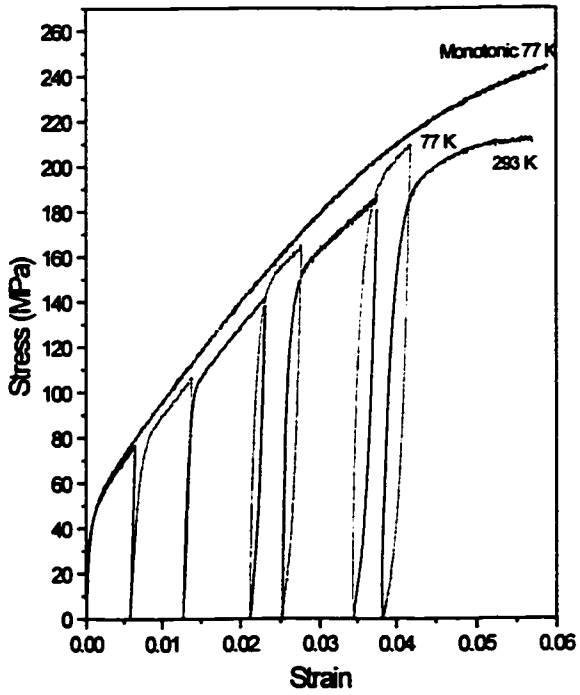

Figure 5.12 Low strain portion of cyclic testing at 293 K and 77 K (Cottrell-Stokes Test).

Once the Cu matrix has fully yielded plastically the mechanical response of the material is observed to come to a second regime of deformation characterized as having a high constant hardening rate (θ). This is clearly seen as the plateau portion of the θ–σ plots of figure 5.11. In this figure the scatter between samples appears to mask any dependence on testing temperature and/or solidification rate on the systematic variation of this slope. It is observed that the hardening rate can be described as falling between a range of 0.1μ to 0.075μ where μ is the shear modulus of Cu.

In order to examine whether the hardening rate is truly temperature independent during this portion of the test, it is useful to carefully examine the flow curves shown in figure 4.33 (e.g. The initial portion of the Cottrell-Stokes test). Figure 5.12 shows the low strain portion of this test corresponding to the elastic/elastic and elastic/plastic portion of the curves. Here, the sample has been loaded in tension at 293 K, unloaded then further loaded at 77 K to obtain a measure of the flow stress of the sample after the pre-strain at 293 K. Just beyond the macroscopic yield stress of the composite the flow stress at 293 K and 77 K coincide and the rates of hardening are nearly equal. However, as the applied stress rises, the hardening rate at 77 K is drops off less quickly than the hardening rate at 293 K. The locus of the measured portions of the flow curves at 293 K and 77 K appear to fall within the range of behaviour for samples tested monotonically at 293 and 77 K (shown as gray lines in figure 5.12). Thus, it would appear that at low stresses (just above the macroscopic yield stress) the flow stress and hardening rate is determined from an approximately athermal process, e.g. elastic loading of the Cr fibres. As straining proceeds, thermally activated processes become more important and tend to reduce the hardening rate at 293 K compared to 77 K.

From equation 5.10 it was shown that the bulk of the imposed load was carried by the Cu phase during elastic deformation simply because the volume fraction of fibres is so low. Upon yielding of the Cu, the rule of mixtures may be extended to describe the elastic/plastic condition,

$$\theta_C = \frac{d\sigma_{Applied}}{d\varepsilon_{total}} = \theta_{Cu}\left(1-V_f\right) + E_{Cr}V_f \qquad (5.14)$$

The upper limit (practically achievable only in single crystals) for the hardening rate of pure Cu is given by the stage two hardening rate typically of the order of $\theta_{Cu} \approx \mu/20$ where μ is the shear modulus (Basinski and Basinski, 1979). If this upper limit hardening rate for Cu is substituted into equation 5.14 and the approximate relation $\mu \approx 3/8E_{Cu}$ is applied one obtains,

$$\theta_C \leq \frac{3}{160}E_{Cu}\left(1-V_f\right) + E_{Cr}V_f \qquad (5.15)$$

This expression shows that the elastic loading of the Cr fibres will contribute much more to the composite hardening rate than the work hardening rate of the matrix during the elastic/plastic response of the composite. It also shows that the fibres will carry an ever increasing proportion of the applied load. Multiplying the above measured values for the hardening rate by the shear modulus of Cu gives upper and lower bounds from the experimental data on the hardening rate as 4.63 GPa and 3.15 GPa. These bounds fall below the value that would be predicted from equation 5.14 if only loading of the Cr fibres is considered, e.g. $\theta \approx V_f E^{Cr}_{[111]} = 0.02(248\,GPa) = 4.96\,GPa$. However, it must be remembered that this is an upper bound approximation assuming that the fibres are aligned along the tensile axis and undergo a strain equal to the applied strain. As with the elastic/elastic response and the yielding of the Cu, grain to grain variations in fibre orientation most likely reduce the measured slope from its ideal value.

Similar conclusions can be drawn from the observations at the mesoscopic scale. Figure 5.13shows a representative plot of the development of elastic strains in the Cu matrix during neutron diffraction experiments. Here, the evolution of lattice strains is only considered within the elastic/elastic and elastic/plastic portions of the flow response as a function of the applied stress. The elastic/elastic portion of

the loading curve is clear in this plot and, as expected from the above discussion, the slope of the initial portion of the curve is close to that expected for pure Cu with no reinforcement; i.e. the Cu sees an elastic strain approximately equal to the macroscopically applied strain. However, upon reaching a critical value of the applied stress, which was observed to vary from sample to sample but was always close to the macroscopic yield stress for the composite, the rate of development of elastic strain with applied stress in the Cu slows drastically. Again, this is consistent with a regime of hardening where most of the increase in applied stress is associated with elastic loading of the fibres. This can be understood in a relatively simple manner if a one dimensional approach is adopted.

If the matrix were to deform in the absence of the Cr fibres other sources of inhomogeneity (e.g. grain boundaries), the lattice strain versus applied stress curve would be linear with a slope equal to the elastic modulus for the material[1]. After pre-straining a material plastically in uniaxial tension the sample will load elastically to an applied stress

$$\sigma = E\varepsilon_{el} \quad (5.16)$$

where ε_{el} is the elastic strain the material carries upon reaching the flow stress upon re-loading. Thus, at any point along the flow curve, the total stress carried by a composite of two phases, where the matrix is deforming plastically and the fibrous phase elastically, may be written as,

$$\sigma_c = E_m \varepsilon_{el}^m (1-f) + E_f \varepsilon_c f \quad (5.17)$$

assuming that both phases experience a total strain (elastic plus plastic) equal to the applied strain; e.g.

$$\begin{aligned} \varepsilon_{el}^f &= \varepsilon_c \qquad (a) \\ \varepsilon_{el}^m + \varepsilon_{pl}^m &= \varepsilon_c \qquad (b) \end{aligned} \quad (5.18)$$

1 In the case of randomly oriented polycrystals, the proper elastic constant to use would be one which is averaged over all orientations that share the scattering direction as a zone axis. Here, due to the large degree of texture it is probably sufficient to simply consider the single crystal modulus.

In the case of figure 5.13, it is the slope of the applied stress (σ_c) versus elastic strain in the matrix phase that needs to be computed. Differentiating equation 5.17 with respect to the elastic strain in the matrix phase gives,

$$\frac{d\sigma_c}{d\varepsilon_{el}^m} = E_m(1-f) + E_f f \frac{d\varepsilon_c}{d\varepsilon_{el}^m} \qquad (5.19)$$

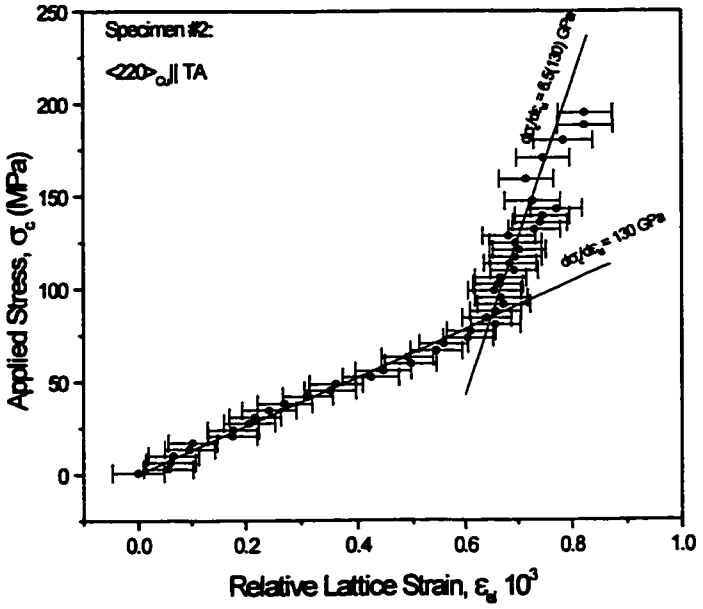

Figure 5.13 Data from Cu phase in specimen #2 during in-situ neutron diffraction experiments. Here, data has only been plotted for the regimes of elastic/elastic and elastic/plastic behaviour.

Considering the in-situ flow response of the matrix, an equation similar to 5.17 can be written relating the elastic strain in the matrix to the current flow stress. Assuming that the total strain is dominated by the plastic strain, and differentiating equation 5.16 with respect to the total strain gives,

$$\frac{d\sigma_m}{d\varepsilon_c} = E_m \frac{d\varepsilon_{el}^m}{d\varepsilon_c} = \theta_m \qquad (5.20)$$

Substituting this expression into equation 5.19 then gives a relation for the slope of figure 5.13 in terms of quantities that are known or can be easily estimated,

$$\frac{d\sigma_c}{d\varepsilon_{el}^m} \approx E_m\left(1+\frac{E_f f}{\theta_m}\right) \qquad (5.21)$$

which is approached in the limit of low volume fractions and no plastic relaxation in the matrix.

Examining this expression shows a number of useful features. First, in the limit of $f = 0$, the slope of a plot of applied stress versus lattice strain in the matrix is predicted to be linear with a slope equal to the matrix

modulus (E_m). Similarly, in the case where both phases deform elastically, $\theta_m = E_m$ and the expression again reduces approximately to give a slope equal to the modulus of the matrix. The data collected in figure 5.13 is from Cu oriented with a <110> along the tensile axis. The initial slope of this curve fits very well to the predicted behaviour $d\sigma_c / d\varepsilon_d^{Cu} \approx E_{[110]}^{Cu} = 130\,GPa$ as given in table 5.2. Once yielding of the Cu occurs, the hardening rate of the Cu has to be accounted for. Assuming that the hardening rate of the Cu in-situ is not affected by the presence of the Cr fibres (at least over the initial 4-5% strain,) an estimate of the hardening rate at room temperature can be made as $\theta_{Cu} = \mu_{Cu}/45$ (from figure 4.43a). Substituting this into equation 5.21 gives a slope of,

$$\frac{d\sigma_c}{d\varepsilon_d^{Cu}} \approx 6.5E_m \qquad (5.22)$$

This is plotted on figure 5.14, again showing reasonably good fit to the experimental data.

Although the above simple analysis seems to reasonably predict the form of the observed behaviour it ignores a number of potentially important issues. Foremost it assumes that the strains are everywhere equal to the applied strain. The small variation in fibre orientation from grain to grain is probably sufficient to produce significant variations in load transfer on the scale of individual grains. This is seen in single-phase materials where differences in grain orientation lead to deviations in the simple linear relationship between applied stress and lattice strain predicted above (Clausen, 1997). In this case, grain to grain variations in the fraction of the load being carried by any particular grain will be a function of a number of parameters. Most important will be the variation in fibre orientation within a grain versus the macroscopic tensile axis.

A second issue with the above treatment is that it assumes that the in-situ flow behaviour of the matrix is unchanged from that observed in bulk specimens. It has been shown that an extra matrix hardening, associated with an increasing difficulty of passing dislocations between the fibres exists in other systems. This "source" shortening stress (Brown and Clarke, 1975) is given approximately as,

$$\sigma_{ss} = kf\mu_m\varepsilon_p \qquad (5.23)$$

where k is a constant of the order of $5/2\pi \sim 3/2\pi$ (Brown and Clarke, 1975, Lilholt, 1993) and ε_p is the plastic strain. This process results in a linear hardening contribution to the rate of work hardening of the matrix. Substituting appropriate values into equation 5.23 for the Cu-Cr system gives an extra hardening rate of $\mu/160$. This is only about 1/3 of the hardening rate observed with no reinforcement and thus should be expected to make a weak contribution to the hardening of the matrix in this system. This result is in agreement with the analysis of Brown and Clarke (1975) who showed that below a volume fraction of approximately 10% the source shortening effect is relatively minor.

The above treatment is also oversimplified by the assumption that the stresses developed during the elastic/plastic deformation are assumed purely uniaxial. Significant triaxiality can develop in two-phase materials during elastic/plastic deformation due to differences in transverse contractions. The degree to which triaxiality plays a part in this case can be checked via the full tensor Eshelby relations. If elastic and plastic isotropy is assumed and the values for the Eshelby tensor are taken from Brown and Clarke (1975) one obtains an internal stress state in the fibre given approximately by,

$$\begin{bmatrix} \sigma^f_{11} \\ \sigma^f_{22} \\ \sigma^f_{33} \\ \sigma^f_{13} \\ \sigma^f_{23} \\ \sigma^f_{12} \end{bmatrix} = \begin{bmatrix} -32 \\ -32 \\ 262 \\ 0 \\ 0 \\ 0 \end{bmatrix} \varepsilon_p \quad (GPa) \qquad (5.24)$$

where σ_{33} is directed along the tensile axis and ε_p is the applied plastic strain. The transverse stresses, being an order of magnitude smaller than the axial stress, result in the predicted uniaxial estimate of the mean stress being accurate to within ~10%. This error is presumably smaller than that associated with assuming that the fibres are perfectly aligned along the tensile axis.

Finally, the strong development of hysteresis in the loading/unloading behaviour of samples as a function of plastic pre-strain during deformation in this portion of the flow curve gives further indication for elastic load transfer to the fibres. The fact that reverse plastic flow of the matrix occurs prior to unloading to

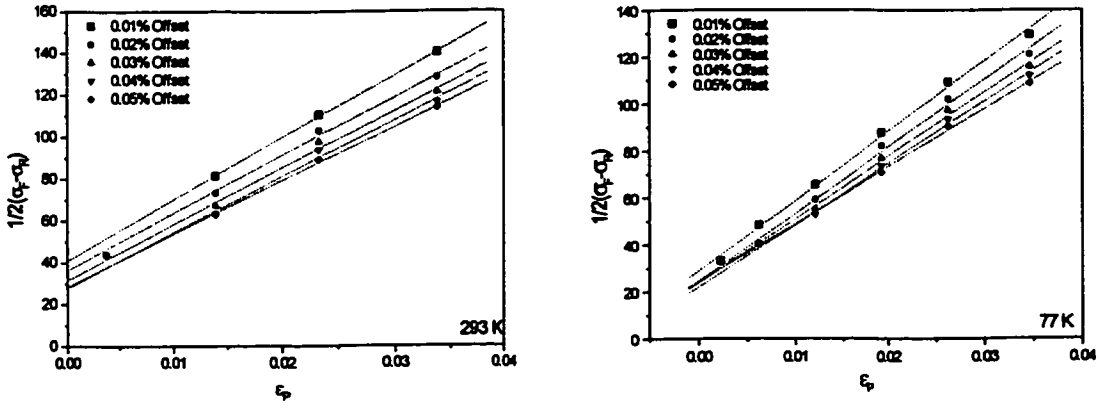

(a) (b)

Figure 5.14 Back stress calculated as half the difference in the forward and reverse (offset) yield strength on unloading and reloading of specimens at a) 293 K and b) 77 K.

zero stress is an indication of the extremely large elastic stresses borne by the Cr fibres. Figure 5.14 shows the calculated back stress measured from the unloading portion of the curve as,

$$\sigma_b = \frac{1}{2}\left(\sigma_F - \sigma_R\right) \qquad (5.25)$$

where σ_f is the forward flow stress prior to unloading and σ_r was defined in figure 4.60. The use of this parameter to describe the level of internal stresses raises some issues regarding its interpretation (Sowerby et al., 1987). If a material were to exhibit an abrupt elastic-plastic transition then the above equation would give a direct measure of the internal stresses acting to aid reverse flow and cause forward hardening. However, when the process of yielding is progressive, the long range internal stresses developed by the composite microstructure may be supplemented by local short range stresses and the stability of the dislocation structure developed upon forward loading. Thus, equation 5.25 probably includes both the effects of the mean internal stress as well as other local effects. However, because the mean stresses are very large in this case, they should dominate the variation of the back stress with plastic strain. This can be seen directly in figure 5.14. The data rises linearly both for tests conducted at 293 K and 77 K with a slope that is approximately independent of the choice of offset used to determine the reverse flow stress. The slopes of these lines are in reasonably good

agreement with the estimates of the rate of internal stress accumulation with plastic strain made from the slope of the macroscopic flow curve. This data suggests that the rate of internal stress development is less than what would be expected from the ideal situation of perfectly aligned fibres with no relaxation, thus indicating that fibre misorientation and/or processes of relaxation are important in reducing the rate of load transfer to the fibres. The presence of relaxation processes can also be inferred from the temperature dependence of the rate of internal stress development. The possible relaxation mechanisms are varied but the most important to consider are,

i) *Fibre Fracture/Decohesion:* these are unlikely as neither was observed experimentally.

ii) *Plastic Yielding of the Fibres:* this will be explored in more detail in the following section. For the moment it sufficient to recognize that, although there is a temperature dependence for the flow stress of the Cr, extensive fibre yielding would be expected to lead to more extensive relaxation than what is observed in this portion of the flow response.

iii) *Relaxation by Plastic Flow in the Matrix:* This is the most likely source of the temperature dependence in the data. The plastic misfit between fibres and matrix that arises during the elastic/plastic regime can be relaxed if extra work is done by plastic flow around the fibres. Without relaxation, compatibility and equilibrium can be maintained between matrix and fibres if passing dislocations leave shear loops around the fibre. This simple situation is not stable over a very large range of strains. It was shown in chapter 4 that even at low strains, dense tangles of dislocations are observed at the phase interface (figure 4.62). Burgers vector analysis showed the presence of 6 different Burgers vectors. Further, the lack of large lattice rotation around the fibres (figure 4.63) is inconsistent with the simple shear loop array (Ashby, 1971).

A number of potential mechanisms may exist to reduce the plastic misfit by plastic flow in the matrix. These include,

i) *Prismatic Punching of Loops:* It was suggested earlier that this may be an important mechanism for the relaxation of thermal residual stresses. The same mechanisms are possible as a means of reducing the

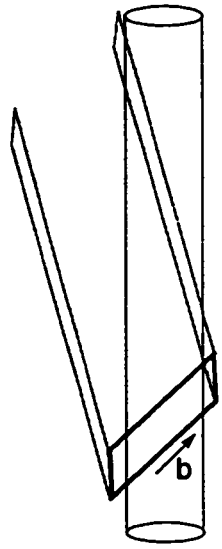

Figure 5.15 Double cross-slip of shear loops around a fibre resulting in a prismatic loop left around the fibre and a prismatic loop in the matrix. Large loops must be produced if cross slip occurs on a system close to the fibre axis. Original shear loop is drawn in black while the two prismatic loops are drawn in gray.

deformation induced residual stresses. However, this mechanism will become more difficult as the density of forest dislocations around the fibre increases.

ii) *Double cross-slip:* This process again is not as efficient in the fibre case as it is in the case of equiaxed particles. In the Cu-Cr system, the most probable cross-slip plane is oriented approximately 9° from being parallel to the fibre axis. As shown in figure 5.15, for the process of double cross-slip to convert a shear loop into either two prismatic loops or a prismatic loop and a shear loop, a very large increase in the line length must occur. For this to happen a large decrease in the stored elastic energy must take place. This will only occur at the highest strains.

iii) *Secondary Slip:* It is possible that the operation of sources on systems other than the primary systems can help to alleviate some of the developed plastic mismatch. This would certainly help to account for the number of observed Burgers vectors. Such a process will, however, be made difficult in this case because the matrix is already undergoing multiple slip.

iv) *Dislocation Reaction:* It has been suggested that dislocation reaction at the phase interface may help to reduce the plastic misfit (Moan, 1977). Assuming the equal operation of four slip systems as described in section 5.3.1.2 and shown in figure 5.6 two of these dislocations may react via,

$$\frac{a}{2}[10\bar{1}]+\frac{a}{2}[011]\rightarrow\frac{a}{2}[110] \qquad (5.26)$$

The resulting dislocation (Lomer-Cottrell dislocation) is a pure edge dislocation located on the (001) plane. As the (001) plane is not a glide plane for fcc metals, this dislocation is sessile. However, its Burgers vector is approximately oriented along the axis of the fibre. As this dislocation is prismatic, it will result in a smaller

displacement at the interface than if either of the two parent dislocations had remained. Not every pair of dislocations of the above type will react to form a Lomer-Cottrell dislocation. The probability will be sensitive to the probability of cross-slip which is strongly temperature dependent.

To summarize the above discussion, it appears that above a stress of approximately 50 MPa in tension, yielding of the Cu matrix results in a strong partitioning of load between the plastically deforming Cu and elastically deforming Cr. This behaviour is consistent, to the first order, with models which treat the material both from the continuum scale as a uniaxial fibre reinforced composite as well as from the mesoscopic scale where the interaction between the two phases at the local level is considered. It is interesting to consider that these relations are obeyed up to applied strains of the order to 4% suggesting that very large loads are borne by the Cr fibres prior to their yield.

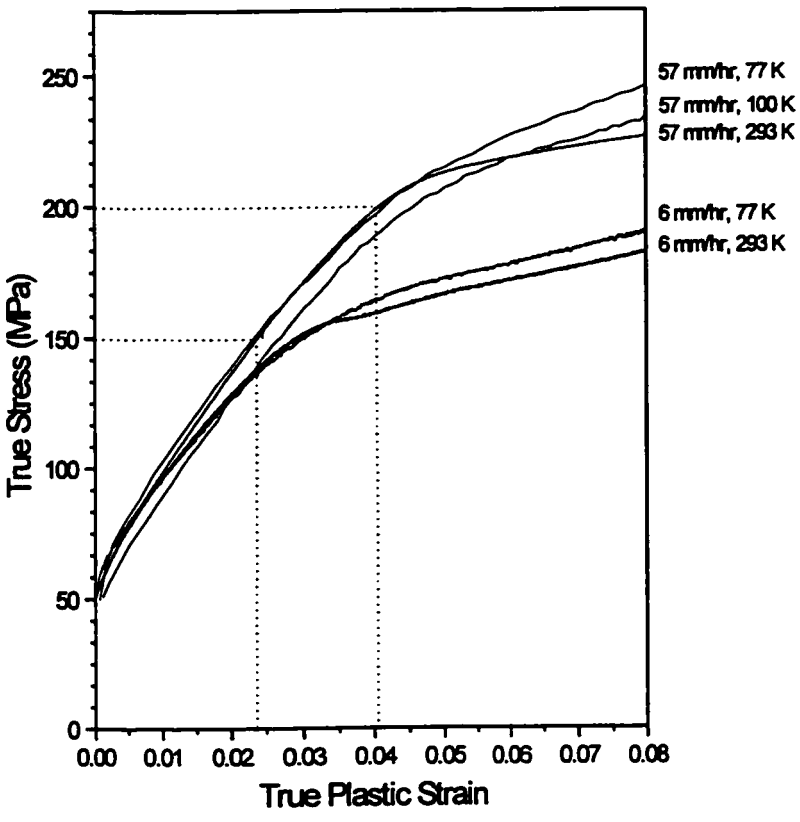

Figure 5.16 Stress/strain curves for directionally solidified Cu-Cr showing the response of material tested under various conditions up to the point of macroscopic fibre yielding.

5.3.5 The Elastic/Plastic - Plastic/Plastic Transition and the Onset of Co-Deformation

To this point the deformation behaviour of the two-phase material can be understood largely with reference to the vast amount of work on dispersion hardened and fibre reinforced metals. Typically, the end of the elastic/plastic regime in these materials would be marked by failure of the material as a whole. However, here it is clear that the Cr fibres are able to

undergo extensive plastic deformation resulting in the high ductilities which are observed. Returning to figures 5.11a and 5.11b, it can be seen that the transition from the elastic/plastic regime to the plastic/plastic regime is marked by the gradual decrease of the hardening rate from its nearly constant level within the elastic/plastic regime. Again, sample to sample scatter precludes a definitive statement from these figures as to whether there is a temperature dependence on the point at which fibre yielding commences for samples solidified at the same rate. There is a clear indication from figure 5.11b, however, that fibre yielding is strongly dependent on the growth rate of the sample and therefore on the cross-sectional dimensions of the fibres. The data in figure 5.8 is limited to stress levels where the first onset of decreasing hardening from the elastic/plastic regime is observed. In figure 5.16, the stress-plastic strain curves, extending from the elastic/plastic portion of the curve to the onset of plastic/plastic deformation, indicate that the macroscopic onset of yielding in the Cr fibres occurs where the σ/ε curve exhibits an obvious "knee" in the flow curves, associated with the bulk yielding of the fibres. The strong dependence between the stress associated with this "knee" in the stress-strain curve and the rate of solidification is clear. A rough estimate of the transition from the elastic/plastic to plastic/plastic regimes is 150 MPa for samples solidified at 6 mm/hr and 200 MPa for samples solidified at 57 mm/hr.

Although it is clear that yielding of the Cr fibres is responsible for the knee in the macroscopic stress-strain curves, observation of TEM foils taken from specimens strained just beyond this point showed no evidence of stored dislocation within the Cr fibres (figure 4.72 a). It is possible that, due to the preparation of the thin foils, dislocations were removed form the Cr fibres. This is possible both because of the very high residual elastic strains carried by the fibres prior to thinning, and the fact that substantial reverse plastic strain is accumulated on unloading tensile specimen. However, it is clear from comparison with the surrounding Cu matrix that the density of dislocations in the Cr is very low compared to the total plastic strain undergone by the sample. The structure developed in the Cu itself undergoes a transition just beyond the knee in the stress-strain curve. During the elastic/plastic portion of the loading curve the predominant feature of the substructure is the tangles of dislocations surrounding the fibres. As previously discussed, the process of load transfer to the fibrous phase during this portion of the curve is often envisioned to occur by means of shear

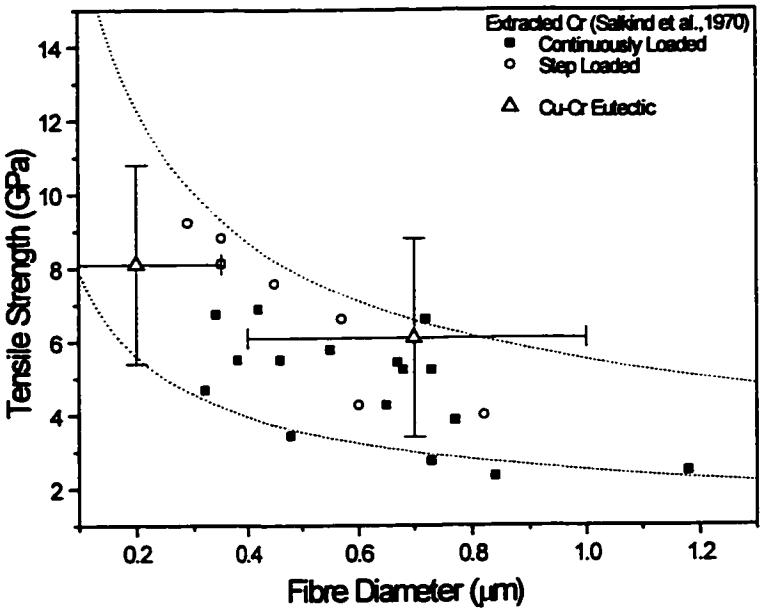

Figure 5.17 Data on the size/strength relationship for extracted Cr whiskers (Salkind et al, 1970). Also included is the estimated strength and size range in the materials studied here.

loops located on a single slip system which encircle the fibres. Obviously this does not fit the observations made here. The interaction of these glide dislocations with the dislocations already present at the interface due to relaxation of the thermal misfit strains can result in a number of reactions leading to a reduced energy of the overall structure. Such a relaxed dislocation structure is what is apparent in images such as figure 4.62. This would further explain the low degree of observed misorientation in the Cu as a function of distance from the phase interface.

The above discussion indicates that the elastic strains borne by the Cr fibres at the point of bulk yielding are very large; of the order of 2 - 3%. Figure 5.17 is taken from the work of Salkind et al. (1970) showing the tensile strength of extracted Cr fibres as a function of their approximate diameter (cf. section 2.3.1). Here, two data points corresponding to the bulk estimates of the in-situ yield strengths given above for samples solidified at 57 mm/hr and 6 mm/hr are included. The large error bars indicate the uncertainty in defining the strain at which yielding commences. The data here appears to fit well into the general trend found by Salkind et al. both in terms of the absolute magnitude of the yield strength for the fibres as well as for the trend of this yield strength with average fibre size. This truly indicates that the eutectic fibres in-situ behave on average like defect-free single crystal whiskers. This was the same conclusion reached by Garmong and Williams (1975) for W fibres in a directionally solidified Ni-W eutectic. In this system an elastic/plastic - plastic/plastic transition very similar to the one observed here was documented. It seems quite likely that the gradual

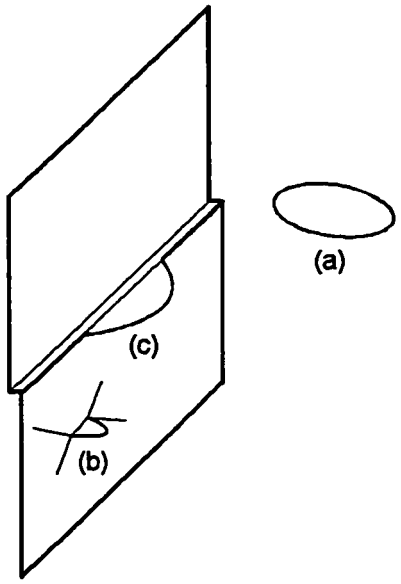

Figure 5.18 Schematic illustrating possible mechanisms for nucleation of slip within Cr fibres. a) Homogeneous nucleation within the fibre. b) Nucleation at the phase interface. c) Bowing of a pre-existing boundary defect into the fibre.

transition from the elastic-plastic to plastic-plastic regime can be attributed to the presence of a statistical distribution in fibre strengths within a sample. This distribution probably reflects a number of different factors, the most important of which are the presence of defects in the as-cast Cr fibres which either act as stress rises or as ready sources for dislocations, and a distribution of fibre orientation with respect to the macroscopic tensile axis. The presence of both of these features has been noted above.

If the Cr fibres truly are defect-free "whiskers" in-situ, their plastic deformation must be, at least initially, controlled by the mechanisms leading to the introduction of dislocations into the fibre. Estimating the stress necessary to nucleate dislocations from a semi-coherent interface is made quite difficult as the detailed atomistic mechanisms are not well understood. Here, because no dislocations could be observed in the fibres at strains just beyond the elastic/plastic - plastic/plastic transition it is difficult to know whether the initial mechanism of yielding is controlled by slip transfer or by nucleation from the phase interface. Regardless, a distinction must be made between three possible mechanisms for the nucleation of dislocations in the Cr fibres (figure 5.18). These mechanisms are;

1. Homogeneous nucleation of a perfect dislocation within the Cr fibres is a possible mechanism for producing glide dislocations in the Cr. In samples deformed to strains > 0.2, TEM observations show the presence of small dislocation loops within fibres. These defects could be the result of the interaction of dislocations on two or more slip systems in the fibre. However, it is also possible to imagine that they are the result of homogeneous nucleation. The shear stress necessary to homogeneously shear a perfect lattice to

produce a dislocation has been shown (Kelly and MacMillan, 1986) to lie typically between $\mu/50$ and $\mu/30$ for metals. However, a slightly more conservative value of $\mu/100$ is often quoted to account for the possibility of thermal activation aiding the nucleation process at high stresses (Cottrell, 1964). In the present case, the stress to expand the loop in the Cr would also need to overcome the image stress resulting from the interaction between the phase interface and the dislocation arising from the difference in elastic compliance across the interface (i.e. the image stress). This image stress can be estimated for a screw dislocation lying parallel to the phase interface as (Hirth and Lothe, 1986),

$$\sigma = M\frac{\beta b \mu_{Cr}\eta}{r}\gamma \quad (5.27)$$

where,

$$\gamma = \frac{\mu_{Cu} - \mu_{Cr}}{\mu_{Cu} + \mu_{Cr}} \quad (5.28)$$

where the factor η accounts for the presence of multiple interfaces that act to reduce the image stress (Kamat et al., 1987). In the limiting cases of no interface $\eta = 0$, while for a single interface $\eta = 1$. All other cases lie between these bounds. For an infinitesimal shear loop lying at a position equally spaced from the two interfaces the net image stress will be zero. However, if the loop is situated closer to one interface, the image stress has a net effect tending to pull the loop into the closer boundary. This effect will increase the stress necessary to expand the loop.

2. The above mechanism gives an absolute upper limit to the stress that would be necessary to cause plastic flow in the fibre. This can be lowered somewhat if a loop is nucleated at pre-existing defects in the phase interface. This may occur by the operation of a dislocation source located in the phase interface as has been previously proposed (Sutton and Balluffi, 1995). The limiting factor in this case is that the dislocation emitted into the fibre will need to overcome a very large image stress. This can be estimated from equations 5.27-5.29. Considering a screw dislocation situated 2b from the phase interface, a stress tending to pull it through the

interface and into the Cu of magnitude $M\mu_{Cr}/85$ will exist. This is of the same order of magnitude as the stress necessary for homogeneous nucleation described above. However, stress will also be reduced by the opposite interface.

3. Finally, similar to the previous mechanism, it is possible that nucleation of a dislocation loop occurs within the phase interface. The result would be the generation of interfacial defects to accommodate the loop that is produced. Again, in order to expand this loop into the Cr it will be necessary to overcome the large image stress considered above.

In all three cases, a stress approaching the theoretical shear strength for metals must be approached in order to produce dislocations within the fibre. Further, it is important to note that the initial thermal stresses will influence the magnitude of tensile load carried by the fibres for a given applied stress. It was shown in section 5.2.2 that the Cr fibres in the as-cast material are under a condition of residual compression along the tensile axis resulting from the difference in coefficient of thermal expansion for the two phases. These stresses are of the order of 500 MPa in the sample analyzed by neutron diffraction. These thermal residual stresses will appear (from macroscopic measurements) to raise the yield stress of the Cr fibres.

Although the above estimates are probably most significant in determining the magnitude of the flow stress of the fibres, it is also necessary to consider the flow stress that would occur for a dislocation already present in the fibre. The contributions to this stress will be,

i) *Lattice Friction,* σ_0: The intrinsic resistance of bcc metals to crystallographic slip is high both at and below room temperature. The Peierls-Nabarro stress in these materials is very strongly temperature and strain rate dependent. As discussed in section 2.3.4, the yield stress of pure bulk Cr as measured by tensile tests on single crystals (Gilbert et al., 1963) and polycrystals (Marcinkowski and Lipsitt, 1962) gives a strongly temperature dependent flow stress that rises from approximately 250 MPa at room temperature to close to 1 GPa at temperatures approaching 77 K (figure 2.45).

ii) *Stress to Bow a Dislocation into the Fibre*: In order for a dislocation to enter a Cr fibre from the phase interface it is necessary for it to bow out of the interface in a manner similar to the schematic of figure 5.18. Although no dislocations were imaged in the Cr fibres at strains close to the point of fibre yield, images from fibres at higher strains (see e.g. figure 4.73) show this mechanism operating very clearly. In order for this process to occur, the interfacial source must be operated by a stress,

$$\sigma \approx M \frac{4\beta\mu_{Cr} b\cos\theta}{t} \ln\left(\frac{t}{2b\cos\theta}\right) \quad (5.29)$$

where $t/\cos\theta$ is the length of the line of intersection between the slip plane and the phase interface (θ is the angle between the slip plane and the interface) and β is a constant equal to either $1/4\pi$ or $1/4\pi(1-\nu)$ depending on whether the dislocation is screw or edge. Here, the outer cutoff radius for the dislocation core has been estimated as 2b. The minimum possible value for $t/\cos\theta$ for the Cr fibres can be estimated as the minimum dimensions of the fibre. The important point regarding equation 5.29 is that it introduces a scale dependent strength into the relation for the flow stress of the fibres. Using values of $t/\cos\theta$ equal to 100 nm and 500 nm for fibres in samples solidified at 57 mm/hr and 6 mm/hr respectively, equation 5.29 gives an approximate contribution of $M\mu_{Cr}/300$ and $M\mu_{Cr}/900$ for the two growth rates. This is well below the stress necessary to form a dislocation in the fibre, however, after very large strains (when the scale of the fibres is reduced significantly) this term may become significant.

Considering the approximate nature of the above calculations, the above values necessary for nucleation appear to be of the proper order of magnitude, particularly for samples solidified at 57 mm/hr. For samples solidified at 6 mm/hr the lowered flow stress most likely arises due to higher density of pre-existing internal defects (e.g. dislocations, boundaries, constrictions) in the slower grown, and therefore larger Cr fibres. A second potential factor that may complicate the interpretation of results from samples solidified at 6 mm/hr are the bands of eutectic-free Cu. However, if the lower apparent Cr yield stress were attributable to preferential yielding of these eutectic-free regions, flow localization within these bands would have been apparent. This was not observed to be the case.

Finally, it is quite interesting to compare the mechanical behaviour of whiskers discussed in section 2.3.1 to the behaviour observed here. As was shown in figure 2.23, large yield drops are observed on free whiskers. This behaviour is associated with nucleation of a Luders front that, once developed, is able to pass through the entire crystal. The resulting debris left in the wake of the front subsequently introduces sources for the creation of new dislocations in the fibres thus allowing for the continued deformation at a stress controlled by the intrinsic flow stress of the material. In the case considered here, the passage of a Luders front along the length of a fibre would require that the Luders front also pass through the adjacent Cu. Such a process would require an organized process of yielding along the length of many fibres. Also counteracting the tendency for the localization of strain is the work hardening of the surrounding Cu. Thus, the presence of the surrounding matrix tends to help retain the strength of the whisker to large strains,(i.e. it requires nucleation at many points on interface). This point will be explored further below.

5.4 Large Strain Behaviour and the Process of Continued Co-deformation

The onset of bulk plasticity in the Cr fibres, as indicated by the sharp change in hardening rate in the macroscopic stress-strain curve, marks the beginning of plastic co-deformation. The complexity involved in interpreting the behaviour of the material during this stage of deformation arises due to the many degrees of freedom the material has in selecting a path that will satisfy the conditions of compatibility and equilibrium throughout the system. While it is clear that the presence of the Cr fibres alters the bulk mechanical behaviour of the eutectic alloy compared to that of pure Cu, it is impossible to deduce the mechanisms responsible for the hardening behaviour by interrogation of the bulk monotonic tensile response alone. In order to make progress towards understanding the mechanisms of co-deformation, the mechanical response of the material has been evaluated in a number of different ways. The key questions that need to be answered in trying to understand the bulk mechanical properties are:

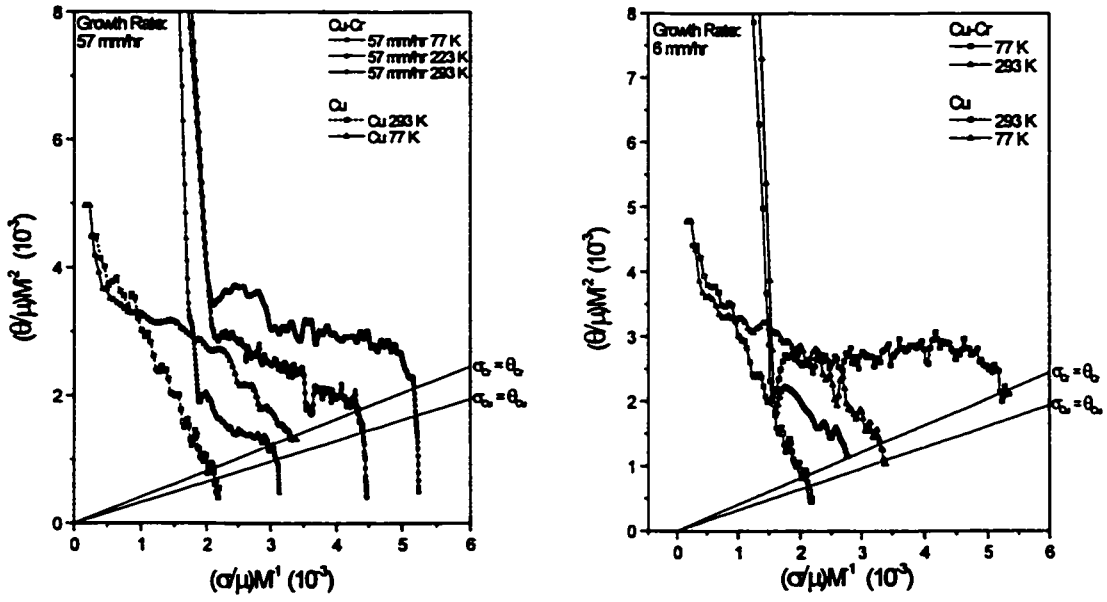

Figure 5.19 K-M plots for directionally solidified Cu-Cr grown at a) 57 mm/hr and b) 6 mm/hr. Also shown are the K-M curves for pure Cu tested at 293 K and 77 K.

i. Do the Cr fibres contribute directly to the hardening behaviour of the eutectic alloy after yielding by either dislocation accumulation and forest hardening within the fibres or further elastic loading? If so, what is the form of this contribution?

ii. How does the presence of the fibres alter the flow behaviour in the Cu? Is the effect localized to a region surrounding the fibres or does it influence the overall development of the substructure in the Cu?

iii. How do the above processes evolve with plastic straining?

iv. What is the relationship between the behaviour of the fibres and the stability of plastic flow in tension?

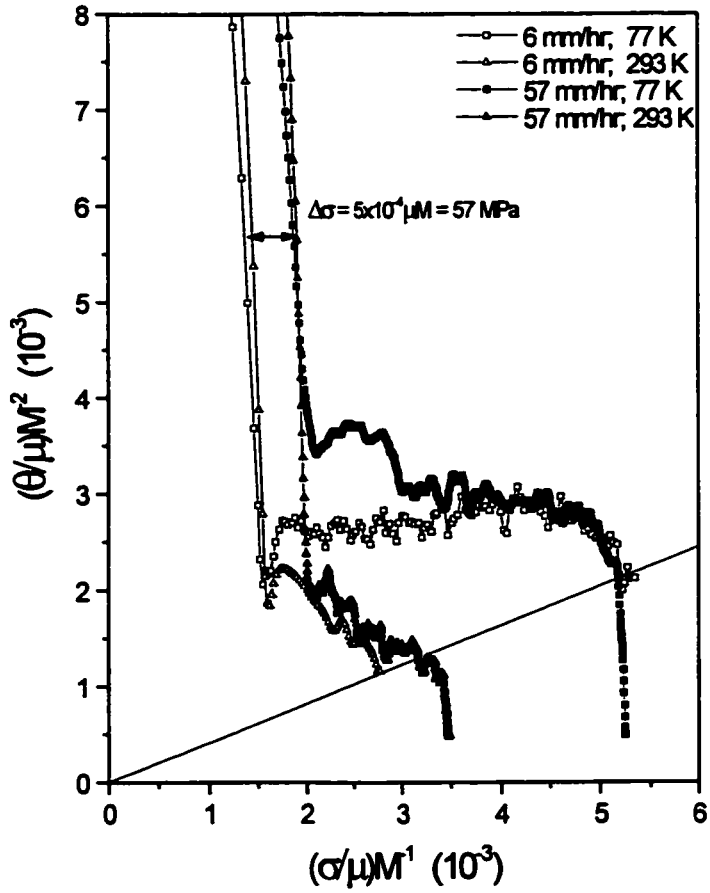

Figure 5.20 Comparison between K-M plots for Cu-Cr solidified at 57 mm/hr and 6 mm/hr.

5.4.1 Macroscopic Response of Cu-Cr During Co-Deformation

Before trying to answer the above questions it is worthwhile to review the bulk mechanical response for the eutectic alloy and directly compare it to the observed behaviour for the pure Cu. In order to do this the mechanical response has been plotted using the Kocks-Mecking (K-M) formalism of plotting the reduced hardening rate ($\theta/\mu M^2$) versus reduced stress ($\sigma/\mu M$) for the regime corresponding to the stress/hardening rate range associated with plastic co-deformation in the eutectic alloys; i.e. the plots are truncated such that the high hardening rate associated with the elastic/plastic regime is not included. Figure 5.19 shows representative K-M curves for a) samples solidified at 57 mm/hr and tested at 77 K, 196 K and 293 K, and b) samples solidified at 6 mm/hr and tested at 77 K and 293 K. In both of these plots the curves corresponding to the measured behaviour of pure Cu tested at 77 K and 293 K have been included for comparison. The salient features to be deduced from this plot are,

i. The magnitude of the hardening rate is higher for the eutectic alloy compared to Cu. Further, the rate at which hardening rate decreases is lower for the eutectic alloy. This is true for all test conditions.

ii. The hardening rate and its decrease with stress are strongly temperature dependent

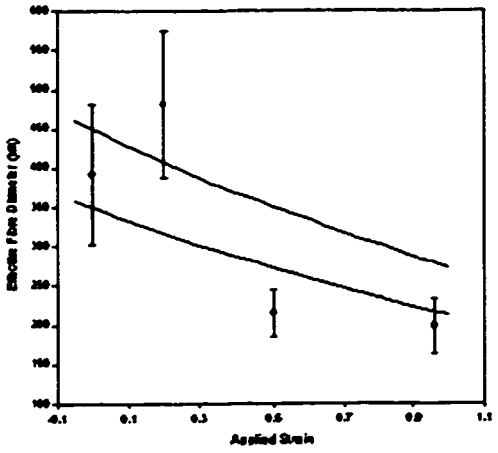

Figure 5.21 Cross-sectional area of Cr fibres as a function of imposed tensile strain. The lines indicate the expected change in area from the imposed strain assuming different starting fibre diameters.

iii. Except for an initial transient, the hardening rate (at a given temperature) is relatively insensitive to the growth rate of the samples and hence the scale of the Cr fibres.

The last point can be clearly seen if the K-M curves for the samples solidified at 6 mm/hr are shifted along the stress axis by an amount equal to the difference in the bulk yield stress for the two solidification conditions (figure 5.20). The net result of these three effects is that the stability of tensile deformation (as defined by Considere's Criterion) is greater for the eutectic alloy, particularly at low temperatures, when compared to pure Cu.

That extensive co-deformation of the Cr fibres, rather than their fracture occurs during this portion of the tensile response is implicit in the large amount of uniform strain that can be obtained in the specimens even at low temperature. This can also be deduced from simple observations of the evolution of the morphology of the microstructure. In a global sense, the deformation of the Cr is relatively homogeneous, particularly at low to moderate imposed strains. This is seen in samples

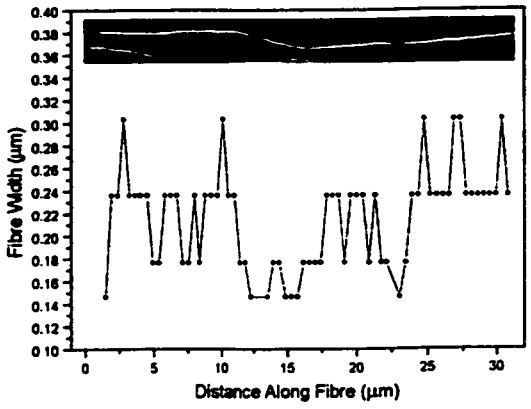

Figure 5.22 Variation in fibre diameter along the length of a single fibre within the neck of a tensile specimen.

strained both at 293 K and 77 K if the average cross-sectional dimension of the fibres is plotted versus the applied strain (figure 5.21). Attempts to correlate the shape of the fibres to the imposed plastic strain are difficult because of the relatively low strains involved in the tensile tests, however, it is clear from figure 5.22 that the bulk shape change of the Cr fibres follows the imposed plastic strain. At a more local level, the strain along a single fibre is quite inhomogeneous. This can be seen in figure 5.22 where the measured variation in fibre cross-section along a single fibre is shown for a fibre lying within the neck of a specimen strained at 293 K. The implication of these observations is that, although on average the fibres deform plastically in an amount similar to the applied strains, local conditions for compatibility require an inhomogeneous pattern of flow. This could reflect either local variations in the plastic strain on the scale of individual cells in Cu, local variations in the flow strength of the Cr fibres, or it could suggest that a process of accommodation occurs that requires an inhomogeneous pattern of flow. It is difficult to differentiate between these processes simply from observations of macroscopic shape changes. This point will be considered later.

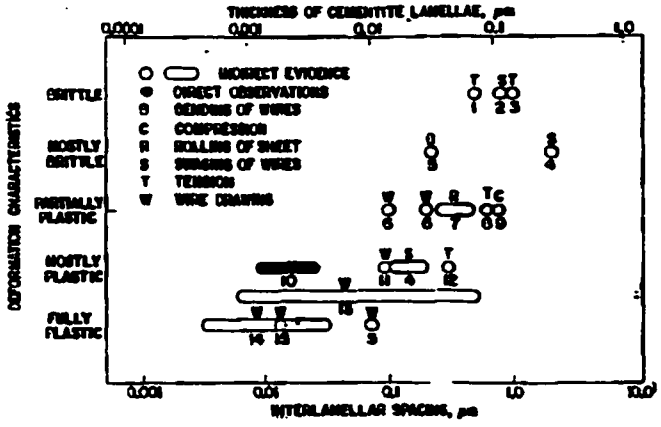

Figure 5.23 The transition from brittle to ductile behaviour of cementite in pearlitic steel as the scale of the carbide is reduced (Langford, 1977).

It is important to make a distinction at this point between the behaviour of the fine-scale (< 1 μm) eutectic Cr phase and larger (> 10 μm) dendritic particles observed in a number of samples. In the former case, extensive plastic deformation is observed, while in the latter fracture was found to occur during tensile testing at 77 K (figure 4.46). This points to the interesting possibility of a scale dependent ductile to brittle transition for the Cr phase. In comparison, high purity bulk Cr single crystals have been observed to exhibit

ductilities of only a few percent in tensile tests at room temperature (Gilbert et al., 1963). Further, in drawn hypereutectic Cu-Cr materials, the dendritic Cr phase has been observed to fracture during tensile testing at room temperature (Lee et al., 2000). These observations are consistent with the observations of Langford (1977) who showed that in drawn pearlitic steel the ability of the cementite phase to deform plastically was largely dependent on the scale of carbide particles (figure 5.23).

5.4.2 Contributions of Cr Fibres to the Mechanical Response During Co-deformation

In the introduction to this section the question of whether the Cr fibres contribute directly to the hardening behaviour of the eutectic alloy was raised. After yielding of the Cr fibres two possibilities exist. Either the fibres can continue to carry an increasing load and thereby contribute to the overall work hardening behaviour of the material, or they can deform under a nearly constant load and contribute nothing to the bulk mechanical response. If the fibres continue to carry an increasing load, it must be the result of continued load transfer. This may occur by a conventional process of work hardening (e.g. forest hardening) in the fibres, or by continued elastic loading of the fibres without the storage of forest defects. Deformation during the elastic/plastic portion of the flow curve represents an upper limit to this latter process in that the elastic strains in the fibres are approximately equal to the applied strains. During plastic co-deformation this condition is relaxed as the fibres are able to accommodate a portion of the applied strains plastically. Thus, the unrelaxed plastic strain during co-deformation arises due to the difference between the amount of plastic

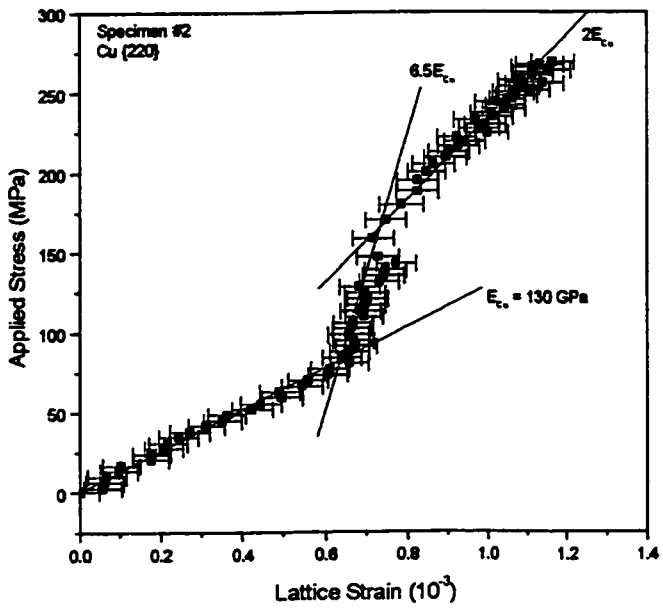

Figure 5.24 Representative Lattice strain versus applied stress for in-situ neutron diffraction experiments (specimen 2). Here, the lattice strains are plotted into the regime of plastic co-deformation are plotted.

strain in the two phases. It was shown that in the elastic/plastic regime the degree of load transfer could be followed by measuring the elastic strains in the matrix directly via diffraction or by estimating the long range internal stresses by examining the degree of anisotropy in the forward and reverse yield strengths. The same approach can be used to examine the degree of load partitioning, and therefore the contribution of the Cr fibres to the bulk hardening behaviour during plastic co-deformation.

A clear indication that load transfer continues during co-deformation can be obtained from neutron diffraction measurements of the lattice strain in the Cu. Figure 5.24 is data taken from the same sample as that shown in figure 5.14. Here, lattice strains in the Cu (along the tensile axis) are plotted against the applied stress for the total strain history of the material. The previously described elastic/elastic and elastic/plastic regimes are included, but now the data obtained after yielding of the Cr fibres are also shown. It is clear that the degree of load partitioning decreases on fibre yielding as indicated by the drop in the slope of the curve above applied stresses of ~ 200 MPa. This behaviour can be rationalized by extending the interpretation presented in section 5.3.4 to the plastic co-deformation regime. For the case of plastic co-deformation with equal *total* strains in the two phases along the tensile axis, equations 5.17 and 5.18 are modified to,

$$\begin{aligned} \sigma_c &= (1-f)E_m\varepsilon_m^{el} + f E_f \varepsilon_f^{el} \\ \varepsilon_c &= \varepsilon_p^m + \varepsilon_{el}^m = \varepsilon_p^f + \varepsilon_p^f \end{aligned} \qquad (5.30)$$

Following the same argument as before (i.e. assuming a dilute composite and considering the composite strain is dominated by plastic strain) equation 5.21 becomes for the plastic/plastic case,

$$\frac{d\sigma_c}{d\varepsilon_{el}^m} \approx E_m\left(1+\frac{E_f f}{\theta_m}\frac{d\varepsilon_p^*}{d\varepsilon_c}\right) \qquad (5.31)$$

where $\varepsilon_p^* = \varepsilon_p^m - \varepsilon_p^f$ is the unrelaxed plastic strain and θ_m is the work hardening rate of the matrix. The upper limit to equation 5.31 is given by the case where the fibres are purely elastically loaded and $\varepsilon_p^* = \varepsilon_p^m \approx \varepsilon_c$. This is simply the elastic/plastic case and thus returns equation 5.27 Alternatively, in the case where no plastic misfit develops between the two phases (e.g. if the fibres offered no further resistance to plastic flow after

yielding) $\frac{d\varepsilon_p^*}{d\varepsilon_C} = 0$ and equation 5.31 simplifies to $d\sigma_c / d\varepsilon_m^{el} = E_m$. In general, the response during plastic co-deformation will fall between these two bounds (e.g. $0 \le d\varepsilon_p^* / d\varepsilon_{el}^m \le 1$) and so the slope of the applied stress-lattice strain curve will fall between that observed during the elastic/elastic and elastic/plastic behaviour. This is exactly the situation observed in figure 5.24. Approximating the portion of the lattice strain/applied stress curve beyond fibre yield as being approximately linear gives a value for the slope of between ~ $1.7E_m$ and $2.0E_m$. Substituting the larger of these two values into equation 5.31 gives,

$$\frac{E_f f}{\theta_m} \frac{d\varepsilon_p^*}{d\varepsilon_c} \approx 1 \qquad (5.32)$$

Re-arranging gives,

$$E_f f \frac{d\varepsilon_p^*}{d\varepsilon_c} \approx \theta_m \qquad (5.33)$$

The term on the left hand side of equation 5.33 represents the rate of increase in the long range internal stresses in the matrix, while the term on the right represents the work hardening rate of the matrix. Thus, this approximate analysis would suggest that the contribution of the continued loading of the Cr fibres to the composite hardening rate is similar in magnitude to the contribution arising from the hardening of the matrix. Although, for clarity, only one set of collected data has been shown in figure 5.24, the above analysis fits well to the behaviour of all samples strained into the co-deformation regime (figure 4.57a).

Corroborating the above evidence for continued elastic loading of the Cr fibres during co-deformation is data collected during load/unload tests in uniaxial tension. Figure 5.25 reproduces representative data measured for the back stress in samples deformed at a) 293 K and b) 77 K as a function of forward plastic strain along with the forward flow stress. In both cases the back stress is plotted for different offsets used to determine the reverse flow stress. Here, as in the elastic/plastic case, it will be assumed that the variation in the

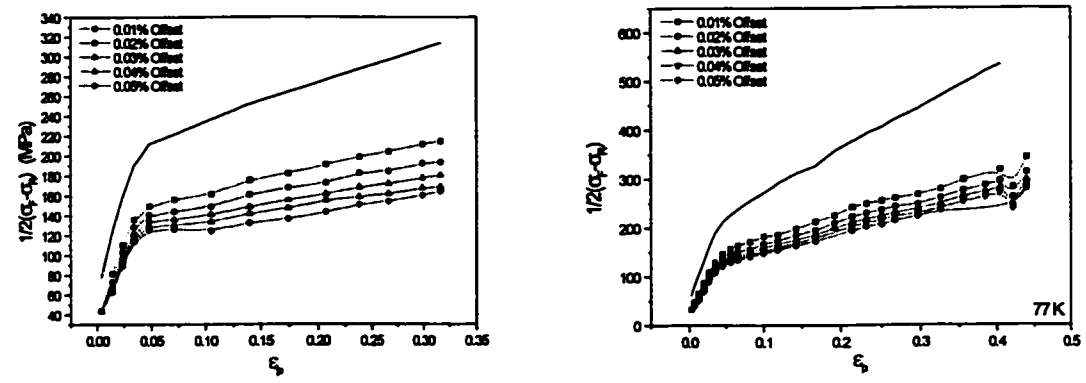

Figure 5.25 Back stress measured for samples tested at a) 293 K and b) 77 K. Also included are the monotonic forward flow curves.

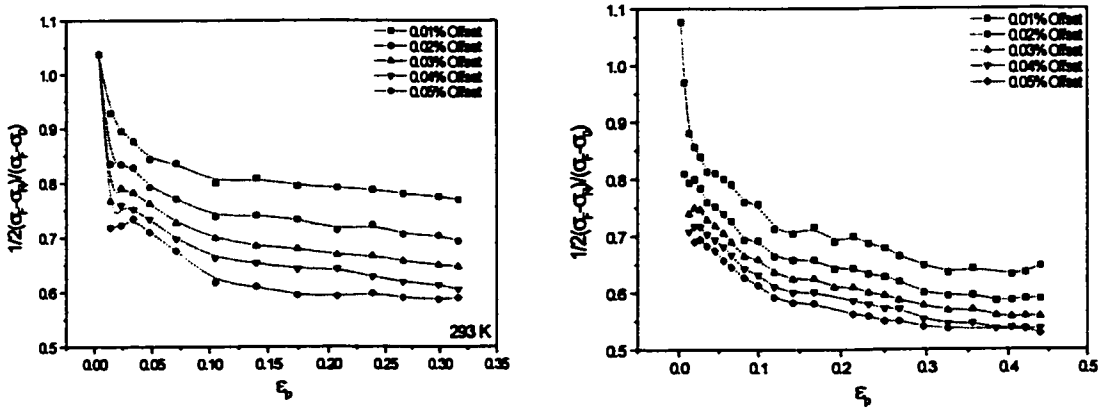

Figure 5.26 Parameter β as a function of plastic strain for samples tested at a) 293 K and b) 77 K.

back stress with forward plastic strain can be attributed primarily to the development of long range internal stresses. Thus, figure 5.25 implies that

i. the internal stresses (and therefore the load carried by the fibres) continues to rise with forward plastic strain

ii. the internal stresses rise approximately linearly with forward plastic strain during co-deformation

iii. the internal stresses are larger and increase faster with strain for samples tested at 77 K compared to samples tested at 293 K.

An alternative way to examine this data is to plot it as the ratio of the back stress to the forward flow stress minus the initial composite yield stress (denoted here as β). In the case where the back stress equals the long range internal stresses this ratio gives the fraction of the total work hardening that arises due to the long range internal stress. In the present case, as the transient portion of the reverse flow curve has been used to deduce the reverse flow stress, the absolute value of β is expected to represent an overestimate of the fraction of hardening attributable to the internal stress. However, again assuming that the variation of the back stress with strain is dominated by the internal stress, the rate of change of β is expected to give a reasonable estimate of the rate of change of the fraction of hardening attributable to the internal stresses. Figure 5.26 shows the variation of β with plastic strain for a) samples deformed at 293 K and b) 77 K. For samples tested at 293 K β initially drops rapidly from the elastic/plastic regime but begins to plateau at higher strains. A constant value of β requires that the rate of accumulation of internal stresses is equal to the work hardening in the matrix. This is equivalent to the conclusion reached from the neutron diffraction results presented above.

For samples tested at 77 K, the value of β continues to decrease out to the largest strains measured. Further, compared to samples tested at 293 K, the value of β is lower for an equivalent plastic strain. This indicates that forest hardening of the matrix is more sensitive to the change in temperature than the mechanisms giving rise to the internal stresses. This important point will be returned to when the detailed processes operating in the matrix are evaluated.

It is possible that the increasing load bearing capacity of the fibres at least partially arises due to conventional work hardening; i.e. the storage of forest dislocations within the fibres. TEM observations appear to preclude this as a possibility. The Cr fibres viewed after increasing amounts of plastic strain appear to be largely devoid of dislocations throughout the range of plastic strains obtained in a tensile test. Even in cases were dislocations are present their densities are $<< 10^8$ m^{-2}. This is clear from the TEM micrographs

shown in section 4.3.3.2 taken from tensile specimens strained various amounts, but similar features can be seen in samples that have been deformed in plane strain compression to strains of ~1.0 (figure 4.80). As mentioned earlier, caution has to be exercised in interpreting these results due to reverse flow on unloading. However, it seems unlikely that obstacles such as cell walls developed within the fibres would be able to completely relax and so some evidence of a substructure would be retained if it were present under load. At higher strains evidence of some dislocation storage in the fibres has been noted (figure 4.81). But those regions containing dislocations are separated by large regions that remain dislocation free.

The observed lack of dislocations within the Cr fibres even after significant amounts of plastic deformation parallels the observations made in many heavily co-deformed materials (e.g. Bevk, 1983, Wood et al., 1996). In these cases it is observed that when the scale of the embedded phase reaches the nanometer scale, the density of dislocations stored within the phase drops drastically. It appears that in the case of Cu-Cr, as has been suggested for heavily co-deformed material (Thilly, 2000, Wood et al.,1996), the storage of dislocations occurs primarily at the phase interface. Further, it suggests that the mechanical properties of the embedded fibres are controlled entirely by processes that occur at the phase interface. It is worthwhile at this point, to compare this behaviour with the behaviour assumed in the two common models for the co-deformation behaviour of two-phase materials. In the case of confined layer propagation models (e.g. Louchet, 1998, Embury and Hirth, 1994) plastic deformation is assumed to be confined to only one phase while the other deforms in an elastic manner only. Although this would predict a large internal stress as observed here, it obviously does not give a physical picture consistent with the results discussed above. Alternatively, the Hall-Petch type models (e.g. Andersen et al., 1999) also fail to capture the salient features of the process. In this case, assuming a fixed barrier strength would predict a negligible change in load borne by the Cr phase as a function of strain as the strains suffered during a tensile test change the scale of the phases by relatively minor amounts. Further, this mechanism would not predict the development of internal stresses or Bauschinger effect within the material. It must be concluded that continued hardening of the Cr fibres is a result of a combination of two mechanisms:,

i. an increasing barrier to the nucleation of slip from the phase interface or for the transmission of slip across the phase interface.

ii. an increasing unrelaxed plastic misfit that causes the fibres to continue to carry ever increasing elastic loads.

Both of the above two mechanisms rely on the storage of defects in the phase interface. Although a distinction has been made between the processes of slip transfer and nucleation of dislocation loops from the phase interface, once co-deformation has begun it becomes difficult to distinguish between the two. If a dislocation is emitted by the phase interface at one position, it must travel across the phase and (if it is not transmitted through into the Cu) it will become incorporated as an extrinsic dislocation in the phase boundary. This configuration is relatively high energy. One potential mechanism to reduce the energy of boundary would be for one of the dislocations in the surrounding Cu to react with the boundary dislocation to lower the overall energy of the configuration. The net resultant dislocation at the phase boundary will have a Burgers vector,

$$\Delta b = \left| b_{Cu} - b_{Cr} \right| \qquad (5.35)$$

The net result of this process, however, is exactly equivalent to the situation that would result from a Cu lattice dislocation being transmitted across the phase boundary and into the Cr fibre (or vice versa). In this case, conservation of Burgers vector at the phase boundary would necessitate a defect to be left in the boundary with a Burgers vector equal to that given in equation 5.35.

If it is assumed that once the reaction given by equation 5.35 occurs at the interface, the resulting defect in the boundary remains a strong obstacle to other dislocations entering or leaving the boundary, then there will be an effective rise in the barrier strength of the boundary. This strengthening may increase with further straining as the density of these defects in the interface increases. If it is assumed that the defects are equally spaced in the boundary then this spacing will be proportional to,

$$\lambda = \frac{L}{n} \propto \frac{b}{\varepsilon \cos\theta} \qquad (5.36)$$

where θ is the angle between the slip direction and the axis of the fibre. If slip occurred on every plane only once and every dislocation thus produced a defect in the interface, equation 5.36 would give the exact spacing. It is clear, however, that this is an overestimate of the rate of storage at the boundary and that mechanisms will exist to relax the structure formed at the boundary. However, using equation 5.36 to estimate the maximum size of source available in the interface or the maximum amount that a dislocation must bend to in order to cross a boundary can be performed using the Orowan equation,

$$\tau = \frac{\mu_{Cr} b}{\lambda} \ln\left(\frac{\lambda}{r_o}\right) \quad (5.37)$$

The combination of equation 5.36 and 5.37 is an overestimate in terms of the strengthening that may be achieved from this process. This is clear as the combination of these two equations would predict at rate of hardening that is a significant fraction of the elastic modulus. The reason for this overestimation may be traced to the implicit assumption that slip occurs only once on every atomic plane and that for each dislocation that crosses the fibre a dislocation is left in the phase interface. Further, it is assumed that these defects are strong obstacles to dislocation nucleation /transmission. Without detailed information concerning the rate of defect storage in the interface and the strength of the defects in the interface it is difficult to refine this argument. This mechanism does, however, predict a linear rate of isotropic work hardening; i.e. the hardening would be predicted to give no yield asymmetry in the forward and reverse directions. Similar arguments have previously been made for increased barrier strengths to slip transmission across grain boundaries in single-phase materials (Sutton and Balluffi, 1995) as well as in metallic multilayers (Misra et al., 2000).

The alternative mechanism for increasing the strengthening of the Cr fibres arises from the same interfacial defects as described above. It has been shown that during elastic/plastic deformation, dislocations are stored as loops around the Cr fibres giving rise to a mean internal stress on the order of,

$$\langle \sigma \rangle_m = E_f f \varepsilon_p \quad (5.38)$$

where ε_P is the applied plastic strain (equal to the plastic misfit between the two phases). Once plastic co-deformation occurs the rate of internal stress accumulation drops substantially as the material can now relax the plastic misfit by plastic flow in the Cr fibres. However, if the rate of straining of the fibres does not exactly balance with that in the matrix a plastic misfit between the two phases will continue to develop. This may occur if the amount of slip on either side of the phase interface is not exactly equal.

The storage of a net residual dislocation in the phase interface is associated with elastic straining of the Cr fibre. The unrelaxed plastic strain in this case is given by,

$$\varepsilon_P^{\bullet} = \frac{n_{Cr}\Delta b}{L} \qquad (5.39)$$

This plastic misfit arising from the residual dislocation left in the boundary will cause an increasing internal stress,

$$\langle\sigma\rangle_m = E_f f \varepsilon_P^{\bullet} \qquad (5.40)$$

If it is assumed that the amount of slip in the matrix is equal to the applied plastic strain then,

$$\varepsilon_P = \frac{n_{Cu} b_{Cu}}{L} \qquad (5.41)$$

The ratio of the plastic misfit between the two phases to the applied plastic strain is then given by,

$$\varepsilon_P^{\bullet} \approx \frac{n_{Cr}}{n_{Cu}} \frac{\Delta b}{b_{Cu}} \varepsilon_P \qquad (5.42)$$

and the rate of work hardening due to the accumulation of internal stresses during co-deformation is,

$$\frac{d\langle\sigma\rangle}{d\varepsilon} \approx E_f f \frac{d\varepsilon_P^{\bullet}}{d\varepsilon_P} \approx E_f f \frac{n_{Cr}}{n_{Cu}} \frac{\Delta b}{b_{Cu}} \qquad (5.43)$$

The ratio n_{Cr}/n_{Cu} gives the ratio of the net number of dislocations to have operated in the two phases. It is possible to annul the creation of the internal stress if this ratio can be made to exactly balance the ratio $\Delta b/b$. This would constitute a process of plastic relaxation as an "extra" amount of slip would be necessary in one of the phases. Since, plastic relaxation of strains accumulated along the tensile axis is expected to be small because of the geometrical constraints, the ratio $n_{Cr}:n_{Cu}$ is probably close to 1.0 (as it would be if every dislocation in the Cu were able to be transmitted through the phase interface and into the Cr) then the rate of work hardening should be linear and proportional to,

i. the modulus of the fibres

ii. the volume fraction of fibres

iii. the difference in Burgers vectors between the two phases

Such a mechanism for continued development of internal stresses in co-deformed two-phase materials has been previously suggested by Louchet (1998). This mechanism would explain the observation in the Cu-Cr system that internal stresses continue to rise during the process of co-deformation. Further, it would also predict the linear rate of hardening. One disagreement with the above model and the experimental observations lies in the fact that the hardening rate of the material is observed to be strongly temperature dependent. Figure 5.27 shows the measured hardening rate during plastic/plastic deformation normalized by the hardening rate in the elastic/plastic portion of the flow curve multiplied by $\Delta b/b_{Cu}$ plotted against test temperature. If the temperature

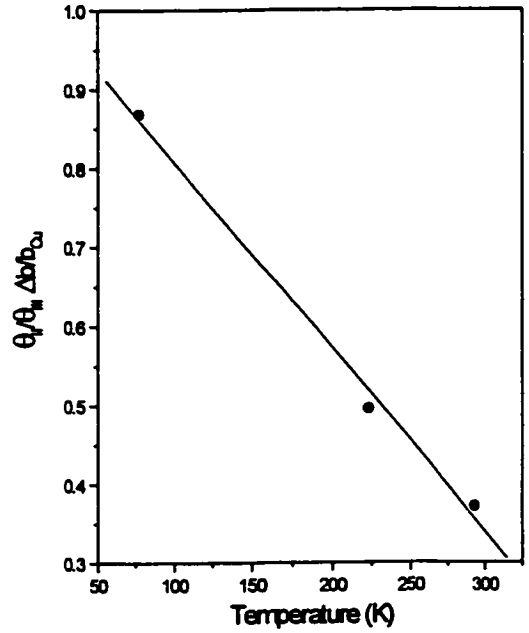

Figure 5.27 Normalized plastic-plastic hardening rate. If there were no relaxation of the structure developed at the boundary this ratio would equal 1.0. The fact that it varies with temperature suggests a thermally activated mechanism of relaxation.

dependence of the hardening rate were solely due to the temperature dependence of the Burgers vector and the elastic modulus, this plot should give a horizontal line. That it does not suggests that there is a thermally activated process reducing the accumulation of plastic misfit. This could arise from a number of processes of plastic relaxation, including those that may occur in the interface itself. It is worth noting that at 77 K the ratio of the plastic/plastic to elastic/plastic hardening rate approaches 1.0 suggesting that at lower temperatures relaxation processes are restricted, and the rate of internal stress accumulation is approximately that given by equation 5.43.

This analysis, although extremely simple, suggests a mechanism by which the elastic strains in the fibre may continue to increase with plastic co-deformation without the necessity of storing dislocations within the fibre. Further, it suggests that the rate of increase of stress carried by the fibres should be approximately proportional to the imposed strain in accord with the experimental results. The above analysis assumes that every dislocation that enters the boundary remains an obstacle to further deformation. This precludes the possibility that mechanisms of relaxation within the boundary exist. It is possible that dislocations entering the boundary may be able to dissociate within the boundary and react with other structural defects (Sutton and Balluffi, 1995). In this way, only some fraction of defects entering the interface will be available to act as barriers to reduce the size of sources within the boundary. The above process must reach a limit associated with the density of defects that can be placed within the boundary. An upper limit to the applicability of this argument must be when the spacing between interfacial defects approaches the core cutoff ($\lambda \approx b$) corresponding to a shear strain of the order of $\gamma = (\cos\theta)^{-1}$. Very high densities of well-arranged interfacial defects have been observed via HRTEM of wire drawn Cu-Nb. In this case dislocations were arranged approximately every 8 atomic planes (Thilly, 2000, Wood et al, 1996) at the interface.

5.4.3 Contribution of Cu to the Mechanical Response During Co-Deformation

From the above discussion it is clear that the fibres contribute directly to the hardening behaviour of the materials by continuing to carry an ever-increasing load after the onset of yielding. The question that remains to be answered is whether the presence of the fibres effects the flow behaviour of the Cu. It was shown during

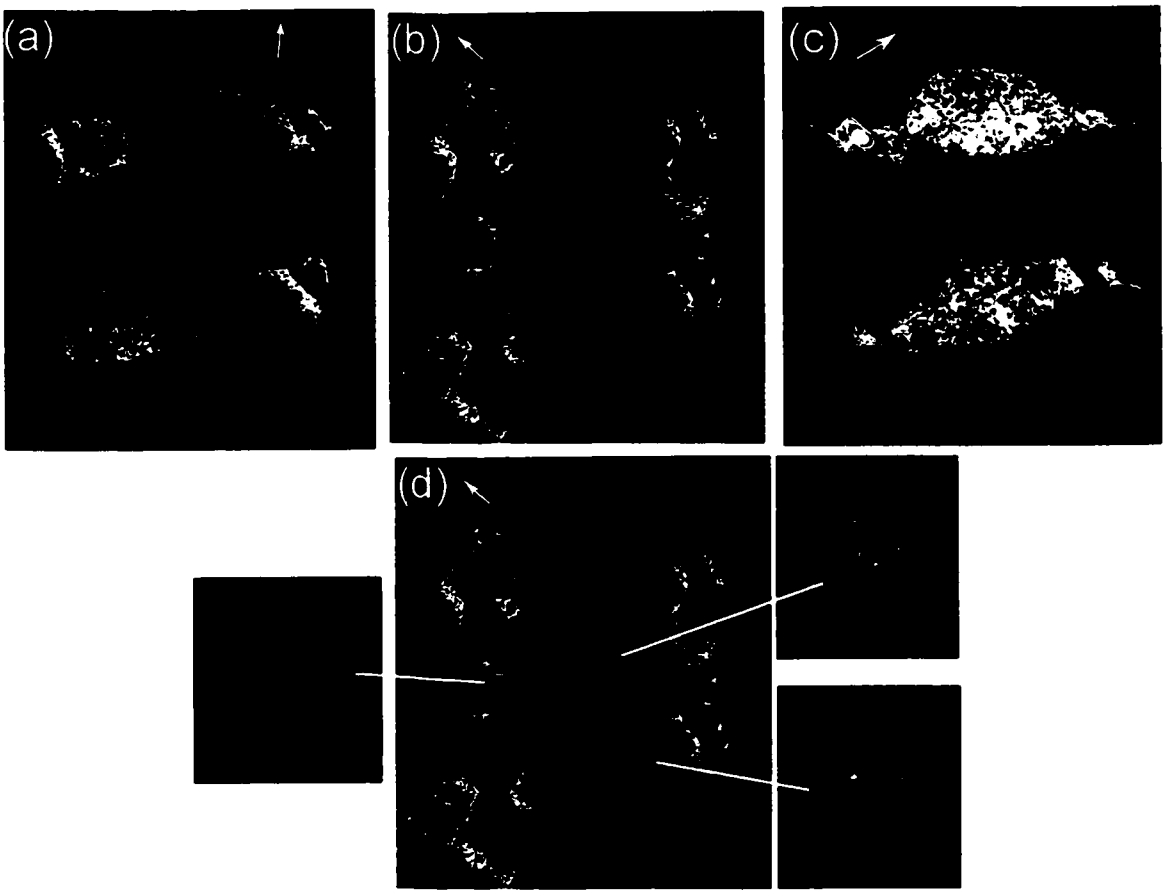

Figure 5.28 DF micrographs taken with the beam direction close to one of the primary slip plane normals showing the lobes of contrast connecting four fibres. a) $\mathbf{g} = [\bar{2}20]$ b) $\mathbf{g} = [\bar{2}02]$ c) $\mathbf{g} = [02\bar{2}]$ d) same as b) but including Kikuchi patterns taken from different regions. The contrast between the bands is seen to arise from a small (~1 - 2°) rotation between different regions.

the elastic/plastic stage of deformation a high rate of dislocation storage occurred close to the fibre matrix interface. If the plastic misfit between the phases continues to increase with co-deformation, this process of dislocation storage must continue at a rate determined by the rate of accumulation of plastic misfit. Again, it must be remembered that the structure viewed in the TEM may differ substantially from the structure that existed under the load. Both reverse plastic flow occurring on unloading of the specimen and loss of dislocations on thinning of the foil will contribute to this. Annealing of the structure formed in specimens tested at 77 K when warmed to room temperature is also a concern. However, it is clear that even under these conditions the structure in the vicinity of the fibres is substantially different from that developed far from the

fibre matrix interface. Detailed interpretation of these structures is difficult in comparison to the idealized structures previously studied in dispersion hardened materials because of relatively high strains and multiple slip encountered here. This was also the conclusion of Gould and Martin (1973). However, it is clear from the micrographs presented in section 4.3.3.1 that there are particular characteristics of the microstructure that appear to be directly correlated with the presence of the fibres. Among the most obvious are;

i. Similar regions of lattice rotation in regions of the Cu surrounding the Cr fibres. The rotations in this region are typically small (of the order of ~ 0 - 5°) and die off quickly from the phase interface (figure 4.68).

ii. Directionality to the structure developed around the fibres was evident in the sense that lobes of contrast are typically observed around the fibres. In regions where fibres are clustered together the lobes appear to run from fibre to fibre.

iii. In fibres viewed in longitudinal sections, the high density of dislocations stored at the phase interface compared to that stored in the regions between fibres is apparent. The spatial heterogeneity of the structure along the length of single fibres should be noted.

The observed substructure develops with strain in a complicated fashion. Figure 4.61shows a series of transverse BF TEM micrographs taken from samples strained various amounts was presented. It can be seen that the characteristic features develop rather quickly after the onset of co-deformation and persist up to the point of necking. After necking, the structure becomes more complicated as the straining becomes inhomogeneous. At low magnifications, the effect of the local storage of dislocations close to the Cr fibres is apparent. At strains just beyond the point at which bulk yielding of the Cr fibres occurs, the substructure in the bulk of the Cu is not well developed. In regions surrounding Cr fibres, however, the development of cell walls and higher dislocation densities can be seen. At higher strains ($\varepsilon \sim 0.2$) a clear cellular structure is developed in the bulk matrix, while the regions surrounding the fibres continue to accumulate dislocations. The scale of the substructure around the fibres appears to remain largely dictated by the local inter-fibre spacing.

The characteristic feature of the microstructure (viewed in the TEM) during homogeneous tensile deformation were the lobes of contrast that appeared to surround the Cr fibres. These lobes appeared, at low magnification, to be similar around all fibres and in many cases appeared to connect adjacent fibres. The lobes appeared to be associated with the predominant facet of the fibre, although two different orientations of these lobes were observed (e.g. see figures 4.66 and 4.64).

Figure 5.28 shows an example of the structure formed about one set of fibres in a sample deformed to ε~0.25. Here the beam direction is close to $[111]_{Cu}$. A high density of dislocations can be seen very close to the fibres. However, this rapidly drops off moving away from the phase interface. The Kikuchi patterns shown in figure 5.28d show the diffraction conditions taken from inside and outside of the lobes of contrast. The local rotations giving rise to the contrast across a lobe are only~1-2°. These features suggest a process of secondary slip occurring in the vicinity of the phase interface.

The difficulty in ascertaining the degree of secondary slip or its origins lies in the fact that the symmetric orientation of the tensile axis of the Cu matrix causes multiple slip from the outset of deformation. Thus, as has already been pointed out, the pattern of slip is complicated from the onset of deformation. The presence of 5 or more slip systems all acting in similar amounts close to the fibre would also tend to cause relatively small lattice misorientations (as observed) particularly compared to the observations made on samples oriented for single slip. Humphreys and Hatherly (1995) have previously commented on the fact that models proposed to predict the rotations around rigid particles in materials undergoing single slip far overestimate the measured degree of misorientation measured in samples that have been deformed under conditions of multiple slip. Other investigators have also observed secondary slip in the vicinity of fine-scale embedded fibrous phases. Garmong (1976) presented observations of slip traces and TEM observations of interfacial sources in a directionally solidified eutectic alloy as evidence for significant secondary slip activity in the vicinity of the fibres. Gould and Martin (1973) observed secondary slip almost immediately from the onset of plastic flow in the Al matrix of directionally solidified Al-Al_3N single crystals, although the starting orientation of the matrix was located within the centre of the primary triangle.

Table 5.3 Transverse Aspect Ratio of Cr Fibres as a Function of Imposed Tensile Strain

	$\varepsilon = 0$	$\varepsilon = 0.25$	$\varepsilon = 0.5$	$\varepsilon = 0.9$
Aspect Ratio	2.20 ± 0.48	1.97 ± 0.40	1.99 ± 0.29	1.83 ± 0.3

As it is quite difficult in fibre reinforced materials to relax plastic misfit along the fibre axis, it should be expected that during co-deformation similar tensile strains must be occur in both phases parallel to the long axis of the fibres. In the transverse direction, on the other hand, a plastic misfit (if it arises) may be accommodated much more easily by processes of secondary slip. In this work it was shown in section 5.3.1.2 that, macroscopically, the tensile specimens develop a nearly plane strain model of deformation due to the $[110]_{Cu}$ texture. However, the Cr fibres are oriented with their axes close (~9° away)to a $[111]_{Cr}$ direction. In this orientation it was shown that the Taylor factor for plane strain deformation, in a manner that is compatible with the plane strain deformation in the Cu, was significantly higher than that for axisymmetric deformation (4.90 versus 3.67 assuming <110>[111] slip). It is possible that instead of undergoing the plane strain mode of deformation imposed by the surrounding Cu, the Cr fibres undergo axisymmetric deformation thereby forcing the Cu to undergo extra deformation in the vicinity of the fibres in order to maintain compatibility. In order to accomplish this, slip must occur on four additional systems in regions adjacent to the fibres. This pattern of flow in the matrix raises the Taylor Factor, and therefore the stress necessary for flow in the vicinity of the fibres, compared to that necessary for axisymmetric flow. The consequence of the different patterns of slip in the matrix will result in the storage of a higher density of dislocations in the vicinity of the fibres, as is observed. Evidence for the axisymmetric deformation of the Cr fibres can be deduced by observing their cross-sectional aspect ratio as a function of strain. Table 5.3 lists the values of the measured aspect ratios of fibres measured from transverse TEM foils after various amounts of tensile strain. It is clear that, while the area of the fibres is continuously reduced, the aspect ratio of the fibres remains close to 2 even up to strains in the neck of the tensile specimen approaching 0.9. This is interesting, considering the opposite effect is observed in wire drawn fcc/bcc materials where the bcc phase is observed to deform in plane strain.

It is clear from the above discussion that the presence of the fibres has an influence on the development of substructure in the Cu, particularly in the regions surrounding the Cr fibres. What must be determined is

whether this extra dislocation activity in the matrix will have an effect on the average flow behaviour of the matrix. An appropriate starting point for a discussion of the influence of embedded phases on substructural strengthening is via Ashby's theory of geometrically necessary dislocations (Ashby, 1971). For material containing second phase particles that have a plastic misfit ε^*_p with the matrix, the misfit may be accommodated through the storage of a density of geometrically necessary dislocations,

$$\frac{d\rho_g}{d\varepsilon} = \frac{\sqrt{f}}{r}\frac{c}{b}\frac{d\varepsilon^*_p}{d\varepsilon} \qquad (5.44)$$

where c is a geometrical constant, $r/\sqrt{f}$= inter-fibre spacing. In the present case, it has been argued that the misfit that must be accommodated by extra deformation in the matrix is associated with the difference in transverse strains between the two phases. However, due to the low volume fraction of fibres in this material, the rate of dislocation accumulation associated with equation 5.44 will be localized into the region adjacent to the fibres. Outside of these regions a cellular structure characteristic of pure Cu is observed. This qualitative argument would suggest that substructural strengthening due to extra dislocation storage in the regions surrounding the fibres should make a minor contribution to the overall strengthening of the material. A fully quantitative comparison of the hardening contribution predicted by equation 5.44 compared to other strengthening methods in the Cu-Cr system will be reserved until later in this section.

Since it has been argued above that the presence of the Cr fibres effects the mechanisms of deformation close to the fibres, it is of interest to probe the substructure that is formed in the eutectic alloy to see if it is similar to that developed in pure Cu under similar testing conditions. Although testing has not been extensive (tests have been limited to samples solidified at 57 mm/hr and tested under only one temperature condition), the temperature sensitivity of the flow stress deduced from Cottrell-Stokes tests has been used to examine the evolution of the structure during straining. From the macroscopic response shown in figure 4.34 it is possible to measure the Cottrell-Stokes ratio. The results of this calculation are shown in figure 5.29. The data is plotted as the ratio of flow stress measured at 293 K to that measured at 77 K as a function of plastic strain. Also plotted is data for pure polycrystalline Cu specimens deduced by Bullen and Hutchinson (1961, Bullen

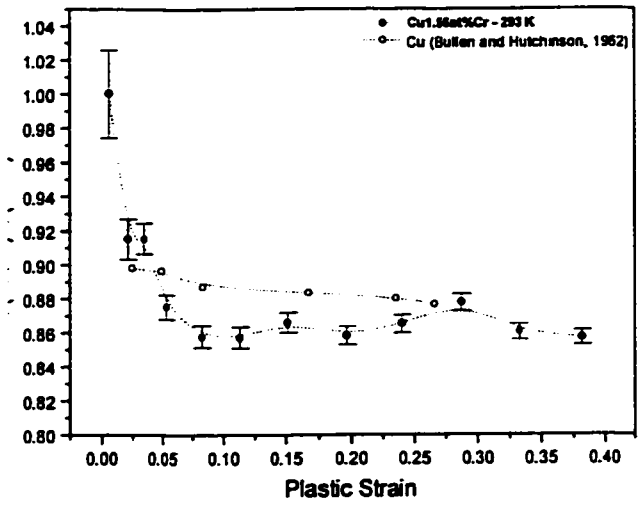

Figure 5.29 Cottrell-Stokes ratio for Cu-Cr (solidified at 57 mm/hr) compared with that of pure polycrystalline Cu (Bullen and Hutchinson, 1963).

and Rogers, 1963, Bullen and Hutchison, 1962). The initial transient in Cottrell-Stokes ratio is indicative of the nearly thermal process of hardening associated with elastic fibre loading during the elastic/plastic portion of the flow curve. Beyond the onset of plastic co-deformation, the Cu-Cr samples obey the Cottrell-Stokes law (constant σ_{293}/σ_{77}). This is in agreement with the above described observations that the structure formed in the Cu appears to be made up of regions consisting of tangles surrounding the fibres and a normal cellular substructure in the bulk of the Cu, i.e. the mechanism of substructural hardening due to forest hardening is similar in both the eutectic alloy and single-phase Cu. Similar results have been obtained for dispersion hardened materials (Bullen et al., 1964). The one significant difference between the C-S ratio for pure Cu and Cu-Cr is that the magnitude of the C-S ratio for Cu-Cr lies below that measured by Bullen and Hutchinson for pure Cu. The magnitude of this effect, although small can be attributed to the variation in Peierls stress of the bcc Cr fibres with temperature and thus a stronger contribution to the flow stress from the fibres at 77 K compared to at 293 K.

5.4.4 A Phenomenological Description of the Bulk Mechanical Response of Directionally Solidified Cu-Cr

At the beginning of this section, the measured mechanical response of the material was plotted as K-M plots. It is worth returning to these observations now to see if the basic form of the curves can be accounted for in a manner that is consistent with the mechanisms discussed above. In this way it appears that it should be possible to account for the overall hardening rate of the material by considering the rate of evolution of three structural parameters:

i. The rate of statistical dislocation accumulation in the bulk of the matrix of the Cu, $d\rho_s/d\varepsilon$

ii. The rate of accumulation of extra dislocations in the matrix surrounding the fibres, $d\rho_g/d\varepsilon$

iii. The rate of accumulation of dislocations in the phase interface associated with the plastic misfit between phases controlling the flow stress of the fibres, $d\rho_f/d\varepsilon$

The phenomenological Kocks-Mecking-Estrin approach (Kocks 1976, Mecking and Kocks, 1981, Mecking, 1977, Estrin and Mecking, 1984, Estrin, 1996) can be used to examine the way in which these three factors contribute to the overall hardening process. The basic starting point is to assume that the average dislocation density can be considered the governing parameter in dictating the mechanical response of the material (for a given set of conditions, e.g. temperature and strain rate) and that the dislocation density can be associated to the mean flow stress via the Taylor equation,

$$\sigma = M\alpha\mu b\sqrt{\rho} \qquad (5.45)$$

Now, in order to find the rate of evolution of the mechanical strength it is necessary to know the rate of evolution of the structure. In a single-phase material it is assumed that this follows,

$$\frac{d\rho}{d\varepsilon} = k_1\sqrt{\rho} - k_2\rho \qquad (5.46)$$

where the first term is the rate of storage assumed to occur on obstacles spaced a distance $1/\sqrt{\rho}$ apart (e.g. forest dislocations). The second term accounts for the process of dynamic recovery. The constants k_1 and k_2 can be determined by interrogating the measured response of samples. It is important to note, however, that k_1 is a constant independent of the test conditions while k_2 is strongly temperature and strain rate dependent. Differentiating equation 5.45 with respect to strain and substituting equation 5.46 then gives the rate of hardening as a function of the applied stress as,

$$\theta = \theta_0 \left(1 - \frac{\sigma}{\sigma_s} \right) \qquad (5.47)$$

where,

$$\begin{aligned} \theta_0 &= M^2 \alpha \mu b k_1 / 2 \\ \sigma_s &= M \alpha \mu b \left(k_1 / k_2 \right) \end{aligned} \qquad (5.48)$$

are the stage II hardening rate (approximately $\mu/20$) and the saturation stress (the stress at which the hardening rate falls to zero) respectively. Equation 5.47 is really only sufficient to explain the range of mechanical response of materials deforming in stage III (e.g. it does not predict a separate stage II and ignores stage IV at high stresses). However, for polycrystals deformed in uniaxial tension the above description appears quite good.

The above formalism has been expanded to account for the possible storage of dislocations at obstacles with a fixed spacing; e.g. second phase particles (e.g. Estrin, 1996). If it is assumed that storage due to second phase particles and storage due to dislocation-dislocation interactions occur in a parallel manner (Estrin, 1996), then equation 5.46 can be rewritten in the form,

$$\frac{d\rho}{d\varepsilon} = k + k_1 \sqrt{\rho} - k_2 \rho \qquad (5.49)$$

where $k = c(b\lambda)^{-1}$, with c a geometrical constant of magnitude close to unity) and $\lambda \approx r/\sqrt{f}$ is the mean spacing between fibrous obstacles. The addition of the strengthening due to dislocation-dislocation interactions and dislocation-particle interactions in the manner depicted in equation 5.49 probably gives an overestimate to the true effect of the hardening due to substructural strengthening unless one of the two terms dominates. Equation 5.49 assumes an addition of dislocation densities of the form,

$$\sqrt{\rho_{eff}} = \sqrt{\rho_s + \rho_g} \qquad (5.50)$$

In the case of the Cu-Cr material, it is apparent that the extra dislocations in the matrix tend to be localized into a volume of material surrounding the fibres. In this case it seems inappropriate to simply average the total dislocation density over the entire volume of the sample as implied by equation 5.49. Instead, the proper addition rule should follow,

$$\sqrt{\rho_{eff}} = f_s\sqrt{\rho_s} + f_g\sqrt{\rho_g} \qquad (5.51)$$

where f_s and f_g reflect the volume fractions of the matrix that store dislocations in a manner independent of the presence of the fibres and in a manner directly dictated by the fibres. Lilholt (1993) has discussed the errors associated with the use of equation 5.50 in place of equation 5.51. The important conclusion is that equation 5.50 leads to an overestimate of the strengthening resulting from the presence of geometrically necessary dislocations. Unfortunately, equation 5.51 makes the K-M approach significantly more complicated to implement, thus the dislocation density is generally averaged over the entire volume of the material (equation 5.50) (Estrin, 1996). This approach will be adopted below, but it will be shown that even with this overestimation, the effect of the geometrically stored dislocations on the overall hardening response is small.

Finally, it is necessary to account for the increasing flow stress of the Cr fibres. It was argued that the flow stress of the fibres may arise from either a mechanism of "source shortening" occurring due to the storage of defects in the phase interface or due to the a small but increasing plastic misfit that continues to rise

with plastic strain. In both cases, a simple model would predict a linear hardening rate from both of these sources. Thus the apparent flow stress of the fibres may predicted as,

$$\sigma = k_3 M \mu_{Cr} \varepsilon \qquad (5.52)$$

where k_3 can be considered a constant reflecting the efficiency of storage of defects in the phase interface (e.g. the rate at which annihilation, cross slip, climb or other processes of dynamic recovery may occur in the interface). It is important to realize that equation 5.52 includes a kinematic hardening mechanism, e.g. it is directional in nature. Equation 5.45 makes no distinction regarding the direction of loading, thus the derivations made below *must be restricted to monotonic, proportional loading*. The predictions made below are not applicable to situations where the strain path is changed during loading.

Adding equations 5.45 and 5.52 then gives the total flow stress in the case of Cu-Cr,

$$\sigma = (1-f) M_{Cu} \alpha \mu_{Cu} b \sqrt{\rho} + f M_{Cr} \mu_{Cr} k_3 \varepsilon \qquad (5.53)$$

Differentiating with respect to strain gives,

$$\theta = (1-f) M_{Cu} \alpha \mu_{Cu} b \frac{1}{\sqrt{\rho}} \frac{d\rho}{d\varepsilon} + f M_{Cr} \mu_{Cr} k_3 \qquad (5.54)$$

In the current case the term (1-*f*) is approximately equal to 1. Equation 5.54 can be rewritten as,

$$\theta = \frac{M_{Cu} \alpha \mu_{Cu} b}{2} \left(\frac{M_{Cu} \alpha \mu_{Cu} b}{\left(\sigma - f M_{Cr} k_3 \mu_{Cr} \varepsilon\right)} k + k_1 - k_2 \left[\frac{\sigma - f M_{Cr} k_3 \mu_{Cr} \varepsilon}{\alpha \mu_{Cu} b} \right] \right) + f M_{Cr} k_3 \mu_{Cr} \qquad (5.55)$$

rearranging and collecting terms gives,

$$\theta = \theta_0 \left(1 - \frac{\sigma}{\sigma_s} \right) + \frac{\left(M_{Cu} \alpha \mu_{Cu} b\right)^2}{2\left(\sigma - f M_{Cr} \mu_{Cr} k_3 \varepsilon\right)} k + f M_{Cr} \mu_{Cr} k_3 \left(1 + \frac{\theta_0}{\sigma_s} \varepsilon \right) \qquad (5.56)$$

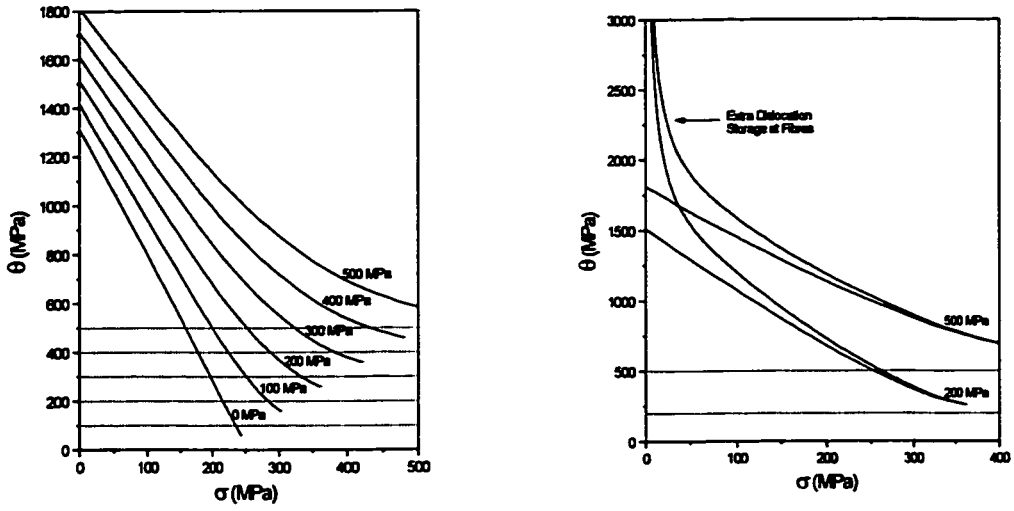

Figure 5.30 Predictions of the described model a) for different levels of elastic loading of the fibres (no extra dislocation storage term) b) comparison of predictions when extra dislocation accumulation is allowed.

At this point it is not possible to simplify this further to remove the strain terms from the above equation to give an analytical result. However, some general comments can be made based on equation 5.56 regarding the shape of the θ–σ curve. For the case where the substructural strengthening due to the fibres can be neglected and in the limit of $\sigma = 0$ and $\varepsilon = 0$ then θ reduces to,

$$\theta(\sigma = 0) = \theta_0 + fM_{Cr}\mu_{Cr}k_3 \qquad (5.57)$$

Alternatively, when σ is allowed to go to infinity,

$$\theta(\sigma \to \infty) = fM_{Cr}\mu_{Cr}k_3 \qquad (5.58)$$

In the case where substructural strengthening is included, the hardening rate still approaches the asymptotic value predicted by equation 5.58 due to the σ^{-1} dependence in the substructural strengthening term.

The results of this K-M model for a material that behaves in the manner described in equation 5.58 is shown in figure 5.30a. Here, various levels of the asymptotic hardening rate (equation 5.58) have been used to

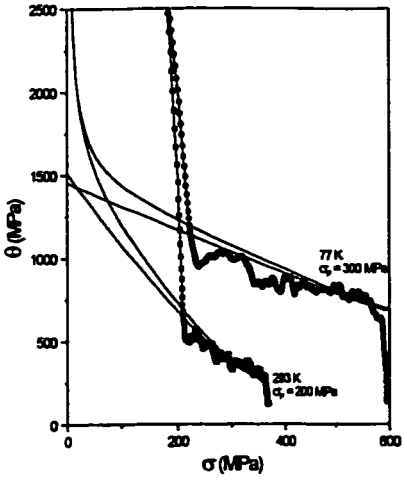

(a)

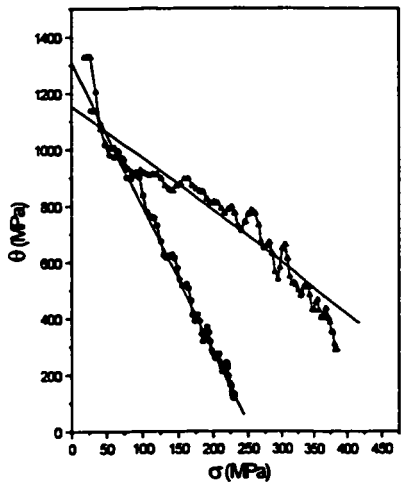

(b)

Figure 5.31 a) Fit of K-M model to directionally solidified Cu-Cr (57mm/hr) at 293 K and 77 K. b) Vocce law fit of pure copper used in model.

generate the plots and the term due to the storage of extra dislocations at the phase interface has been neglected. Figure 5.30b shows the effect of including the extra dislocation storage term. Instead of approaching zero at a saturation stress, the hardening rate of the composite material asymptotically approaches the hardening rate given by equation 5.58. It is important to note that this asymptotic hardening rate is temperature dependent through the temperature dependence of k_3 and the shear modulus of the Cr.

Figure 5.31a shows the fit of the above model to the experimentally determined K-M plots for Cu-Cr solidified at 57 mm/hr and tested at 293 K, and 77 K using parameters describing the behaviour of the matrix derived from the plots in figure 5.31b. In both figure 5.31, curves are drawn for the model that includes the substructural strengthening due to geometrically necessary dislocations and for the model that neglects this contribution. Assuming an inter-fibre spacing of $0.1\mu m/\sqrt{0.02} = 1$ μm gives results for the two models that differ by an insignificant amount. Consideration of the TEM micrographs presented above (e.g. figure 4.26) suggests that an inter-fibre spacing of 1 μm represents a lower limit, thus it must be concluded that the storage of geometrically necessary dislocations has a relatively minor effect in this material. This is consistent with the observations discussed above.

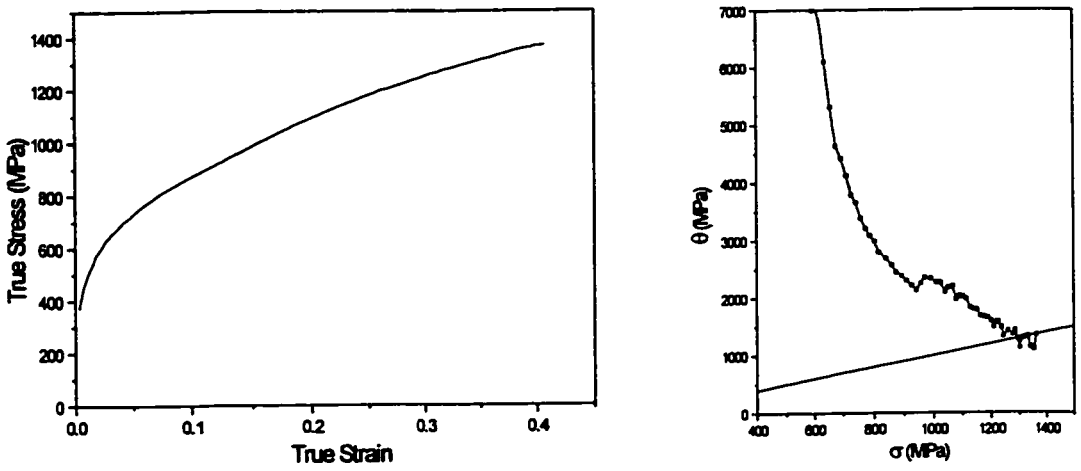

Figure 5.32 a) Stress/strain response and b) K-M plot for directionally solidified Ni-W

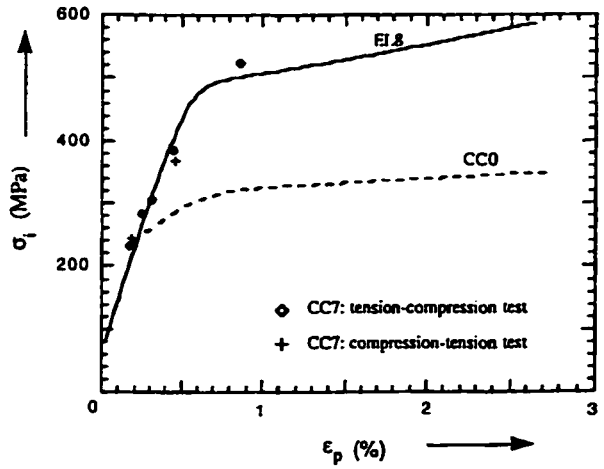

Figure 5.33 Back stress in austenoferritic stainless steel as a function of plastic strain (Verhaeghe, 1996).

In fitting the above model to the experimental K-M curves, it was necessary to choose values for the asymptotically approached hardening rate for the Cr fibres; i.e. a value for $k_3 f M_{Cr} \mu_{Cr}$. It was found that the best fit values of this slope correspond well to the slopes deduced from the rate of back stress evolution during co-deformation shown in figures 5.25a and 5.25b for samples tested at 293 K and at 77 K. This would suggest that the main source of the increased load bearing capacity of the fibres arises due to the small plastic misfit that continues to develop during plastic co-deformation.

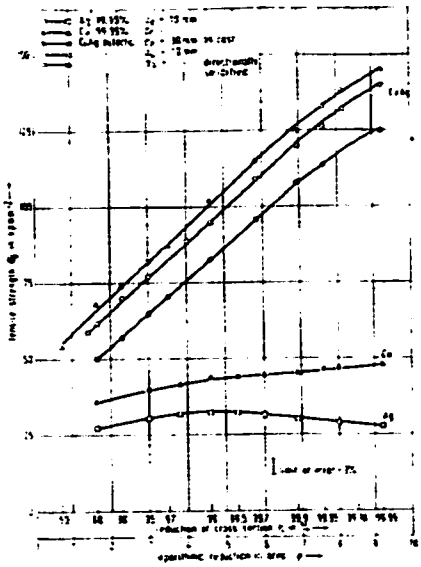

Figure 5.34 Hardening behaviour of Cu-Ag eutectic deformed by wire drawing (Frommeyer and Wassermann, 1975).

It is interesting to compare the above described behaviour with other similar materials deformed by co-deformation. Unfortunately, as was discussed in Chapter 2, there is a general lack of literature regarding the tensile response of simple directionally solidified eutectic materials tested from the as-cast state during plastic co-deformation. Figure 5.32a reproduces the tensile response for a directionally solidified Ni-W eutectic alloy tested by Garmong and Williams (1975). From this data the K-M plot for the material has been deduced and plotted in figure 5.32b. As in the case of the Cu-Cr alloy, this alloy exhibits a slowly decaying hardening rate from an initial plateau region associated with the elastic/plastic regime of deformation. Although no data was presented for this material in terms of the rate of internal stress accumulation, it seems clear that the material must deform in a similar manner to the Cu-Cr, continuing to have a slowly increasing plastic misfit between the two phases. The fact that internal stresses do continue to increase after the onset of plastic co-deformation has been observed for an austenoferritic stainless steel (Verhaeghe, 1996). Although the microstructure is not nearly as simple as the directionally solidified material, it is clear that the internal stresses (as measured by the Bauschinger effect) are very large in this material and continue to increase after the yielding of the ferritic phase (figure 5.33).

At large strains, the above model would continue to predict a constant rate of hardening. Wire drawing of directionally solidified Ni-W was carried out by Kubisch and Courtney (1986). Here, the eutectic alloy continues to harden at strains well beyond the onset of stage IV in single-phase materials. This is also seen in published data on wire drawn Cu-Ag eutectic alloys (Frommeyer and Wassermann, 1975). Figure 5.34 is reproduced from the work of Frommeyer and Wassermann and shows the nearly linear increase in the flow stress of the eutectic alloy drawn to various strains along with the strength of pure Cu and Ag wires drawn to

similar strains. It is tempting to suggest that in such materials, the hardening mechanisms discussed for the Cu-Cr alloy studied here continue to contribute to this linear hardening rate even at very large strains. It is important to note, however, that other hardening mechanisms will also tend to become important particularly as the interphase spacing continues to be reduced. In particular, the dimensional constraint imposed by continuously reducing spacing between phases will result in strengthening due to a Hall-Petch effect of the type described originally by Embury and Fisher (1966). Rollet (1988) has restated the original Embury-Fisher model in the Kocks-Mecking-Estrin formalism as,

$$\theta = \frac{(\alpha\mu b)^2}{2\sigma} k d_o^{-1} \exp(\varepsilon/2) \qquad (5.59)$$

where d_o is the starting spacing between phases and ε is the imposed strain. In the limit of high strains this gives a hardening contribution that increases with stress approximately as,

$$\theta = \sigma/4 \qquad (5.60)$$

Thus, at high strains this mechanism will tend to maintain the hardening rate at a finite level.

The above discussion has shown that very high strengths can be obtained in materials that undergo a process of co-deformation. In such materials the strengthening mechanisms tend to suppress processes leading to instability because of the high ratio of hardening rate to flow stress. However, it is interesting to consider whether there are mechanisms in such materials that may act to destabilize the deformation and eventually lead to failure. This point will be considered next.

5.4.5 The Onset of Non-uniform Deformation in Tension and the Influence of Cr Fibres

It was shown above that one of the effects of the Cr fibres was to stabilize plastic flow in tension against macroscopic instabilities by increasing the work hardening rate of the material. However, at some point the condition for instability is reached and the sample begins to deform with a pattern of flow that is macroscopically inhomogeneous. In tension, the instability that eventually leads to failure is localized shear banding (figure 4.50). Similarly, when samples are deformed in plane strain compression (or equivalently in

rolling), macroscopically homogeneous deformation gives way to inhomogeneous deformation in the form of localized shear bands (figure 4.77 and 4.78). Shear bands are a common occurrence in rolled and plane strain compressed polycrystalline fcc metals (e.g. see Humphreys and Hatherly, 1995) but have also been observed to develop in single crystals of pure fcc metals oriented for duplex slip in tension (Siamoto et al., 1965, Puttick, 1963). In the case of the eutectic Cu-Cr material it is clear that the presence of the Cr fibres influences not only the strain at which instability is reached but the rate at which the material localizes once instability is reached.

This is shown quite clearly by a simple comparison between the behaviour of the fully eutectic material and the hypoeutectic material containing only ~ 10vol% eutectic (figure 4.41). The hypoeutectic specimen initially hardens at a slightly higher rate than it would if no fibres were present. Upon fibre yielding the hardening rate falls to approximately that of pure Cu and instability ensues with little further hardening. In contrast to the fully eutectic material, localization does not lead to a rapid load drop and subsequent shear failure. Instead the material progressively localizes into two conjugate bands in a manner similar to that observed by Siamoto et al. (1965) for pure Cu single crystals oriented for duplex slip. Final failure occurs by the formation and growth of a single internal void at the point were the two bands intersect (figure 4.41b). It appears that, although the Cr fibres initially aid in promoting stability of flow, once shear localization has begun the localization of strain into the bands occurs at a much faster rate than it would were there fewer (or no) fibres present.

The classical explanation for such behaviour in fibre reinforced materials is based on the idea that the large local strains within a shear band cause fibre fracture which subsequently allows for an acceleration of the localization process via the accumulation of damage along a shear band (e.g. see McClintock and Argon, 1966). This was the argument used by Hertzberg and Kraft (1963) to explain the rapid localization of strain during tensile testing of directionally solidified Cu-Cr specimens similar to those studied here. However, in that study the observation of fibre fracture was limited to one or two relatively low magnification optical micrographs taken from specimens whose surfaces were polished prior to being bent. From the observations presented in chapter 4 it appears clear that in the samples tested in this current study no brittle fracture of eutectic fibres was observed even after the onset of shear localization. This is clear from the series of

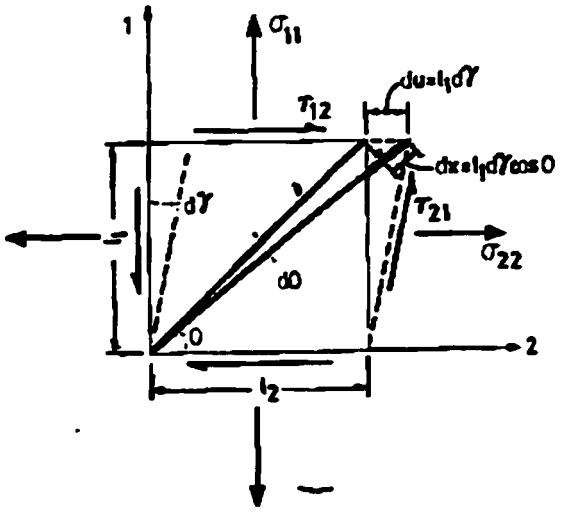

Figure 5.35 Geometry for a fibre rotating into a shear band (Zok, 1988).

micrographs presented in figure 4.49. Fibres plastically deform extensively into shear bands prior to rupturing plastically at the shear band/matrix interface. No voiding, decohesion or fracture was observed in the sample up to this point. Continued deformation leads to segments of the fibres lying within the shear bands rotating into the direction of shear and for macroscopic shear bands crossing the entire specimen to become visible to the naked eye.

In an analogous fashion, shear bands were observed to be the most predominant feature of specimens deformed in plane strain compression to Von Mises equivalent strains > 0.5. As with specimens deformed in uniaxial tension, the fibres deform into the bands prior to being segmented into the bands (figure 4.78). At high strains, the portions of fibre lying within the shear bands are oriented along the direction of shear.

A simple physical picture can be developed in order to explain the onset of shear banding in the eutectic alloy. The flow stress of the composite can be written as a simple rule of mixtures, both when the material is deformed in uniaxial tension and in simple shear (as in shear band),

$$\sigma = (1-f)\sigma_M + f\sigma_f \qquad (5.61)$$

In uniaxial tension the above equation, when coupled with the assumption of equal strain, is approximately true when the average fibre orientation is close to the tensile axis. However, as is seen in the compressive deformation of fibre reinforced composite, a small local rotation of fibres in the path of a shear band can substantially alter the ability of the fibres to contribute to the strengthening of the material. In the case of a shear band, equation 5.61 can be altered to account for this (Zok, 1988),

$$\sigma = (1-f)\sigma_m + f\sigma_f \frac{\sin 2\theta}{2} \qquad (5.62)$$

where θ is the angle between the fibre axis and the direction of shear. The angular factor in equation 5.62 accounts in an approximate fashion for the fact that load transfer becomes less effective to the fibres when they are misaligned. When deformation occurs within a shear band the action of the shear band will be to tend to rotate the segment of fibre lying within it into the shear band. From equation 5.62, as the angle between the direction of shear and the fibre axis decreases the degree of load transfer to the fibres decreases. Thus, in this manner a form of localized geometrical softening may be realized within the shear band.

The condition for localization within a shear band is stated as (Gil Sevillano et al., 1981),

$$\frac{d\bar{\sigma}}{d\bar{\varepsilon}} = 0 \qquad (5.63)$$

where the stress and strain in the above equation refer to effective quantities. Differentiating equation 5.62 one obtains,

$$\frac{d\sigma}{d\varepsilon} = (1-f)\frac{d\left(M_m \tau_m\right)}{d\varepsilon} + f\frac{d\sigma_f}{d\varepsilon} + f\sigma_f \cos 2\theta \frac{d\theta}{d\varepsilon} \qquad (5.64)$$

The rate of angular rotation of the fibre within the shear band can be obtained from figure 5.35 giving,

$$\frac{d\theta}{d\varepsilon} = -\tan\theta \qquad (5.65)$$

Substituting back into equation 5.64 results in,

$$\frac{d\sigma}{d\varepsilon} = (1-f)\left[\tau_m \frac{dM_m}{d\varepsilon} + M_m^2 \theta_m\right] + fM_f^2\theta_f - f\sigma_f \cos 2\theta \tan\theta = 0 \qquad (5.66)$$

Collecting terms that can lead to hardening within the band on the left hand side and terms that may contribute to softening on the right gives the condition for the onset of shear instability,

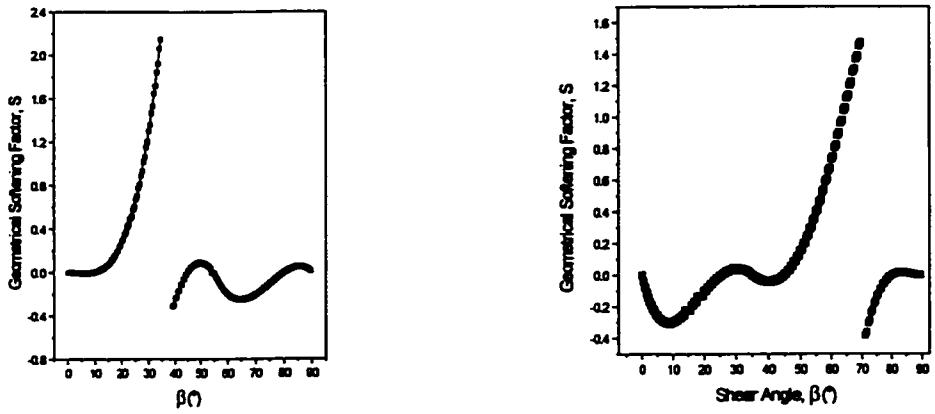

(a) (b)

Figure 5.36 Textural softening parameter for shear at an angle β to the a) tensile axis and b) rolling direction for the Cu in the material studied here. Several minima occur suggesting the possibility for shear localization.

$$(1-f)M_m^2\theta_m + fM_f^2\theta_f \approx M^2\theta = f\sigma_f \cos 2\theta \tan\theta - (1-f)\frac{\sigma_m}{M_m}\frac{dM_m}{d\varepsilon} \qquad (5.67)$$

where M and θ refer to an effective composite Taylor Factor (assuming similar values for M for matrix and fibre) and composite hardening rate.

Equation 5.67 shows that there are two possible modes by which geometrical softening may be obtained. First, as is commonly discussed in single-phase materials, textural softening may give rise to instability. The textural softening parameter proposed by Dillamore et al. (1979) as,

$$S = \frac{1}{M}\frac{dM}{d\varepsilon}\cos 2\theta \qquad (5.68)$$

can be computed for the Cu in specimens tested in plane strain compression and uniaxial tension. The predominant texture developed on plane strain compression is the Cu component (<111>{112}) while in uniaxial tension, approximately plane strain conditions develop by material elongating along <110> and contracting along <001> (see section 5.2.2). Using these ideal textures, the values of S for shear bands (characterized as bands of simple shear) at angles ranging from 0 to 90° from the rolling and tensile axes (β)

have been computed and plotted in figure 5.36. Softening (corresponding to negative values of S) occurs over various ranges of angles with minimum occurring at approximately 19° and 35° for both the plane strain compressed and tensile specimens. Yueng and Duggan (1986) have argued that plots such as that in figure 5.36 are ambiguous in that they contain discontinuities arising from cusps in the variation of M with β. However, for the purposes here it is sufficient to argue that textural softening exists and could potentially aid shear banding. The observations made on the plane strain compressed samples are similar to those made by others on plane strain compressed <111>{112} single crystals (Jasienski et al., 1996, Nakayama and Morii, 1982, Morii and Nakayama, 1981) suggesting that textural softening alone can account for the formation of shear bands in plane strain compression. However, in the case where aligned fibres, which continue to carry increasing stresses at large strains, are present a greater degree of softening will be necessary for the textural softening to outweigh the net rate of hardening.

The second route for softening is through fibre rotation within the shear band. At relatively large strains the inhomogeneous morphology of the Cr fibres developed during homogeneous deformation may lead to segments that are slightly misoriented with respect to the tensile axis. These regions may subsequently act as positions for the nucleation of micro bands. Once the density of these micro bands (formed within the diffuse neck of tensile specimens or in plane strain compressed samples) becomes sufficiently high within some volume a macroscopic shear band may be formed, spreading across a grain or the entire specimen. Subsequent deformation within the shear (or micro) bands will rotate the fibres into the bands in a manner similar to that seen in figure 4.78a. The shear flow stress is decreasing as this process continues. At some point plastic rupture at the fibre/matrix interface will occur. Once the fibre has been completely segmented from its lengths lying outside of the shear band the flow strength within the shear band will fall to that of the Cu matrix. This is due to the fact that the short fibre segment left within the shear band may (approximately) accommodate the shear strain within the shear band by a rigid rotation.

Similar arguments of a two-phase microstructure influencing the development of shear instabilities have been previously made (Piehler and Sematin, 1979, Yeung and Duggan, 1986, Yueng and Duggan, 1987, Nakayama and Morii, 1982, Morii and Nakayama, 1981, Zok, 1988). The argument made here closely

follows the argument made by Zok who observed shear localization in directionally solidified Ni-Ni_3Al eutectic deformed under large superimposed hydrostatic pressure. The difference between the behaviour of this material and the Cu-Cr eutectic studied here is that extensive fracture of the Ni_3Al was obvious in Zok's work. Thus, it is likely that fibre fracture and subsequent rotation of the fractured segments of the fibres into the shear band (at a flow stress essentially equivalent to the shear flow stress of the matrix) allows for the development of the shear bands. The effect of the superimposed hydrostatic pressure in this case causes the suppression of dilatational void growth at the point of fibre fracture thus allowing for the development of shear bands.

Finally, it is interesting to point out that the above discussion has relevance to current models for the formation of shear bands in single phase alloys. Morii and Nakayama (1981) suggested, in a qualitative manner, that shear bands formed in rolled Cu may be the result of local lattice "disturbances" associated with

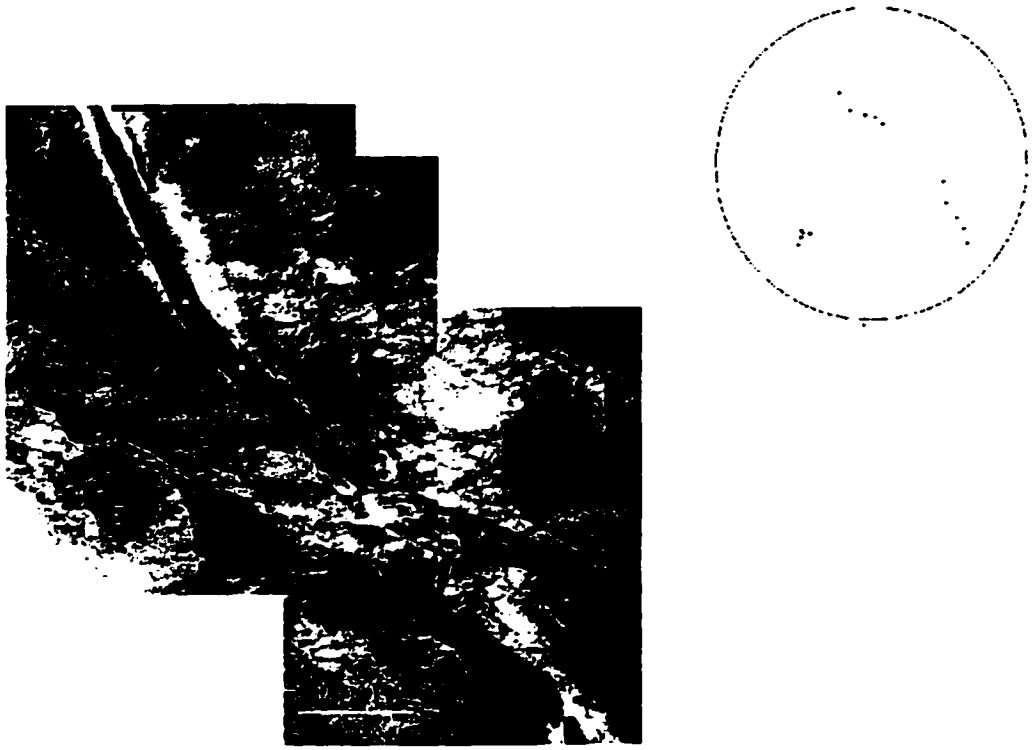

Figure 5.37 Orientation measurements made along the length of a Cr fibre deforming into a shear band in the neck of a tensile specimen. {100} pole figure in the upper right hand corner indicates the orientation of the points indicated in the micrograph. The tensile axis is vertical in both cases.

deformation twins (at low temperature) or the substructure in Cu alloys. Yueng and Duggan (1987) attempted to quantify this by using a simple model for internal necking in rolled laminates as a basis for understanding the nucleation of shear bands, and their resulting macroscopic angle to the rolling direction. If a composite view of the substructure developed in deformed single phase materials is adopted (e.g. see Sevillano, 1993) then the analogy between the case discussed above and rolled single-phase materials is clear. In rolled materials which have a substructure elongated along the rolling direction, the rotation of "hard" regions of the substructure (e.g. twins, cell walls, misoriented cells) into shear bands can lead to a process of progressive softening.

To this point little has been said about the detailed mechanisms which allow the Cr fibres to deform to such large strains within the shear bands. The micrographs presented in figure 4.78 suggest that the fibres lying within the shear bands undergo large plastic strains. One possible mechanism for the deformation of the

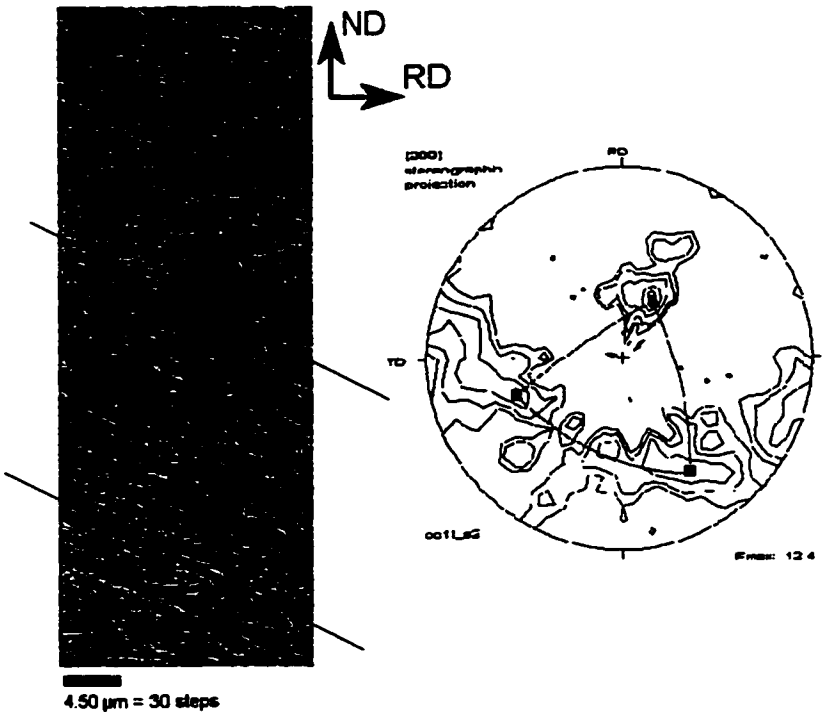

Figure 5.38 Measurements of Cr orientation within a shear band from a sample deformed in plane strain compression to a strain of 1.0. The image quality map for the region analyzed is shown on the left. The texture of the fibers, as indicated by the {100} pole figure on the right shows a weak texture with rotation of the texture approximately about the shear band normal. Note the similarity between the pole figure here and that shown in figure 5.37.

fibres into the shear bands is single slip within the fibres. This would require that the fibres be oriented such that a system is oriented along the shear band and would result in no lattice rotation and no storage of (geometrically necessary) dislocations within the fibres. Figure 5.37 shows that this does not occur. This image shows the same fibre as previously described in figure 4.74 and 4.75. This longitudinal TEM image was taken from within the neck of a sample solidified at 57 mm/hr and tested at 293 K. The shear band running across the fibre is apparent and the sharp deformation of the fibre into the band is apparent. At the point where the fibre bends into the shear band a series of dislocations are accumulated within the Cr fibre. Most of these dislocations appear to belong to a single slip system and form what appear to be simple tilt walls. A rough calculation of the radius of curvature of the fibre from this micrograph gives,

$$\phi \approx 9^0 \qquad (5.69)$$

From figure 4.75 an approximate dislocation density within the Cr fibre can be estimated as 4×10^{14} /m^2. Using this value and assuming that all of the dislocations are arranged into simple tilt walls gives a rotation of

$$\phi \approx \rho b = 5.5^0/\mu m \qquad (5.70)$$

which is within a factor of two of the value given in equation 5.69.

Measurements of lattice rotation in the Cr fibres deformed into the shear bands in samples deformed in plane strain compression and uniaxial tension show similar characteristics. Figure 5.38 shows EBSD measurements of lattice rotation made on ~150 fibres. Also shown in this plot are the approximate shear plane and shear plane normal. It appears that the lattice rotation occurs approximately about the shear plane normal, although a large amount of scatter occurs in the orientation measurements. Measurements made in the TEM on the sample shown in figure 5.37 show a similar characteristic rotation, although in this case it is more difficult to determine whether the rotation is about the shear plane normal. The most likely source of these rotations is that the portion of the fibre lying in the shear band attempts to rotate to orient its long direction along the direction of shear. As discussed above, once rotated into the direction of shear, the segments of fibres offer little resistance to further deformation along the shear band.

6. EXTENSIONS FOR FUTURE WORK

The work presented here uses well-controlled model materials to study basic aspects of co-deformation related both to the behaviour of dispersion hardened two-phase materials and the more recent work on heavily co-deformed two-phase materials. While the current study has helped to provide some insight into the regime of deformation linking the low and high strain behaviour, more experiments on this and other materials systems are necessary if a complete understanding of this complicated problem is to be obtained. Below, six possible extensions of this project are suggested.

i. *Large Strain Behaviour of Cu-Cr:* The present work has focused on the behaviour of directionally solidified materials tested in uniaxial tension with uniform strains ranging from 0 to ~0.5. Although larger strains were approached in the tests carried out in plane strain compression, the non-uniform flow field developed in this mode of deformation made a detailed analysis difficult. Thus, it would be interesting to deformation process the directionally solidified Cu-Cr eutectic alloys by wire drawing both at 293 K and 77 K. In this way, large strains may be imposed on the Cr fibres. These experiments would be of interest both in terms of probing the range of strains over which uniform co-deformation could be obtained, and in the mechanical properties that could be developed. Probing the limit to which the nearly constant rate of hardening can be maintained would be of particular interest. It would be expected that continued elastic loading of the fibres must reach a limit beyond which the fibres cannot continue to accept elastic strain. However, large strengths could be obtained in this material if this process were to continue in a uniform manner to strains of 1 - 2. Figure 6.1a shows a compilation of the hardening rates for various heavily co-deformed two phase materials over different strain regimes. Included as well is the hardening rate for the Cu-Cr system studied here. It is interesting to note that the hardening rates at high strains is lower in the highly co-deformed systems than in the Cu-Cr system studied here. Although the elastic strain data shown in figure 2.35 would suggest that the elastic loading of the embedded phase continues to contribute to the hardening behaviour of the heavily co-deformed two phase

	f(%)	E_f (GPa)	θ (MPa)	ε range	$\theta/E_f f$	Reference
Cu-Cr	15	250	83	0 - 8	0.002	Adachi et al. 1997
Cu-V	18	127	185	0 - 11	0.005	Bevk, 1983
Cu-Fe	30	212	133	5 - 7.5	0.002	Bevk, 1983
			400	7.5 - 9	0.006	
Cu-Nb	18.2	104	115	5.0 - 9.0	0.006	Spitzig et al., 1987
			425	9.0 - 11.0	0.023	
	20		70	0 - 9.0	0.003	
			225	9 - 12.0	0.011	
Cu-Ta	20	184	80	0 - 5.0	0.008	Spitzig et al., 1987
			300	5.0 - 10.0	0.008	
Cu-Ag	31	79	100	0 - 10.0	0.003	Frommeyer et al., 1975
Cu-Cr	2	250	200	0 - 0.3	0.04	This Work

(a)

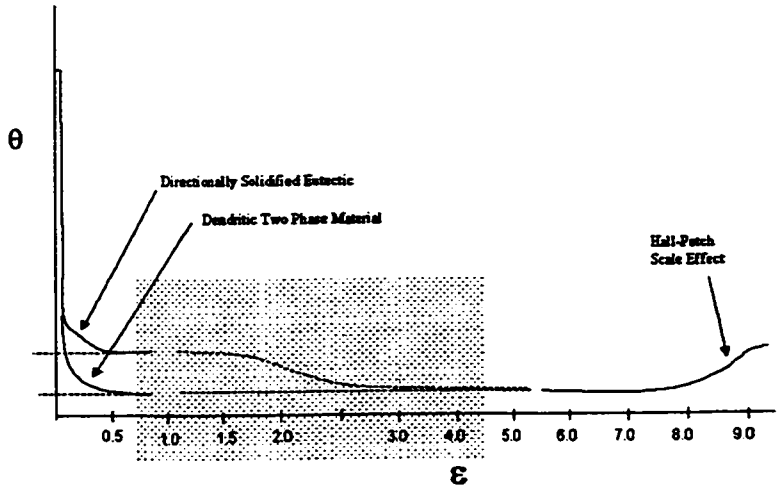

(b)

Figure 6.1 a) Table summarizing the hardening rate for a number of heavily co-deformed two phase materials. The hardening rate is also given normalized by the volume fraction of embedded phase and elastic modulus of the embedded phase. b) Schematic suggesting the manner in which the hardening rate varies with strain in the materials. It is particularly difficult to make extrapolations due to the lack of knowledge of the behaviour of these materials over the rage of strains between ~ 1.0 and 5.0 (shown as shaded box).

material, the lack of data over the range of strains from 1.0 - 5.0 makes it difficult to extrapolate this mechanism to the behaviour of the heavily co-deformed two phase materials.

In a practical sense, it would be interesting to evaluate the usefulness of this material as a candidate for high-strength conductors. Figure 6.1 shows a compilation of data on a number of high strength Cu based conductors. It is apparent that even at the low strains imposed in this work, the directionally solidified Cu-Cr material compares favourably with other candidate high-strength conductors. A particular advantage of the

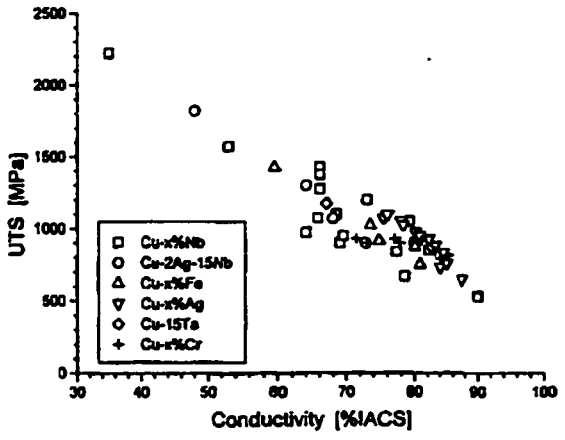

Figure 6.2 The strength and conductivity of a number of high strength conductors (Wood et al., 1997).

current material is that, unlike precipitation hardened materials and heavily co-deformed materials containing higher volume fractions of embedded phase, both the density of interfaces and the amount of solute in the material is relatively low favouring high conductivity. Further, because the Cr fibres in this case are present as aligned whiskers from the as-cast state, much lower applied strains should be necessary for an optimized strength/conductivity condition.

ii. Direct Measurements of Elastic Strains Carried by Cr Fibres: In the current investigation it was not possible to obtain unambiguous diffraction information from the Cr phase during in-situ straining. It would be well worth attempting these experiments again to make measurements on a diffraction system equipped with a position sensitive detector. This would greatly simplify the process of finding peaks to measure in the heavily deformed material. Further, measurements taken in this way would allow for peak shifting and broadening due to plastic deformation. In this sense it would be worth considering experiments performed on synchrotron x-ray beam lines.

iii. Examination of the Thermal Stability of Co-deformed Two-phase Materials with Particular Emphasis on Recrystallization and the Influence of Phase Interfaces: Theories for the nucleation of recrystallization in the presence of non-deforming inclusions are mature. Few experiments have been carried out to deduce the mechanisms of recovery/recrystallization in the presence of fine-scale co-deforming embedded phases. Studies on the thermal stability of heavily co-deformed two-phase materials have been limited (e.g. Sun et al., 1995, Wood, 1994) and mainly focused on the change of mechanical properties resulting from thermal treatments. It would be interesting to consider whether new processes driving recovery and/or recrystallization may exist in materials that are characterized by a high density of interfaces that are subjected to large tractions. One possibility may be that the interfaces themselves may act as sources of recrystallization

Figure 6.3 Overview BF TEM image showing partially recrystallized Cu-Cr.

nuclei. In this case the driving force would be the reduction of interfacial energy associated with the development of a new interfacial energy and orientation relationship. A similar process of boundary splitting as proposed for single-phase materials could be a mechanism for this process. A limited number of observations have been made during the course of this work on the recrystallization behaviour of rolled directionally solidified Cu-Cr. Figure 6.2 shows a low magnification BF TEM image showing the partially recrystallized microstructure. There is some evidence from these observations that recrystallization occurs by grains growing parallel to the axis of fibres. There does appear to be an interaction between fibres and the advancing recrystallization front as shown in figure 6.3. Recrystallization nuclei have been observed just ahead of the advancing recrystallization front at the phase interface. Figure 6.4 shows such a nuclei and the corresponding Kikuchi patterns in the surrounding regions. Further, it is interesting to note the presence of a high density of annealing twins in the recrystallized material and the fact that they are often bounded by two Cr fibres.

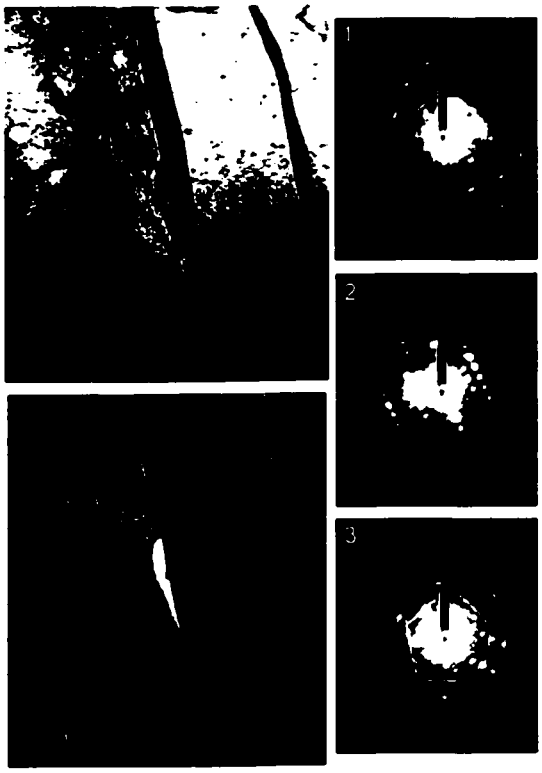

Figure 6.4 BF and DF images (left) at the recrystallization front showing a nuclei situated at the phase boundary. From the Kikuchi patterns and DF image it is clear that the nuclei has an orientation distinct from that of the recrystallized material on the opposite side of the fibre.

iv. Studies on the Functional Properties of As-cast and Co-deformed Eutectic Cu-Cr: Bulk Cr undergoes a second order magnetic phase transition at approximately 310 K. Below this temperature (the Néel temperature) Cr exhibits an incommensurate antiferromagnetic structure. When the length scale of metals approaches a small enough scale it is often possible to frustrate the system such that phase transitions or properties observed in the bulk state may be suppressed or enhanced, e.g. the influence of the proximity effect on causing a Cu-Ag-Nb containing only 4vol% Nb filaments to have a T_c close to that of bulk Nb (Raabe and Mattissen, 1999). In the case of directionally solidified Cu-Cr it would be interesting to observe the effect of the scale and internal stresses on the magnetic properties of the Cr fibres.

v. The Scale Dependence of the Competition Between Plasticity and Fracture in Embedded Phase: In this work, it has been suggested that the observation of fracture of Cr dendrites at 77 K versus the ductility of eutectic fibres at all observed temperatures suggests the presence of a scale dependent competition between fracture and plasticity. Further, there may be a dependence of the morphology and distribution of Cr phase on this process as suggested by Funkenbusch et al. (1989). A systematic study of this could be carried out by the production of off-eutectic materials by directional solidification such that the scale and morphology of the Cr phase could by varied from isolated dendrites embedded within a eutectic matrix to a percolated network structure of Cr surrounding eutectic. Further, it would be of interest to attempt to produce material by rapid solidification thereby allowing for a further reduction in the scale of the microstructure beyond what is possible from directional solidification. The tensile behaviour (in particular the damage of the Cr phase) could then be followed in a systematic manner with test temperature, phase morphology, and microstructural scale.

vi. Studies on the Co-deformation Behaviour of Other Directionally Solidified Eutectic Alloys: In many ways the low volume fraction of Cr phase in the Cu-Cr eutectic makes the observation of their behaviour by simple experimental techniques difficult. It would be worth extending this work to other simple binary fcc/bcc directionally solidified eutectic alloys. Of particular interest would be the systems of Ni-W and Ni-Cr. Both systems have much higher volume fractions of eutectic phase than the Cu-Cr system.

7. CONCLUSIONS

The work presented here is a starting point or framework for further detailed examinations of the co-deformation of two-phase materials using simple model material systems. It has been shown that simple material systems can be used to examine the important processes involved in poly-phase plasticity problems under well-controlled conditions. This approach offers a great advantage over studies on heavily co-deformed materials in the sense that it avoids the complicated deformation history necessary to produce the high-strength fine-scale microstructure. In the present case this approach has proven that it is possible to relate the details regarding the deformation behaviour to the mechanisms that operate on different length scales within the microstructure. In this way it has been possible to follow the deformation behaviour throughout the entire range of imposed strain.

Specifically, a directionally solidified Cu-Cr eutectic alloy has been produced and characterized at multiple length scales so as to act as a well defined starting point for further co-deformation studies. It was found that the eutectic solidifies so as to produce defect free sub-micron fibres of Cr embedded within a coarse grained, highly textured Cu matrix. The fibres are well aligned with the macroscopic axis of the ingot, although variations in growth direction can be associated with individual grains. Thermal residual stresses do exist resulting from the differential contraction of the two species on cooling from solidification. However, processes of plastic relaxation in the matrix appear to reduce these stresses. On the microscopic scale, the fibres and matrix exhibit a well defined Kurdjumov-Sachs orientation relationship that gives rise to preferred habit planes and growth directions for fibres. The crystallography of the two phases appears to be the same as that deduced for solid state precipitates of Cr in Cu.

The deformation behaviour of this model two phase material has highlighted a number of important and interesting aspects of the process of co-deformation in materials consisting of phases with very different mechanical responses. First, it has been observed that extensive co-deformation is possible between the Cu

and Cr phases although Cr in its bulk form is a nominally brittle metal. This is apparently linked both to the embedded nature of the Cr fibres as well as to their fine scale. The macroscopic result of the co-deformation of these two phases is that high strengths and ductility are obtained for a relatively low volume fraction of Cr phase. The key to understanding these mechanical properties appears to be the influence of the phase interface on plasticity. This is particularly true for the Cr fibres where it is observed that the presence of the phase interface inhibits the normal processes of dislocation storage observed in bulk materials. Instead, the phase interface is observed to control both the processes of nucleation and storage of dislocations for the Cr fibres. Thus, relations normally used to describe the dependence of flow stress on dislocation density are inappropriate for this phase. In this case a simple continuum view of load transfer is insufficient and instead it is the detailed process of the transfer of plasticity that must be considered. The process of interface controlled plasticity results in a small but continued accumulation of unrelaxed plastic misfit between the two phases. The continued storage of elastic strain in the fibres is quite remarkable considering the high stresses that are developed in the embedded phase with continued plastic straining. It is this continued plastic misfit that causes the hardening rate of the bulk material to be maintain at a significant level compared to most pure metals that approach a saturation stress at relatively low strains in uniaxial tension. Further experiments are needed to probe the behaviour of these simple model materials at larger strains in order to evaluate the effectiveness of this mechanism at strengthening materials after large reductions. Detailed modelling of the processes that occur at the atomic level within the interface will be invaluable to helping to understand the complex phenomena associated with bulk mechanical properties that are controlled not by normal processes of dislocation storage and annihilation, but by the mechanisms of plasticity that is controlled by the phase interface.

BIBLIOGRAPHY

Abel, A., *Mat. For.*, 1987, vol. 10, no.1, p. 11.

Adachi, K., Sumiyuki, T., Takeuchi, T., Suzuki, H. G., *J. Japan Inst. Metals*, 1997a, vol. 61, p. 397.

Adachi, K., Sumiyuki, T., Takeuchi, T., Suzuki, H. G., *J. Japan Inst. Metals*, 1997b, vol. 61, p. 391.

Adnyana, D. N., Ph. D. Thesis, Katholieke Universiteit Leuven, 1982.

Allen, A. J., Bourke, M. A. M., Dawes, S., Hutshings, M. T., Withers, P. J., *Acta Metall. Mater.*, 1992, vol. 40, p. 2361.

Allen, A. J., Hutchings, M. T., Windsor, C. G., *Adv. Phys.*, 1985, vol. 34, p. 445.

Anderson, P. M., Foecke, T., Hazzledine, P. M., *MRS Bull.*, 1999, vol. 24, p. 27.

Ashby, M. F., in *Strengthening Methods in Crystals*, A. Kelly, R. B. Nicholson, eds., Wiley, New York, 1971, p. 137.

Atkinson, J. D., Brown, L. M., Stobbs, W. M., *Phil. Mag.*, 1974, vol. 30, p. 1247.

Bacon, G. E., *Neutron Diffraction*, Clarendon Press, Oxford, 1975.

Bazinski, Z. S., Basinski, S. J., in *Dislocations in Solids*, F. R. N. Nabarro ed., Ch. 16., North-Holand, New York, 1979.

Bergmann, H. W., Frommeyer, G., Wassermann, G., in *Textures of Materials: Proc. of the Fifth Int. Conf. on Textures of Materials*, G. Gottsteain, K. Lucke eds., Springer-Verlag, Berlin, 1978, p. 371.

Bevk, J., *Ann. Rev. Mater. Sci.*, 1983, vol. 13, p. 319.

Bevk, J., Harbison, J. P., Bell, J. L., *J. Appl. Phys.*, 1978, vol. 49, p. 6031.

Brenner, S. S., in *Growth and Perfection of Whiskers*, R. H. Doremus, B.W. Roberts, D. Turnbull eds., Wiley, 1958, p. 157.

Brenner, S. S., *J. Appl. Phys.*, 1956, vol. 27, p. 1484.

Brenner, S. S., *J. Appl. Phys.*, 1957, vol. 28, p. 1023.

Brokmeier, H. G., *Mater. Sci. For.*, 1994, vol. 157-162, p. 59.

Brown, L. M., Clarke, D. R., *Acta Metall.*, 1975, vol. 23, p. 821.

Brown, L. M., Clarke, D. R., *Acta Metall.*, 1977, vol. 25, p. 563.

Brown, L. M., *Scripta Metall.*, 1977, vol. 11, p. 127.

Brown, L. M., Stobbs, W. M., *Phil. Mag.*, 1971, vol. 23, p. 1201.

Brown, L. M., Stobbs, W. M., *Phil. Mag.*, 1976, vol. 34, p.351.

Bullen, F. P., Hutchison, M. M., *Phil. Mag.*,1962, vol, 7, p. 557.

Bullen, F. P., Hutchison, M. M., *Phil. Mag.*,1963, vol. 8, p. 461.

Bullen, F. P., Rogers, C. B., *Phil. Mag.*,1964 a, vol. 9, p. 401.

Bunge, H.-J., *Z. Metallkd.*, 1985, vol. 76, p. 92.

Cabrera, N., Price, P. B., in *Growth and Perfection of Whiskers*, R. H. Doremus, B.W. Roberts, D. Turnbull eds., Wiley, 1958, p. 157.

Carroll, H. E., Whitehouse, A. F., *Scripta Mater.*, 2000, vol. 42, p. 1133.

Carter, D. H., Bourke, M. A. M., *Acta Mater.*, 2000, vol. 48, p. 2885.

Carter, D. H., Ph.D. Thesis, University of California, 1999.

Chakrabarti, D. J., Laughlin, D. E., *Bull. Alloy Phase Diag.*, 1984, vol. 5, p. 59.

Cheskis, H. P., Heckel, R. W., in *Metal Matrix Composites, ASTM STP 438*, 1968, p. 76.

Cheskis, H. P., Heckel, R. W., *Met. Trans.*, 1970, vol. 1, p. 1931.

Clarke, D. R., Lilholt, H., *Scripta Metall.*, 1975, vol. 9, p. 93.

Clarke, D. R., Stobbs, W. M., *Metals Sci.*, 1974, vol. 8, p. 242.

Clausen, B., Ph. D. Thesis, Technical University of Denmark, 1997.

Clyne, T. W., Withers, P. J., Introduction to Metal Matrix Composites, Cambridge, New York, 1993.

Cooper, G. A., *J. Mech. Phys. Solids*, 1966, vol. 14, p. 103.

Cottrell, A. H., *The Mechanical Properties of Matter*, Wiley, New York, 1964.

Cottrell, A. H., Stokes, R. J., *Proc. Roy. Soc. A*, 1955, vol. 233 A, p. 17.

Dahmen, U., *Acta Met.*,1982, vol. 30, p. 63.

Dahmen, U., *Scripta Metall.*, 1981a, vol. 15, p. 73.

Dahmen, U., *Scripta Metall.*, 1981b, vol. 15., p. 77.

Davies, G. V., in *Strengthening Methods in Crystals*, A. Kelly, R. B. Nicholson, eds., Wiley, New York, 1971, p. 485.

Deschamps, A., M. Eng. Thesis, McMaster University, 1994.

Dillamore, I. L., Roberts, J. G., Bush, A. C., *Met. Sci.*, 1979, p. 73.

Dunand, D. C., Mortensen, A., Acta Metall. Mater., 1991a, vol. 39, p. 1405.

Dunand, D. C., Mortensen, A., Acta Metall. Mater., 1991b, vol. 39, p. 1417.

Dunsmuir, P., *Brit. J. of App. Phys.*, 1952, vol. 3, p. 264.

Edington, J. W., *Practical Electron Microscopy in Materials Science*, Van Nostrand Reinhold Co., New York, 1976.

Embury, J. D., Fischer, R. M., *Acta Met.*, 1966, vol. 14, p. 147.

Embury, J. D., Hirth, J. P., *Acta Metall. Mater.*, 1994, vol. 42, p. 2051.

Engler, O., Hirsch, J., Lücke, K., *Z. Metallkd.*, 1995, vol. 86, p. 475.

Eshelby, J. D., *Proc. Roy. Soc.*, 1957, vol. A241, p. 376.

Eshelby, J. D., in *Prog. Solid Mech.*, I. N. Sneddon and R. Hill eds., 1961, p. 89.

Estrin, Y., Mecking, H., *Acta Metall.*, 1984, vol. 32, p. 57.

Estrin, Y., in *Unified Constitutive laws of Plastic Deformation*, A. S. Krausz and K. Krausz eds., Academic Press, San Diego, 1996, p. 69.

Everett, R. K., *Scripta Metallurgica*, 1988, vol. 22, p. 1227.

Fat-Halla, N., Takasugi, T., Izumi, O., *Trans. Met. Soc. AIME*, 1979, vol. 10A, p. 1341.

Frommeyer, G., Wassermann, G., *Acta Metall.*, 1975, vol. 23, p. 1353.

Fujii, T., Nakazawa, H., Kato, M., Dahmen, U., *Acta Mater.*, 2000, vol. 48, p. 1033.

Funkenbusch, P. D., Courtney, P. D., *Scripta Metallurgica,* 1989, vol. 23, p. 1719.

Funkenbusch, P. D., Courtney, T. H., Kubisch, D. G., *Scripta Metallurgica*, 1984, vol. 18, p. 1099.

Garmong, G., J. *Mater. Sci.*, 1976, vol. 11, p. 328.

Garmong, G., Williams, J. C., *Metall. Trans*, 1975, vol. 6A, p. 1711.

George, F. D., Ford, J. A., Salkind, M. J., *Metal Matrix Composites,* STP 438, ASTM, Philadelphia, 1968, p. 59.

Gilbert, A., Reid, C. N., Hahn, G. T., *J. Inst. Metals*, 1963, vol. 92, p. 351.

Godfrey, A., Hu, D., Loretto, M. H., *Phil. Mag. A*, 1998, vol. 77, no. 2, P. 287.

Gould, D., Martin, J. W., *In-Situ Composites*, National Materials Advisory Board, NMAB-303-11, Washington, D.C., vol. 1, 1973, p. 225.

Hall, M. G., Aaronson, H. I., *Acta Metall.*, 1986, vol. 34, p. 1419.

Hashin, Z., Rosen, B. W., *J. App. Mech.*, 1964, vol. 31E, p. 223.

Henager Jr., C. H., Heinisch, H. L., Kurtz, R. J., Hoagland, R. G., *Mat. Res. Soc. Symp. Proc.*, 2001, vol. 634, p. B4.8.1.

Herring, C., Galt, J. K., *Phys. Rev.*, 1952, vol. 85, p. 1060.

Hertzberg, R. W., Kraft, R. W., *Trans. Met. Soc. AIME*, 1963, vol. 227, p. 580.

Hertzberg, R. W., Lemkey, F. D., Ford, J. A., *Trans. Met. Soc. AIME*, 1965, vol. 233, p. 342.

Hertzberg, R.W., *Transactions of the ASM*, 1964, vol. 57, p. 434.

Hertzberg, R. W., in *Mechanical Properties of Metallic Composites*, S. Ochiai ed., Marcel Dekker, New York, 1993, p. 350.

Hirth, J. P., Loethe, J., Theory of Dislocations, McGraw-Hill, New York, 1986.

Hogan, L. M., Kraft, R. W., Lemkey, F. D., *Advan. Mater. Res.*, 1971, vol. 5, p. 83.

Holden, T. M., *J. Neutron Research*, 1999, vol. 7, p. 291.

Hong, Sun I. G., Hill, M. A., Sakai, Y., Wood, J. T., Embury, J. D., *Acta Metall. Mater.*, 1995, vol. 43, p. 3313.

Hosford, W. F., *Trans. Met.*, 1964, vol. 230, p. 12.

Humphreys, F. J., Hatherly, M., *Recrystallization and Related Annealing Phenomena*, Pergamon, Oxford, 1995.

Jackson, P. W., Cratchley, D., *J. Mech. Phys. Solids*, 1966, vol. 14, p. 49.

Jasienski, Z., Baudin, T., Piatkowski, A., Penelle, R., *Scripta Mater.*, 1996, vol. 35, no. 3, p. 397.

Janecek, M., Louchet, F., Doisneau-Cottignies, B., Brechet, Y., *Phil. Mag. A*, 2000, vol. 80, p. 1605.

Jin, Y., Adachi, K., Takeuchi, T., Suzuki, H. G., *Mater. Sci. Eng.*, 1996, vol. A212, p. 149.

Jones, O., *Phil. Mag.*, 1924, vol. 48, p. 207.

Kelly A., MacMillan, N. H., *Strong Solids*, Clarendon Press, New York, 1986.

Kelly, A, in *Strengthening Methods in Crystals*, A. Kelly, R. B. Nicholson eds., Wiley, New York, 1971.

Kelly, A., Davies, G. J., *Met. Rev.*, 1965, vol. 10, p. 1.

Kelly, A., *Met. Trans.*, 1972, vol. 3, p. 2313.

Kelsey, R. H., in *Whisker Technology*, A. P. Levitt ed., Wiley-Interscience, New York, 1970, p. 135.

Kocks, U. F., *Met. Trans.*, 1970, vol. 1, p. 1121.

Kocks, U. F., *J. Eng. Mater. Technol.*, 1976, vol. 98, p. 76.

Kocks, U. F., Tome, C. N., Wenk, H.-R., *Texture and Anisotropy*, Cambridge University Press, 1998.

Köstor, W., *Z. Metallkde.*,1948, vol. 39, p. 145.

Kubisch, D. G., Courtney, T. H., *Met. Trans.*, 1986, vol. 17A, p. 1165.

Kung, H., Jervis, T. R., Hirvonen, J. P,Embury, J. D., Mitchel, T. E., Nastasi, M., *Phil. Mag. A*, vol. 71, p. 759.

Kraft, R. W., *J. Metals*, 1966, vol. 8, p. 192.

Lahaie, D., Ph.D. Thesis, McMaster University, 1998.

Langford, G., *Met. Trans.*, 1977, vol. 8A, p. 861.

Lasalmonie, A., Martin, J. W., *Scripta Metall.*, 1974, vol. 8, p. 377.

Lavelle, B., *J. of Crystal Growth*, 1987, vol. 85, p. 440.

Lee, K. L., Carroll, H. E., Whitehouse, A. F., *Mater. Sci. Tech.*, 2000, vol. 16, p. 811.

Lemkey, F. D., Hertzberg, R. W., Ford, J. A., *Trans. Met. Soc. AIME*, 1965, vol. 233, p. 334.

Lilholt, H., *Acta Metall.*, 1977a, vol. 25, p. 571.

Lilholt, H., *Acta Metall.*, 1977b, vol. 25, p. 587.

Lilholt, H., in *Mechanical Properties of Metallic Composites*, S. Ochiai ed., Marcel Dekker, New York, 1993, p. 389.

Louchet, F., in *Constitutive and Damage Modeling of Inelastic Deformation and Phase Transformation, Proc. of Plasticity '99, 7th Intern. Symp. on Plasticity and its Current Applications*, A. S. Khan ed., Neat, Maryland, 1998, p. 585.

Luo, C. P., Dahmen, U., *Acta Mater.*, 1998, vol. 46, p. 2063.

Luo C. P., Dahmen, U., Westmacott, K.H., *Acta Metall. Mater.*, 1994, vol. 42, p. 1923.

Marcinkowski, M. J., Lipsitt, H. A., *Acta Metall.*, 1962, vol. 10, p. 95.

McLean, M., *Directionally Solidified Materials For High Temperature Service*, The Metals Society, 1983.

McClintock, F. A., Argon, A. S., Mechanical Behaviour of Materials, Addison-Wesley, New York, 1966.

Mecking, H., in *Work Hardening in Tension and Fatigue*, A. W. Thompson ed., New York, TMS AIME 1977, p. 67.

Mecking, H., Nicklas, B., Zarubova, N., Kocks, U. F., *Acta Metall.*, 1986, vol 34, p. 527.

Mecking, H., Kocks, U. F., *Acta Metall.*, 1981, vol. 29, p. 1865.

Misra, A., Gibala, R., *Metall. Mater. Trans. A.*, 1999, vol. 30, p. 991.

Misra, A., Hirth, J. P., Kung, H., Hoagland, R. G., Embury, J. D., *Mat. Res. Soc. Symp.*, 2001, vol. 634, p. B4.2.1.

Misra, A., Verdier, M., Lu, Y. C., Kung, H., Mitchell, T. E., Nastasi, M., Embury, J. D., *Scripta Mater.*, 1998, vol. 39, p. 555.

Moan, G. D., Ph.D. Thesis, McMaster University, 1977.

Morii, K., Nakayama, Y., *Trans. JIM*, 1981, 1981, vol. 22, p. 857.

Nakayama, Y., Morii, K., *Trans. JIM*, 1982, vol. 23, p. 422.

Nittono, O., *Jpn. J. Appl. Phys.*, 1971, vol. 10, p. 188.

Nix, W. D., *Metall. Trans. A*, 1989, vol. 20A, p. 2217.

Nohara, A., *Jpn. J. Appl. Phys.*, Part I, 1982, vol. 21, p.1287.

Ozturk, T., Mirmesdagh, J., Ediz, T., *Mater. Sci. Eng.*, 1994, vol. A175, p. 125.

Pearson, W. B., *A handbook of lattice spacings and structures of metals and alloys*, Pergamon, London, 1967.

Pragnell, P. B., Stobbs, W. M., Withers, P. J., *Mater. Sci. Eng.*, 1992, vol. A159, p. 51.

Pragnell, P.B., Downes, T., Withers, P. J., Lorentzen, T., *Mater. Sci. Eng.*, 1995, vol. A197, p. 215.

Puttick, K. E., *Acta Metall.*, 1963, vol. 11, p. 986.

Raabe, D., Heringhaus, F., Hangen, U., Gottstein, G., *Z Metalkd.*, 1995, vol. 86, p. 405.

Raabe, D., Mattissen, D., *Acta Mater.*, 1999, vol. 47, p. 769.

Randle, V., Engler, O., *Introduction to Texture Analysis: Macrotexture, Microtexture, and Orientation Mapping*, Gordon and Breach, Netherlands, 2000.

Rao, S. I., Hazzledine, P. M., *Phil. Mag. A*, 2000, vol. 80, p. 2011.

Rao, S. I., Hazzledine, P. M., *Scripta Mater.*, 2000, vol. 41, p. 1085.

Reid, C. N., Gilbert, A., Hahn, G. T., *Trans. Met. Soc. AIME*, 1967, vol. 239, p. 467.

Rollet, A. D., Ph. D. Thesis, Drexel University, 1988.

Rosen, B. W., Friedman, E., in *Whisker Technology*, A. P. Levitt ed.,Wiley-Interscience, New York, 1970.

Russell, A. M., Chumbley, S., Tian, Y., *Adv. Eng. Mat.*, 2000, vol. 2, p. 11.

Saimoto, S., Hosford Jr., W. F., Backofen, W. A., Phil. Mag., 1965, vol. 12, p. 319.

Salkind, M.J., Lemkey, F. D., George, F. D., in *Whisker Technology*, A. P. Levitt ed., Wiley-Interscience, New York, 1970, p. 343.

Semiatin, S. L., Peihler, H. R., *Met. Trans. A*, 1979, vol. 10A, p. 1107.

Gil Sevillano, J., in *Materials Science and Technology, A comprehensive Treatment*, vol. 6, R. W. Cahn, P. Haasen, E. J. Kramer eds., Ch. 2, 1993.

Gil Sevillano, J., Van Houtte, P., Aernoudt, E., *Prog. Mat. Sci.*, 1981, vol. 25, p. 69.

Sowerby, R., Uko, D. K., Tomita, Y., *Mater. Sci. Eng.*, 1987, vol. 141, p. 43.

Spitzig, W. A., Krotz, P. D., *Acta Metall.*, 1988, vol. 36, p. 1709.

Spitzig, W. A., Krotz, P. D., *Scripta Metallurgica*, 1987, vol. 21, p. 1143.

Spitzig, W. A., Pelton, A. R., Laabs, F. C., *Acta Metall.*, 1987, vol. 35, no. 10, p. 2427.

Stobbs, W. M., Paetke, S., *Acta Metall.*, 1985, vol. 33, p. 77.

Strid, J., Easterling, K. E., *Scand. J. of Metall.*, 1982, vol. 11, p. 295.

Suri, S., Viswanathan, G. B., Neeraj, T., Hou, D.-H., Mills, M. J., *Acta Mater.*, 1999, vol. 3, p. 1019.

Sutton, A. P., Balluffi, R. W., *Interfaces in Crystalline Materials*, Oxford, New York, 1995.

Taylor, G. I., *J. Inst. Metals*, 1938, vol. 62, p. 307.

Thilly, L., Ph.D. Thesis, l'Institut National des Sciences Appliquees de Toulouse, 2000.

Verhaeghe, B., Brechet, Y., Louchet, F., Massoud, J. P., Touzeau, D., *Phys. Stat. Sol. (a)*, 1996, vol. 153, p. 47.

Wassermann, G., Bergmann, H. W., Frommeyer, G., in *Textures of Materials: Proc. of the Fifth Int. Conf. on Textures of Materials*, G. Gottsteain, K. Lucke eds., Springer-Verlag, Berlin, 1978, p. 37.

Wassermann, G., *Z. Metallkde*, 1973, vol. 64, p. 844.

Weatherly, G. C., Humble, P., Borland, D., *Acta Metall.*, 1979, vol. 27., p. 1815.

Weatherly, G. C., Zhang, W. -Z., *Metall. Mater. Trans. A.*, 1994, vol. 25 A, p. 1865.

Webb, W. W., Forgeng, W. D., *Acta Metall.*, 1958, vol. 6, p. 462.

Williams, J. C., Garmong, G., *Proceedings of the Conference on In Situ Composites, National Research Council*, 1973, p. 149.

Wilcox, D., Dove, B., McDavid, D., Greer, D., *ImageTool*, University of Texas Health Science Center, San Antonio Texas, ver. 2.00, 1996.

Wilson, D. V., Konnan, Y. A., *Acta Metall.*, 1964, vol. 12, p. 617.

Withers, P. J., Stobbs, W. M., Pederson, O. B., *Acta Metall. Mater.*, 1989, vol. 37, p. 3061.

Wlodek, S. T., Webb, W. W., Forgeng, W. D., *J. Metals*, 1959, vol. 11, p. 590.

Wood, J. T., Embury, J. D., *Fatigue Fract. Engng. Mater. Struct.*, 1995, vol. 18, no 7-8, p. 747.

Wood, J. T., Ph.D. Thesis, McMaster University, 1994.

Wood, J. T., Griffin, A. J., Embury, J. D., Zhou, R., Nastasi, M., Veron, M., *J. Mech. Phys Solids*, 1996, vol. 44, p. 737.

Yeung, W. Y., Duggan, B. J., *Acta Metall.*, 1987, vol. 35, no. 2, p. 541.

Yeung, W. Y., Duggan, B. J., *Mater. Sci. Technol.*, 1986, vol. 2, p. 552.

Yoshida, K., Goto, Y., Yamamoto, M.., *J. Phys. Soc. Japan*, 1966, vol. 21, p. 825.

Young, C. T., Steele, J. H., Lytton, J. L., *Met. Trans.*, vol. 2, p. 2081.

Yurgartis, S. W. Comp. Sci. Tech., vol. 30, 1987, p. 279.

Zener, C., Trans. AIME, vol. 167, 1946, p. 550.